

# **Wave Propagation and Scattering in Communication, Microwave Systems and Navigation**

A conference of ITG Commission 7.5 "Wave Propagation"  
25<sup>th</sup> – 27<sup>th</sup> November 2009

---

## Conference Proceedings

---

Conference Venue: Günnewig Hotel Chemnitzer Hof  
Theaterplatz 4  
09111 Chemnitz  
Germany

**ITG** INFORMATION TECHNOLOGY  
SOCIETY WITHIN VDE



CHEMNITZ UNIVERSITY  
OF TECHNOLOGY

*Proceedings of Wave Propagation and Scattering in Communication,  
Microwave Systems and Navigation, WFMN09, Chemnitz, Germany.*

Edited by Prof. Dr. rer. nat. Madhukar Chandra

Published by Universitätsverlag der Technischen Universität Chemnitz, 2010

ISBN 978-3-941003-25-5

## Conference Board

### *General Chairman*

Prof. Dr. rer. nat. Wolfgang Keydel

### *Scientific Committee*

Prof. Dr. rer. nat. Madhukar Chandra (TU Chemnitz)

Prof. Dr.-Ing. Gerd Wanielik (TU Chemnitz)

Prof. Dr.-Ing. Thomas Kürner (TU Braunschweig)

### *Conference Committee*

Dr. Ute Böttger (DLR, Berlin)

Dr.-Ing. Andreas Danklmayer (DLR, Oberpfaffenhofen)

Dipl.-Ing. Ferdinand Gerhardes (Agilent Technologies)

Dr. Frank Gekat (SELEX Sistemi Integrati, Gematronik Weather Radar Systems, Neuss)

Dr. Achim Hornbostel (DLR, Oberpfaffenhofen)

Dipl.-Ing. Karl Nestler (TU Chemnitz)

Dipl.-Ing. Tobias Otto (TU Delft)

Dr. Achim Quellmalz (Südwestrundfunk, Baden-Baden)

Dr.-Ing. Volker Schanz (ITG, VDE)

Dipl.-Ing. Jörg Steinert (TU Chemnitz)

Dipl.-Ing. Patrick Tracksdorf (TU Chemnitz)

Dipl.-Ing. Ralf Zichner (Fraunhofer ENAS)

### *Conference Organisation*

Prof. Dr. rer. nat. Madhukar Chandra (Chairman, ITG-Commission 7.5)

Dr. Volker Schanz (Managing Director, ITG)

### *Conference Support Staff*

Jana Vießmann (TU Chemnitz)

Eileen Raudnitschka (TU Chemnitz)

## Authors Index

### A

Antreich, F. WFMN09\_III\_C4 p. 102

### B

Bachmann, M. WFMN09\_I\_C2 p. 20  
 Bamler, R. WFMN09\_I\_A3 p. 5  
 Baumann, R. WFMN09\_I\_B3 p. 13  
 Bauschert, T. WFMN09\_II\_C1 p. 50  
 Böer, J. WFMN09\_I\_C2 p. 20  
 Bonitz, F. WFMN09\_I\_C1 p. 14  
 Böttger, U. WFMN09\_III\_B1 p. 87

### C

Chandra, M. WFMN09\_II\_B3 p. 40  
 WFMN09\_II\_B4 p. 45  
 WFMN09\_II\_B5 p. 49  
 WFMN09\_II\_D1 p. 51  
 WFMN09\_III\_B2 p. 88  
 Chee, K.L. WFMN09\_III\_C3 p. 95  
 Chwala, C. WFMN09\_II\_D2 p. 58

### D

Danklmayer, A. WFMN09\_III\_A1 p. 75  
 Dreher, A. WFMN09\_I\_B2 p. 12  
 Dreyßig, S. WFMN09\_III\_B2 p. 88

### E

Eibert, T. WFMN09\_II\_D2 p. 58

### F

Fiedler, H. WFMN09\_I\_C2 p. 20  
 Fišer, O. WFMN09\_III\_A2 p. 83

### G

Geise, A. WFMN09\_I\_B1 p. 6  
 Gergis, L.F. WFMN09\_III\_C2 p. 94

### H

Hagen, M. WFMN09\_II\_B1 p. 35  
 WFMN09\_II\_B5 p. 49  
 Helbig, M. WFMN09\_I\_C1 p. 14  
 Herrmann, R. WFMN09\_I\_C1 p. 14  
 Hipp, S. WFMN09\_II\_D2 p. 58  
 Hirtz, G. WFMN09\_III\_D1 p. 109  
 Hornbostel, A. WFMN09\_II\_A1 p. 25  
 WFMN09\_III\_C4 p. 102  
 Hübers, H.W. WFMN09\_III\_B1 p. 87  
 Hueso Gonzales, J. WFMN09\_I\_C2 p. 20

### J

Jacob, A. WFMN09\_I\_B1 p. 6

### K

Keydel, W. WFMN09\_I\_A2 p. 4  
 Kmec, M. WFMN09\_I\_C1 p. 14  
 Krieger, G. WFMN09\_I\_C2 p. 20  
 Kuhlmann, K. WFMN09\_I\_B2 p. 6  
 Kunstmann, H. WFMN09\_II\_D2 p. 58  
 Kupfer, K. WFMN09\_I\_C1 p. 14  
 Kürner, T. WFMN09\_I\_A1 p. 1  
 WFMN09\_III\_C3 p. 95

### L

Leonhardt, V. WFMN09\_II\_E2 p. 60  
 Lietz, H. WFMN09\_II\_E3 p. 67

### M

Mathar, R. WFMN09\_III\_C1 p. 89

### O

Otto, T. WFMN09\_II\_D1 p. 51

### R

Rauschenbach, P. WFMN09\_I\_C1 p. 14  
 Reimann, J. WFMN09\_II\_B2 p. 36  
 Reyer, M. WFMN09\_III\_C1 p. 89

### S

Sachs, J. WFMN09\_I\_C1 p. 14  
 Schilling, K. WFMN09\_I\_C1 p. 14  
 Schröder, F. WFMN09\_III\_C1 p. 89  
 Siart, U. WFMN09\_II\_D2 p. 58  
 Steinert, J. WFMN09\_II\_B3 p. 40  
 Steingaß, A. WFMN09\_II\_A2 p. 34  
 Suchy, O. WFMN09\_II\_B4 p. 45

### T

Thomanek, J. WFMN09\_II\_E3 p. 67  
 Tracksdorf, P. WFMN09\_II\_B5 p. 49

### V

Vergara, M. WFMN09\_III\_C4 p. 102

### W

Wagner, N. WFMN09\_I\_C1 p. 14  
 Wanielik, G. WFMN09\_II\_E1 p. 59  
 WFMN09\_II\_E2 p. 60  
 WFMN09\_II\_E3 p. 67

### Z

Zetik, R. WFMN09\_I\_C1 p. 14  
 Zichner, R. WFMN09\_I\_B3 p. 13  
 WFMN09\_III\_B2 p. 88  
 Zink, M. WFMN09\_I\_C2 p. 20

# Towards Wireless Multi-Gigabit Systems – Channel Models for mm- and sub-mm wave Communication

Thomas Kürner, *Senior Member, IEEE*

**Abstract**— This paper contains a brief summary of this invited key note talk, which gives an overview of current issues in the field of mm-wave and THz communications. References to the original work are given. The talk starts by providing the motivation for the development of multi-gigabit wireless systems and gives an overview of the status quo of standardization and regulatory activities with emphasis on IEEE802.11 TGad, IEEE802.15 IGTHz and the preparation of the next WRC in 2012. The main part of the talk deals with concept for radio channel modeling which is presented together with the latest channel investigation results at 60 GHz and 300 GHz, respectively. IEEE 802 is currently standardizing Wireless Local Area Networks (WLAN) systems for very high throughput (beyond 1 Gbps) operating at 60 GHz. One of the first steps is the definition of appropriate channel models. Focus of the work is the extension of state-of-the-art channel models by including double-directional channel characteristics, polarization effects and the influence of moving people on the propagation channel. Results from detailed measurement campaigns together with preliminary models of the above mentioned effects are presented. To achieve even higher transmission rates (beyond several tens of Gbps), large bandwidths with several 10's of GHz are required, which are available beyond 300 GHz. A couple of years ago, first activities on channel characterization in this frequency range have started. A summary on the results of these investigations achieved by the Terahertz Communications Lab is given.

**Index Terms**—Multi-Gigabit Indoor Communication, 60 GHz Channel Model, THz Communications, Standardization

## I. MOTIVATION

Today, commercially available systems for Wireless Local Area Networks (WLAN) or Wireless Personal Area Networks (WPAN), for example based on the IEEE standards 802.11n or 802.15.3c standard [1], achieve data rates of up to around 1 Gbps. However, it is foreseeable that within the next decade requirements for data rates will develop even beyond 100 Gbps [2]. Potential applications requiring such high data rates are wireless extensions of Gigabit Ethernet LANs, point-point-links connecting a hard drive or a camera to a computer, e. g., or wireless kiosk down loading applications. Recently, a

lot of mid- and longterm development and standardization activities have been started. Midterm activities are dealing with systems operating in the 60 GHz band [3,4,5,6,7], where 7 GHz of bandwidth have been allocated for worldwide use allowing the development of systems with data rates of several Gbps. In the longterm, data rates beyond 100 Gbps require the allocation of a multitude of 10 GHz of spectrum. Such an amount of spectrum is available only at frequencies beyond 300 GHz. First trials and concepts targeting wireless beyond 100 GHz are reported in [8,9]. In 2008, a THz Interest Group has been established within IEEE 802.15 to explore the possibilities to standardize a WPAN operating beyond 300 GHz [10].

Both in the 60 GHz and the 300 GHz frequency band the path loss is significant and appropriate measures to mitigate effects in none-line-of-sight (NLOS) cases, caused e. g. by the influence of moving people, are required. Advanced antenna techniques, like beam forming or beam switching are a prerequisite to guarantee seamless service. In order to consider such techniques in the standards development, the propagation channel operating at these mm- and sub-mm wave bands in realistic environments must be well understood. Therefore intensive channel modeling activities have been done at 60 and 300 GHz. This invited key note talk provides an overview of the corresponding channel modeling activities with the focus on those parts that are performed at Terahertz Communications Lab (TCL) in Braunschweig [11,12].

The paper is organized as follows. Section II describes the channel modeling activities in the 60 GHz band, followed by a summary about propagation conditions beyond 100 GHz in Section III. Section IV includes an outlook to future work.

## II. CHANNEL MODELS FOR 60 GHz SYSTEMS

Although the 60 GHz model has already been investigated for a couple of years [7] yielding also channel models used in standardization [13], there are still a couple of relevant aspects and phenomena requiring a more intensive study for the development of upcoming standards. Such features are for example the descriptions of NLOS situation, the effect of polarization, the influence of moving people and a joint consideration of Angle-of-Arrival (AoA) and Angle-of-Departure (AoD) yielding a double directional channel model.

Manuscript received July 23, 2010.

Thomas Kürner is with the Institut für Nachrichtentechnik at Technische Universität Braunschweig, Schleinitzstr. 22, D-38092 Braunschweig, Germany (e-mail: t.kuerner@tu-bs.de).

### A. IEEE 802.11 TGad Channel Model

IEEE 802.11 Task Group ad targeting at a very high throughput system operating at 60 GHz and compatible with the IEEE 802.11 standards family has defined standard application scenarios to be used for system evaluations. These scenarios are defined in a home living room, an office conference room and an enterprise cubicle environment. For these environments, statistical channel models have been developed [14] by exploring both measurement campaigns from various groups and ray-tracing simulations.

### B. 60 GHz Channel Modeling activities at TCL

Apart from developing and improving a detailed ray-tracing model at TCL, a three-step approach has been applied to achieve statistical channel models at 60 GHz [15]. First an extensive measurement campaign for the conference room and the home living room environment has been applied [15, 16] along with measurements of material parameters in the frequency range of interest [17]. These measurements have been used to verify the ray-tracing algorithm in a second step in order to derive the ray-tracer to develop statistical channel models. The focus in these investigations so far has been on modeling the dynamic behavior of the channel due to movements of human beings. The corresponding dynamic statistical model [16] has been included as a part of the above mentioned IEEE 802.11ad channel model [14].

## III. PROPAGATION CONDITIONS BEYOND 100 GHz

First demonstrations have shown that setting up wireless communications beyond 100 GHz is feasible [8,18]. In order to design and improve these systems, a deep knowledge about the propagation channel is required. At TCL, a detailed analysis of the basic propagation phenomena together with first measurements in a realistic environment has been done.

### A. Measuring Basic Propagation Phenomena

At frequencies beyond 100 GHz the attenuation is high enough to neglect transmission and diffraction as relevant propagation mechanism in indoor environments. As a consequence communication links operated in NLOS situations, where the direct link between transmitter and receiver is blocked, have to rely on reflection and scattering processes. Therefore, a proper modeling of scattering and reflection processes for typical building materials is required. At TCL, typical building materials have been measured for these three effects using either THz time domain spectroscopy (THz-TDS) or a vector network analyzer (VNA). Due to the small wave length, which is already in the order of the magnitude of the surface roughness or the thickness of a wall paper, e. g., the following three mechanisms have to be measured and modeled:

- *Reflection on smooth surface:* This phenomenon can be modeled using Fresnel's coefficients. The corresponding measurement results and material parameters can be found in [19,20].

- *Scattering on rough surfaces:* In specular direction, modified Fresnel coefficients have to be considered taking the surface roughness into account. Measurements on the scattering loss and the surface roughness are reported in [21] for scattering in specular direction.
- *Reflection on multi-layer objects:* In this case the reflection loss can be calculated using the transfer matrix method. Measurements and modeling results can be found in [22,23].

### B. Measurements in more realistic scenarios

A likely application for THz communication systems is the wireless interconnection of different electronic devices for ultra fast file transfer. For this use case the channel behavior at distances less than 1 meter has been characterized experimentally and compared to a simple model for frequencies between 290 and 300 GHz [23]. The investigation described in [24] provides additional results by presenting measurements involving reflection, scattering and diffraction in a realistic indoor scenario. Furthermore, the effect of antenna misalignment is investigated. The results from [23] and [24] can be used to derive a 300 GHz channel model.

## IV. FUTURE WORK

In order to have a complete channel model at 60 and 300 GHz available, the verification of a complete ray-tracing simulation in more complex realistic environments is required. Apart from this, modeling and measurements of scattering in non-specular reflections as well as of the combination of rough surface scattering and multiple-layer reflection are required. This will enable in-depth channel characterization allowing system simulations required for the development of a complete system architecture.

## ACKNOWLEDGMENT

The author wants to thank his colleagues from the Terahertz Communications Lab at Technische Universität Braunschweig and at Physikalisch-Technische Bundesanstalt for their contributions to the work described in this overview paper.

## REFERENCES

- [1] <http://standards.ieee.org/getieee802/>
- [2] Cherry, S., "Edholm's law of bandwidth", *IEEE Spectr*, Vol. 41, No. 7, p. 50, July 2004.
- [3] "Standard ECMA-387, High Rate 60GHz PHY, MAC and HDMI PAL," <http://www.ecm-international.org/publications/standards/Ecma-387.htm>, 2008.
- [4] "WirelessHD Specification Version 1.0 Overview," [http://www.wirelesshd.org/pdfs/WirelessHD\\_Full\\_Overview\\_071009.pdf](http://www.wirelesshd.org/pdfs/WirelessHD_Full_Overview_071009.pdf), 2007.
- [5] E. Perahia, "VHT 60 GHz PAR plus 5Cs, doc.: IEEE 802.11-08/0806r6," <https://mentor.ieee.org/802.11/documents>, 2008.
- [6] E. Perahia, "TGad Functional Requirements, doc.: IEEE 802.11-09/0228r3," <https://mentor.ieee.org/802.11/documents>, 2009.

- [7] S. Yong and C. Chong, "An overview of multigigabit wireless through millimeter wave technology: potentials and technical challenges," *EURASIP Journal on Wireless Communications and Networking*, vol. 2007, pp. 1–10, 2007.
- [8] A. Hirata et. al., "120-GHz-band millimeter-wave photonic wireless link for 10-Gb/s data transmission," in *IEEE Transactions on Microwave Theory and Tech.*, vol. 54, no. 5, 2006, pp. 1937–1944.
- [9] R. Piesiewicz et. al., "Short-Range Ultra-Broadband Terahertz Communications: Concepts and Perspectives," *IEEE Ant. And Prop. Magazine*, vol. 49, no. 6, pp. 24–39, 2007.
- [10] <http://www.ieee802.org/15/pub/IGthz.html>.
- [11] [www.tcl.tu-bs.de](http://www.tcl.tu-bs.de).
- [12] M. Jacob et. al., "An Overview of Ongoing Activities in the Field of Channel Modeling, Spectrum Allocation and Standardization for mm-Wave and THz Indoor Communications", IEEE Globecom 2009.
- [13] IEEE 802.15; Channel Model Sub-committee Final Report: 07/584r1; [http://www.ieee802.org/15/pub/TG3c\\_CFPdoc&Proposals.html](http://www.ieee802.org/15/pub/TG3c_CFPdoc&Proposals.html).
- [14] A. Maltsev et. al., "Channel Models for 60 GHz WLAN Systems, doc.: IEEE 802.11-09/0334r8," <https://mentor.ieee.org/802.11/documents>.
- [15] T. Kürner et. al., "Application of Ray-Tracing to derive Channel Models for future Multi-Gigabit-Systems", Proc. International Conf. on Electromagnetics and Advanced Applications, ICEAA '09, Torino, September 2009.
- [16] M. Jacob, C. Mbianke, Th. Kürner, A Dynamic 60 GHz Radio Channel Model for System Level Simulations with MAC Protocols for IEEE 802.11ad, Proc. 14th International Symposium on Consumer Electronics, Braunschweig June 2010.
- [17] M. Jacob and T. Kürner, "Radio Channel Characteristics for Broadband WLAN/WPAN Applications Between 67 and 110 GHz", 3rd European Conference on Antennas and Propagation, 23-27 March 2009, Berlin
- [18] C. Jastrow et. al., "300 GHz Transmission System," *Electron. Lett.*, vol. 44, pp. 213–214, 2008.
- [19] R. Piesiewicz et. al., "Reflection and Transmission Properties of Building Materials in W-band," *The Second European Conference on Antennas and Propagation (EuCAP) 2007*, pp. 1–5, 2007.
- [20] R. Piesiewicz et. al., "Properties of building and plastic materials in the THz range," *International Journal of Infrared and Millimeter Waves*, vol. 28, no. 5, pp. 363–371, 2007.
- [21] R. Piesiewicz et. al., "Scattering analysis for the modeling of THz communication systems," *IEEE Trans. on Ant. and Prop.*, vol. 55, no. 11 Part 1, pp. 3002–3009, 2007.
- [22] C. Jansen et. al., "The Impact of Reflections from Stratified Building Materials on the Wave Propagation in Future Indoor Terahertz Communication Systems," *IEEE Trans. on Ant. and Prop.*, vol. 56, no. 5, pp. 1413–1419, 2008.
- [23] R. Piesiewicz et. al., "Measurements and Modeling of Multiple Reflections Effect in Building Materials for Indoor Communications at THz Frequencies," *Proc. German Microwave Conference GEMIC, S. 3089-3092, Hamburg, March 2008*.
- [24] Th. Kürner et. al., Measurements of the Channel Characteristics at 300 GHz – Preliminary Results, IEEE 802 Plenary Session, San Francisco, July 2009, IEEE 802.15 document 15-09-0496.
- [25] Th. Kürner et. al., Measurements of the Channel Characteristics at 300 GHz, IEEE 802 Plenary Session, Atlanta, November 2009, IEEE 802.15 document 15-09-0756.

**Thomas Kürner** (S'91-M'94-SM'01) received the Dipl.-Ing. degree in Electrical Engineering from Universität Karlsruhe (Germany) in 1990 and the Dr.-Ing. degree in 1993 from the same university. From 1990 to 1994 he was with the Institut für Höchstfrequenztechnik und Elektronik (IHE) at the University of Karlsruhe working on wave propagation modelling, radio channel characterization and radio network planning. From 1994 to 2003 he was with the radio network planning department at the headquarters of the GSM 1800 and UMTS operator E-Plus Mobilfunk GmbH & Co KG, Düsseldorf, where he was team manager radio network planning support being responsible for radio network planning tools, algorithms, processes and parameters. Since 2003 he has been a Professor for Mobile Radio Systems at the Institut für Nachrichtentechnik (IfN) at Technische Universität Braunschweig. His working areas are propagation, traffic and mobility models for automatic planning of mobile radio networks, planning of hybrid networks, car-to-car communications as well as indoor channel characterization for high-speed short-range systems including future terahertz communication systems. He has been engaged in several international bodies such as ITU-R SG 3, UMTS Forum Spectrum Aspects Group, COST 231/273/259, where he chaired the working group "Network Aspects", and COST 2100. He was also a work package leader in the European IST-MOMENTUM project working on methods for "Automatic Planning of large-scale Radio Networks" and is now active in the European ICT-SOCRATES project. Currently he is chairing IEEE802.15 IG THz. He has served as Vice-Chair Propagation at the European Conference on Antennas and Propagation (EuCAP) in 2007 and 2009 and is Associate Editor of IEEE Transactions on Vehicular Technology since 2008. He is a member of VDE/ITG, VDI and Senior Member of the IEEE.

## Understanding the Physical Basics of Microwave Applications for Remote Sensing, Navigation, & Communication (Distinguished lecture)

W. Keydel

Microwaves and Radar Institute, DLR Oberpfaffenhofen,  
Contact address: Mittelfeld 4, D-82229 Hechendorf

Most important properties of Electromagnetic Waves for remote sensing, navigation and communication applications as well are their coherence and the resulting interference phenomena.

Goal of the presentation is to point out exemplarily the influence of coherence and interference effects on the performance of Microwave systems and Microwave techniques mainly with respect to measurement accuracy and resolving power.

Rayleigh's definition of the resolving power makes use of the antenna pattern's zero points caused by diffraction at the edges of the antenna aerial, and, therefore, this definition is based on interference as well as the Radar Cross Section diagram's of objects with their, normally, many and deep nulls resulting from the superposition of the many reflection points illuminated by the footprint of the antenna simultaneously. The latter is the fundamental reason of the speckle in radar images also, especially in Synthetic Aperture Radar, SAR, images. For SAR coherence is a "conditio sine qua non". Principally, the SAR raw data form basically and essentially a hologram, and the SAR processing procedure uses basically the same algorithms in the digital world.

Positive interference phenomena, on the one side, can provide extra ordinary improvements of resolution and measurement accuracy, especially in Microwave Interferometry Systems. Microwave Interferometry, currently, is the most accurate existing remote sensing technique with extra ordinary obtainable resolution power. With Very Long Baseline Interferometry, for instance, by using space telescopes with the Japanese HALCA satellite in an elliptical Earth orbit, height between 21,000 km and 560 km, at 22 GHz a resolving power has been reached which is equivalent to being able to see a tennis ball on the Moon. With normal and differential interferometry using SAR interferometer mounted on aircraft (E-SAR), space shuttle (SRTM) and satellites (Terra-SAR-X) and with the relatively new technique of GPS-Reflectometry and -Scatterometry a dazzling variety of new applications showed up during the last decade.

On the other side, however, negative interference effects can cause dramatic measurement errors due to the so called image effect and multipath propagation also. Examples for such effects causing positioning errors in GPS and errors in radar bearing will be shown exemplarily.

With Microwave Radiometry using the interference effect of thin film colours, which is well known from optics, an operational Airborne Surveillance System for Identification of Marine Pollution, the "Mehrfrequenz Radiometer zur Erkundung der Seeoberfläche", MERES, has been developed. Results will be shown as further examples for positive Interference phenomena.

## **Interferometric Potential of High Resolution SAR Satellite Systems**

(Key note extension lecture on remote sensing)

R. Bamler

Institut für Methodik der Fernerkundung, DLR, Wessling

Interferometric SAR (InSAR) has become a well established remote sensing technology. DEM generation, ground deformation measurement, or monitoring of glacier dynamics are prominent examples.

The German satellite TerraSAR-X, launched in 2007, is one of the first of a new SAR system generation. The leap from medium resolution (10 - 25 m), like ERS and ENVISAT/ASAR, to very high resolution (VHR) as well as the diverse new imaging modes opens up novel application fields.

The low bandwidth-to-carrier frequency ratio of only 32 lets the regimes of InSAR and radargrammetry overlap with interesting consequences, i.e. absolute phase determination. Persistent scatterer interferometry (PSI) with hundreds of exploitable scatterers on a single building allows for the first time the measurement of structural deformation and stress from space. Differential SAR tomography can be applied for the 3D reconstruction of buildings and their deformations. But also speckle and feature tracking for robust motion estimation is now feasible from space with unprecedented accuracy and resolution. All this is facilitated by TerraSAR-X's extremely high absolute geolocation accuracy of about 30 cm.

In 2010 a second similar satellite will be launched, TanDEM-X. It will fly in a close formation with TerraSAR-X. Both satellites will form a single-pass interferometer for acquiring data for a global DEM of HRTI-3 standard. Selected areas like flood-plains will be mapped even to HRTI-4 accuracy.

The presentation will introduce TerraSAR-X and the TanDEM-X mission concept. Several innovative interferometric applications and research topics will be presented. An outlook to an L-band mission concept, Tandem-L will be given.

# Ka-Band Terminal Antennas for Mobile Satellite Communications

Alexander Geise<sup>1</sup>, Karsten Kuhlmann<sup>2</sup>, and Arne F. Jacob

<sup>1</sup> Now with: Astrium GmbH, 81663 München, Germany, Email: alexander.geise@astrium.eads.net

<sup>2</sup> Now with: Physikalisch-Technische Bundesanstalt, 38116 Braunschweig, Germany, Email: karsten.kuhlmann@ptb.de  
Technische Universität Hamburg-Harburg, 21073 Hamburg, Germany, Email: jacob@tuhh.de

**Abstract**—Terminal antenna concepts for mobile satellite communications at Ka-band are reviewed. Some recent technological advancements in the field of digital beamforming arrays are presented.

## I. INTRODUCTION

To satisfy the ever growing need of bandwidth more and more communication satellites today are equipped with Ka-band hardware. In the future, they are to provide broadband services also to mobile users. In a possible implementation, spot beams with alternating frequency and polarization could provide the necessary ground coverage [1]. Desirable application scenarios include, for instance, in-flight entertainment on board commercial airliners and fast Internet access in maritime environments.

These developments are very challenging not only for the satellite system but also for the ground segment. They call, in particular, for advanced terminal antenna solutions. Indeed, to meet the demands of such high data rate applications, two key issues have to be dealt with. The first one concerns the mobility requirements. The relative motion between satellite and user requires

- sufficiently fast beam steering for reliable satellite tracking,
- flexible beam forming, e.g. to satisfy sidelobe constraints,
- and possibly multi-beam capability to maintain communication during satellite handover.

The second one is related to the technological implications of the high operating frequencies, the relatively large bandwidth, and the required polarization agility. Frequencies in the 20 GHz- and 30 GHz-range for downlink and uplink, respectively, imply high packing density of electronic circuitry in the case of active antennas, as the available space is dictated by wavelength. The spatial constraints are even more severe, if polarization multiplexing is to be implemented. Classical antenna architectures relying on conventional packaging approaches then soon reach their limits, and novel concepts are needed.

This contribution intends to highlight some recent developments in the area of terminal antennas for such applications. After a brief review of the principal beam steering concepts and the system implications, the focus will be laid on work performed at the Institut für Hochfrequenztechnik, Technische Universität Hamburg-Harburg, in collaboration with its partners in the frame of the SANTANA project funded by the German Aerospace Agency [2].

## II. SYSTEM CONCEPTS

The principal beam steering methods are reviewed in the following. The intention is to roughly categorize them in terms of their major performance characteristics and of the respective technological implications. The presented overview is thus necessarily incomplete. Obviously, variants as well as combinations of the presented approaches are established, known, or at least imaginable.

### A. Mechanical Beam Steering

This is the most popular and probably the most widespread beam steering method. Depending on the angular coverage required by the application, the antenna is mounted on a one- or a two-axis stand allowing for the desired rotation. The antenna itself is often but not necessarily of the reflector type with a central feed. The latter is connected to the transmit/receive (Tx/Rx or T/R) unit and all the (digital) signal processing hardware, as sketched in Fig. 1.

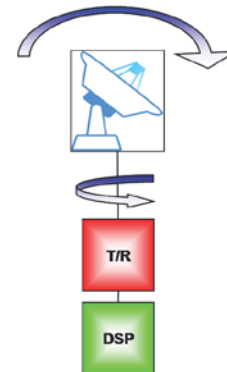


Fig. 1. Mechanically steered reflector antenna.

The advantages are

- the straightforward system architecture,
- the proved robustness and reliability,
- and the reasonable cost.

The drawbacks, on the other hand, are

- the limited steering velocity,
- the lacking beamforming and multi-beam capabilities,
- as well as size, weight, and mechanical noise.

Worldwide, a substantial number of commercial airliners has been equipped with systems of this kind for broadband communications with geostationary satellites at Ku-band.

### B. Electronic Beam Steering

To avoid the mechanical complexity of the above approach electronic means are required for beam steering. This calls for antenna arrays with individually addressable elements. As is well-known, the array beam can be tilted by properly adjusting the phase of each element. The classical realization as phased arrays relies on phase shifters [3]. As the latter are quite lossy in general, amplifiers are often added for compensation. The amplifiers, in turn, allow for some amplitude tapering and, thus, beamforming. The antenna elements are again connected to a common transmit/receive chain with attached digital signal processing unit, as shown in Fig. 2.

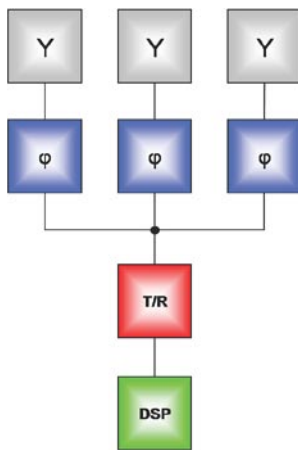


Fig. 2. Phased array concept.

This calls for a proper distribution network which adds to the overall complexity. Phased arrays can be characterized as follows:

- they allow for fast beam steering,
- possess a rather high circuit complexity,
- and exhibit moderate flexibility.
- They are often realized in planar technology. This is beneficial to size and weight, but imposes limits on scanning range and antenna efficiency.

### C. Digital Beam Steering

This approach goes one step further than the previous one. Instead of a single signal processing chain for the whole array, each element now has its own complete Tx/Rx unit. The latter includes the RF (*Radio Frequency*) frontend, which, at high frequencies, must be placed close to the antenna, the IF (*Intermediate Frequency*) circuitry, and parts of the DSP (*Digital Signal Processor*) for baseband signal treatment, as visualized in Fig. 3.

In the Rx case, the signals of the individual array elements are collected and superimposed in the DSP. By properly weighting their phase and amplitude, the antenna beam can be formed and steered digitally according to the needs. This aspect coins the usual name DBF (*Digital BeamForming*) of this approach. Obviously, antenna calibration can be performed in the DSP, as well. Even more, the concept enables multi-beam

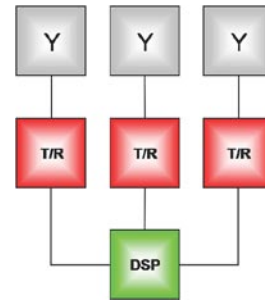


Fig. 3. Digital beamforming concept

operation, allowing, for instance, the simultaneous reception of signals from different directions. The DOA (*Direction Of Arrival*) of these signals can be estimated autonomously [4], [5]. Once established, the link is easily maintained by numerical tracking procedures [6]. Interfering signals can be suppressed in the DSP by adequate beamforming, i.e., nulling. By updating the software the system flexibility can be adapted to match the state-of-the-art or simply changing needs.

The Tx path relies on DOA information, e.g., from the Rx system. The tasks to be performed in software are thus simpler, as they are limited to beamforming and steering. In contrast to the system concepts presented above, the transmitted power stems from a large number of (medium) power amplifiers. Although this avoids the complication coming along with a single high power unit, it is nevertheless challenging because of the limited available space and the resulting technological implications, such as cooling.

This last aspect applies to the DBF concept as a whole. The challenges stemming from the packing density increase with frequency, as antenna scaling is dictated by this parameter. High frequency applications, e.g. in the millimeter-wave range, might thus require novel antenna architectures. High data rates represent another bottleneck in system design. Indeed, as each of the  $N$  elements of an array carries the whole amount of data, the processing power scales with  $N$ , and a powerful DSP is thus needed.

### D. A Hybrid Approach

To cope with this last aspect a hybrid approach combining features of phased arrays and DBF was recently proposed [7]. As explained there, the total signal processing effort scales with  $\sqrt{N}$ . This comes mainly at the expense of flexibility. For instance, multi-beam capability is strongly impaired. Very large arrays become realizable at reasonable cost, though.

## III. ANTENNA ARCHITECTURES

The antenna architectures reported in this section are suitable for DBF and the hybrid approach mentioned above. As they were developed in the frame of the SANTANA project, the underlying system parameters adopted in this research are briefly summed up first. Then, some of the past achievements are highlighted as they motivated the most recent and still ongoing developments which are presented at last.

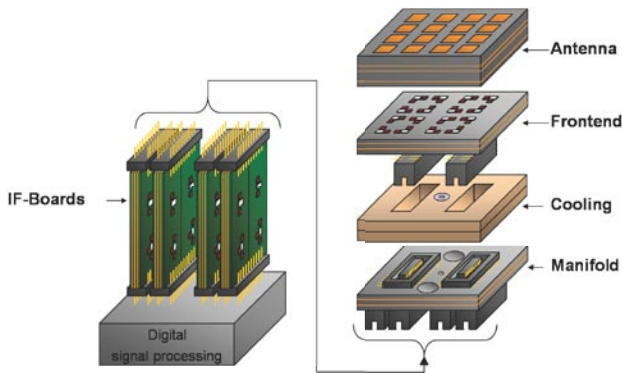


Fig. 4. Hybrid architecture of DBF array.

### A. The SANTANA Concept

The SANTANA project aims at demonstrating advanced technologies and antenna architectures as proof of concept. The system specifications were derived from link budget calculations based on a realistic satellite scenario taken as reference [8], [9]. The down- and uplink frequencies thus range from 19.7 GHz to 20.2 GHz and from 29.5 GHz to 30.0 GHz, respectively.

The preferred half-wave array element spacing derived from antenna theory implies high packing density at these frequencies. It also means quite different antenna sizes for up- and downlink. As a result, the Rx and Tx arrays are implemented as separate units.

Reasonable data rates require terminal arrays with several thousand elements. These cannot be realized as a single antenna because of the high technological complexity. Thus, a modular approach was adopted, each module comprising 4x4 elements. This results in a module size of 3x3 cm<sup>2</sup> and 2x2 cm<sup>2</sup> for Rx and Tx, respectively. More recently, the feasibility of 8x8 units is investigated. By this modular approach, the final array size is flexibly adapted to the particular link budget requirements.

### B. System Demonstrator

The previous phase of the SANTANA project aimed at demonstrating the performance of the system as a whole in a mobile scenario. Before reporting on the experiments conducted in this context, the technological status by then is briefly reviewed in the following. Fig. 4, which shows the exploded view of a complete module illustrates the hybrid

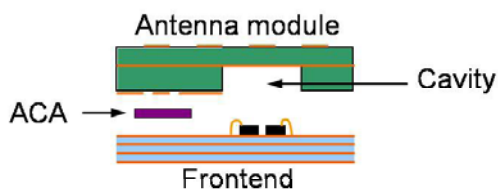


Fig. 5. Multilayer assembly.

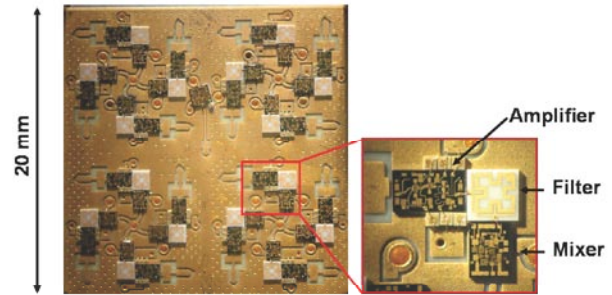


Fig. 6. 30 GHz 4x4 Tx frontend.

architectural approach.

The RF boards are horizontally layered, which is usually referred to as tile arrangement [10]. They consist of three multilayers with the circularly polarized patch antennas, the MMICs (Monolithic Microwave Integrated Circuits), and a manifold for signal routing, respectively. A liquid cooled metal plate is sandwiched between the manifold and the frontend multilayer. The IF boards are arranged vertically in the so-called brick architecture [10].

In this design the connection between frontend and antenna multilayer is very challenging. The adopted solution is sketched in Fig. 5. Cavities in the antenna multilayer host the MMICs. The high frequency connections are realized by means of anisotropically conducting adhesive [11]. Fig. 6 illustrates the packing density of the 30 GHz frontend with its 4x4 RF transmitters, a LO (*Local Oscillator*) distribution network, and a calibration receiver.

After an extensive laboratory characterization a scaled but otherwise complete system consisting of Rx and Tx units equipped with four antenna modules each, the DSP, and the whole DBF software was tested in field experiments [12]. It was kept at a fixed position on the ground. A beacon system with conventional antenna technology served as communication counterpart. The first mobility tests were conducted on the ground. To this end the beacon was mounted on a car. In this way, various system parameters and, in particular, the

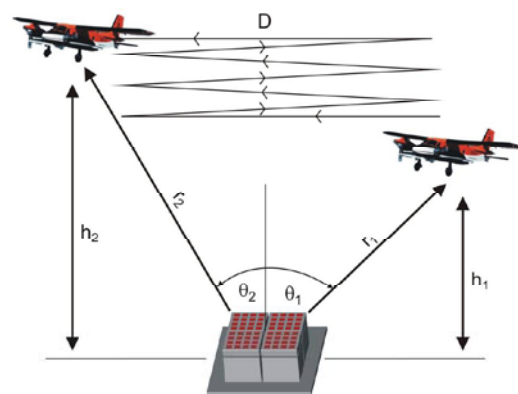


Fig. 7. Exemplary flight scenario during field tests.

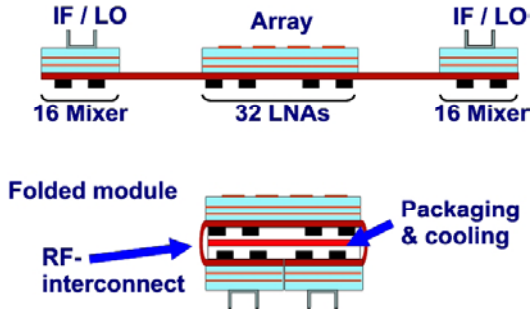


Fig. 8. Flex-rigid architecture.

DOA and tracking ability could be assessed under controlled mobility conditions. The full system autonomy could be demonstrated. This paved the way for airborne tests. These provide a more realistic scenario, allowing for communications over larger distances, at defined and variable angular velocities, and covering the whole hemisphere. A variety of flight maneuvers were conceived for this purpose. An example is shown in Fig. 7. High data rate communications could reliably and consistently be demonstrated, thus validating the proposed technology.

C. Advanced Concepts

The system discussed so far was conceived for only one circular polarization. This is not sufficient, however, for future satellite communications which will use both polarizations [1]. Thus, terminal antennas will have to feature polarization multiplex. As the packing density limits the functionality achievable with the architectural concept presented above, advanced concepts are needed. Two approaches are proposed in the following.

1) *Flex-Rigid Architecture*: Fig. 8 depicts a stack of rigid and flexible multilayer substrates, the latter allowing to fold the arrangement. In this way, more MMICs – needed for increased functionality – can be accommodated in a module of given size. In the final setup, the patch antennas are situated on the top surface, while the MMICs, placed on the inner layers close to a cooling gear, are mechanically protected. The flexible substrate provides the RF and DC interconnects and also includes the IR (*Image Reject*) filters.

As described in [13] a 4x4 Rx antenna module was realized, each array element featuring both left and right hand circular

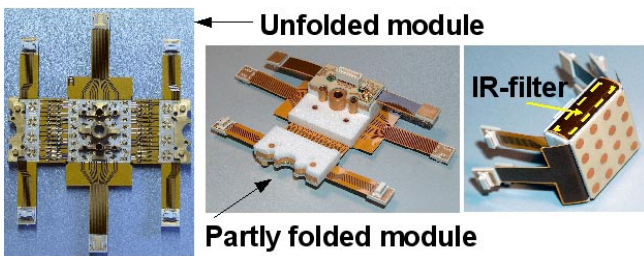


Fig. 9. Flex-rigid antenna module.

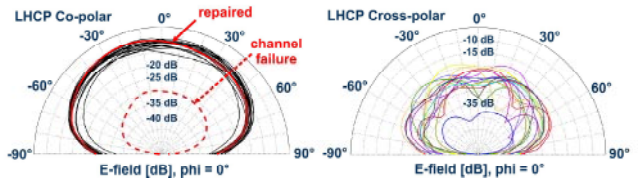


Fig. 10. LHCP measurements of flex-rigid module.

polarization (LHCP / RHCP). The module thus comprises 32 sets of MMICs. The flexible and the rigid substrates are Rogers’ Ultralam 3000 and RO4003 [14], respectively. Fig. 9 shows photographs of the demonstrator. The left picture represents the unfolded module. One can distinguish the brass heat sink with apertures for the heat pipes. One further recognizes the MMICs, the LNAs being mounted on the central multilayer and the mixers on the two lateral ones. The IR filters are printed on the connecting flexible substrates. The center photo shows the partly folded module. A sturdy foam spacer (Rohacell® [15]) has been added. The final assembly appears in the right picture.

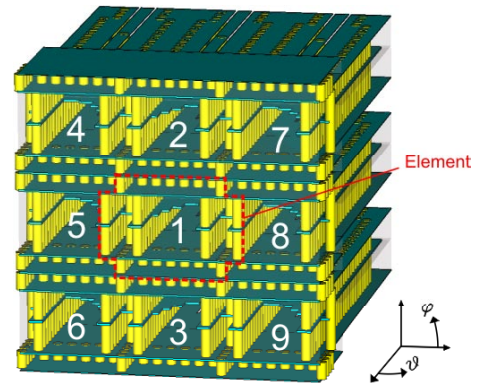


Fig. 11. Brick architecture topology (simulation model).

The potential of the approach is illustrated in Fig. 10 which depicts the measured co- and cross-polarized radiation patterns of each array element for LHCP. As indicated, one defect channel could be repaired. The cross-polarization suppression

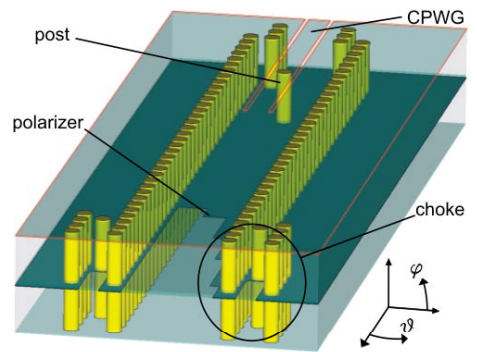


Fig. 12. Substrate integrated antenna element with septum polarizer.

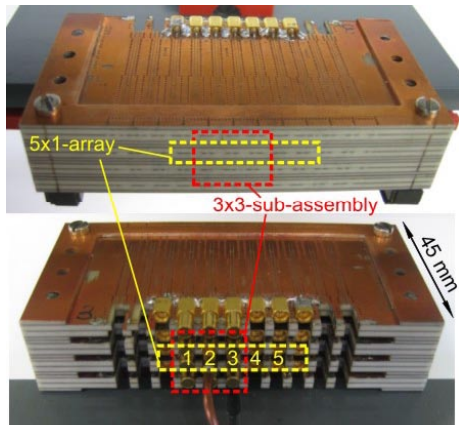


Fig. 13. 30 GHz antenna array (integrated brick architecture).

exceeds 17 dB and can be improved by proper calibration. For increased functionality the concept can be expanded to include even more layers. The approach features a simple RF interface between layers, advantageous manufacturing, and easy maintenance.

2) *Integrated Brick Architecture*: The well-known brick architecture in general requires axial radiators which are aligned with the electronic circuitry. This arrangement greatly relaxes the spatial constraints imposed by the array element spacing. Fig. 11 illustrates the concept pursued here. The array consists of a stack of SIW (*Substrate Integrated Waveguides*) separated by chokes for improved matching. As can be seen from Fig. 12 each element is made of two halves separated by a septum and fed by a coplanar waveguide (CPWG) each. The septum serves as polarizer enabling full polarization multiplex. Depending on the input signals, either circular or linear polarization is possible. A more detailed description of the functionality can be found in [16], [17].

A first realization for the 30 GHz band is shown in Fig. 13. It comprises twenty substrate layers (five for each brick), yielding an 11x4 array. The co- and cross-polarized radiation patterns obtained with a 5x1 subset of this array are presented in Fig. 14.

These curves are synthesized from the measured individual element patterns. The effect of inter-element coupling can be removed by adequate calibration, as demonstrated in [18]. The integration of active MMIC circuits is described in [19].

Also this approach allows easy manufacturing and simple maintenance. It has very good potential for applications at much higher frequencies at the expense of an increased thickness.

#### IV. CONCLUSION

Terminal antenna concepts for mobile applications are reviewed. The focus is on satellite communications at Ka-band. Technological implications of system requirements on digital beamforming arrays are discussed. Recently proposed advanced antenna architectures allowing for highest system flexibility are presented.

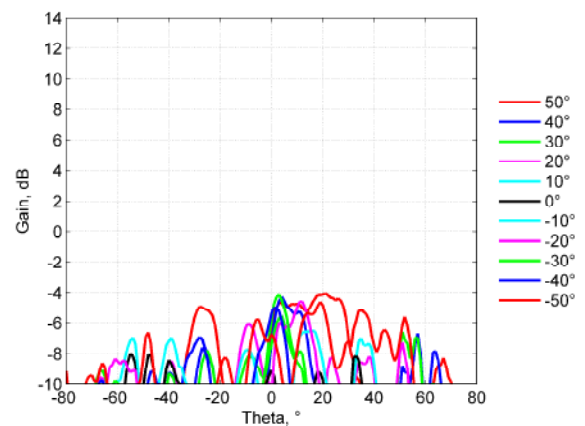
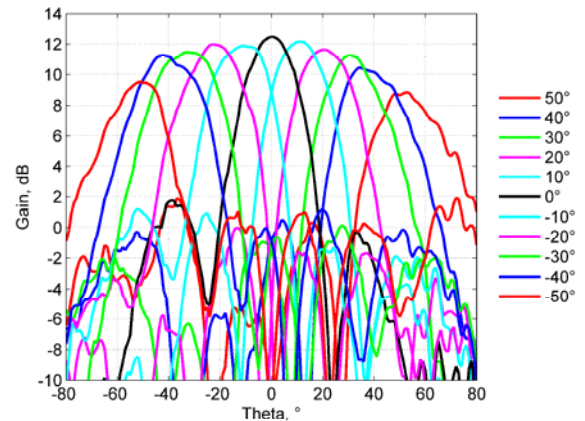


Fig. 14. Measured co- and cross-polarized radiation patterns.

#### ACKNOWLEDGMENT

The authors wish to acknowledge funding and support of this work by the German Aerospace Center (DLR) on behalf of the German Federal Ministry of Economics and Technology (BMWi) under research contract 50YB0709.

#### REFERENCES

- [1] S. Voigt and A. Pagels, "The Heinrich Hertz Mission," in *Countdown 11 – Topics from DLR Space Agency, Issue 3/09*, Bonn, Germany, Nov. 2009, pp. 3–7.
- [2] DLR, "Deutsches Zentrum für Luft- und Raumfahrt e.V.," [www.smart-antennas.de](http://www.smart-antennas.de), 2010.
- [3] R. C. Hansen, *Phased Array Antennas*, 2nd ed. New York, NY: John Wiley & Sons, Inc., 1998.
- [4] R. O. Schmidt, "Multiple Emitter Location and Signal Parameter Estimation," *IEEE Trans. Antennas Propagat.*, vol. 34, no. 3, pp. 276–280, 1986.
- [5] L. Kühnke, "Realisierung und Kalibrierung aktiver Antennensysteme mit digitaler Strahlformung," Ph.D. dissertation, Universität Hannover, 2001.
- [6] R. Gieron and P. Siatchoua, "Application of 2D-Direction Locked Loop Tracking Algorithm to Mobile Satellite Communications," in *Proc. 4th IEEE Workshop on Sensor Array and Multichannel Processing*, Waltham, Massachusetts, July 2006, pp. 546–550.
- [7] A. Stark, A. Dreher, H. Fischer, A. Geise, R. Gieron, M. V. T. Heckler, S. Holzwarth, C. Hunscher, A. F. Jacob, K. Kuhlmann, O. Litschke, D. Lohmann, W. Simon, F. Wotzel, and D. Zahn, "SANTANA: Advanced Electronically Steerable Antennas at Ka-Band," in *Proc. 3rd*

- European Conference on Antennas and Propagation*, Berlin, Germany, Mar. 2009, pp. 471–478.
- [8] Alenia Aeronautica, “EuroSkyway,” [www.alenia-aeronautica.it](http://www.alenia-aeronautica.it), 2007.
- [9] Telesat Canada, “Anik F2,” [www.telesat.ca](http://www.telesat.ca), 2008.
- [10] S. Sanzgeri, D. Bostrom, W. Pottenger, and R. Q. Lee, “A Hybrid Tile Approach For Ka-Band Subarray Modules,” *IEEE Trans. Antennas Propagat.*, vol. 43, no. 9, pp. 953–959, Sept. 1995.
- [11] Delo, “Intelligent and Industrial Adhesives,” [www.delo.de](http://www.delo.de), 2008.
- [12] A. Geise, A. F. Jacob, K. Kuhlmann, H. Pawlak, R. Gieron, P. Siatchoua, D. Lohmann, S. Holzwarth, O. Litschke, M. V. T. Heckler, L. Greda, A. Dreher, and C. Hunscher, “The Santana Project,” in *Proc. Deutscher Luft- und Raumfahrtkongress*, Berlin, Sept. 2007, pp. 481–486.
- [13] A. Geise and A. F. Jacob, “Flex-rigid architecture for millimeter-wave antenna arrays,” in *IEEE MTT-S International Microwave Symposium Digest*, Boston, June 2009, pp. 809–812.
- [14] R. Corporation, “High Performance Materials & Components,” [www.rogerscorporation.com](http://www.rogerscorporation.com), 2009.
- [15] Rohacell, “Structural Foam for Lightweight Construction,” [www.rohacell.com](http://www.rohacell.com), 2009.
- [16] K. Kuhlmann, K. Rezer, and A. F. Jacob, “Circularly Polarized Substrate-Integrated Waveguide Antenna Array at Ka-Band,” in *Proc. German Microwave Conference*, Hamburg, Germany, Mar. 2008, pp. 471–474.
- [17] —, “Far Field Measurement on Ka-band Substrate-Integrated Waveguide Antenna Array with Polarization Multiplexing,” in *IEEE MTT-S International Microwave Symposium Digest*, Atlanta, GA, June 2008, pp. 1337–1340.
- [18] K. Kuhlmann, D. J alas, and A. F. Jacob, “Mutual Coupling in Ka-Band Antenna Array with Polarization Multiplexing,” in *Proc. 10th European Conference on Wireless Technologies*, Rome, Italy, Sept./Oct. 2009, pp. 152–155.
- [19] K. Kuhlmann and A. F. Jacob, “Active 30 GHz Antenna Array for Digital Beamforming and Polarization Multiplexing,” in *IEEE MTT-S International Microwave Symposium Digest*, Anaheim, CA, May 2010.

## **Microstrip Antennas and Arrays in Communications, Navigation and Radar**

(Review lecture)

A. Dreher

German Aerospace Center (DLR), Institute of Communications and Navigation, Oberpfaffenhofen, 82234 Wessling

Nearly half a century ago, the concept of microstrip antennas has been proposed. After a long period of being employed only for special military use, they have now found a broad and still strongly increasing field of applications mainly driven by modern communication and navigation technology. Microstrip antennas are well known for several advantages: They are mainly flat, lightweight and can be produced easily and inexpensively in several technologies suitable for RF circuits. This also offers the possibility to integrate them with active devices even as a part of an MMIC-chip. In this way, very small radiating front ends and smart antenna systems can be built up. For high frequencies beginning with Ku-band, LTCC-technology is often used to build multilayer structures with many layers and active and passive components. Large arrays, including complex networks for beamforming and steering, can be fabricated in PCB-technology either as a single multilayer board or in a modular architecture. If they are printed on a flexible substrate they may conform to a given surface and thus can be integrated seamlessly in an aircraft or any other vehicle to reduce drag and meet aesthetical requirements.

This talk will present the fundamental concept of microstrip antennas and discuss some basic methods and guidelines for analysis and design. Several examples for their application will then be given including antenna arrays with dual polarization and special networks for beamforming which are used in synthetic aperture radar as well as narrowband, broadband and multifrequency antennas for advanced navigation receivers employing digital beamforming and array processing to mitigate interferes and multipath signals. In communications, some examples for different microstrip antenna technologies especially for high frequency applications in user terminals of satellite systems will be shown.

## Adjusted Antenna Designs for Special RFID Applications

R. Zichner<sup>1</sup>, R. R. Baumann<sup>2</sup>

<sup>1</sup> Fraunhofer Research Institution for Electronic Nano Systems ENAS, 09126 Chemnitz

<sup>2</sup> Chemnitz University of Technology, Institute for Print and Media Technology, 09126 Chemnitz

For the future, the development of specially adjusted antenna designs for RFID applications is essential. So far, the Radio Frequency Identification (RFID) technology is well - established in various industrial sectors, e.g. logistics, wholesale trade and automotive engineering. Their advantages (controlling, identification ...) and benefits (process optimization and monitoring ...) are obvious. However, the step into new fields towards the realization of the internet of things [1] is difficult. One reason besides the currently high costs of the RFID transponders (chip + antenna) is the limited functionality of the passive systems in distinct industrial environments. In and near diverse materials the received electromagnetic waves are reflected, diffracted and damped in different ways leading to a bias in transponder functionality.

To minimize the costs of the transponders and increase their efficiency, cheap manufacturing and specially adjusted antenna designs are required. Printing processes, which enable low cost fabrication, offer a solution. However, also for these production processes the antenna design has to be adjusted concordantly to the dielectric environment to gain the maximum performance.

The objective of the current research is to develop optimized antenna designs for the UHF band, which offer an individually high performance in their specific environment. In the course of the work dependences between antenna parameters and varying dielectric environments could be shown by measurements as well as simulations. The functionality of the RFID technology for UHF applications is therefore directly depending on the properties of the transponder antenna. As a result of this issue adjusted antenna designs are essential to establish RFID technology in further fields of application.

[1] International Telecommunication Union: "ITU Internet Reports 2005: The Internet of Things", 7th edition 2005 ([www.itu.int/internetofthings/](http://www.itu.int/internetofthings/))

# Ultra Wideband Radar Sensors –State of the Art and Scope for Moisture Measurements.

Frank Bonitz<sup>1</sup>, K. Kupfer<sup>1</sup>, N. Wagner<sup>1</sup>, M. Helbig<sup>2</sup>, R. Herrmann<sup>2</sup>, M. Kmec<sup>2</sup>, J. Sachs<sup>2</sup>, K. Schilling<sup>2</sup>, R. Zetik<sup>2</sup>, P. Rauschenbach<sup>3</sup>

**Abstract**—The article gives an overview about ultra-wideband (UWB) sensors. First some basic definitions were given followed by a comparison of two time domain measurement devices (TDR 100 and m-sequence sensor). Subsequently a review of the m-sequence method for UWB signal generation is discussed. After that an experimental setup for permittivity measurements of the introduced UWB sensor is presented. The sensitivity of the used sensor is discussed. Finally a broad variation of different applications for the proposed UWB system is depicted.

**Index Terms**— ultra wideband, pn-code, nondestructive testing, moisture measurements.

## I. INTRODUCTION TO UWB

### A. What is UWB?

In general a system (sensor or communication device) is considered as ultra-wideband if it is capable of dealing with time signals that occupy a broad spectrum in the frequency domain (e.g. dirac impulse, chirp, multi sine signal and m-sequence). The bandwidth is determined by the lower  $f_l$  and upper  $f_u$  cut-off frequency of a system. The reference level of the cut-off frequency is -10 dB from the maximum spectral value. A signal or system is considered as ultra-wideband either it has a fractional bandwidth (1) greater than 20% or an absolute bandwidth (2) greater than 0.5 GHz [1].

$$\text{fractional bandwidth : } b_f = \frac{2(f_u - f_l)}{f_u + f_l} \quad (1)$$

$$\text{absolute bandwidth : } B = f_u - f_l \quad (2)$$

Manuscript received February 28, 2010. This work was supported in part by the Thuringian Development Bank, DFG (SA 1035/4-1, HE 3642/1-1), German Federal Ministry of Economics and Technology (BMWi) under grant #161N0338 and German Federal Ministry of Education and Research (BMBF) under grant #2C1194.

<sup>1</sup>Institute for Materials Research and Testing at the Bauhaus-University Weimar, Moisture Measurement Methods, Weimar, 99423, Germany (phone: +493643/564-367; e-mail: frank.bonitz@mfpa.de).

<sup>2</sup>Technical University of Ilmenau, Electronic Measurement Lab, Ilmenau 98693, Germany, (phone: +493677/ 69-2623, e-mail: juergen.sachs@tu-ilmenau.de)

<sup>3</sup>Meodat GmbH, Ilmenau, 98693, Germany, (phone: +493677/ 466-2921, e-mail: pey@meodat.de)

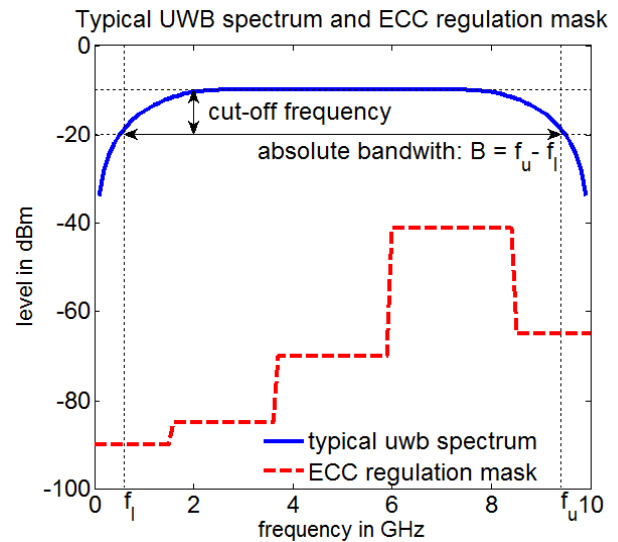


Fig. 1. Typical ultra-wideband spectrum (continuous line) at a maximum level of -10 dBm with a lower  $f_l$  and upper  $f_u$  cut-off frequency; ECC regulation mask (dashed line) [2].

In this work it is referred to systems which have an absolute bandwidth greater than 2 GHz. The time-bandwidth product for these sensors is around one.

The usage of frequency bands is regulated by ITU-R, ETSI, ECC and FCC committees. For sensor applications the baseband (DC to 10 GHz) is of main interest, simply because the penetration of materials is better for lower frequencies. In this frequency range the regulation bodies require an EIRP down to -90 dBm/MHz [2]. Figure 1 shows an overlay of a typical UWB spectrum and the ECC regulation mask.

### B. Generation of the UWB Signal

A wide spectrum could either be created in the frequency domain or in time domain. In frequency domain a stepped sine wave or a chirp signal are generated. These principles are used in FMCW radar or in vector network analyzers (VNA) [3].

Another possibility is to generate a sub-nano second impulse which has a wide spectrum. One challenge for pulse generators is the handling of high peak voltages and especially the high power output at a certain time [4]. A further possibility for impulse generation is the correlation of a pseudo random binary sequence (m-sequence) [5] which will be addressed in more detail in the following paragraph.

### C. Why using UWB?

As noted above a higher bandwidth results in a smaller pulse width, which induces a better range resolution and therefore provides an improved separation of different objects or layers. In this way more precise run time measurements can be done.

There are many different frequencies of interest for most scenarios under test. The greater the bandwidth, the greater is the information about the scenario or object under test, e.g. wideband radar cross section (RCS) measurements could provide a better classification of different objects.

## II. OVERVIEW ULTRA -WIDEBAND SYSTEMS

The performance of the used systems was determined in measuring the output signals of a UWB m-sequence and TDR 100 device. Figure 2 shows the UWB raw output signal and the first derivative of the TDR 100 voltage step signal. The following characteristics were determined out of the measurements and summarized in Table 1:

1. *Full width half max (FWHM)* and *bandwidth* to get a measure for the maximum range resolution.
2. *Sample time* is the time which is needed to get one discrete point of the overall signal.
3. *Measurement time* is the time needed to get one frequency point.
4. *Jitter* is a measure for the time drift of the output signal.
5. *Maximum Signal to Noise Ratio ( $SNR_{max}$ )*
6. *Spurious Free Dynamic Range (SFDR)* is a measure of the signal level versus the level of the highest signal distortion.

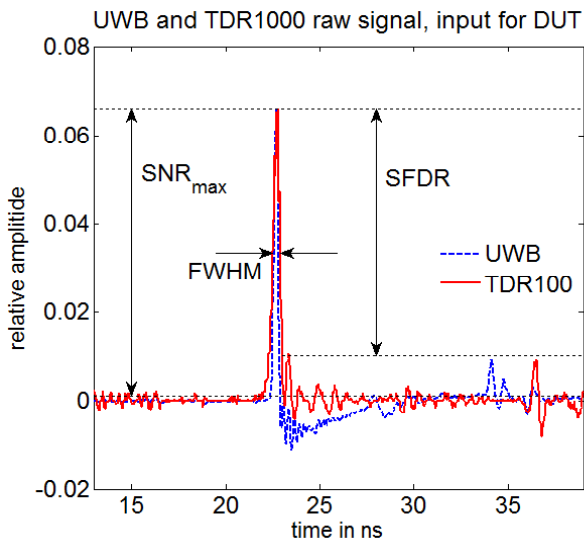


Fig. 2. Measurement of an UWB signal and first derivative of the TDR 100 step signal. The diagram depicts the main signal peaks and some distortions.

In contrast to the measurements some characteristics from a R&S vector network analyzer (VNA) taken from [6] are provided in Table 1.

TABLE I  
COMPARISON OF MEASUREMENT DEVICES

Table Head	Table Column Head		
	UWB	TDR100	VNA <sup>a</sup>
FWHM	248 ps	435 ps	25 ps
bandwidth	4 GHz	2,3 GHz	40 GHz
sample-time	111 ps	4 ps	430 ns <sup>b</sup>
Measurement time $\mu$ s/point	0.05 <sup>c</sup>	500	2
Jitter	2 ps	50 ps	/
$SNR_{max}$	70 dB	47 dB	150dB
SFDR	15 dB	9 dB	/

<sup>a</sup> the values are not measured and taken from [6]. <sup>b</sup>The values should not be directly compared because of a big difference between frequency domain measurement (VNA) and time domain measurement (UWB, TDR100) <sup>c</sup> sample time is multiplied by a factor of 512, based on system concept [5]

A stepped sine wave is a very accurate way to measure the frequency response of a system. Out of this the time behavior could be derived. Disadvantage of this method is the time consumption because a measurement needs to be taken for each frequency. When time and frequency signals are converted in each other special care should be taken to a adequate window function. The generation of sub-nano second pulses is hard to manage because it needs to deal with high peak voltages and powers. For this reason the correlation method provides a good alternative. This is focus of the next paragraph.

## III. THE M-SEQUENCE PRINCIPLE/SYSTEM

The ultra-wideband impulse is generated by autocorrelation of a pseudo-random-binary-noise sequence (pn- or m-sequence). Figure 3a shows a 4<sup>th</sup> order m-sequence with a corresponding period of  $T_0=N \cdot t_c$  with  $N=2^n-1=15$  chips. One chip is the time interval (sample time)  $t_c=1/f_c$  between two binary states, where  $f_c$  is the sampling frequency (or clock rate). The spectrum of the m-sequence is a SI-function (Figure 3b). 80% of the signal energy is contained up to the frequency of  $f_c/2$ . An increase of the clock rate results in a lower spectral resolution  $1/T_0$ . This could be compensated by an increase of the order of the m-sequence. Autocorrelation of the time signal generates the signal depicted in Figure 3c. The ambiguity range of one correlation peak to another one is  $T_0$ . If multiple reflections, e.g. from mismatched connectors are not abated in that time they occur at undefined distances.

A 9<sup>th</sup> order m-sequence system operates with a peak-peak-voltage of around 400 mV. In contrast to a 30 V peak output of an impulse generator [4] this is a tremendous difference. For a more detailed review of the signal generation and circuit design be referred to [5] and [7]. The ultra-wideband m-sequence system could be used as a standard time domain reflectometer. On the other hand the system is capable of operating like a multiport network analyzer for reflection and transmission measurements if there are added some switching blocks.

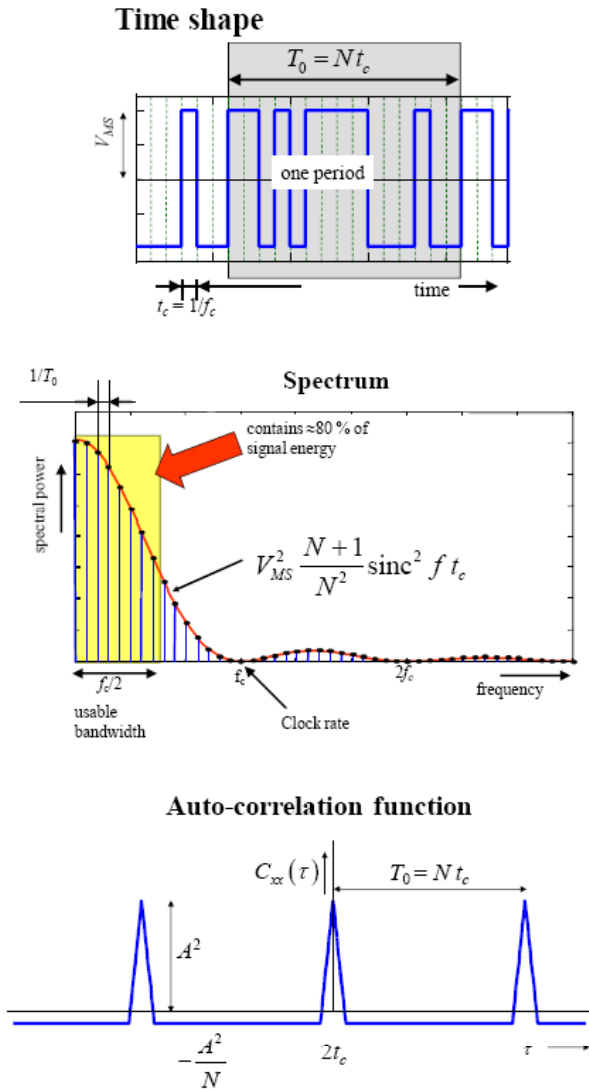


Fig. 3. (a) time signal of a 4<sup>th</sup> order m-sequence. (b) spectrum of the time signal (c) auto correlation of the time signal [7]

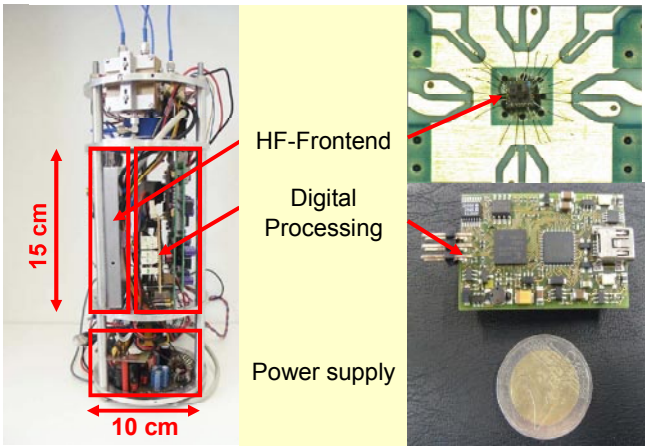


Fig. 4. (left) UWB hardware for recent measurements (right) HF-frontend integrated in a single chip and miniaturized digital unit.

The development of the described system was an evolutionary process. Figure 4 depicts the HF-Frontend and a digital unit for analog to digital conversion, hardware pre-processing and

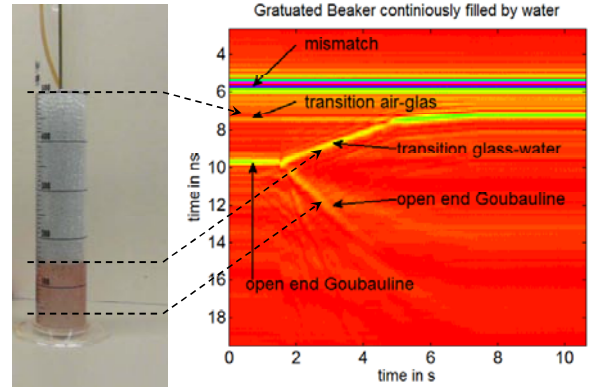


Fig. 5. UWB measurement of beaker continuously filled by water.

transmission to the PC. The HF-Frontend consists of four main elements: two receivers, one transmitter and a clock divider. Until now all measurements are made with systems that take these parts as basic components. Current developments integrate the HF-Frontend into a single chip system and miniaturize the digital unit (Figure 4 right). Further research is done. Scope and applications of such a sensor system is depicted in the next paragraphs.

IV. SCOPE: UWB MOISTURE MEASUREMENTS

In this work the focus is set on moisture measurement methods that are based on the interaction of electromagnetic waves with a medium. For a detailed review of different methods be referred to [8]. Moisture measurements are relevant for levee monitoring, surface irrigation in agriculture and long term observation of disposal zones. In this study a Goubau line is used as probe. In laboratory tests the described m-sequence system and the Goubau line are evaluated for their sensitivity to detect changing permittivity (and therefore changing moisture content) around the Goubau line. Figure 5 (left) depicts the measurement setup: a beaker is filled with glass spheres of 5 mm diameter (with a combined  $\epsilon_r = 3.3$ ), a Goubau line is inserted into the beaker; the beaker is continuously filled with water ( $\epsilon_r \approx 81$ ). The right picture of Figure 5 shows the radargram of this process: the y-axis describes the time in range direction; the x-axis is equal to the measurement time. At the beginning of the measurement ( $x = 0$  s) three main peaks are illustrated: at  $y = 6$  ns occurs the mismatch between the coaxial line and the Goubau line, around  $y = 7.5$  ns appears the transition between air ( $\epsilon_r \approx 1$ ) and glass spheres as surrounding material of the line; at  $y = 10$  ns turns up the reflection at the open end of the line. With proceeding measurement time the reflection at the open end of the line splits up into two peaks at the moment the water level reaches the end of the Goubau line. Due to the fact of an increasing water level a second transition appears between glass and water as surrounding media of the line. Water supply was stopped at the moment the water level reaches the level where the transition air-glass appeared before. Now at the time  $y = 7.5$  ns an new transition between air and a mixture of water and glass spheres is generated. Because of

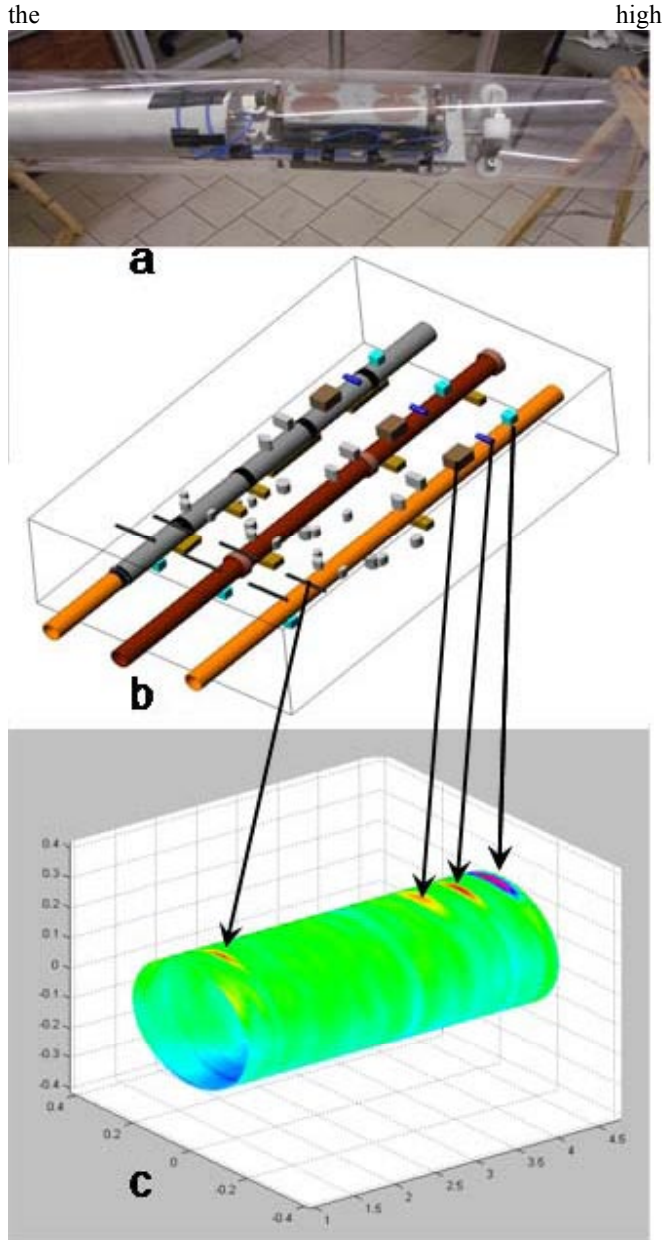


Fig. 6. (a) prototype system in transparent pipe (b) outdoor test bed with inhomogeneities around the pipes (c) measurement result, 3d volume

attenuation effects of water the reflection from the open end of the Goubau line disappears at a certain water level. As result of the experiment the sensitivity of the sensor configuration to resolve transitions between media with a small (air-glass spheres) and huge (glass spheres-water) contrast in  $\epsilon_r$  have been proven.

V. FURTHER APPLICATIONS AND RESEARCH

For a detailed description of the measurement setups, results and challenges be referred to [7-18]. The following examples will only give a short overview to demonstrate the variety of using the m-sequence principle.

A. Nondestructive Testing

Figure 6a shows a prototype system for quality assurance of

high new layed pipe systems and pipe inspection [7, 9, 10]. The



Visualisation of structural defects

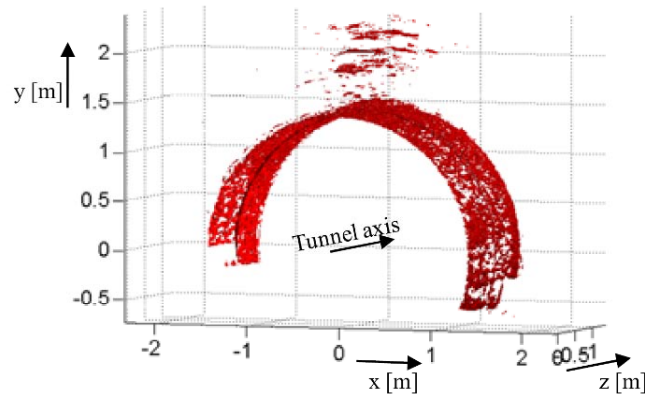


Fig. 7. (top) UWB hardware for measurements in salt mine tunnels (bottom) 3d volume of the disaggregation zone taken by an UWB scan.

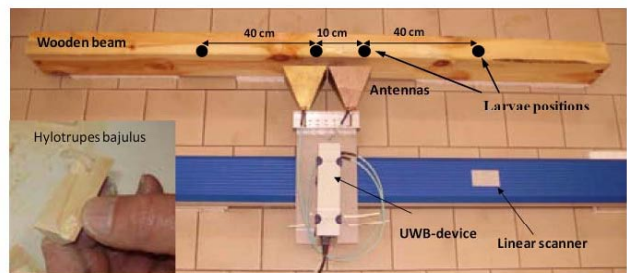


Fig. 8. Bistatic measurement setup for detection of woodworm larvae. [7]

system uses a 4 GHz bandwidth baseband system with a bistatic antenna arrangement and contains the hardware depicted in the left of Figure 4. A test bed (Figure 6b) was built to evaluate the performance of the prototype. It contains the mostly used pipe types (concrete, stoneware and pvc) and several objects (building rubble, stones, etc.) around the pipes to simulate a perturbation of the bedding zone. Measurements were performed as a C-scan. So it is possible to generate a full 3d volume (Figure 6c) of the surrounding area of the pipe. The image depicts a volume cut over the whole length at a certain radius from the center of the pipe. Four disturbances could be seen which correspond to the inhomogeneities in the test bed.

For characterizations of the disaggregation zone of salt mine tunnels an advanced ultra wideband sensor system with

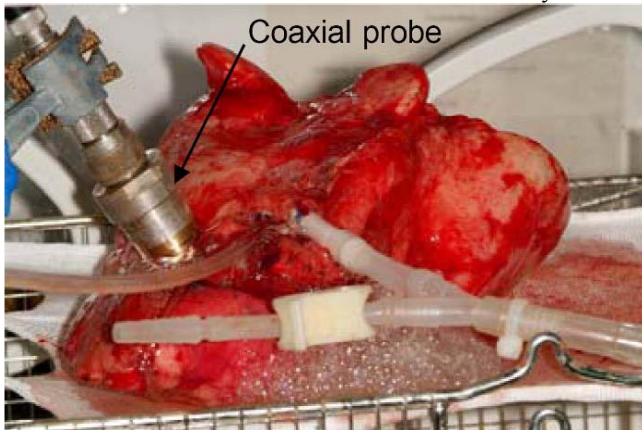


Fig. 9. Measuring the moisture content in a lung with a coaxial probe [12, 13]



Fig. 10. UWB imaging of a female chest. [14]

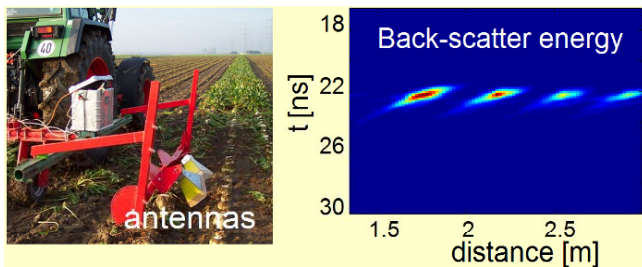


Fig. 11. sugar beat detection and crop estimation with an UWB device [15]

12 GHz bandwidth (1-13 GHz) was developed [7, 11]. The system depicted in Figure 7a uses a monostatic measurement setup with an integrated calibration unit. It is possible to measure sub mm cracks. This system is capable of providing full polarization measurements and 3d volume data which can be seen in Figure 7b. Structural changes can be clearly seen, especially in a 12 o clock direction.

Wood beams, antique furniture, wooden floors are often infested with vermin. Larva inside the wood can not be seen before they pupate and leave their food source. Often some sound can be heard if they eat through the wood. When they eat they have to move and these small movements can be detected with UWB. In Figure 8 a wood beam is scanned linearly with a bistatic measurement arrangement, to get a feeling for the size of the vermin a larva is depicted at the bottom left of the figure [7].

### B. Medical Engineering

In medical science it is often necessary to get real time information about the condition of the patient. There is collected data about the blood pressure, pulse rate, breathing frequency and so on. An important area is the preventional healthcare like early diagnosis of cancer. Figure 9 shows an experimental setup for a study of the moisture content in pulmonary tissue. A coaxial probe is used for reflection coefficient measurements. Out of this the frequency dependant permittivity could be calculated. Cancerous tissue has higher moisture content and therefore is separable from healthy tissue [12, 13].

Another setup is depicted in Figure 10 and shows a high resolution image of a female chest. Boundary scattering method is used to generate this point cloud out of the UWB raw data [14].

### C. Agriculture & Forest

Agriculturists want to know the expected crop yields. Figure 11 (left) shows an example of a sugar beat harvester with a mounted UWB device. Under good conditions the sugar beats could be detected and a difference in size could be verified. Goal was to detect the size and estimate the mass of the sugar beats. Challenges in this scenario are the high water content in the leaf, which disturbs the signal.

Another application for determination of commodity quantities is the bark thickness estimation of trees to get information about the real amount of the harvested lumber.

### D. Search and Rescue, Humanitarian Aid

In the occurrence of natural disasters (earthquakes, flooding, etc.) people often get buried by rubble but are still alive. The rescue forces have to act quickly to pick up life signs. Ultra-wideband signals up to a frequency of 2 GHz could be used to penetrate building rubble up to 2 m. Small movements of objects could be detected (body movement and breathing detection). At smaller distances even the movement of a beating heart can be detected [7, 16].

Former regions of war are often contaminated with landmines. UWB-signals offer a chance to do ground penetrating radar (GPR) measurements with higher resolution and a more precise image processing. [17]

### E. Automotive

Current adaptive cruise control systems (ACC) use radar for range and speed estimation of other vehicles [18]. UWB could be used for better classification of the different objects, e.g. cars, humans or rods. There is also the possibility to monitor viability of the driver (heartbeat, eye movement, seat occupation, etc).

### F. Defense and Security

UWB in general and the described m-sequence system could be an advancement of current security systems. The huge frequency band covers much information. Even if the object under test has a good absorption at one frequency other frequencies would be detectable. A second factor is the

improvement of the range resolution and therefore a better object separation and a more exact tracking result.

## VI. CONCLUSION

In this work a short introduction to UWB and its basic concepts was given. With the help of an m-sequence UWB sensor it was demonstrated the suitability for the resolution of small dielectric contrasts which is essential to estimate the moisture content of a sample. The variety of different applications for UWB systems was demonstrated by many examples and therefore the potential of the UWB sensor was pointed out.

## REFERENCES

- [1] J. D. Taylor, Introduction to ultra-wideband radar systems, CRC Press, 1995, p. 2.
- [2] H. Nikoogar, R. Prasad, Introduction to Ultra Wideband for Wireless Communications Signals and Communication Technology, Springer-Verlag, 2008, ch. 10.
- [3] D. M. Pozar, Microwave Engineering, 2<sup>nd</sup> ed., John Wiley & Sons, 1998, pp-205-206
- [4] J. D. Taylor, Introduction to ultra-wideband radar systems, CRC Press, 1995, pp. 287-296
- [5] J. Sachs, *M-sequence radar*. In *Ground Penetrating Radar*, 2nd edition, D.J. Daniels ed., IEE Radar, Sonar, Navigation and Avionics Series 15, pp. 225-237, 2004
- [6] R&S Data Sheet, R&S®ZVA Vector Network Analyzer Specifications, München, 2009
- [7] J. Sachs, F. Bonitz, M. Kmec, M. Helbig, R. Herrmann, K. Schilling, P. Rauschenbach, E. Zaikov, *Ultra-wideband pseudo-noise sensors and their application in medical engineering, nondestructive testing and for search and rescue*, in proc. of the 55th IWK – Internationales Wissenschaftliches Kolloquium, Ilmenau, 2009
- [8] K. Kupfer, *Electromagnetic Aquametry. Electromagnetic Wave interaction with Water and Moist Substances*, Springer Verlag, Heidelberg 2005, pp. 312
- [9] F. Bonitz, R. Herrmann, M.Eidner, J. Sachs, H.Solas, *Application of ultra-wideband radar sensors for non-destructive testing of pipe systems and salt mine tunnels*, in proc. of the 55th IWK – Internationales Wissenschaftliches Kolloquium, Ilmenau, 2009
- [10] F. Bonitz, J. Sachs, R. Herrmann, M. Eidner, *Radar Tube Crawler for Quality Assurance Measurements of Pipe Systems*, EURAD 2008: Proceedings of the 5th European Radar Conference; 27-31 October 2008; Amsterdam, The Netherlands.
- [11] R. Herrmann, J. Sachs, K. Schilling, F. Bonitz, *12-GHz Bandwidth M-Sequence Radar for Crack Detection and High Resolution Imaging*; GPR 2008: 12th International Conference on Ground Penetrating Radar; June 16-19, 2008; Birmingham, UK.
- [12] M. Schaefer, K. Nowak, B. Kherad et al., *Monitoring water content of rat lung tissue in vivo using microwave reflectometry*, Med. Biol. Eng. Comput., 42, 577-580, 2004.
- [13] M. Helbig, J. Sachs, U. Schwarz et al., *Ultrabreitband-Sensorik in der medizinischen Diagnostik*, in 41. Jahrestagung der Deutschen Gesellschaft für Biomedizinische Technik (BMT 2007), Aachen (Germany), 2007.
- [14] M. Helbig, C. Geyer, M. Hein et al., „A breast surface estimation algorithm for UWB microwave imaging,” Proc. EMBEC 2008, Antwerpen, 760-763, 2008.
- [15] M. Konstantinovic, S.Wöckel, P. Schulze Lammers, J. Sachs, *Evaluation of a UWB radar system for yield mapping of sugar beet*, Annual Conference of the American Association of Agricultural and Biological Engineers (ASABE), USA, June 2007.
- [16] E. Zaikov, J. Sachs, M. Aftanas et al., “Detection of trapped people by UWB radar,” in German Microwave Conference (GeMiC 2008), Hamburg (Germany), 2008
- [17] Crabbe,S., Sachs,Jürgen, Peyerl,P., Alli,G., Eng,L., Khalili,M., Busto,J., Berg,A., “Results of field testing with the multi-sensor DEMAND and BIOSENS technology in Croatia and Bosnia developed in the European Union’s 5th Framework Programme,” SPIE 2004, Detection and Remediation Technologies for Mines and Minelike Targets IX, Orlando, Florida, Vol. 5415 Part One, pp. 456, April 2004.
- [18] J. Mühlfeld, “Inbetriebnahme und Evaluierung eines 76,5 GHz Long Range-Radars zur Personendetektion”, B.Sc. thesis, Dept. Electron. Eng., Technical University of Ilmenau, Ilmenau, Germany, 2009

# TanDEM-X Mission and DEM Accuracy

Jaime Hueso Gonzalez, Markus Bachmann, Johannes Böer,  
Hauke Fiedler, Gerhard Krieger, *Member, IEEE*, and Manfred Zink

**Abstract**—TanDEM-X (TerraSAR-X Add-on for Digital Elevation Measurements) is currently implemented as a national Earth observation mission by the German Aerospace (DLR) and EADS Astrium GmbH. This first bistatic satellite synthetic aperture radar (SAR) mission opens a new era in spaceborne radar remote sensing. The tandem configuration is formed by flying TanDEM-X and TerraSAR-X in a closely controlled helix formation. The primary mission goal is the derivation of a high-precision global Digital Elevation Model (DEM) with 12 m resolution, 10 m absolute height accuracy and 2 m relative height accuracy. This paper provides an overview of the mission with main focus on the data acquisition concept for the interferometric radar data and the derivation of the specified accurate global DEM.

**Index Terms**—Digital elevation model, InSAR, satellite remote sensing, synthetic aperture radar, TanDEM-X.

## I. INTRODUCTION AND OBJECTIVES

THE TanDEM-X system [1] is a synchronized SAR satellite formation consisting of the TerraSAR-X satellite (TSX) and its twin satellite TanDEM-X (TDX). Their combined operation allows single-pass SAR interferometry (InSAR) with variable cross-track baselines typically between 250 and 500 m. The instruments on both satellites are advanced high resolution X-band SAR systems based on active phased array technology, which can be operated in Spotlight, Stripmap, and ScanSAR mode with full polarization capability [2]. The center frequency of the instruments is 9.65 GHz with a selectable SAR chirp bandwidth of up to 300 MHz. The active phased array antenna, which has an overall aperture size of  $4.8 \text{ m} \times 0.7 \text{ m}$ , is mounted on one side of the hexagonal spacecraft body. It consists of 12 panels with 32 dual-polarization waveguide sub-arrays each. This enables extremely flexible beam steering and shaping options.

The primary mission goal is the derivation of a global DEM of the Earth surface within four years after launch. The aimed DEM resolution is 12 m (independent posting), and the DEM height requirements are 10 m absolute and 2 m relative accuracy in regions with  $100 \text{ km} \times 100 \text{ km}$  size [1]. This has

Manuscript received January 20, 2010. This work was supported in part by the German Federal Ministry for Economics and Technology (Förderkennzeichen 50 EE 0601).

The authors are with the Microwaves and Radar Institute, German Aerospace Center (DLR), 82234 Wessling, Germany (e-mail: [jaime.hueso@dlr.de](mailto:jaime.hueso@dlr.de)).

been only achieved up to now by local scale DEM products.

To achieve these goals, around 3 years of combined satellite operations are required. TSX has been in orbit since June 2007, and the launch of TDX is planned for the first half of 2010. Considering the current TSX satellite resources status, it is expected that the satellite exceeds its nominal lifetime of  $5\frac{1}{2}$  years, so that the 3 years overlap with TDX are maintained. In addition, to achieve the demanding relative height accuracies, DEM systematic errors have to be corrected. Therefore, a robust DEM calibration concept has been implemented [3].

Secondary mission goals are the experimentation of several SAR techniques, like along-track interferometry (ATI) for measuring the velocity of moving objects with a high accuracy, digital beam-forming, bi-static experiments and local DEMs with increased accuracy for selected terrain (local areas with high reflectivity, low noise, high correlation, suitable observation conditions).

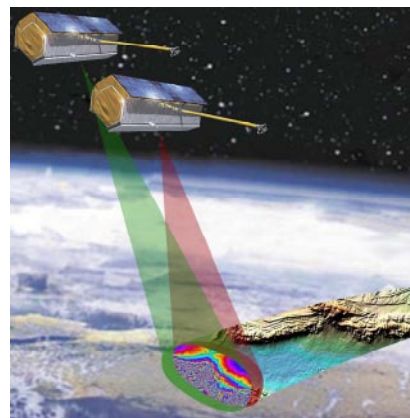


Fig. 1. Illustration of the TanDEM-X constellation. One of the satellites transmits the radar pulses, while the reflected signal from the Earth surface is received by both SAR antennas. On ground, an InSAR-derived DEM is generated.

## II. MISSION DESCRIPTION

### A. Acquisition Modes

Interferometric data acquisition with the TanDEM-X satellite formation can be achieved in different operational modes. Examples are bistatic, monostatic, and alternating bistatic operation, which are illustrated in Fig. 2. The three interferometric configurations may further be combined with different TSX and TDX SAR imaging modes like Stripmap, ScanSAR, Spotlight, and Sliding Spotlight.

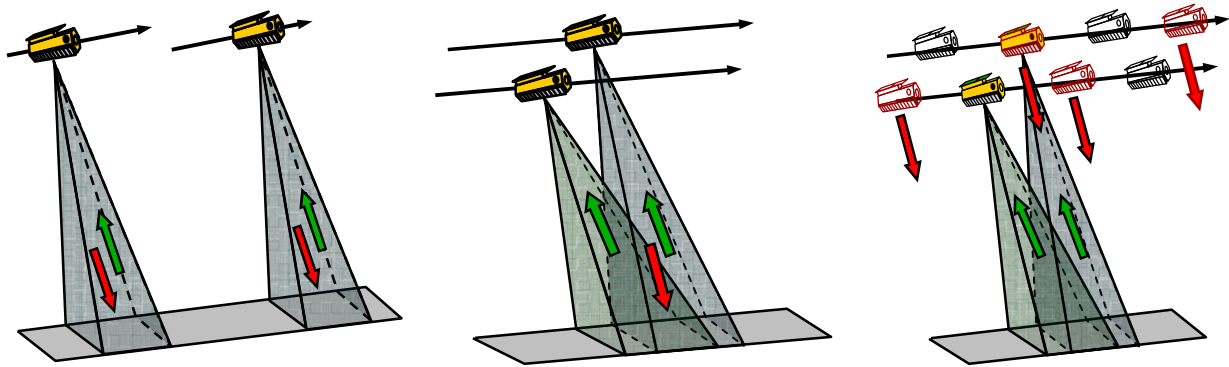


Fig. 2. Data acquisition modes for TanDEM-X: Pursuit monostatic mode (left), bistatic mode (middle), and alternating bistatic mode (right).

Operational DEM generation is planned to be performed using the bistatic InSAR Stripmap mode shown in the center of Fig. 2. This mode uses one satellite as a transmitter to illuminate a common radar footprint on the Earth's surface. The scattered signal is then recorded by both satellites simultaneously. This simultaneous data acquisition makes dual use of the available transmit power and is mandatory to avoid potential errors from temporal decorrelation and atmospheric disturbances.

### B. Satellite Formation

The TanDEM-X operational scenario requires the coordinated operation of two satellites flying in close formation. A so-called “helix” satellite formation, shown in Fig. 3, has been chosen for the operational DEM generation.

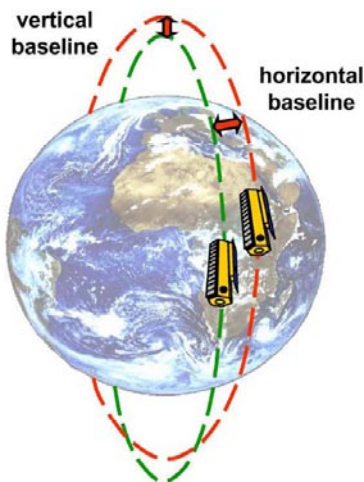


Fig. 3. Orbit planes of the TanDEM-X constellation. Horizontal separation in the equator; vertical separation in the poles. This results in a relative helix movement between the satellites with one orbit periodicity.

This formation combines an out-of-plane (horizontal) orbital displacement by different ascending nodes with a radial (vertical) separation by different eccentricity vectors resulting in a helix-like relative movement of the satellites along the orbit. Since there exists no crossing of the satellite orbits, arbitrary shifts of the satellites along their orbits are

allowed. This enables a safe spacecraft operation without the necessity for autonomous control.

The “helix” formation allows a complete mapping of the Earth with a small number of formation settings. Southern and northern latitudes can be mapped with the same formation setting by using ascending orbits for one and descending orbits for the other hemisphere. A fine tuning of the cross-track baselines can be achieved by taking advantage of the natural rotation of the eccentricity vectors due to secular disturbances, also called motion of libration. The phases of this libration can be kept in a fixed relative position by scheduling small maneuvers using the cold gas thrusters on a daily basis, while major formation changes as well as a duplication of the orbit keeping maneuvers required by TSX will be performed by the hot gas thrusters. This flexibility in the baseline configuration permits the implementation of a robust acquisition strategy against phase unwrapping errors, as will be explained in the following Section II.C.

It is furthermore possible to optimize the along-track displacement at predefined latitudes for different applications. While cross-track interferometry aims at along-track baselines as short as possible to ensure an optimum overlap of the Doppler spectra and to avoid temporal decorrelation in vegetated areas, other applications like along-track interferometry or super resolution require selectable along-track baselines in the range from hundred meters up to several kilometers.

### C. DEM Acquisition Plan

The TanDEM-X mission should not interfere in the fulfillment of the TerraSAR-X mission. To minimize conflicts, TerraSAR-X datatakes will be distributed on both satellites. This leaves sufficient satellite resources for the DEM acquisition. For coordinating the data acquisition, a “Joint TerraSAR-X & TanDEM-X Acquisition Concept” has been developed, which is capable of handling acquisition requests of both missions based on a simple priority concept, already established for the TerraSAR-X mission. According to this concept, the TanDEM-X datatakes for global DEM generation are planned well in advance for a long time span (e.g. one year) and are set to high priority. Nonetheless a

DEM acquisition can still be overruled by another high-priority acquisition, but it is ensured by the ground segment ordering chain that the skipped acquisition is shifted automatically to one of the following orbit repeat cycles, where it is scheduled with highest priority. The same re-ordering concept applies for the case of unexpected data loss.

In order to achieve the required global DEM accuracy, the height of ambiguity of the interferometric acquisition should be as homogeneous as possible for all datatakes. Therefore the satellite formation is not kept fix, but permanently and slowly drifting. For example, the horizontal baseline at the ascending node (see Fig. 3) will drift from a starting value of  $\sim 230$  m to higher values ( $\sim 400$  m) over mission time. As a consequence, the height of ambiguity is changing slowly for a given beam and latitude. Acquisitions are planned starting from geographical positions with lower latitudes and finally reaching polar regions. The whole Earth land surface can be recorded in less than a year.

According to this, in the first year of TanDEM-X mission the full Northern Hemisphere will be acquired during ascending orbits and the Southern Hemisphere during descending orbits, resulting in a complete mosaic of parallel adjacent datatakes. Relatively small effective baselines will be used, resulting in a large height of ambiguity of around 45 m. The consequences of a large height of ambiguity are a simplification of the phase unwrapping procedure of the interferograms and a low height accuracy (compared to requirements). Hence, a full coverage Earth DEM with a reduced accuracy could be derived already after the first year of TanDEM-X operation.

In the second year, it is foreseen to repeat the same first year acquisitions with a scaled helix formation. This will mean larger effective baselines and smaller heights of ambiguity (around 30 m). Such configuration has two advantages with respect to the first year: a better height resolution and a high robustness against phase unwrapping errors. The latter is achieved by combining the two overlapping acquisitions with different heights of ambiguity employing multi-baseline phase unwrapping methods (resulting height of ambiguity lies around 90 m).

In the third year, the acquisition will focus on difficult terrain. This comprises e.g. mountainous regions, which will

be acquired with a third effective baseline and/or from crossing orbits. Along the equator, the acquisition of long crossing orbits at equally spaced intervals can aid in the DEM calibration. Additionally, datatakes from the first two years specially affected by shadowing, layover or foreshortening effects will be acquired again from different incidence angles.

All this should be accomplished in the first half of the third year. In the second half, the satellites will be separated in along track to perform ATI scientific experiments like traffic, ocean current or glacier monitoring. The process of along-track separation is suited for experiments that require large bistatic angles.

#### D. Global DEM Processing Chain

The DEM processing chain (see Fig. 4) is a key part of the TanDEM-X ground segment. Focusing on the upgrades with respect to the TerraSAR-X mission, the processing chain combines the two SAR images (one monostatic and the other bistatic) recorded by the satellites and generates the interferogram. It has to be noted that either TSX or TDX can act as active satellite in a DEM acquisition. The instrument calibration is responsible of correcting the instrument drifts at this early phase, as well as known phase trends originated, e.g. by the SAR antenna phase center or by its phase diagram. The phase errors originated by the relative frequency drifts between the two instrument oscillators are also corrected at this stage by evaluating the synchronization information recorded within the radar data (see also Section III.C).

The raw DEM can then be derived. However, and according to the acquisition strategy introduced in Section II.C, the TanDEM-X processor will wait until the end of the second year acquisitions to operationally generate the raw DEMs, in order to minimize phase unwrapping and typical side-looking geometry errors.

Once a whole stack of raw DEMs is available for a large region (e.g. a fraction of a continent) in the database, the DEM Mosaicking and Calibration Processor (MCP) [4] takes care of correcting the residual systematic height error contributions, aided by a precise height references database, and generate the accurate TanDEM-X global DEM (see [3]).

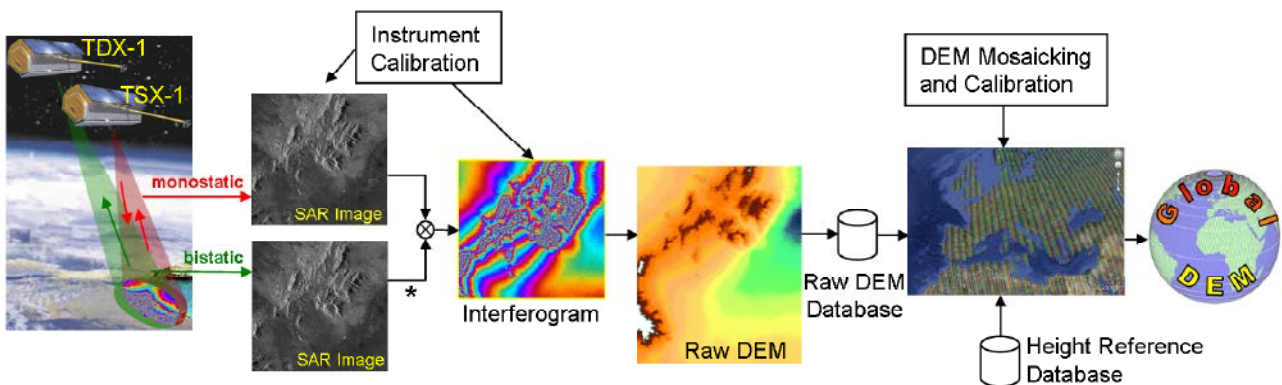


Fig. 4. TanDEM-X DEM processing chain.

### III. CHALLENGES CONSTELLATION

#### A. Collision Avoidance

The absolute distance between the satellites in orbit oscillates between around 500 m to several kilometers, and their altitude over the Earth surface is around the 520 km. This gives an idea about the precision required to control the relative position between the satellites and to avoid any collision risk.

The helix formation described in Section II.B has a passive stability, as both orbit trajectories never cross. Nevertheless, several measures have been implemented to avoid uncontrolled thruster activities and constantly monitor the status of the satellites.

On the one hand, the ground operations and stations network have been adapted to ensure S-band telemetry contacts with a maximum separation of 6 hours. This allows the early detection of a potential event or anomaly in any of the satellites, and provides a sufficient reaction margin.

On the other hand, the Automatic Safe Mode (ASM) of the two satellites has been optimized. In the original design, in case of an event or anomaly in the satellite, the instruments entered in the so-called “safe mode”, in which most of the satellites electronics are cautiously shut down. In order to allow the maintenance of the orbit during an ASM, the thrusters started automatically regulating the satellite position. A potential error in the thrusters’ activity could not be detected on ground on time, which could cause a collision in the worst case. In order to avoid this, the thruster activity during safe mode has been now disabled, allowing only a slow magnet torquer attitude regulation of the satellites.

#### B. Exclusion Zones

Another challenge of the close flying formation of the TanDEM-X constellation is the risk of mutual SAR illumination. During certain orbit periods, one of the satellites might be located in the area illuminated by the SAR antenna main lobe of the other satellite (see Fig. 5), risking potential damage of electronic units on the irradiated satellite. Therefore, exclusion zones have to be defined along the orbit for each satellite, in which the transmission by the SAR antenna is disabled. Due to the helix formation, the exclusion zones are almost periodic with the orbit, and both satellites can never be simultaneously in an exclusion zone. Thus, TanDEM-X mission datatakes are never affected by them.

The exclusion zones are checked twice on ground before commanding the datatakes, and a third time on the satellite just before each acquisition starts. Additionally, two other techniques are used to allow the satellites to monitor the status of its neighbour and verify its nominal operation without needing the intervention of the ground. In case the opposite satellite does not respond or indicates an anomaly, its position is considered unknown, thus the requesting satellite automatically switches off its transmit capabilities to prevent radiation.

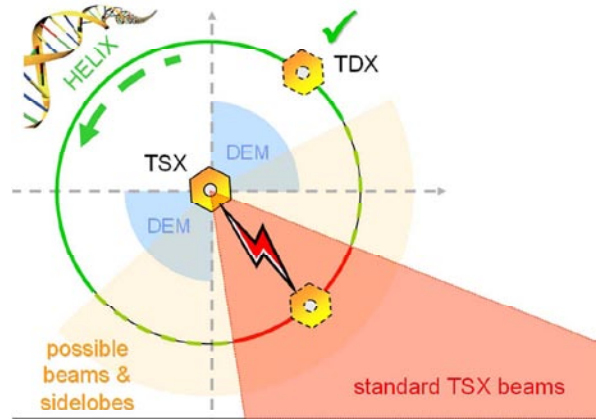


Fig. 5. View of the relative satellite movement (flight direction into the paper) and definition of an exclusion zone to avoid SAR illumination.

One of these methods is the inter-satellite link, through which house-keeping (HK) data are exchanged. The other procedure is the exchange of “sync warning” pulses through the synchronization link. This bi-directional check is possible after a software update on the satellites which allows for interpreting the sync pulses and setting an expected receive power threshold on board. If the received pulse is below the threshold or no pulse can be detected, it means that the neighbouring satellite is not in its nominal position, and could have traveled, in a worst case, towards the region of maximum SAR antenna radiation of the other satellite. The “sync warning” procedure quickly switches off transmission, and sets the satellite in standby. The problem is then analyzed and solved on ground, the current satellite positions are tracked again and commands are uploaded to resume nominal operations.

#### C. Synchronization

The bistatic data acquisitions are based on the use of two independent oscillators for modulation and demodulation of the radar pulses. The impact of oscillator phase noise in bistatic SAR has been analyzed in [5], where it is shown that oscillator noise may cause significant errors in both the interferometric phase and SAR focusing. The stringent requirements for interferometric phase stability in the bistatic mode will hence require an appropriate relative phase referencing between the two SAR instruments or an operation in the alternating bistatic mode.

In TanDEM-X, a dedicated inter-satellite X-band synchronization link has been established, through which special radar pulses are mutually exchanged (see Fig. 6). For this, the nominal bistatic SAR data acquisition is shortly interrupted, and a radar pulse is redirected from the main SAR antenna to one of six dedicated synchronization horn antennas mounted on each spacecraft. The pulse is then recorded by the other satellite, which in turn transmits a short synchronization pulse. By this, mutual phase referencing can be achieved without exact knowledge of the actual distance between the satellites.

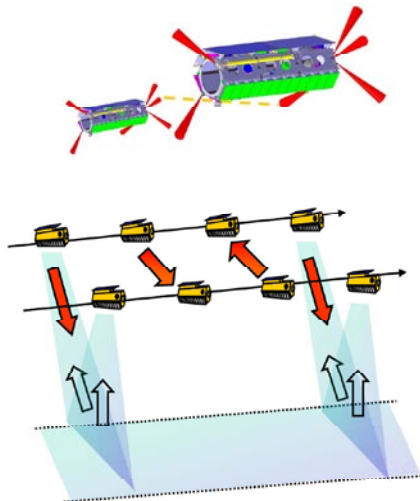


Fig. 6. On the top, sync horns (in red) ensure the constant communication in all directions regardless of the formation relative position. On the bottom, the synchronization pulses sequence is shown.

On ground, a correction signal can then be derived from the recorded synchronization pulses, which compensates the oscillator induced phase errors in the bistatic SAR image. In addition, synchronization is also required for datatake commanding. TSX and TDX trigger the start of a datatake via GPS, but the radar pulse timing is then derived internally from the Ultra Stable Oscillators (USO). A deviation of the two USO frequencies would hence lead to a drift of the receiving window of one satellite with respect to the transmit event of the other, and may by this prevent a proper recording of the echo signal. TanDEM-X accounts for this by introducing empty pulse repetition intervals (leap PRIs) configured to readjust the position of the receiving window.

#### IV. DEM CALIBRATION

A detailed height performance model was developed for the bistatic mode, the main mode for DEM generation [1]. It showed that very precise knowledge of interferometric baseline is required in order to achieve the specified height accuracy. Even so, residual baseline errors are present. In addition, and regardless of all the efforts along the DEM processing chain to eliminate height error sources, instrument error components will also remain [3].

Examples of systematic slow changing errors for baseline determination are inaccuracies in the relative orbit and attitude determination of the TanDEM-X helix formation and variations in the SAR antenna phase centre. On instrument side, slow errors occur due to remaining interpolation errors after internal calibration and phase drifts during synchronization pulse sequences in the amplifiers not compensated by the internal calibration. When a datatake is acquired, these phase errors lead to a height error in the resulting raw DEM.

The DEM calibration strategy concentrates on eliminating the systematic components of these baseline and instrument

residual errors, which is sufficient to accomplish the height error requirements. With the aim of guaranteeing the correct adjustment of the final DEM by the TanDEM-X MCP, height references are required.

On the one hand, they provide absolute height calibration. The references have to be adequately distributed, with coverage on all significant isolated land masses and a known accuracy that fulfils the requirements [3]. Several suitable sources of height reference data have been identified, including global data sets (e.g. ICESat laser altimetry data), GPS tracks, ground targets (corner reflectors, transponders) and local highly accurate DEMs from airborne LIDAR, photogrammetry and SAR [6].

On the other hand, the height references are used for the relative adjustment of the raw DEMs, aided by tie-points [3]. Tie-points are spots of a DEM with a high coherence and radar cross section, located in overlapping regions between adjacent datatakes.

A functional model based on the expected error behaviour has been developed to correct the systematic height error components. This model is a simple 2D polynomial function with up to 6 coefficients. The complete system of 2D polynomial functions in a full datatake scene is solved by a least-squares method, and the coefficients are determined by applying all high quality height references and tie-points available over the region.

This DEM calibration strategy ensures the generation of an accurate TanDEM-X global DEM.

#### REFERENCES

- [1] G. Krieger, A. Moreira, H. Fiedler, I. Hajnsek, M. Werner, M. Younis, and M. Zink, "TanDEM-X: A satellite formation for high-resolution SAR interferometry," *IEEE Trans. on Geoscience and Remote Sensing*, vol. 45, no. 11, pp. 3317–3341, Nov. 2007.
- [2] M. Stangl, R. Werninghaus, B. Schweizer, C. Fischer, M. Brandfass, J. Mittermayer, H. Breit, "TerraSAR-X technologies and first results," *IEE Proc. - Radar, Sonar and Navigation*, vol. 153, pp. 86–95, 2006.
- [3] J. Hueso Gonzalez, M. Bachmann, G. Krieger, and H. Fiedler, "Development of the TanDEM-X Calibration Concept: Analysis of Systematic Errors," *IEEE Trans. on Geoscience and Remote Sensing*, TerraSAR-X Special Issue, vol. 48, no. 2, in print, Feb. 2010.
- [4] B. Wessel, A. Gruber, J. Hueso Gonzalez, M. Bachmann, and A. Wendleder, "TanDEM-X: DEM calibration concept," in *Proc. IEEE IGARSS*, Boston, MA, Jul. 2008, pp. III-111–III-114.
- [5] G. Krieger, M. Younis, "Impact of Oscillator Noise in Bistatic and Multistatic SAR," *IEEE Geoscience and Remote Sensing Letters*, vol. 3, pp. 424–428, 2006.
- [6] J. Hueso Gonzalez, M. Bachmann, H. Fiedler, G. Krieger, and M. Zink, "TanDEM-X DEM Calibration Concept and Height References," *Proceedings of European Conference on Synthetic Aperture Radar (EUSAR)*, Friedrichshafen, Germany, Jun. 2008.

# GNSS Overview with Emphasis on Propagation Issues

Achim Hornbostel

*DLR, Institute of Communications and Navigation*

**Abstract**— Today, satellite navigation with GPS is well established and widely used. The European satellite navigation system Galileo is under development and first services shall start in early 2014. The status and planning of existing and future Global Navigations Satellite Systems (GNSS) is summarized based on currently available information with the emphasis on the different signals and services offered. The benefits of the new signals for reduction of errors induced by propagation phenomena are discussed.

**Index Terms**—Galileo, GNSS, GPS, Ionosphere, Multipath, Navigation Signals, Satellite Navigation Systems, Troposphere

## I. INTRODUCTION

THE positioning with satellite navigation systems like GPS or Galileo is based on time of arrival measurements of the signals transmitted from the satellite at the receiver. The measured signal delays are converted to pseudoranges by multiplication with the speed of light. The prefix ‘pseudo’ signifies the fact that they do not correspond to the real geometrical ranges from the receiver to the satellites, because the receiver clock is not synchronized to the satellite system time and the measured delays include additional contributions by system and propagation errors which must be corrected for. For synchronization of the receiver clock to the system time measurement data from at least four satellites must be available. Then the receiver clock bias can be solved for as a fourth unknown together with the three unknown co-ordinates of the position  $x$ ,  $y$ ,  $z$  by triangulation. While system errors can normally not be corrected in real time, propagation errors can be reduced by models or advanced signal processing, where the remaining errors depend on the type of measurements, e.g. single frequency or multi frequency measurements, signal characteristics, e.g. carrier frequency and bandwidth, and the quality of the models used. Satellite navigation signals are extremely weak when they arrive at the user antenna; the nominal GPS power received at ground is -157 dBW, which is below the noise level. Therefore, the signal reception is sensitive to shadowing by

buildings or attenuation by vegetation. Navigation signal are spread spectrum signals, which are recovered from noise by despreading in the receiver, i.e. by correlation with a replica of the satellite code. By this correlation process also the time of arrival, i.e. the delay of the received satellite code is determined. If the direct signal is superposed with reflected signals from the user environment due to multipath propagation, the peak of the correlation function becomes less unique and the accuracy of the delay measurement is reduced.

Most mass market receivers today still just use GPS L1 C/A code single frequency measurements. Table I shows an error budget for the GPS standard positioning services with the L1 C/A code. Shown is the User Equivalent Range Error (UERE), which is the RMS range error that the user must expect in the worldwide average. It is important to note, that these are the residual errors after correction. Besides orbit and satellite clock errors which may also be reduced in the future by better technology, propagation effects in the atmosphere and multipath propagation in the user environment are the dominant error contributions. The ionosphere error is even the dominant contributor in the whole error budget.

New signals at different carriers with higher bandwidth and improved signal characteristics which will be made available also for the civilian user by the modernized GPS, Galileo and other future GNSS have the potential to reduce the propagation errors significantly.

TABLE I  
GPS L1 C/A ERROR BUDGET (UERE) [1]

Component	Error
Ephemeris	2.1 m
Satellite clock	2.1 m
Ionosphere	4.0 m
Multipath	1.4 m
Troposphere	0.7 m
Receiver noise	0.5 m
Total (RMS)	5.3 m

A. Hornbostel is with the Institute of Communications and Navigation at the German Aerospace Center (DLR e.V.), Oberpfaffenhofen, D-82230 Weßling, P.O. Box 1116, Germany (phone: +49 8153 282318, fax:+49 8153 282328, email: achim.hornbostel@dlr.de).

## II. PRINCIPLE OF SATELLITE NAVIGATION

For positioning with satellite navigation signals the signal delay from the transmitting satellites to the user receiver is measured. The signal delays are converted to so-called pseudoranges by multiplication with the vacuum speed of light. The pseudoranges contain all propagation effects and the offset of the receiver clock to the satellite system time. The measured pseudorange to satellite  $i$  can be written as:

$$PR_i = \sqrt{[X_i - X]^2 + [Y_i - Y]^2 + [Z_i - Z]^2} - c \cdot (T_{Sat} - T_{Rx}) + \varepsilon_i, \quad (1)$$

where  $X_i, Y_i, Z_i$  are the coordinates of satellite  $i$  and  $X, Y, Z$  are the coordinates of the unknown 3D receiver position. The satellite coordinates  $X_i, Y_i, Z_i$  (orbit parameters) are transmitted in a low data rate navigation message by each satellite.  $T_{Sat}$  is the satellite system time to which all satellites are synchronized and  $T_{Rx}$  is the time of unsynchronized receiver clock. The variable  $\varepsilon_i$  denotes all measurement errors including propagation effects on path  $i$ . After correction of the propagation effects and other measurement errors the four unknowns  $X, Y, Z$  and  $\Delta T = T_{Sat} - T_{Rx}$  can be determined from independent measurements to four different satellites. Thus, at least four satellites must be in view of the user antenna. From (1) it can be also seen that any uncorrected error or residual error after correction will bias the ranges and the position solution.

Satellite navigation signals are spread spectrum signals, which are extremely weak (about -157 dBW) and below the thermal noise level when arriving at the user antenna. For recovering the signals from noise (despreading) the incoming signals are correlated with a local copy (replica code) of their known spreading codes in the receiver. By this correlation process also the signal propagation time from the satellite to the user receiver is determined: The measured signal delay (equivalent to the pseudorange) is the time shift which must be applied to the code of the incoming signal to match exactly with the replica code, i.e. to reach the correlation peak. After despreading the navigation message with the satellite orbit parameters can be decoded and (1) can be solved.

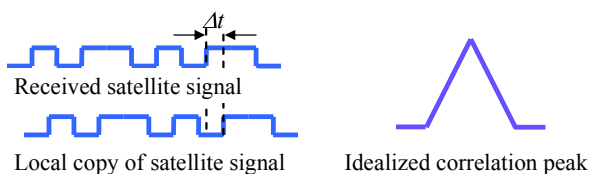


Fig. 1. Correlation of incoming satellite signal and replica signal

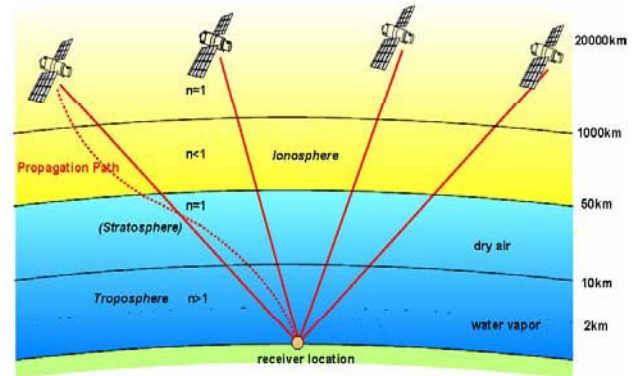


Fig. 2. Structure of the atmosphere and influence on propagation path

## III. SUMMARY OF PROPAGATION EFFECTS

Fig. 2 shows the propagation path of the GNSS signals through the different layers of the atmosphere. Starting from the top, the signals first reach the ionosphere, where due to the existence of free electrons the refractive index is smaller than 1. Between 50 and 100 km above ground the free electrons disappear and the signals start to propagate through the neutral atmosphere which is composed of different atmospheric gases. With lower altitudes the air pressure and density of the atmospheric gases increase and the refractive index grows accordingly to values larger than 1. The variation and gradient of the refractive index causes as main effect a change of the signal propagation speed but as secondary effect also a curvature of the propagation path. Both effects result in an additional delay of the signal at the user receiver compared to the signal propagation in vacuum. The propagation delay can be expressed as excess path relative to the geometrical range from the satellite to the user by multiplication with the speed of light. The measured pseudoranges must be corrected for this excess path. The following paragraphs provide a summary of the main propagation effects which are discussed in more detail e.g. in references [1]-[4].

### A. Ionosphere error

The ionosphere is characterized by ions and free electrons which are created by UV and X-ray radiation of the sun. Therefore, the ionosphere state is coupled to the 11 year cycle of solar activity, to day and night time and to the season. The relevant layer which contains most of these particles extends between 80 and 1000 km above the earth surface. The key parameter for navigation is the Total Electron Content TEC, which is the integral of the total electron density in a column of  $1\text{m}^2$  from the observation point to the satellite:

$$TEC = \int_{path} N_e dl \quad [\text{el}/\text{m}^2]. \quad (2)$$

The ionospheric excess path is directly proportional to the TEC and inversely proportional to the square of the carrier frequency [3], [4], [5]:

$$\Delta L = \pm \frac{40.3}{f^2} \int_{path} N_e dl = \pm \frac{40.3}{f^2} TEC. \quad (3)$$

The plus sign applies for the group delay which is relevant for the code phase measurements of the navigation signals and the minus applies for the phase delay which is relevant for the carrier phase measurements. The opposite sign of code and carrier delay means that code and carrier diverge in the ionosphere, because the code is delayed but the carrier phase is advanced.

Table II presents typical values of the ionosphere excess path dependent on the carrier frequency for low and high TEC values for the currently used and planned L-Band frequency bands and allocated GNSS frequency bands in S- and C-band. The vertical excess path lies normally between these values. The GPS, GLONASS and Galileo frequencies are between 1200 and 1600 MHz.

If signals on two measurement frequencies are available the ionosphere error at each of these frequencies can be determined by measurement of their differential group delay  $\delta(\Delta t) = \Delta t_2(f_2) - \Delta t_1(f_1)$ . By division with the speed of light  $c$  it follows from (3):

$$\delta(\Delta t) = \frac{40.3}{c} TEC \left( \frac{1}{f_2^2} - \frac{1}{f_1^2} \right) = \Delta t_1 \frac{f_1^2 - f_2^2}{f_2^2}, \quad (4)$$

$$\Delta t_1 = \frac{f_2^2}{f_1^2 - f_2^2} \delta(\Delta t), \quad (5)$$

$$\Delta t_2 = \frac{f_1^2}{f_1^2 - f_2^2} \delta(\Delta t). \quad (6)$$

The dual frequency measurements are influenced by all other errors on the measurement path. If these errors do not cancel out each other in the dual frequency difference (e.g. multipath errors on the two frequencies can be different), these errors are multiplied with the frequency ratio  $f_i^2/(f_1^2 - f_2^2)$  with  $i=1,2$ . Therefore, the two measurement frequencies should not be too

close to each other. For instance, for dual frequency corrections on GPS  $L_1=1.575$ GHz with help of the second frequency  $L_2=1.227$  GHz the ratio is 1.54. The accuracy of the dual frequency correction is also limited by the receiver noise and is in the decimeter level.

Single frequency users require a correction model which predicts the ionosphere error without measurement data. The most common model is the Klobuchar model [6], [7]. Its accuracy is only about 50%. Therefore, the ionosphere error is the dominant contribution in the error budget for single frequency GNSS users. This was one reason for the introduction of the wide area augmentation systems like the American Wide Area Augmentation System (WAAS) and the European Global Navigation Overlay System (EGNOS). These systems derive the ionosphere error from dual frequency measurements in a regional ground station network and transmit differential corrections and integrity data in a grid via geostationary satellites.

### B. Troposphere error

In the navigation community the delay in the neutral atmosphere is usually just called troposphere delay, although strictly speaking the troposphere is just the lower part of the neutral atmosphere, which extends to about 8-18 km height depending on latitude [8].

Introducing the refractivity  $N = 10^6 (n-1)$ , where  $n$  is the refractive index, the excess path (or delay in m) can be written as:

$$\Delta L = 10^{-6} \int_{S_{tropo}} N(s) ds, \quad (10)$$

The refractive index of the neutral atmosphere is [9]:

$$N = 77.6 \frac{P_d}{T} + 64.8 \frac{P_w}{T} + 3.776 \cdot 10^5 \frac{P_w}{T^2} = N_d + N_w, \quad (11)$$

where  $P_d$  is the partial pressure of dry air in hPa,  $P_w$  is the partial pressure of water vapor in hPa and  $T$  is the temperature in K.  $N$  can be separated in a dry part  $N_d$  depending on  $P_d$  and  $T$ , and in a wet part depending on  $P_w$  and  $T$ .  $N$ , and consequently the tropospheric delay, do not depend on frequency for frequencies below 30 GHz, i.e. in contrast to the ionosphere error the troposphere error cannot be corrected by dual frequency measurements within the allocated navigation frequency bands.

Common correction models do not apply (10) directly, but calculate the tropospheric delay from measured or predicted values of the refractive index at ground. For instance, the well-known Hopfield model [10] computes the dry and wet components of the zenith delay  $L^Z$  from the surface values of the dry and wet refractivity components  $N_{ds}$  and  $N_{ws}$  and two different scale heights  $H_d$  and  $H_w$  and then maps both components to the slant path delay by multiplication with two mapping functions  $m_d(E)$  and  $m_w(E)$ , where  $E$  is the elevation angle of the path to the satellite:

TABLE II  
IONOSPHERE EXCESS PATH

Frequency	TEC= $10^{16}$ el/m <sup>2</sup>	TEC= $10^{18}$ el/m <sup>2</sup>
1176 MHz	0.29 m	29 m
1207 MHz	0.28 m	28 m
1278 MHz	0.25 m	25 m
1575 MHz	0.16 m	16 m
2483 MHz	0.065 m	6.5 m
5000 MHz	0.016m	1.6m

$$\Delta L^Z = \Delta L_d^Z + \Delta L_w^Z = \frac{10^{-6}}{5} (N_{ds} H_d + N_{ws} H_w), \quad (12)$$

$$\Delta L(E) = \Delta L_d^Z \cdot m_d(E) + \Delta L_w^Z \cdot m_w(E). \quad (13)$$

The wet scale height is set to a constant value around 13000 m and the dry scale height is computed from the temperature in K at ground:

$$h_d = 148.98(T - 4.11). \quad (14)$$

Most other models work in a similar manner. A special class of models, the so-called blind models, does not require estimated or measured meteorological input data and computes the surface refractivity and the corresponding zenith delay depending on user location and day of the year by regression formulas derived from global statistics of surface refractivity of pressure, water vapor and temperature.

Typical values of the total zenith tropospheric delay (ZTD) for a ground-based user at heights near mean sea level are about 2.3 - 2.5 m. Although the wet delay contributes normally only with 5% - 15% to the total delay, the high temporal and spatial variability of the water vapor in the troposphere makes the wet delay to the most crucial component if accuracies in the decimeter or centimeter range are required.

The accuracy of different correction models [10]-[20] was investigated in [21]. In the global mean the 1-sigma residual zenith error, i.e. the residual error in zenith direction which is not exceeded for 68% of time, is about 3.5-4 cm, but there are locations where it exceeds 5 cm. The residual zenith error may appear to be not significant, but it is multiplied with the mapping function for other elevation angles. Also the mapping functions itself can introduce an additional error [22]. Fig. 3 provides the RMS-error of the different models including mapping function versus elevation angle. With exception of one model, the different mapping functions show more or less the same performance for elevation angles above 10° and the resulting error can be kept below 30-40 cm. However, for lower elevation angles, there are significant differences.

TABLE III  
ATTENUATION BY WALLS [24], [25]

Type of building	Attenuation
Dwelling houses:	5 - 15 dB
Historical buildings:	25 - 35 dB
Office buildings:	30 dB
Underground garages:	> 30 dB

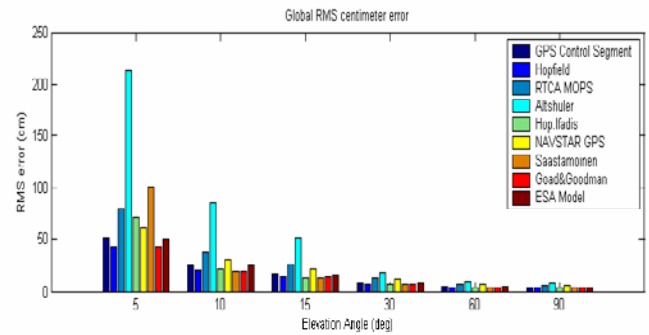


Fig. 3. RMS error vs. elevation angle for different correction models, average of 11 globally distributed stations and 10 years of radiosonde data [21].

### C. Shadowing and Attenuation

Signal attenuations due to atmospheric gases, cloud and rain are negligible in L-Band. However navigation signals can easily be attenuated by vegetation and walls or completely be shadowed by buildings and other obstacles. The specific attenuation for woodland at 1.6 GHz (ca. GPS L1) is about 0.3 dB/m [23]. Some values for attenuation by walls are given in Table III. Attenuation by walls is a particular problem for indoor navigation. However, methods have been developed to enhance the sensitivity of receivers by advanced signal processing. Indoor navigation can also be assisted by other means, e.g. by sending of a priori information via mobile communication links to the navigation receivers or by aiding with other sensors.

### D. Multipath

Signals which are reflected by the ground, buildings or other obstacles and superpose with the direct signal at the user antenna disturb the correlation function and reduce the ranging accuracy. The error depends on the amplitude, phase and the delay of the echo relative to the line-of-sight signal.

Fig. 4 shows the error envelopes for a BPSK and a binary offset carrier signal (BOC, see paragraph V), when one multipath signal with half amplitude of the line-of-sight signal is superposed with the line-of-sight signal. The envelopes represent the maximum error which occurs when the multipath signal is in phase or in opposite phase (180°) with the line of sight signal. For all other phases the error lies between the envelopes. The figure illustrates also, that BOC signals are more robust against multipath propagation than BPSK signals.

In real environments normally several multipath signals are present simultaneously. Fig. 5 shows a simulation of the development of multipath signals for a car that drives through a synthetic urban environment. The y-axis shows the position of the car in the main street and the x-axis the excess delay of the echoes relative to the line-of-sight signal. The echoes are presented by blue symbols. The red marks highlight echoes with long (1), very short (2) and short (3) lifetime [27]. It can be seen that some echoes exist relatively long, whereas others have only a short or very short lifetime.

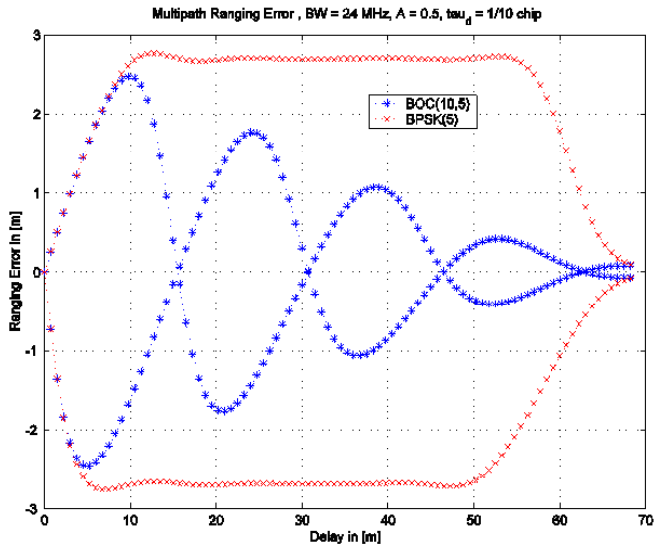


Fig. 4. Multipath error envelope: The picture shows the envelope of the resulting ranging error derived from receiver simulations for one multipath signal with half amplitude of the line-of-sight signal vs. the delay of the echo. The receiver bandwidth is 24 MHz and the correlator spacing is 0.1 code chip. Red: BPSK signal with 5MHz chip rate, blue: BOC-signal with  $5 \cdot 1.023$  MHz chip rate and  $10 \cdot 1.023$  MHz subcarrier modulation [26].

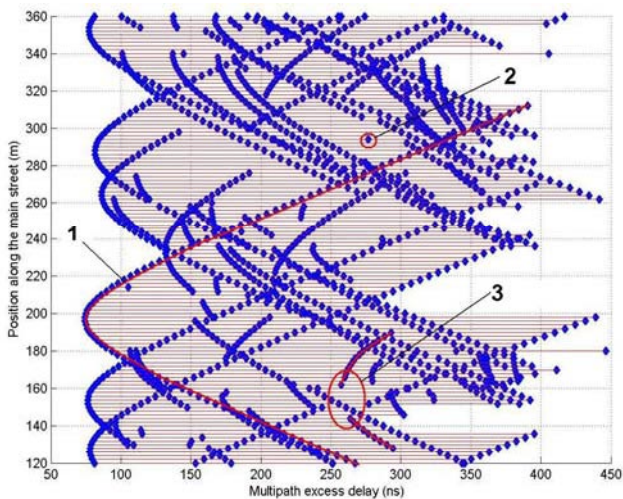


Fig. 5. Simulated multipath echoes for a car driving through an urban environment [27].

#### IV. GNSS OVERVIEW

##### A. GPS and GLONASS

GPS was the first operational satellite navigation system. Its history goes back to 1973. Today 31 satellites in Medium Earth Orbits (MEO) are operational. Table IV shows the key events of the GPS history and Table V presents the main constellation parameters. For comparison, Table V includes also the constellation parameters of the Russian GLONASS system, which was the second available GNSS, and of the future European Galileo system. GLONASS and Galileo use also MEO constellations.

The Ground control system of GPS consists of the GPS Master Control Station (MCS) in Colorado Springs and six Monitor Stations (MS) in Colorado Springs, Hawaii, Ascension Island, Diego Garcia, Kwajalein, and Cape Canaveral. The last four MS include also a dedicated Ground Antenna (GA) for uplink. The GLONASS ground control system consists of a MCS in Moscow and 4 MS/GA distributed over the territory of the former Soviet Union.

Table VI presents the main signal parameters of GPS and GLONASS which are available on all satellites. Both GPS and GLONASS transmit signals on 2 frequencies. The civilian GPS signal (C/A-Code) is on the carrier frequency L1 and has a chip rate of 1.023 Mcps. A chip is a symbol of the PRN (pseudo random noise) sequences used as unique spreading codes for each satellite. The length of 1 C/A code chip is about 1  $\mu$ s, which corresponds to a chip width or code wavelength of 300 m. The military GPS signal (P-Code) is transmitted on carrier frequencies L1 and L2 and has a 10 times higher chip rate of 10.23 Mcps. Correspondingly the P-code chip width is 30 m. The GPS C/A code (coarse acquisition code) repeats every 1ms, where the P-code

TABLE IV  
HISTORY OF GPS

1973	Decision to build a new satellite navigation system based on previous systems Transit (1960), Timation (1967), Project 621 B (1972) of the US Air Force and US Navy
1974-1979	System tests
1978-1985	Launch of 11 Block I GPS satellites
1989	Launch of first Block II satellite
1993	Announcement of Initial Operational Capability (IOC), final authorization for world wide civilian use free of charge
1994	Last Block II satellite completes constellation (24 satellites)
17.7.1995	Announcement of Full Operational Capability (FOC)
1.5.2000	Final deactivation of selective availability (SA) improves accuracy for civilian users from 50-100m to 5-20m.
20.3.2004	Launch of 50 <sup>th</sup> GPS satellite
25.9.2005	Launch of first IIR(M) satellite with military M-code and new second civil signal L2C
24.3.2009	Launch of IIR(M)-20 satellite with a third civil signal L5 (still not operational)

TABLE V  
GNSS CONSTELLATION PARAMETERS

Parameter	GPS	GLONASS	Galileo
Nominal no. of satellites	21+3	21+3	27+3
Active satellites	31	19	2 (GIOVE)
Orbital planes	6	3	3
Orbital height	20 183 km	19 133 km	23 222 km
Revolution period	11h 57'	11h 16'	14h 4'
Repetition of ground track	1 day	8days	10 days
Inclination	55°	64,9°	56°
Satellite per orbital plane	4, unevenly distributed	8	10

TABLE VI  
GPS AND GLONASS SIGNAL PARAMETERS

Parameter	GPS	GLONASS
Access scheme	CDMA	FDMA
Carrier frequency L1	1574.42 MHz	1602+k·0.5625 MHz
Carrier frequency L2	1227.6 MHz	1246+k·0.4375 MHz
Navigation data rate	50 bps	50 bps
Navigation frame	12.5 min	2.5 min
Chip rate C/A-Code	1.023 Mcps	0.511 Mcps
Chip rate P-Code	10.23 Mcps	5.11 Mcps
Pulse form	NRZ	RZ
Modulation	BPSK	BPSK

(precision code) has a duration of 1 week. Since 1994 the P-codes are encrypted and referred to as Y-code.

### B. Galileo

The plans for Galileo go back to 1999, when the ideas for a European GNSS were harmonized. The Galileo Program was agreed upon officially between EU and ESA in 2003. In 2005 and 2006 first concession agreements were made. A further important decision was made in 2007, when the EU agreed to take the complete funding for the implementation of system. The technical development started with the Galileo System Test Bed GSTB V1 in 2003, where new concepts were tested with GPS signals. At 28<sup>th</sup> December 2005 the GSTB V2 started with the launch of the first experimental Galileo satellite GIOVE A. The second experimental Galileo Satellite GIOVE B was launched at 28<sup>th</sup> April 2008. Both satellites are still operational [28].

In 2010 the In-orbit Validation (IOV) phase will start with the launch of two Galileo satellites end of 2010 and two further satellites in early 2011. These four satellites will be already part of the real Galileo constellation which will finally consist of a MEO constellation with 30 satellites and should be completed up to 2015. In early 2014 first services (OS, PRS and SAR) will be offered with a reduced constellation of 16 or 18 satellites. The main constellation parameters are shown in Table V. The Galileo ground control system will consist of two master control centers in Oberpfaffenhofen

(Germany) and Fucino (Italy), 30-40 worldwide distributed sensor stations, 9 uplink stations in C-band and 5 TT&C stations in S-band [29], [28].

Galileo will offer an Open Service (OS) which will be free of charge for all users, a Safety-of-Life service (SoL) which includes integrity, a Commercial Service (CS) and a Public Regulated Service (PRS). The different services are mapped on 10 different signal components which are transmitted in 3 frequency bands: E1, E5, E6. [28]. (The band E1 is often separated in E1-L1-E2 in frequency allocation tables, compare Fig. 8). The signal parameters and service mapping are presented Table VII. The signal details will be discussed in chapter V. Galileo will also offer a Search and Rescue Service (SAR), which is not further discussed here, on a further frequency.

### C. COMPASS, IRNSS and QZSS

COMPASS is the Chinese Global Navigation Satellite System. It will consist of 35 satellites in medium Earth (MEO), geostationary (GEO) and geosynchronous (GSO) orbits [34]. So far only L-band signals are allocated, which partly overlap with Galileo E1, E2, E5b and E6 bands, but a further signal in S-band could be possible. Three satellites have already been launched.

The Indian Regional Navigation Satellite System IRNSS will consist of a seven satellites constellation and a support ground segment. Three of the satellites in the constellation will be in geostationary orbit (GEO) and the remaining four in geosynchronous inclined orbit. The navigation signals will be transmitted in the L5 band and in S-band between 2.483.5-2.5 GHz. IRNSS shall provide an absolute position accuracy of 10 - 20 meters throughout India and within a region extending approximately 2,000 km around it. The entire constellation is announced for 2012 [32], [33].

QZSS will be a regional navigation satellite system over Japan for augmentation of GPS. It will consist of three satellites in periodic highly elliptical orbit (HEO) and will be compatible with GPS. The first satellite shall be launched in

TABLE VII  
GALILEO SIGNAL PARAMETERS AND SERVICE MAPPING

Channel	Signal Modulation	Carrier-freq. [MHz]	Chipping Rate (Mcps)	Service	Code Length [ms]	Primary Code	Secondary Code	Nav data rate [sps]	Integrity	
						Length [chips]	Length [chips]			
1	E5a,I	BPSK(10)	1176.45	10.23	OS	20	10230	20	50	
2	E5a,Q	BPSK(10)	1176.45	10.23		100	10230	100	pilot	
3	E5b,I	BPSK(10)	1207.14	10.23	OS, CS, SoL	4	10230	4	250	yes
4	E5b,Q	BPSK(10)	1207.14	10.23		100	10230	100	pilot	
5	E6,A	BOC <sub>c</sub> (10,5)	1278.75	5.115	PRS	n/a	n/a	n/a	n/a	yes
6	E6,B	BPSK(5)	1278.75	5.115	CS	1	5115	no	1000	
7	E6,C	BPSK(5)	1278.75	5.115		100	5115	100	pilot	
8	E1A	BOC <sub>c</sub> (15,2.5)	1575.42	2.5575	PRS	n/a	n/a	n/a	n/a	yes
9	E1B	CBOC(6,1,1/11)	1575.42	1.023	OS, CS, SoL	4	4092	no	250	yes
10	E1C	CBOC(6,1,1/11)	1575.42	1.023		100	4092	25	pilot	

summer 2010. The full constellation shall be in place 2013.

## V. GALILEO SIGNALS AND BENEFITS FOR PROPAGATION

Table VII presents the signal parameters of the different Galileo signals. A detailed description of the signals and their performance can be found in [31]. Some new features are evident for the Galileo signals in comparison with the current GPS and GLONASS signals:

- Galileo offers all services including the Open Service (OS) on two or three carrier frequencies. This will enable the users to do reduce the ionospheric error to the decimeter level compared to a residual error of some meters in case of single frequency measurements. Some receivers in particular cheap mass market receivers may still use just the L1/E1 band of the OS. For these users Galileo offers also a correction model called NeQuick, which has a comparable performance as the GPS Klobuchar model. Triple frequency measurements are of particular interest for the ambiguity resolution in the case of carrier phase measurements. Carrier phase measurements are much more precise than code measurements, if the ambiguity (i.e. the integer number of wavelengths on the path) can be solved.

- Higher signal bandwidths with higher chip rates will provide higher ranging accuracy. For instance, the chip rate is 10 times higher for the OS in E5a and E5b than for the GPS L1 C/A Code. Since the thermal noise error of the DLL in meters is proportional to the chip width, it is reduced by a factor of 10 for equal loop parameters. In the same way also the multipath error is reduced, if the line of sight signal is still visible and tracked. Moreover, delays longer than 1 chip are canceled out by the correlation process. However, this means also that in case of sudden shadowing or attenuation of the LOS the receiver loses more often tracking, because the DLL has less multipath signals within the width of its correlation function on which it could keep on tracking. It depends on the application whether this is an advantage or disadvantage, because in the case that the loop keeps tracking only on a multipath without LOS the signal availability is higher, but the range and position estimation have a relative large error.

- Longer codes, combination of primary and secondary codes, and new code families provide better cross correlation isolation between the codes of different satellites. This leads in particular to an improvement with respect to acquisition and false acquisition performance in indoor and urban canyon environments where the received signals can have very different received signal powers.

- Pilot channels without data bit transitions enable long coherent integration times. In contrast, for the data channels the coherent integration time is limited by the length of one data symbol. With long coherent integration times, weak signals e.g. in indoor environments can still be acquired. Long integration times reduce also the thermal noise error for code and carrier tracking and thus provide higher accuracy in case low  $C/N_0$ . Pilot channels without data bits also improve the phase tracking threshold of the PLL by about 6 dB.

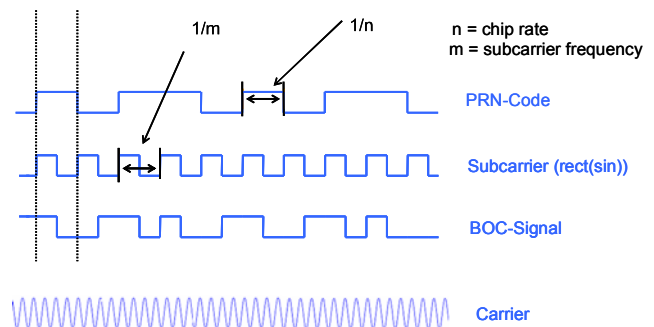


Fig. 6. Binary Offset Carrier (BOC) modulation

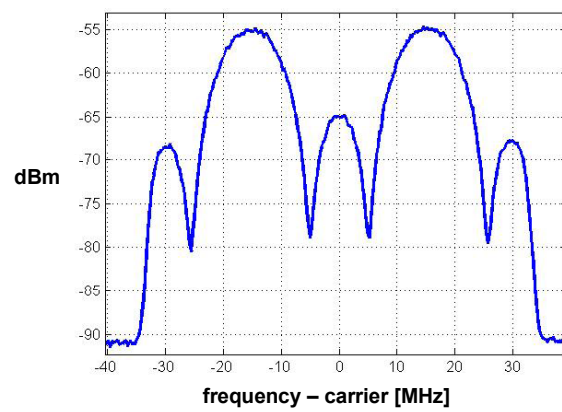


Fig. 7. Bandpass filtered spectrum of Galileo E5 AltBOC (15,10) signal normalized to center frequency

- Some Galileo signals apply Binary Offset Carrier (BOC) modulation, where an additional binary subcarrier is modulated on the signals, see Fig. 6. The sub carrier modulation produces two main lobes in the signal frequency spectrum where the signal energy is concentrated and thus moves the main signal energy away from the center of the spectrum, see Fig. 7. The position of the two main lobes relative to the center depends on the subcarrier frequency. By this way different signals and services in overlapping frequency bands can be spectrally separated so that intra- and intersystem interference is minimized. BOC signals have also a better multipath performance, because their multipath error envelopes have several zeros and the maxima decrease with increasing delay of the multipath, compare Fig. 4. Finally, also the thermal noise error of the DLL is reduced compared to the tracking of a BPSK signal with same loop parameters.

## VI. MULTI CONSTELLATION MULTI FREQUENCY GNSS

Some of the new Galileo signal features will be also available in the modernized GPS and other future GNSS. For instance the new civil signals of GPS L2C and L5 will also have higher longer codes with 10230 chips. L5, which overlaps with Galileo E5a, will have a 20 MHz bandwidth

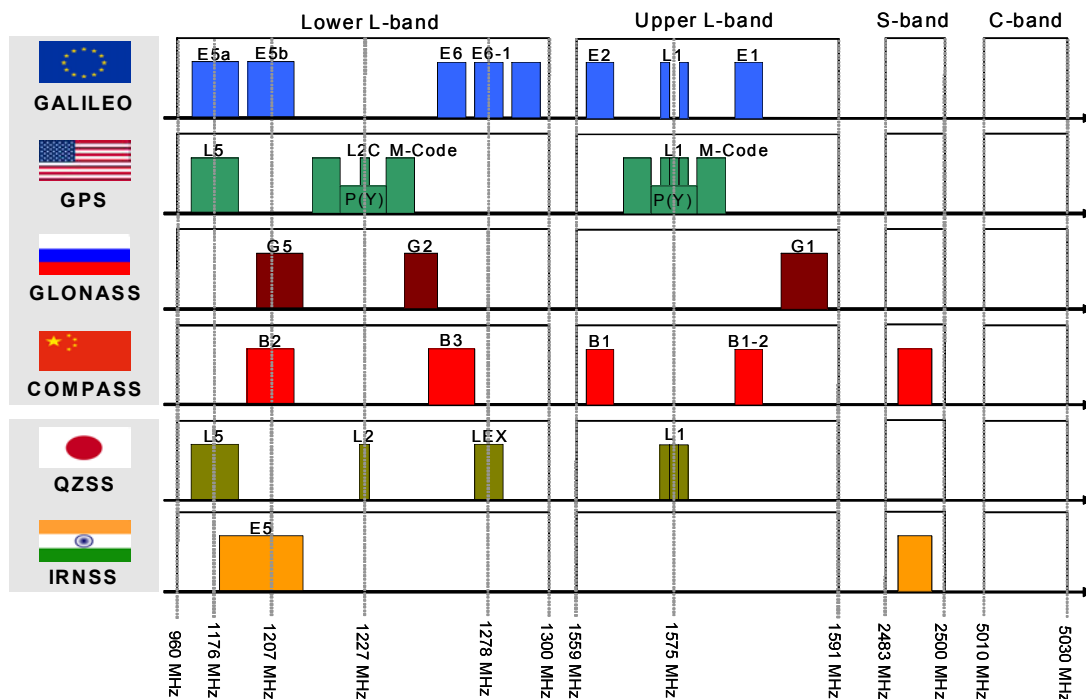


Fig. 8. Frequency allocation for current and future satellite navigation systems

with a chip rate of 10.23 Mcps. L2C will also provide an additional very long code on a data free signal similar to a pilot signal [35]. L2C is already transmitted by 7 GPS satellites and the new civil L5 signal is transmitted by one satellite which, however, is not set healthy yet. The new GPS L1C signal will also apply BOC-modulation. The first satellite with L1C shall be launched in 2016 [36], [37].

A further advantage of the availability of Galileo and other future GNSS together with modernized GPS and GLONASS in the timeframe of 2015-2020 is the higher number of satellites in view. If the signals of the different systems are combined, this leads to a much higher signal and position availability in urban canyons and other environments with shadowing by buildings or other obstacles. From a receiver point of view the signal combination is easiest, when the signals of the different systems share the same frequency bands, e.g. the GPS and Galileo open service signals in the L1/E1 and the L5/E5a bands.

## VII. CONCLUSION

New signals available with Galileo, modernized GPS and other future GNSS will enable a better reduction of propagation impacts on the satellite navigation ranging and positioning performance. In particular, dual or triple frequency open services will nearly eliminate the ionosphere error, which currently is one of the main error sources, also for the civil user. Signals with higher bandwidths, higher chip rates, and new modulation schemes will reduce the receiver noise and multipath errors and thus enhance the ranging and positioning accuracy. Longer and new codes, combination of

primary and secondary codes and the transmission of pilot signals will provide higher cross correlation isolation and allow longer coherent integration times and thus increase sensitivity, acquisition performance and tracking availability for weak signals in harsh environments like indoor.

Last but not least the combination of signals from different GNSS will increase significantly the service and position availability in difficult reception environment like urban canyons, where signals can only be received from a limited number of directions due to shadowing of signals coming from other directions.

## ACKNOWLEDGMENT

I thank my colleagues Holmer Denks and Felix Antreich, both from DLR Institute of Communications, for providing some graphics for this paper.

## REFERENCES

- [1] B.W. Parkinson, "GPS Error Analysis," in *Global Positioning System, Theory and Applications*, Volume I, B.W. Parkinson B.W. and J. J. Spilker Jr., Ed. American Institute of Astronautics and Aeronautics, Washington DC, 1996.
- [2] A. Hornbostel: "Propagation Problems in Satellite Navigation", *Radio Science Bulletin*, No.329, June 2009.
- [3] B. Hoffman-Wellenof, H. Lichtenberger, and J. Collins., *Global Positioning System, Theory and Praxis*, Springer, Wien, New York; 4<sup>th</sup> edition, 1997.
- [4] A. Leick, *GPS Satellite Surveying*, John Wiley and Sons, New York, 1989.
- [5] J. A. Klobuchar, "Ionospheric Effects on GPS," in *Global Positioning System, Theory and Application*, Volume I, B. W. Parkinson and J. J. Spilker Jr., Ed., American Institute of Astronautics and Aeronautics, Washington DC, 1996.

- [6] J. A. Klobuchar, "Ionospheric Time-Delay Algorithm for Single-Frequency GPS Users," *IEEE Transactions on Aerospace and Electronic Systems*, Vol. AES-23, No.3, May 1987, pp. 325-331.
- [7] ICD-GPS 200c, NAVSTAR GPS Space Segment/ Navigation User Interfaces, ARINC Research Corporation.
- [8] J. J. Spilker Jr., "Tropospheric Effects on GPS," in *Global Positioning System, Theory and Application*, Volume I, B. W. Parkinson and J. J. Spilker Jr., Ed., American Institute of Astronautics and Aeronautics, Washington DC, 1996. pp. 517-546.
- [9] G. D. Thayer, "An Improved Equation of Refractive Index of Air," *Radio Science*, Vol. 9, 1994, pp. 803-807.
- [10] H. S. Hopfield, "Two Quadratic Tropospheric Refractivity Profile for Correcting Satellite Data," *Journal of Geophysical Research*, Vol. 74, No.18, August 20, 1969, pp. 4487-4499.
- [11] J. Saastamoinen, "Contributions to the Theory of Atmospheric refraction," *Bulletin Geodesique*, 1973, Vol.105, pp. 279-298, Vol.106, pp. 383-397, Vol.107, pp. 13-14.
- [12] H. D. Black, "An Easily Implemented Algorithm for the Tropospheric Range Correction," *Journal of Geophysical Research*, Vol. 83, No. B4, April 10, 1978, pp. 1825-1828.
- [13] I. Ifadis, "The Atmospheric Delay of Radio Waves, Modeling the Elevation Dependence on a Global Scale," Technical Report no. 38L, School of Electrical and Computer Engineering, Chalmers University of Technology, Göteborg, Sweden 1986.
- [14] C. C. Goad and L. Goodman, "A Modified Hopfield Tropospheric Refraction Correction Model," Presented Paper, *AGU Annual Fall Meeting*, San Francisco, 1974
- [15] *Technical Characteristics of the NAVSTAR GPS*, NATO + NAVSTAR Technical Support Group, 1991.
- [16] E.E Altshuler and P.M. Kalaghan, "Tropospheric range error corrections for the NAVSTAR system," AFCRL-TR-74-0198, April 1974.
- [17] E.E. Altshuler, "Tropospheric Range-Error Correction for the Global Positioning System," *IEEE Trans. on Antennas and Propagation*, Vol. 46, No. 5, May 1998, pp. 643-649.
- [18] *Minimum Operational Standard for global positioning/wide area augmentation system airborne equipment*, RTCA/DO-229A, June 8, 1998.
- [19] *GALILEO Reference Troposphere Model for the User Receiver*, Issue 2, ESA, 10th July 2003.
- [20] ESA Blind Model 2.3 issued on 28/01/2004 (MATLAB Code).
- [21] A. Hornbostel and M.M. Hoque, "Analysis of Tropospheric Correction Models for Local Events within the GSTB Test Case APAF," in *Proc. of ION-GNSS 2004*, Institute of Navigation, Sept. 2004.
- [22] A. Hornbostel, "Simulation of Tropospheric Effects for Satellite Navigation", in *Proc. European Telemetry Conference*, Garmisch, May 2000.
- [23] *Attenuation in Vegetation*, ITU-R Rec. 833-2.
- [24] W.C. Stone, *Electromagnetic Signal Attenuation in Construction Materials*, NIST Report 605, National Institute of Standards, Gaithersburg, Maryland, 1997.
- [25] B. Eissfeller, A. Teuber, and P. Zucker, "Untersuchungen zum Satellitenempfang in Gebäuden," in *Allgemeine Vermessungsnachrichten* 4/2005, pp. 137-145. Herbert Wichmann Verlag, Heidelberg, 2005.
- [26] H. Denks, "Übersicht über die geplanten Signale bei Galileo mit Schwerpunkt BOC-Signale," Technical Note, GalileoNAV-3100-1, Revision 1.2, DLR Institute of Communications and Navigation, 2003.
- [27] O. Esbri-Rodriguez, A. Konovaltsev, and A. Hornbostel: "Modeling of the GNSS Directional Radio Channel in Urban Areas Based on Synthetic Environments," in *Proc. ION National Technical Meeting*, San Diego (USA), 26-28 January 2004.
- [28] <http://www.esa.int/esaNA/galileo.html>
- [29] [http://ec.europa.eu/transport/galileo/index\\_en.htm](http://ec.europa.eu/transport/galileo/index_en.htm)
- [30] Galileo OS ICD, Draft1, February 2008, ESA/GSA 2008
- [31] O. Julien, C. Macabiau, and J.-L. Issler: "Structure and Performance of the Future Galileo Civil Signals," *Radio Science Bulletin*, No. 330, September 2009.
- [32] [http://en.wikipedia.org/wiki/Indian\\_Regional\\_Navigational\\_Satellite\\_System](http://en.wikipedia.org/wiki/Indian_Regional_Navigational_Satellite_System).
- [33] <http://www.oosa.unvienna.org/pdf/icg/2008/expert/2-3.pdf>
- [34] C. Cao, G- Jing, and M. Luo: "COMPASS Navigation Satellite System Development", PNT Challenges and Opportunities' Symposium, Nov. 5th-6th, 2008 Stanford University [http://scpnt.stanford.edu/pnt/PNT08/Presentations/8\\_Cao-Jing-Luo\\_PNT\\_2008.pdf](http://scpnt.stanford.edu/pnt/PNT08/Presentations/8_Cao-Jing-Luo_PNT_2008.pdf)
- [35] R. W. Fontana, W. Cheung, T. Stansell: "The modernized GPS L2C Signal", *GPS World* September 2001
- [36] <http://www.space.commerce.gov/gps/modernization.shtml#signals>
- [37] <http://www.navcen.uscg.gov/GPS/modernization/default.htm>

**On Channel Models for Satellite Navigation** (Review lecture)

A. Steingaß

Institut für Kommunikation und Navigation, DLR, Wessling

## **Polarimetric Weather Radar Remote Sensing (Review Lecture)**

M. Hagen

Institut für Physik der Atmosphäre, DLR Oberpfaffenhofen, 82234 Weßling, Germany

Advanced polarimetric Doppler weather radar systems offer a wide range of applications compared to conventional Doppler weather radars. Polarimetric weather radars have been implemented for research some 20 years ago, meanwhile most weather services in Europe are upgrading their radar networks and in the course of the next decade most of the about 170 European weather radar systems will be advanced polarimetric Doppler radar systems.

Polarimetric weather radar has the potential to improve rain rate estimation considerable by using additional information on the shape of the raindrop size distribution. In addition, the correction of attenuation by rain is possible to a certain degree. Other valuable radar products are the hydrometeor classification, which allows to distinguish between the different kinds of hydrometeors (rain, snow, hail, graupel, ...) but also to identify non-meteorological targets like aircraft, ground clutter, birds, or chaff. This gives valuable information for nowcasting of severe weather events. However, it has been observed that it is necessary to implement sophisticated data quality algorithm, otherwise the advantages of polarimetry can not be fully exploited. The presentation will not only present current techniques and show examples of advanced polarimetric and Doppler weather radar observations, but will also identify their limitations.

# Using Polarimetric Quantities for Improved Clutter Detection

Jens Reimann

Institute for Atmospheric Physics  
German Aerospace Center  
Muenchner Strasse 20  
82234 Wessling

**Abstract**—Removing spurious echoes from weather radar data is not very desiring but necessary. Many further processing step will depend on it. Now, as more and more weather services introduce polarimetric systems new parameters of the target become available. It will be shown that these new quantities can be used to better distinguish between clutter and precipitation. A new algorithm is proposed using this technique. At the end, a qualitative and quantitative evaluation of the algorithm will also be presented.

## I. INTRODUCTION

Removing spurious echoes was ever since a great challenge when dealing with weather radars. Starting in the past with pure static clutter maps, the development of Doppler radars improved clutter filtering a lot. It takes advantage of the fact that ground clutter does not move. Nowadays, as polarimetric weather radars become widely available, there is a new chance to boost clutter detection again.

### A. The POLDIRAD Radar

POLDIRAD is a full polarimetric C-Band weather radar [1] which is operated by the German Space Agency (DLR) in Oberpfaffenhofen, near Munich in Germany. Most time it runs in the H/V switching mode gathering the full scattering matrix. It transmits alternating horizontal and vertical linear polarized waves and receives the horizontal as well as the vertical polarized echo of each pulse. Using this scheme there is a small time lag between both columns of the scattering matrix. This has to be taken into account when calculation the polarimetric quantities. The big advantage of this switching scheme is the direct measurement of the linear depolarization ratio ( $LDR$ ), which is an important entity for classification algorithm as the one described in [2].

### B. Polarimetric quantities

There are several quantities which are used in the weather radar community to describe polarimetric properties.

The differential reflectivity equals the difference between the logarithmic reflectivity of the horizontal and vertical polarized echo. As rain drops get flattened when falling through the air,  $Z_{DR}$  becomes slightly positive. Because larger drops get more flattened than smaller ones,  $Z_{DR}$  includes information about the drop size.

$$Z_{DR} = 10 \cdot \log \frac{Z_{HH}}{Z_{VV}} \quad (1)$$

The linear depolarization ratio can be calculated for both, horizontal and vertical polarization. It characterize how much of the wave gets depolarized while scattered on slated or irregular shaped particles. Depolarization of the wave can also occur along the path to the scatterers.

$$LDR_H = 10 \cdot \log \frac{Z_{VH}}{Z_{HH}} \quad (2)$$

$LDR$  is not available on many operational weather radars. Substituting  $\rho_{HV}$ , the correlation of horizontal and vertical echo, can be used which has similar properties. In the H/V switching mode, which is used by POLDIRAD, this quantity is not easily derivable, because the co-polarized horizontal and vertical have a time lag of one PRT (pulse repetition time).

$$|\rho_{HV_H}(1)| = \frac{\left| \frac{1}{n} \sum_{i=1}^n \underline{S}_{HH}(i) \cdot \underline{S}_{VV}^*(i) \right|}{\sqrt{\frac{1}{n} \sum_{i=1}^n |\underline{S}_{HH}(i)|^2 \cdot \frac{1}{n} \sum_{i=1}^n |\underline{S}_{VV}(i)|^2}} \quad (3)$$

Assuming a Gaussian spectral  $\rho_{HV}(0)$  can be estimated by using:

$$|\rho_{HV_H}(0)| = \frac{\rho_{HV}(1)}{[\rho_{HV}(2)]^{0.25}} \quad (4)$$

With  $\rho_{HV}(2)$  as the correlation of time lag two. This is similar to a spectral width of the Doppler spectrum.

Even the phase contains polarimetric information. The differential phase shift  $\phi_{DP}$  between horizontal and vertical polarization can indicate anomalous propagation effects and attenuation along the path. When measuring the phase difference it is inevitable to also estimate the back scatter phase. Fortunately, this phase is zero for Rayleigh scattering, which is common for C band radars viewing rain drops.

$$\Phi_{DP} = \Phi_v - \Phi_h = \phi_{DP} + \delta \quad (5)$$

Often it is more convenient to used the range derivative of  $\phi_{DP}$  which is called  $K_{DP}$ , the specific differential phase.

While not directly a polarimetric quantity, the velocity and the spectral width are polarization dependent, but are calculated the usual way [3].

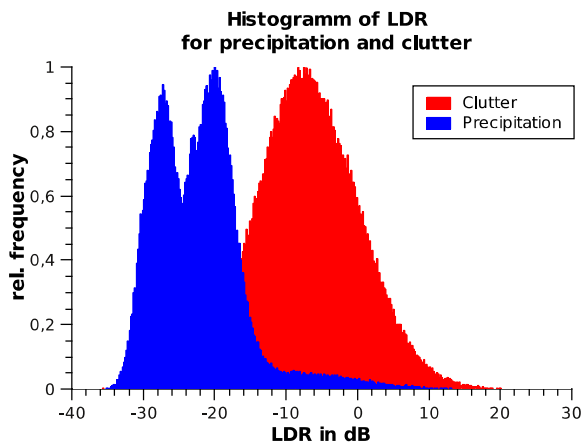
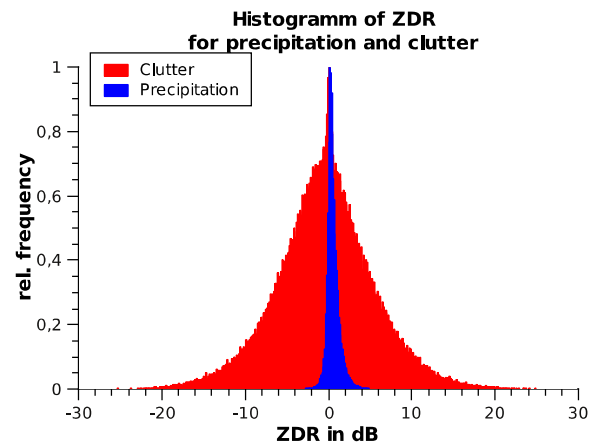


Fig. 1. Histogram of LDR for precipitation and clutter

Fig. 2. Histogram of  $Z_{DR}$  for precipitation and clutter

$$v_{HH} = -\frac{\lambda \cdot 2 \cdot PRF}{4\pi} \arg \left( \frac{1}{n-1} \sum_{i=0}^{n-1} \underline{S}_{HH}(n) \cdot \underline{S}_{HH}^*(n+1) \right) \quad (6)$$

$$\sigma_{HH} = \frac{1}{2} \ln \left( \frac{\frac{1}{n} \sum_{i=1}^n \underline{S}_{HH}(i) \cdot \underline{S}_{HH}^*(i)}{\frac{1}{n-1} \sum_{i=1}^{n-1} \underline{S}_{HH}(i) \cdot \underline{S}_{HH}^*(i+1)}} \right) \quad (7)$$

### C. Typical Properties of Clutter

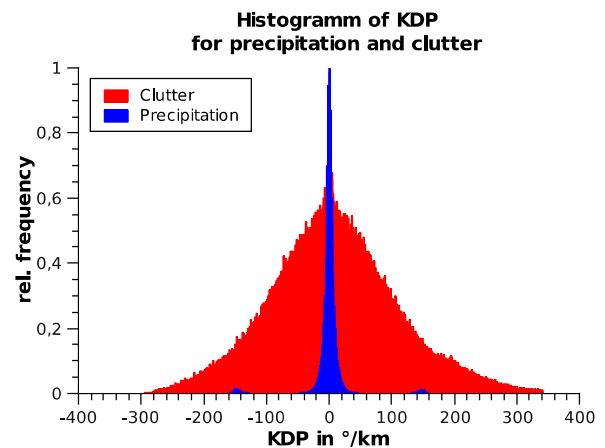
Ground clutter has some typical properties when compared to weather targets. First of all it is a coherent target while weather targets are distributed scatterers. Therefore the spectral width for clutter is assumed to be (nearly) zero, just because the target is invariant in time. Ground targets are mostly non-moving objects which results in no Doppler velocity.

These are characteristics which are used in all modern clutter detection algorithms. But both quantities can be superposed by errors: Spectral width is broadened by antenna rotation speed and Doppler shift may be created through moving parts on the objects (e.g. windmills [4]).

Ground clutter often shows high reflectivity values. It should be emphasized that weather radar systems use the pulse-volume-equation to calculate the reflectivity of the scatterers. Thereby it assumes a homogeneous filled volume. However, this is not true for ground clutter. Reflectivity calculation for ground clutter will be wrong in most weather radar systems.

Polarimetric quantities give additional information about the target to create a better classification. Many ground targets are found to have high  $LDR$  value [5], while most weather targets have a low linear depolarization ratio (Fig. 1).

It is also found that  $Z_{DR}$  and  $\Phi_{DP}$  as well as  $K_{DP}$  is highly variable for ground clutter [6]. This can also be used to distinguish between weather targets and ground clutter (Fig.

Fig. 3. Histogram of  $K_{DP}$  for precipitation and clutter

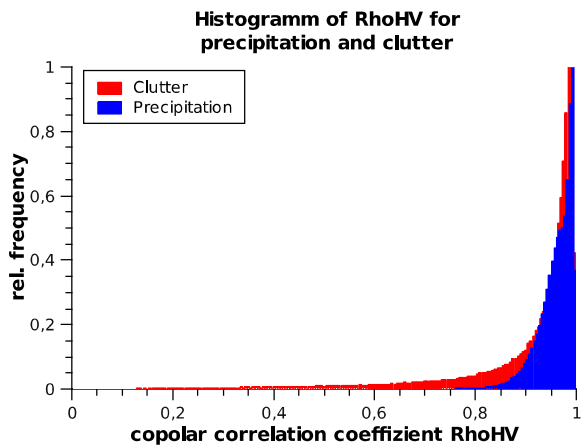
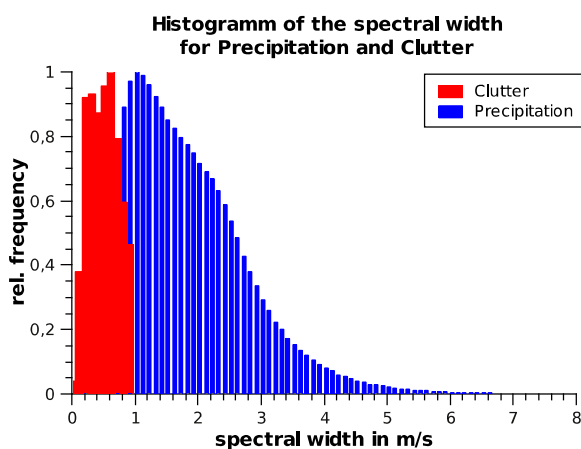
2 and Fig. 3). The reason for this behavior is most certain the highly inhomogeneous structure of the ground clutter combined with small differences in the antenna pattern for the different polarizations (e.g. side lobes). Other effects may be possible too.

The polarimetric quantity  $\rho_{HV}$  may also be used. But it is highly depended on the decorrelation generated by the antenna rotation itself.

### D. Designing an algorithm

As POLDIRAD is a research weather radar, it fortunately saves all scan to an archive. But many of these data are not clutter filtered. One of the constraint in designing this clutter filter was, that it should be applicable to these old data sets. Therefore it can only use the processed data which prevents spectral clutter filtering. This is why, the approach tries to analyze the recorded scan data to find usable features for clutter filtering.

1) *Gathering data:* The first step needed, is selecting scans which can be used for a analysis. As a research radar, many work is done on the radar, which may changes its properties

Fig. 4. Histogram of  $\rho_{HV}$  for precipitation and clutterFig. 5. Histogram of the spectral width  $\sigma$  for precipitation and clutter

from time to time. To ensure a good data quality only the year 2008 was chosen. This concurs with the time when POLDIRAD returned from a field campaign to Oberpfaffenhofen. The radar was completely reassembled, including the dish of the antenna and all cables.

2) *Building statistics:* The challenge in building a good statistic, is to distinguish between clutter and precipitation without using the properties to analyze. Hence the characteristics for clutter where build on clear sky days with just ground echoes, while for precipitation the areas of known clutter were ignored. The first few kilometers where also ignored, because of the saturation engendered by the main bang and near range clutter. The received  $I/Q$  data were correlated and the quantities are calculated as described above.

3) *Algorithm:* Fuzzy logic was not used, because of the huge amount of possible member functions and transitions, which can be used, but may have no physical cause. The attention was laid on the polarimetric data and not to the most sophistic processing. Hence the threshold values for the members where also selected by hand, just to be meaningful

(Table I).

If one of these defined threshold is exceeded, it indicates either clutter or precipitation. The ratio between the both counters is the clutter probability. If none of the thresholds are meet, not classification is done. This can arise e.g if no echo was received within the given range gate. The Doppler velocity is handled separately. For physical reasons high Doppler velocity can not be ground clutter. Hence a high velocity is used to reset the clutter counter and thus prevents a classification as clutter.

Parameter	Threshold	Event
$Z_{HH}, Z_{VV}$	$> 41 \text{ dBZ}$	Clutter
$Z_{HV}, Z_{VH}$	$< 2 \text{ dBZ}$	Precipitation
$Z_{DR}$	$> 4 \text{ dBZ}$ or $< -2 \text{ dBZ}$	Clutter
$W_{HH}, W_{VV}$	$> 1 \text{ m s}^{-1}$	Precipitation
$K_{DP}$	$< -35^\circ \text{ km}^{-1}$ or $> 35^\circ \text{ km}^{-1}$	Clutter
$\rho_{HV}$	$< 0,8$	Clutter
$v_{HH}, v_{VV}$	$< -1 \text{ m s}^{-1}$ or $> 1 \text{ m s}^{-1}$	Precipitation

TABLE I  
THRESHOLD VALUE FOR CLASSIFICATION

### E. Examples

The application of the clutter detection is shown for a data set from 22 August 2008. There was a cold front over France and another appeared in the south east of Germany on this day. The reflectivity,  $Z_{DR}$  and Doppler velocity are shown in Fig. 6 along with the clutter algorithm. Obviously the clutter detection is working well. Even the ground clutter near the radar is treated right although the definition of the algorithm was done with clutter further away.

### F. Comparison to classical Doppler clutter filter

		Doppler filter			$\Sigma$
		Precipitation	Unclassified	Clutter	
new	Precipitation	84,78	0,28	0,1	85,15
	Unclassified	0,17	0,13	0,79	1,1
	Clutter	1,07	1,1	11,59	13,76
$\Sigma$		86,02	1,5	12,48	100

TABLE II  
CONFUSION MATRIX

Classical Doppler clutter filters are widely used. Unfortunately, it can not be directly comparable to the proposed one. While the first uses the spectra to directly remove clutter, the latter one has no spectra available and does only a classification. Nevertheless, it could be done by applying a classification to the Doppler filter. For this comparison all echoes which are at least reduced by  $10 \text{ dB}$  by the Doppler filter are treated as precipitation, while all echoes reduced more than  $20 \text{ dB}$  are treated clutter. The filter coefficients were taken from the "User's Manual" from SIGMET Inc. [3]. This filter has  $40 \text{ dB}$  stop band and 7% Nyquist interval as the band width. The confusion matrix for both routines (Table II) shows that about 96% of all data bins are classified identically by both algorithms. The polarimetric version tends to detect more

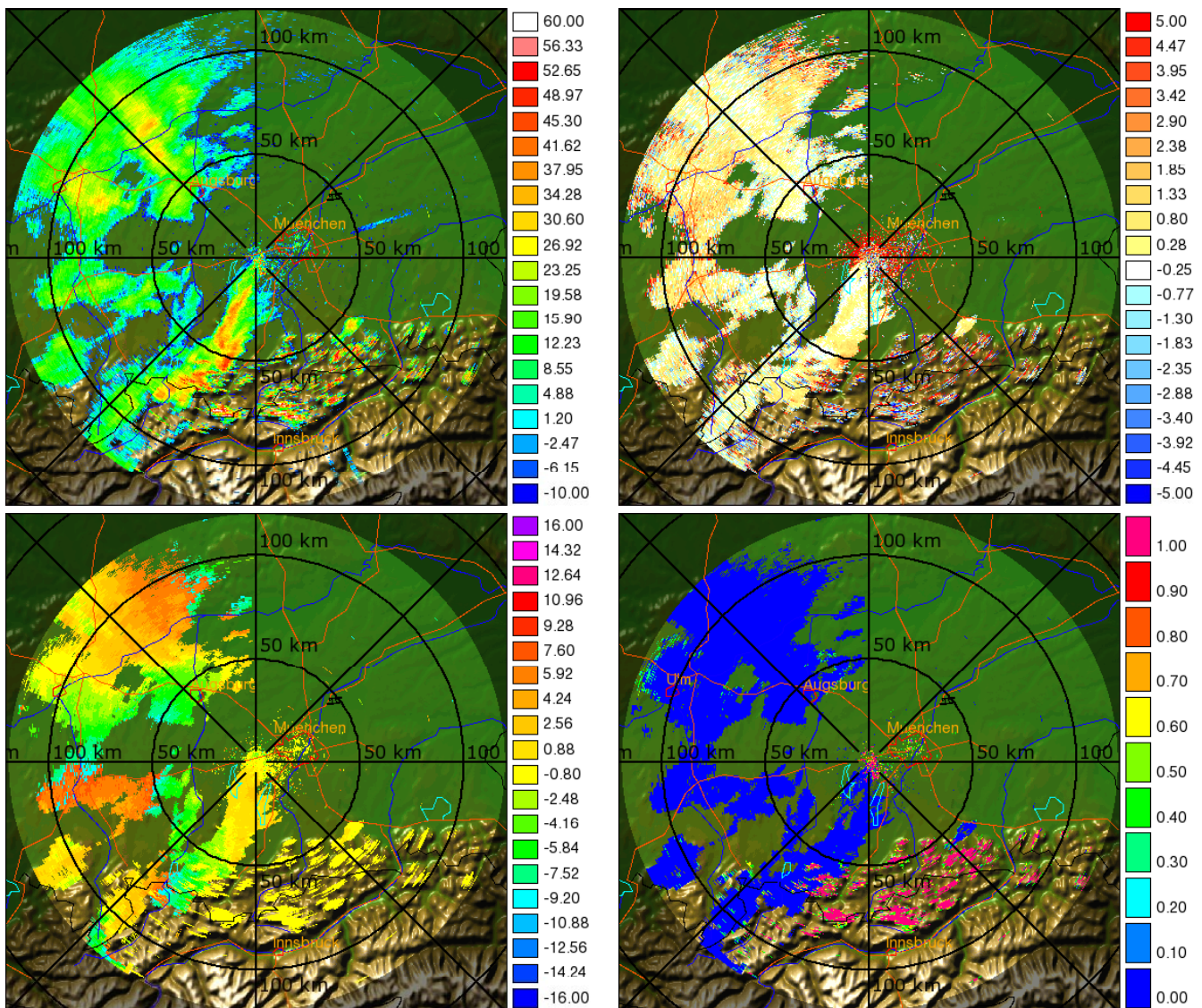


Fig. 6. Example from 08/22/2008 14:05 MET (top left: Reflectivity  $Z_{HH}$ , top right:  $Z_{DR}$ , bottom left: Doppler velocity, bottom right: Clutter probability)

clutter (13.76% compared to 12,48%) and less precipitation (85.15% compared and 86,02%). This may be convenient for further processing as removing parts of precipitation is less harmful to them than treating clutter as a weather target. Most remarkable is that there are only 1.1% unclassified, which is more than 35% less than the non-polarimetric filter.

## II. CONCLUSION

A new algorithm for clutter detection was proposed. It depends mostly on polarimetric quantities, while there is not demand for the whole Doppler spectra of each range gate. Although non of the advanced processing techniques like fuzzy logic or neuronal networks were used, it shows benefits compared to classical Doppler clutter filters. It can be concluded that polarimetric weather radar data can greatly improve clutter detection.

## REFERENCES

- [1] A. C. Schroth, M. Chandra, and P. F. Meischner, "A c-band coherent polarimetric radar for propagation and cloud physics research," *Journal of Atmospheric and Oceanic Technology*, vol. 5, pp. 803–822, Dec. 1988.
- [2] H. Höller, V. N. Bringi, J. Hubbert, M. Hagen, and P. F. Meischner, "Life cycle and precipitation formation in a hybrid-type hailstorm revealed by polarimetric and doppler radar measurements," *Journal of Atmospheric Science*, vol. 51, pp. 2500–2522, 1994.
- [3] *RVP7 Doppler Signal Processor User's Manual*, SIGMET Inc., 2003, <ftp://ftp.sigmet.com/outgoing/manuals/rvp7user/> (21.01.2009).
- [4] B. M. Isom, R. D. Palmer, G. S. Secrest, R. D. Rhoton, D. Saxion, T. L. Allmon, J. Reed, T. Crum, and R. Vogt, "Detailed observations of wind turbine clutter with scanning weather radars," *Journal of Atmospheric and Oceanic Technology*, vol. 26, no. 5, p. 894–910, May 2009.
- [5] M. Hagen, "Identification of ground clutter by polarimetric radar," *28th Conference on Radar Meteorology*, pp. 67–68, 1997.
- [6] J. J. Gourley, P. Tabary, and J. P. du Chatelet, "A fuzzy logic algorithm for the separation of precipitation from nonprecipitating echos using polarimetric radar observations," *Journal of Atmospheric and Oceanic Technology*, vol. 24, pp. 1439–1451, Aug. 2007.

# Hydrometeor classification: A differentiation in solid, melting and liquid particles by weather radar

Jörg Steinert

Professorship of Microwave Engineering and Photonics  
Chemnitz University of Technology  
Chemnitz, Germany  
Email: joerg.steinert@etit.tu-chemnitz.de

Madhu Chandra

Professorship of Microwave Engineering and Photonics  
Chemnitz University of Technology  
Chemnitz, Germany  
Email: madhu.chandra@etit.tu-chemnitz.de

**Abstract**—The humidity in the troposphere is the reason for the development of clouds with different characteristics. The building blocks of clouds are particles made of water in various states (hydrometeors). In the past the research on weather radar data and other measurement devices showed differences in the characteristics of the hydrometeor types. The paper gives a short introduction into the micro-physical behaviour of raindrops, melting particles and ice crystals. Furthermore, the analysis of the particles with polarimetric weather radar and with it the differentiation between several particle types will be presented and demonstrated by examples.

## I. INTRODUCTION

By looking at precipitating weather events and the corresponding clouds, the existence of small particles that creates these formations is reasonable. With the weather radar we are able to analyse the cloud structure. A weather radar transmits pulses of electromagnetic waves (EM waves) resulting in the observation of pulse volumes of several millions of  $\text{m}^3$ . In such a volume we will have different hydrometeor types of particles, obviously. Usually, the overall size of one particle is in the area of few millimetre. The challenge is now to distinguish between the different hydrometeor types by polarimetric weather radar observations. This paper can be seen as the combination of the results from [1], [2] and [3].

In section II the cloud types and the analyzing hardware will be introduced. The explanation of the simulation is presented in section III. Followed in section IV by the different characteristics of liquid, melting and frozen hydrometeors. Section V then gives an impression of the application of the previous received knowledge from the simulation part.

## II. ANALYZING CLOUD STRUCTURE BY WEATHER RADAR

For EM waves the transmission frequency is a key aspect. For sensors operating at the optical frequency range, clouds are non-transparent and cover the area behind. This is related to the short wavelength of visible light between 0.4 and 0.75  $\mu\text{m}$ . Weather radars work usually with a transmission frequency between 3 and 10 GHz. So the wavelength is in the range of cm and therewith larger than the dimension of the cloud particles or hydrometeors. There is a correspondence between the state, the shape and the size of the hydrometeors with the weather radar measurements. So, for instance, raindrops look like oblate spheroids and ice crystals like

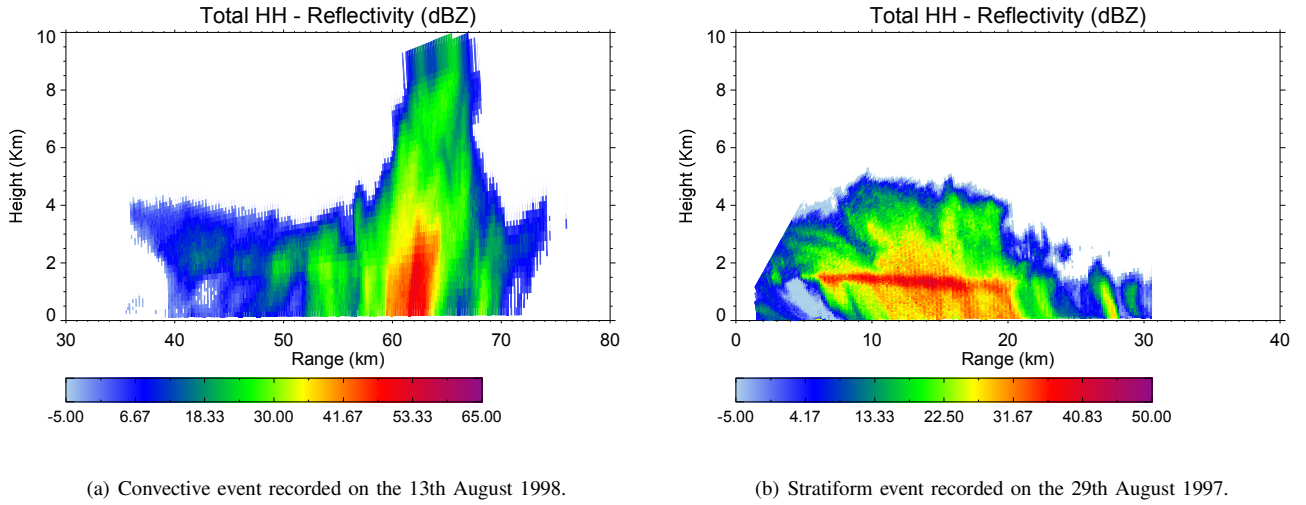
cylinders with a hexagonal ground plane (Fig. 4). These differences have to be known for the simulation of the backscattered signal in the next section.

The weather events can be roughly separated in stratiform and in convective storms. Examples are presented in Fig. 1. The difference is the inner structure and so the arrangement and the appearance of the different hydrometeor types. In convective events (Fig. 1(a)) we have a vertically spreaded convective cell, that is seen by very high reflectivity values corresponding to large raindrops and hail signatures. This cell is surrounded by layers with equal reflectivities due to strong updrafts and downdrafts. In contrast to this, stratiform storms (Fig. 1(b)) have a very straight structure with horizontally spreaded layers. Additionally, a so called melting layer is present that separate the liquid particles below from the frozen particles above. This melting zone is characterized by high reflectivity values due to the melting process.

For this study, the DLR research radar POLDIRAD (radar site Oberpfaffenhofen, Germany) delivered the radar datasets. POLDIRAD is a C-band (5.5 GHz) dual polarimetric weather radar. Important characteristics of the radar are for instance the pulse width of 1  $\mu\text{s}$  and the beamwidth of  $1^\circ$  that specify the size of the pulse volume, [4]. Due to the research aspect of analyzing the structure and the fall behaviour inside the storm the usage of different elevations is recommended. Because of this, range height indicators (RHI) were chosen as observation scheme.

## III. SIMULATION OF HYDROMETEORS

The scattering path of the EM waves is related to the forward scattering and therewith gives an impression about the attenuation in the way of propagation. The backward scattering is deeply connected to the scatterers in the radar pulse volume. As mentioned earlier, the characteristics of the scattering particle are the shape, the size and the dielectric constant, that distinguish the backscattering cross section (BCS)  $\sigma$  in  $\text{mm}^2$ . So with the estimation of  $\sigma$  the backscattering coefficient, namely the reflectivity, can be calculated by

Fig. 1. RHI of  $Z_{hh}$  in dBZ.

$$Z_{xy} = 10 \cdot \lg \left( \frac{\lambda^4}{\pi^5 \cdot |K|^2} \cdot \int_{D_e} \sigma_{xy}(D_e) \cdot N(D_e) dD_e \right) \quad (1)$$

in dBZ with the operating wavelength  $\lambda$  in mm, the dielectric factor  $K = \frac{\epsilon - 1}{\epsilon + 2}$  and the complex permittivity  $\epsilon$ . The subscript x is related to the polarisation on receive and y is for the polarisation on transmit case.  $N(D_e)$  stands for the number of particles for an assigned size  $D_e$  in mm and is also known as the particle or drop size distribution (DSD). The volume of the hydrometeor is thereby equal to that of a sphere with the equivolume diameter  $D_e$ . One widely addressed method for estimation of  $\sigma$  is the Rayleigh-Gans approximation (e.g., [5]) that is just applicable for particles, that have dimensions up to one tenths of the wavelength. So for POLIRADS C-band, particles up to 5 mm in size are well simulated and with it the major part of hydrometeors are covered. Just larger drops or irregular crystals need more accurate methods like T-Matrix method (shown in [6]) or the Fredholm Integral method (FIM) (explained in [7]). The shape and therefore the dimension in different directions is important if the radar operates with EM waves at specific polarisations. In particular, the linear vertical and horizontal polarisations are important because with them the estimation of further useful parameter can be done. Namely the differential reflectivity  $Z_{DR}$  with  $Z_{DR} = Z_{hh} - Z_{vv}$  in dB, a combination of the horizontal transmitted/received signal and vertical transmitted/received signal. Therewith  $Z_{DR}$  gives information about the mean shape of the particles in the pulse volume.

#### IV. HYDROMETEOR TYPES

The separation of hydrometeors can be done with different characteristics like size or aggregate state and in several degrees of depth. For the comparison we will focus the compilation of classes on raindrops, melting particles and

ice crystals as representatives. The specific characteristics are given in the following subsections.

##### A. Raindrops

Modelled typically as rotational spheroids the Rayleigh approximation for the backscattering cross section is well established. For larger drops the axial ratio  $AR$ , the relation between the vertical and the horizontal dimension decreases. That is due to flattened drops resulting from the air resistance. The number of drops over the size ( $N(D_e)$  in eq. 1) can be seen in general as a gamma distribution, [8], whereas some authors (i.e. [9]) used an exponential distribution, a special case of the gamma DSD with the parameter  $\mu = 0$ . An estimated DSD for raindrops is given with

$$N_{rain}(D_e) = 1.52 \cdot 10^4 \cdot e^{-3.67 \frac{D_e}{D_0}} \quad 1/\text{cm} \cdot \text{m}^3 \quad (2)$$

and shown in red color in Fig. 2. The median drop diameter  $D_0$  is in the range of 0.75 and 1.9 mm for raindrops in stratiform rainclouds, [1].

##### B. Melting particles

The shape of hydrometeors that transforms from raindrops to ice crystals is comparable to raindrops. The reason is, that at the beginning of melting the liquid coating pretend a high backscattering like from a liquid raindrop due to the high dielectric constant of water in relation to ice. But not only the shape is similar to raindrops, also the size distribution is assumed as gamma DSD, [10] and [11]. The estimated equation for the DSD that is related to the data of POLDIRAD is given in [3] with

$$N_{melting}(D_e) = 3.18 \cdot 10^{10} \cdot D_e^{3.43} \cdot e^{-7.1 \frac{D_e}{D_0}} \quad 1/\text{cm} \cdot \text{m}^3. \quad (3)$$

The median diameter corresponds to the rain rate of the raindrop that results from the melting particle. The black

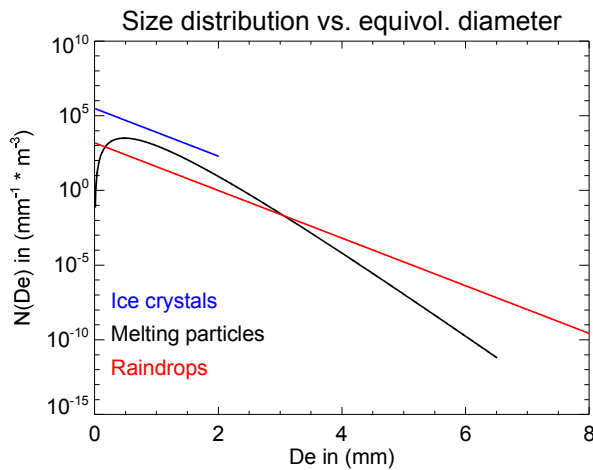


Fig. 2. DSD for ice crystals (blue), melting particles (black) and raindrops (red) for a median diameter  $D_0$  of 1 mm.

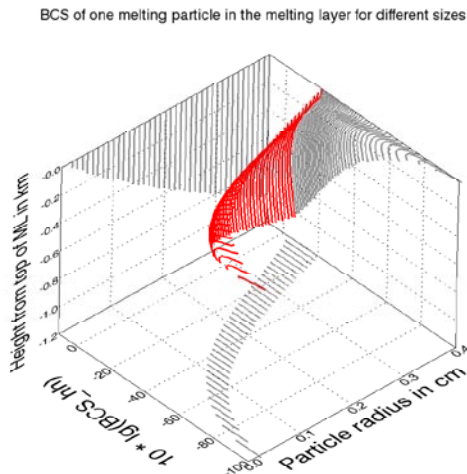


Fig. 3. Logarithm of backscattering cross section (BCS) in horizontal polarization of one melting particle through the melting process (red). Additionally, the 2D projections are plotted (grey).

curve in Fig. 2 gives an impression of the distribution that lay partially between the distribution of ice crystals (blue curve) and raindrops (red curve).

Important is, that the permittivity and therewith the backscattering cross section depends on the status of melting. So it has to distinguish between non-melted (solid ice), partly melted and completely melted (liquid raindrops) particles. Whereas the partly melted hydrometeors are related to the stage inside the melting process. An example of  $\sigma$  of a particle through the melting process is shown in Fig. 3.

Here you can see, that in the melting process the BCS increases for larger particles. They also have a maximum in the vertical profile that is more pregnant for larger particles. The weighting of the particles is done by the particle size

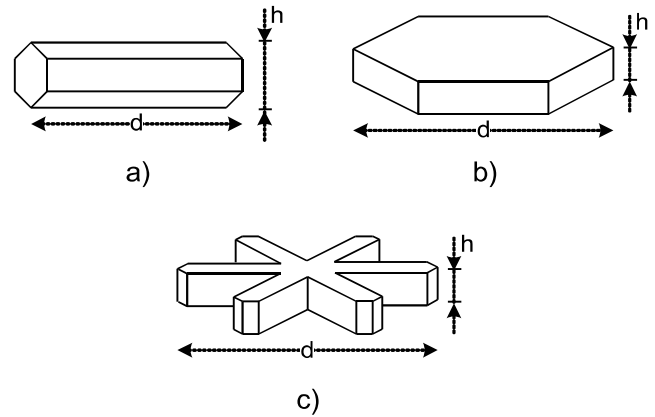


Fig. 4. The three shapes of ice crystals for simulation. a) column, b) plate, c) stellar based on [13].

distribution and so the height of the peak varies depending on the rain rate. This high values for the reflectivity can be proven by the dataset in Fig. 1(b) inside the melting layer at a height of 1.5 km.

### C. Ice crystals

With sizes below 1 mm in the large dimension the exact shape of the ice crystals is not that important for the back scattering at the C-band frequency, [12]. So equivolume spheroids with the Rayleigh-Gans approximation were taken for the simulation. Nevertheless three main shapes of the ice crystals were studied: plates, stellars and colums. Shown are sketches of the three types in Fig. 4.

Ice crystals occur in much higher numbers than raindrops resulting from the smaller size. The comparison of eq. 2 with eq. 4 shows the linear relation by a factor of 200,

$$N_{crystals}(D_e) = 303 \cdot 10^4 \cdot e^{-3.67 \frac{D_e}{D_0}} \text{ 1/cm} \cdot \text{m}^3. \quad (4)$$

The difference between the two types is visible with a offset between the blue and the red curve in Fig. 2, too.

By the way, more typical is the analysis on ice crystals at higher frequencies in the area of 100 GHz or above like in [14]. For the mm wavelengths the simulation of backscattering have to be done in a more precise way. So here other algorithms as the previous mentioned T-Matrix method or the discrete dipole approximation (e.g. [15]) are appropriate.

By simulations at C-band the measurement of high  $Z_{DR}$  values could be confirmed. So flattened stellars or plates can reach values up to 5 dB in the differential reflectivity. The considerable parameter is, as by the other hydrometeor types, the permittivity that is for ice much lower as for water. So the reflectivity is downgraded on the one hand by the small particle size and on the other hand by the smaller dielectric constant (c.f., eq. 1). At this point we will find the discrepancy between measurement and the theory of simulation. Because of the fact, that the radar signal processor does not know the

hydrometeor type one dielectric constant for  $K$ , compare eq. 1, is implemented. Usually, the one of water is chosen. To respect this point the reflectivity is called equivalent reflectivity  $Z_e$ . For the comparison of the reflectivities from the simulation results with the radar measurements, this has to be taken into account.

## V. CLASSIFICATION EXAMPLE

As seen in the previous sections the melting layer and therewith the melting particles play a major role for the classification. So the estimation is the key to a correct classification of stratiform weather events. The estimation of the height of the  $0^\circ\text{C}$  isotherm as the upper border is for example done by the adiabatic interpolation of the ground temperature. Due to the low number of temperature measurements (sometimes just one for the whole dataset) the curve in the RHI is a simple horizontal line, that didn't reflect the reality. The stratiform dataset of figure 1(b) is classified with this melting height estimation and the result in figure 5(a) gives an impression of it. The classification of the classes was done with the help of [1] and [2]. The difficulties are due to the similar signatures of small raindrops and snow crystals, that were separated just by the  $0^\circ\text{C}$  isotherm. A more accurate estimation of the melting layer height was then done with the help of the analysis of the melting particles in [16] and [3]. Therewith the height of the melting layer was dedicated for several ranges in the RHI. The classification of the former stratiform dataset give then the plot in figure 5(b). The additional melting layer class shows the variance of the reflectivity peaks in the vertical profiles.

## VI. CONCLUSION

The polarimetric weather radar is a tool that takes the analysis of weather events many steps further. This study on the classification just give one application. Other aspects will be more detailed estimations of size distributions or analysis of the attenuation effects in the scattering path.

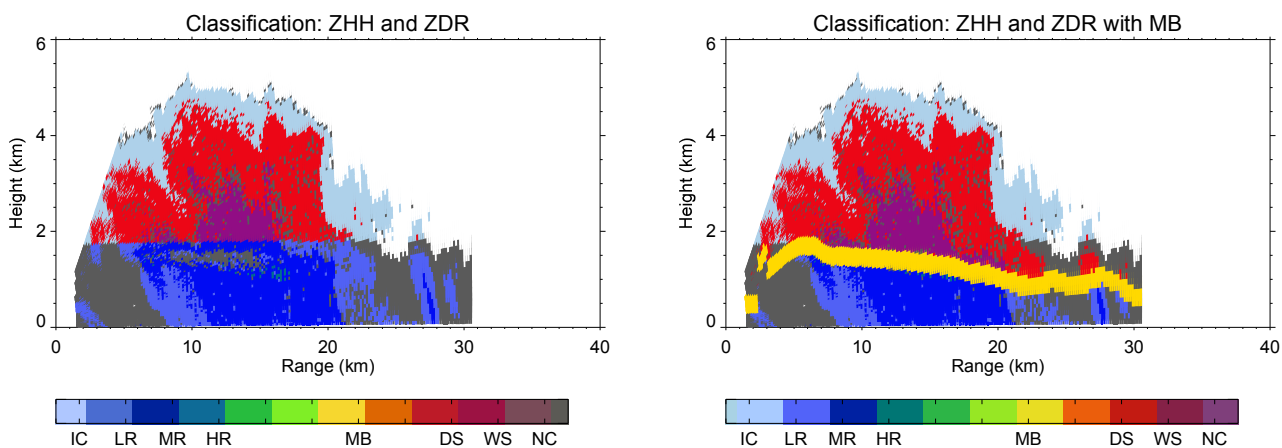
First, signatures of raindrops, melting particles and ice crystals were simulated for the co-polar reflectivities  $Z_{hh}$ ,  $Z_{vv}$  and the differential reflectivity  $Z_{dr}$ . The analysis on the different shapes, DSDs and dielectric constants built thereby the base for the simulation. Then classes were created with the help of measured signatures from stratiform clouds. The estimation of the melting layer class improved the classification in relation to the previous estimation of the  $0^\circ\text{C}$  isotherm (c.f. Fig. 5(a) and Fig. 5(b)).

The presented algorithm is not applicable for all weather events. Actually, the method just works if a melting layer is adaptable and so only for stratiform storms. For convective events algorithms like that of [17] shall be considered.

The road to the future is clear as to investigate a classification method that works for the most clouds or precipitation types. The demand for the operation at every case can be assumed just as idealistic and is difficult to achieve.

## REFERENCES

- [1] J. Steinert and M. Chandra, "Cloud physical properties and empirical polarimetric measurements of rain signatures at c-band," *URSI Germany: Advances in Radio Science*, vol. 6, pp. 315–318, 2008.
- [2] —, "Classification of ice-crystals at c-band," *URSI Germany: Advances in Radio Science*, vol. 7, pp. 273–277, 2009.
- [3] —, "Melting-layer modelling at c-band," *URSI Germany: Advances in Radio Science*, vol. 8, p. accepted, 2010.
- [4] A. C. Schroth, M. S. Chandra, and P. F. Meischner, "A c-band coherent polarimetric radar for propagation and cloud physics research," *J. Atmos. Oceanic Technol.*, vol. 5, pp. 803–822, December 1988.
- [5] T. Oguchi, "Electromagnetic wave propagation and scattering in rain and other hydrometeors," *Proceedings of the IEEE*, vol. 71, no. 9, pp. 1029–1078, Sept. 1983.
- [6] M. I. Mishchenko, L. D. Travis, and D. W. Mackowski, "T-matrix computations of light scattering by nonspherical particles: A review," *J. Quant. Spectrosc. Radiat. Transfer*, vol. 55, no. 5, pp. 535–575, 1996.
- [7] N. U. A.R. Holt and B. Evans, "An integral equation solution to the scattering of electromagnetic radiation by dielectric spheroids and ellipsoids," *IEEE Trans. Antennas Propag.*, vol. AP-26, no. 5, pp. 706–712, September 1978.
- [8] C. W. Ulbrich, "Natural variations in analytical form of the raindrop size distribution," *J. Climate Appl. Meteor.*, vol. 22, pp. 1764–1775, October 1983.
- [9] J. Marshall, R. Langille, and W. Palmer, "Measurement of rainfall by radar," *J. Meteor.*, vol. 4, pp. 186–192, December 1947.
- [10] W. Zhang, "Scattering of radiowaves by a melting layer of precipitation in backward and forward directions," *IEEE Trans. Antennas Propag.*, vol. 42, no. 3, pp. 347–356, March 1994.
- [11] W. Zhang, J. K. Tervonen, and E. T. Salonen, "Backward and forward scattering by the melting layer composed of spheroidal hydrometeors at 5-100 ghz," *IEEE Trans. Antennas Propag.*, vol. 44, no. 9, pp. 1208–1219, September 1996.
- [12] J. Vivekanandan, V. Bringi, M. Hagen, and P. Meischner, "Polarimetric radar studies of atmospheric ice particles," *IEEE Trans. Geosci. Remote Sens.*, vol. 32, no. 1, pp. 1–10, Jan. 1994.
- [13] A. H. Auer and D. L. Veal, "The dimensions of ice crystals in natural clouds," *J. Atmos. Sci.*, vol. 27, pp. 919–926, September 1970.
- [14] K. Aydin and C. Tang, "Millimeter wave radar scattering from model ice crystal distributions," *IEEE Trans. Geosci. Remote Sens.*, vol. 35, no. 1, pp. 140–146, Jan. 1997.
- [15] K. F. Evans and J. Vivekanandan, "Multiparameter radar and microwave radiative transfer modelling of nonspherical atmospheric ice particles," *IEEE Trans. Geosci. Remote Sens.*, vol. 28, no. 4, pp. 234–437, July 1990.
- [16] J. Steinert and M. Chandra, "Cloud profiles from c-band ground-based radar," in *Proceedings of the 8th International Symposium on Tropospheric Profiling, 1923 October, Delft, The Netherlands*, W. M. A. A. Pituley, H.W.J. Russchenberg, Ed., 2009.
- [17] H. Hoeller, V. Bringi, J. Hubbert, M. Hagen, and P. Meischner, "Life cycle and precipitation formation in a hybrid-type hailstorm revealed by polarimetric and doppler radar measurements," *J. Atmos. Sci.*, vol. 51, no. 17, pp. 2500–2522, September 1994.



(a) Differentiation between raindrops and crystals was done by an interpolated height of 0°C isotherm.

(b) The melting layer (yellow), that was estimated from vertical reflectivity profiles, was used for the separation of frozen particles above and liquid particles below.

Fig. 5. Classification on the stratiform event recorded on 29th August 1997. The hydrometeor classes are: ice crystals (IC), light rain (LR), medium rain (MR), heavy rain (HR), melting band (MB), dry snow (DS), wet snow (WS) and no classification (NC).

# Scattering Dependence of Doppler Moments obtained from Polarimetric Weather Radar Echoes

Ondrej Suchy, Madhu Chandra, *University of Technology Chemnitz*

**Abstract**-Using simulated polarimetric weather radar signal, it will be demonstrated that the Doppler moments (mean velocity and spectral width) are not independent of polarization. This polarization dependence of Doppler moments has its origin in the scattering coefficients that ‘weight’ the contribution from the raindrops contained in the radar pulse volume. In the paper we shall detail this dependence.

## I. INTRODUCTION

Polarimetric doppler weather radar is capable of sending orthogonally polarized signals and of decomposing the received signals into the orthogonal polarizations by means of orthogonal transducer and dual receiver. In this paper, dependence of the Doppler spectral estimates from a meteorological target on the polarization state of electro-magnetic wave (EM) and backscattering cross section will be examined. Weather radar signals obtained from precipitation can be seen as composite signals, resulting from the totality of individual weather scatterers contributions. Contribution of each scatterer to the total returned radar signal is given by the range to the radar and its backscattering amplitude, which depends on the size and orientation of scatterers, the frequency of the incident electro-magnetic wave and the polarization state of the transmitted EM wave. Accordingly, the received voltage  $V(t)$  is after down-conversion to the frequency baseband

$$V(t) = \sum K_i(t) S_i(t) e^{-j2k_0 r_i(t)}, \quad (1)$$

where  $K_i$  is the dependence on the radar parameters and range,  $S_i$  is the backscattering amplitude of the  $i$ -th hydrometeor,  $r_i$  is the distance of the  $i$ -th

particle to the radar and  $t$  is time. Because of the Doppler effect, the frequency analysis of the baseband signal samples from a pulse volume of a meteorological target obtained over short time of many milliseconds gives the radial Doppler Spectrum of hydrometeors (Figure 1). The Power Spectrum Density (PSD) of the signal samples is transformed to the Doppler radial velocity distribution by the relation between the Doppler shift  $\Delta f$  and the velocity  $v = -\lambda \cdot \Delta f / 2$ , where  $\lambda$  is the wavelength of the transmitted wave.

The Doppler velocity spectra are biased and do not reflect the true velocity distribution of hydrometeors, because of the dependence of the distributed radar target signal on the radar cross sections (Figure 2).

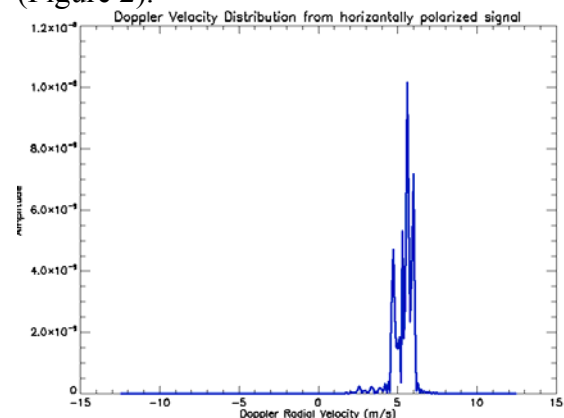


Figure 1: Simulated Doppler Spectrum from precipitation for vertical linear polarization

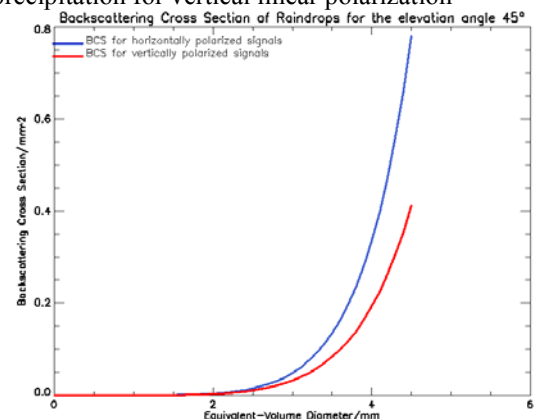


Figure 2: Backscattering Cross Sections for the equivalent-volume diameters of spherical raindrops

## II. DOPPLER MOMENTS

Two common parameters computed from the estimated Doppler velocity spectrum, obtained from the radar measurements, are the mean Doppler velocity and the velocity width. The mean Doppler velocity is the first spectral moment estimated from the Doppler spectrum

$$\bar{v}(r) = \frac{\int_{-\infty}^{\infty} vS(v)dv}{\int_{-\infty}^{\infty} S(v)dv}, \quad (2)$$

with  $S(v)$  is the Doppler Spectrum,  $r$  is the distance from the radar to the pulse volume. The velocity width is usually defined as the square root of the second central moment or standard deviation of the hydrometeors velocity distribution.

$$\sigma(r) = \sqrt{\frac{\int_{-\infty}^{\infty} (v - \bar{v}(r))^2 S(v)dv}{\int_{-\infty}^{\infty} S(v)dv}}. \quad (3)$$

The estimate of the radial mean Doppler velocity (1) can also be simplifying expressed as a mean of radial velocities weighted by the back-scattering cross sections

$$\bar{v}_p(r) = \frac{\sum N(D)\sigma_p(D)v_r(D)dD}{\sum N(D)\sigma_p(D)dD}, \quad (4)$$

where  $D$  is a diameter of an equivalent-volume spherical raindrop,  $N(D)$  is the drop size distribution,  $\sigma_p(D)$  is the backscattering cross section and the index  $P$  stands for the transmitted polarization state of transmitted EM wave, which is for this purpose either linear horizontal (H) or linear vertical (V) and  $v_r(D)$  is the radial terminal velocity of a raindrop with equivalent-volume diameter  $D$ . Similarly, the radial velocity width estimate can be written as

$$\sigma_p(r) = \sqrt{\frac{\sum [(v_r(D) - \bar{v}_p(r))]^2 N(D)\sigma_p(D)dD}{\sum N(D)\sigma_p(D)dD}}. \quad (5)$$

Thus  $\bar{v}(r)$  and  $\sigma(r)$  in (2),(3),(4) and (5) depend on the scattering properties and size distribution of the hydrometeors.

The real physical radial mean velocity or the center of the mass is then the velocity mean without weighting by the backscattering cross sections

$$\bar{v}(r) = \frac{\sum N(D)v_r(D)dD}{\sum N(D)dD} \quad (6)$$

and the real velocity width

$$\sigma(r) = \sqrt{\frac{\sum [v_r(D) - \bar{v}(r)]^2 N(D)dD}{\sum N(D)dD}}. \quad (7)$$

## III. Simulation

The estimates of Doppler velocity estimates for the case of horizontal and vertical polarizations and real velocity estimates for different rain rates and different elevation angles were compared. Terminal fall velocities without turbulences of the raindrops were estimated by the formula from Atlas (1973) [2, p. 216]

$$v(D) = 9.65 - 10.3 \exp(-600D) \text{ms}^{-1}.$$

For the raindrop distribution, the exponential Marshall-Palmer data were supposed [2, p.213].

$$N(D) = N_0 \exp(-\Lambda D)$$

$$\Lambda = 4.1R^{-0.21} \text{mm}^{-1}$$

$$N_0 = 8 \cdot 10^3 \text{m}^{-3} \text{mm}^{-1}$$

, where  $R$  is the rainfall rate. The back-scattering cross section (Figure 1) is computed from back-scattering amplitude  $S_p$  with

$$\sigma_p = 4\pi |S_p|^2.$$

Back-scattering amplitudes for equivalent-volume diameters of spherical raindrops

can be expressed with Rayleigh-Gans theory [3]:

$$S_{vv} = \left(\frac{2\pi}{\lambda}\right)^2 [(p_v - p_h) \cos^2 \delta \cos^2 \psi + p_h]$$

$$S_{hh} = \left(\frac{2\pi}{\lambda}\right)^2 [(p_v - p_h) \cos^2 \delta \sin^2 \psi + p_h],$$

where

$$p_{h,v} = \frac{ab^2}{3} \left[ \frac{m^2 - 1}{A_{h,v}(m^2 - 1) + 1} \right]$$

$$A_v = \frac{1}{e^2} \left[ 1 - \left( \frac{1 - e^2}{e^2} \right)^{1/2} \sin^{-1}(e) \right] = 1 - 2A_h$$

and  $m$  is the refractive index of water and  $e$  is the ellipticity of an oblate spheroid

$$e = \left[ 1 - \left( \frac{a}{b} \right)^2 \right]^{1/2}, \text{ where } a \text{ and } b \text{ are axes}$$

of the hydrometeor ellipsoid. The ratio  $(a/b)$  for equivalent-volume diameters between  $0.5 \leq D \leq 4.5 \text{ mm}$  was estimated in [4]:

$$(a/b) = 1.030 - 0.124D.$$

Raindrops oscillations were not considered, the alignment of the major axes of droplets to the electrical field was assumed, thus horizontal polarized backscattering amplitude is independent of elevation angle (Fig.3). The figure 4 shows the Doppler spectra obtained from horizontal and vertical polarized signals and the corresponding real velocity spectrum. It can be seen, that due to the non-linear increase in the backscattering cross sections for greater equivalent-volume diameters the weighting for the higher velocities is greater than in the real velocity spectrum, despite lower amount of the bigger droplets due to the exponential raindrops distribution. The spectrum from linear polarization has a greater magnitude than the vertical polarized one, because of the greater horizontal dimensions of raindrops for higher diameters.

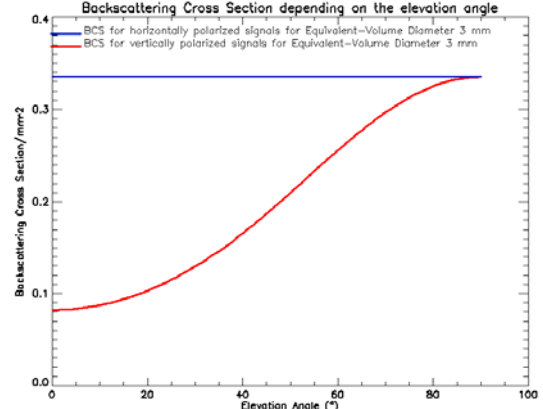


Figure 3: Dependence of BCS on the elevation angle for a hydrometeor with  $D=3\text{mm}$

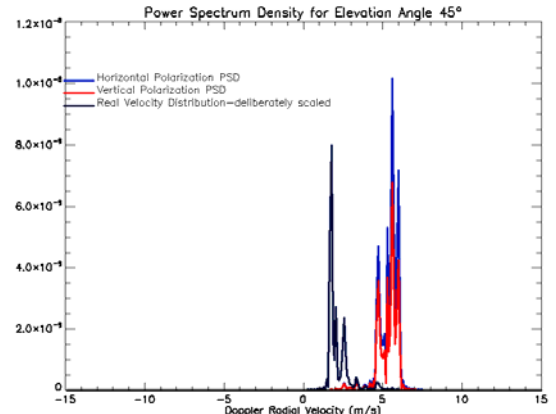


Fig.4: Simulated Doppler Spectra for rain rate 50 mm/h

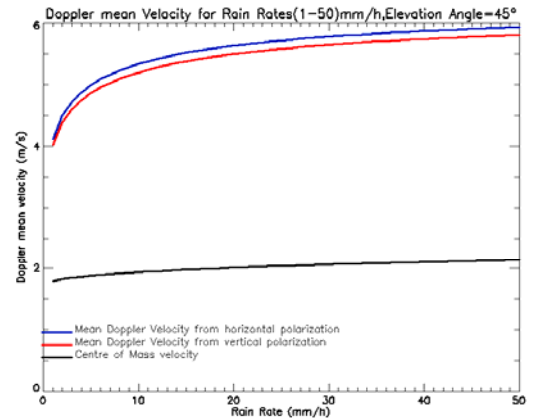


Fig.5: Mean Doppler and real velocity estimates for rainrates 1-50 mm/h

#### IV. Conclusions

Figures 4,5 and 6 show simulated mean velocities. Physical mean velocity is considerably lower than the simulated Doppler mean velocity by the factor of 2-3 and the Doppler mean velocity from vertical polarization is slightly lower than from the horizontal one. Fig. 5 shows the

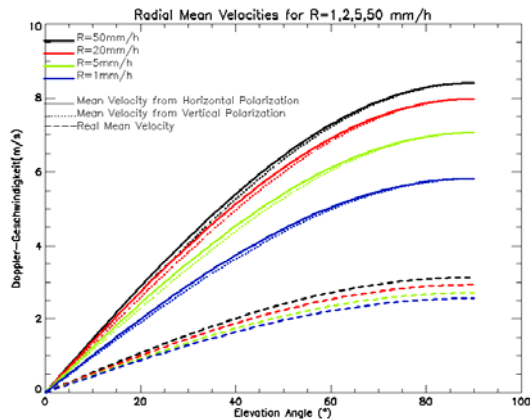


Figure 6: Mean Doppler Velocities depending on the beam elevation angle.

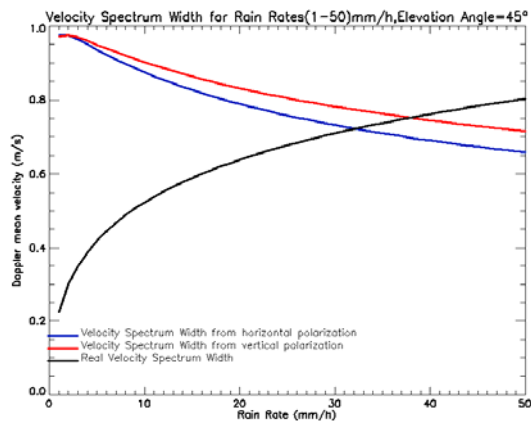


Fig. 7: Velocity Spectrum Width Estimations

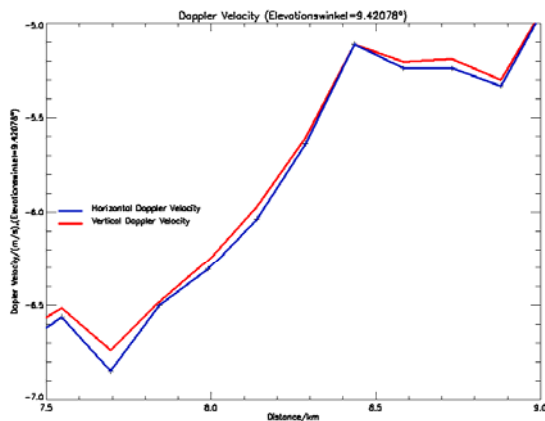


Fig. 8: Estimated Doppler velocity from precipitation for linear horizontal and vertical polarizations measured from a rain on the 17<sup>th</sup> September 1997, Data from Poldirad Radar DLR, Oberpfaffenhofen, Germany

real physical mean velocity versus the Doppler mean velocity for rain rates from 0 to 50 mm/h and beam elevation angle of 45°. Because meteorological target is distributed one with hydrometeors of different sizes, the Doppler-velocity estimates depends on the polarization of

the transmitted electromagnetic wave. Due to non-linear increase of horizontal hydrometeor dimensions compared to the vertical ones is the Doppler velocity estimate greater for horizontal polarization. Doppler velocity of a point target is identical to the real radial velocity of this target (Eq. 4). Figure 7 shows velocity width for the different rain rates and the beam elevation angle of 45°, where no broadening effects except different terminal fall velocities were considered. In Figure 8 are estimates of Doppler velocities from real weather radar data from horizontal and vertical polarized signals. The Doppler velocity estimates from horizontally polarized signal are greater in the absolute value than the ones from vertically polarized. The reflectivity from horizontal polarized signal in this precipitation region was between 38 and 40 dBZ.

## References

- [1] V.N. Bringi and V. Chandrasekar, 'Polarimetric Doppler Weather Radar', pp. 262 -263
- [2] R.J. Doviak, D. S. Zrníc, Doppler Radar and weather observations.
- [3] D.P. Stapor, T. Pratt, A generalized analysis of dual-polarization radar measurements of rain, Radio Science, Volume 19, Number 1, Pages 90-98, January-February 1984
- [4] H.R. Pruppacher, K.V. Beard, A wind tunnel investigation of the internal circulation and shape of water drops falling at terminal velocity in air, J.R. Met. Soc. (1970), 96, pp. 247-256

## **Parameterisation of the raindrop size distribution using polarimetric weather radar measurements**

P. Tracksdorf<sup>1,2</sup>, M. Chandra<sup>2</sup>, M. Hagen<sup>1</sup>

<sup>1</sup> Deutsches Zentrum für Luft- und Raumfahrt in der Helmholtz Gemeinschaft e.V., Institut für Physik der Atmosphäre, Wolkenphysik und Verkehrsmeteorologie, Münchner Str. 20, 82234, Oberpfaffenhofen-Wessling, Germany

<sup>2</sup> Professorship of Microwave Engineering and Photonics, Faculty of Electrical Engineering and Information Technology, Chemnitz University of Technology, Reichenhainer Str. 70, 09126, Chemnitz, Germany

The quantitative areal precipitation estimation by using ground based weather radar measurements is an appropriate method for researchers and end-users in the fields of meteorology, hydrology and water management. Although there are existing single-parameter algorithms, such as the reflectivity-rainfall rate-relations, which are often used to estimate the quantitative areal precipitation when having nonpolarimetric weather radar measurements, these algorithms are often very inaccurate. A more accurate estimation of the quantitative areal precipitation is possible when having a more detailed knowledge of the raindrop size distribution within the observed radar resolution volume. This work will reflect upon the parameterisation of the raindrop size distribution using polarimetric weather radar measurements (coherent polarimetric C-band weather radar POLDIRAD, DLR site Oberpfaffenhofen) and will give a comparison with ground based disdrometer point measurements with special regards on the quality control of the polarimetric weather radar measurements and the disdrometer measurements. The results of this work will be presented and summarised in the form of empirical relationships between the polarimetric weather radar measurements and the parameters of the raindrop size distribution.

**Increasing the efficiency of mobile networks by dynamic (radio) resource management - challenges and future trends (Review lecture)**

T. Bauschert

Professur für Kommunikationsnetze, TU Chemnitz, Chemnitz

# Comparison of methods for the attenuation correction of C-band polarimetric weather radar measurements at linear horizontal / vertical polarisation basis

Tobias Otto

Remote Sensing of the Environment  
International Research Centre of Telecomm. and Radar  
Delft University of Technology, The Netherlands  
t.otto@tudelft.nl

Madhu Chandra

Professorship of Microwave Engineering and Photonics  
Chemnitz University of Technology, Germany  
madhu.chandra@etit.tu-chemnitz.de

**Abstract**—Linear horizontal / vertical polarisation basis are the preferred choice for weather radar measurements since the depolarisation due to precipitation in the troposphere is low. Thus, the reflectivity measurements have only to be corrected for attenuation before using them to quantitatively estimate precipitation parameters such as the rain rate or the liquid water content.

We applied various attenuation correction methods to C-band polarimetric weather radar data of rain measured by the POLDIRAD, DLR, Oberpfaffenhofen. We compared the specific attenuation at horizontal polarisation and the differential attenuation estimated by the attenuation correction methods with an attenuation correction method that imposes self-consistency among the weather radar observables. Three attenuation correction methods are identified and presented that yield reasonable attenuation estimates.

## I. INTRODUCTION

In order to measure the spatial distribution and the temporal evolution of precipitation, ground-based weather radars are an essential measurement device. For this purpose, only in Europe more than 150 C-band weather radars<sup>1</sup> are operated today by the meteorological services. However, the backscattered power that is measured by the radars does not only contain the intrinsic contribution of the backward-scattering of the corresponding range-bin. While propagating through precipitation, the electromagnetic waves encounter propagation effects such as attenuation or depolarisation. Linear horizontal / vertical polarisations are close to the characteristic polarisations of precipitation, thus, depolarisation is low. Hence, power measurements at linear horizontal / vertical polarisation basis need only to be corrected for attenuation. The precipitation-induced attenuation is small at S-band, but it is not at higher frequencies, e.g. C- and X-band, Bringi et al. (1990). In the early years of weather radar observations, Hirschfeld and Bordan (1954) proposed a method to estimate the attenuation

based on the co-polarised power measurement only. However, they already pointed out, that their approach should be constrained by independent measurements, e.g. rain gauges. Polarimetric weather radars operating at linear horizontal / vertical polarisation offer an estimate of the differential phase between the co-polarised echoes. This differential phase is like attenuation a forward-scattering effect. Scattering computations show that the differential phase and the attenuation can be linked to each other, Holt (1988), however, this relation varies with respect to the microphysics of the observed storm, Bringi et al. (1990). Nonetheless, the attenuation of each range-bin can be estimated from the range derivative of the differential phase. The differential phase can also be seen as a microwave link that provides an estimate of the path-integrated attenuation (*PIA*) for each antenna position. Testud et al. (2000) provided a formulation to bound the attenuation correction method of Hirschfeld and Bordan (1954) with the *PIA* estimated by the differential phase. The attenuation correction method of Testud et al. (2000) was extended by self-consistency approaches in order to account for the variability of the relation between the differential phase and the *PIA*, Bringi et al. (2001), Gorgucci et al. (2006), Gorgucci and Baldini (2007). A refinement of the method of Testud et al. (2000) including self-consistency was provided by Lim and Chandrasekar (2006) in the sense that beside the reflectivity, also the differential reflectivity is coupled with the estimation of the attenuations. Hogan (2007) combined the polarimetric weather radar observables in a variational scheme in order to correct for attenuation and to estimate the rain rate. In this approach the multiplicative coefficient between the reflectivity and the rain rate is determined by minimising a cost function that combines the weather radar measurements with a forward model. Beside the differential phase, also the assumption that the differential reflectivity should be close to 0 dB behind a convective cell may be employed as a constraint, Smyth and Illingworth (1998). However, this constraint can only be employed in case of strong differential attenuation. Another

<sup>1</sup>OPERA - Operational programme for the exchange of weather radar information, <http://www.knmi.nl/opera>

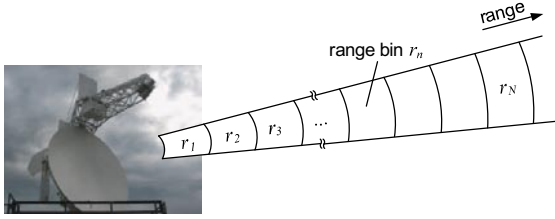


Fig. 1. Radar geometry.

attenuation correction method is based on the retrieval of the raindrop-size distribution, Chandra et al. (1990).

Using radar data acquired by the C-band polarisation diversity radar (POLDIRAD), DLR, Oberpfaffenhofen, we compare the attenuations derived by several methods amongst each other. As a reference, the method of Gorgucci and Baldini (2007) is employed that imposes self-consistency among all weather radar observables involved in the attenuation correction.

## II. BASICS

The variability of rain can be described by a three-parameter raindrop-size distribution (RSD) normalised with respect to the liquid water content, Bringi and Chandrasekar (2001),

$$N(D) = N_w f(\mu) \left( \frac{D}{D_0} \right)^\mu e^{-(3.67+\mu)\frac{D}{D_0}} \quad (1)$$

with

$$f(\mu) = \frac{6}{3.67^4} \frac{(3.67 + \mu)^{\mu+4}}{\Gamma(\mu + 4)}. \quad (2)$$

$D$  is the equivolumetric raindrop diameter,  $D_0$  is the median volume diameter,  $N_w$  is the concentration, and  $\mu$  is the shape parameter.

The calibrated measurements of an homogeneous ensemble of raindrops by polarimetric weather radars at linear horizontal / vertical polarisation basis expressed in terms of the RSD, and the scattering amplitudes of the raindrops are given as:

$$Z_{hh} = 10 \log_{10} \left( \frac{\lambda^4}{\pi^5 |K|^2} \int_D \sigma_{hh}(D) N(D) dD \right) \quad (3)$$

$$Z_{dr} = 10 \log_{10} \left( \frac{\int_D \sigma_{hh}(D) N(D) dD}{\int_D \sigma_{vv}(D) N(D) dD} \right) \quad (4)$$

$$K_{dp}^{1-way} = \frac{180}{\pi} \lambda \int_D \Re[f_{hh}(D) - f_{vv}(D)] N(D) dD. \quad (5)$$

The intrinsic weather radar observables in Eqs. (3) to (5) are the co-polarised reflectivity at horizontal polarisation  $Z_{hh}$  (dBZ), the differential reflectivity  $Z_{dr}$  (dB), and the specific differential phase  $K_{dp}^{1-way}$  ( $^{\circ}/\text{km}$ ) which is the range derivative of the differential propagation phase  $\Psi_{dp}$ . Furthermore,  $\lambda$  is the wavelength,  $|K|^2$  is a dielectric factor,  $\sigma_{hh,vv}$  are the radar cross sections, and  $f_{hh,vv}$  are the forward scattering amplitudes of the raindrops at linear horizontal and linear vertical polarisation. Numerical values of the radar cross sections

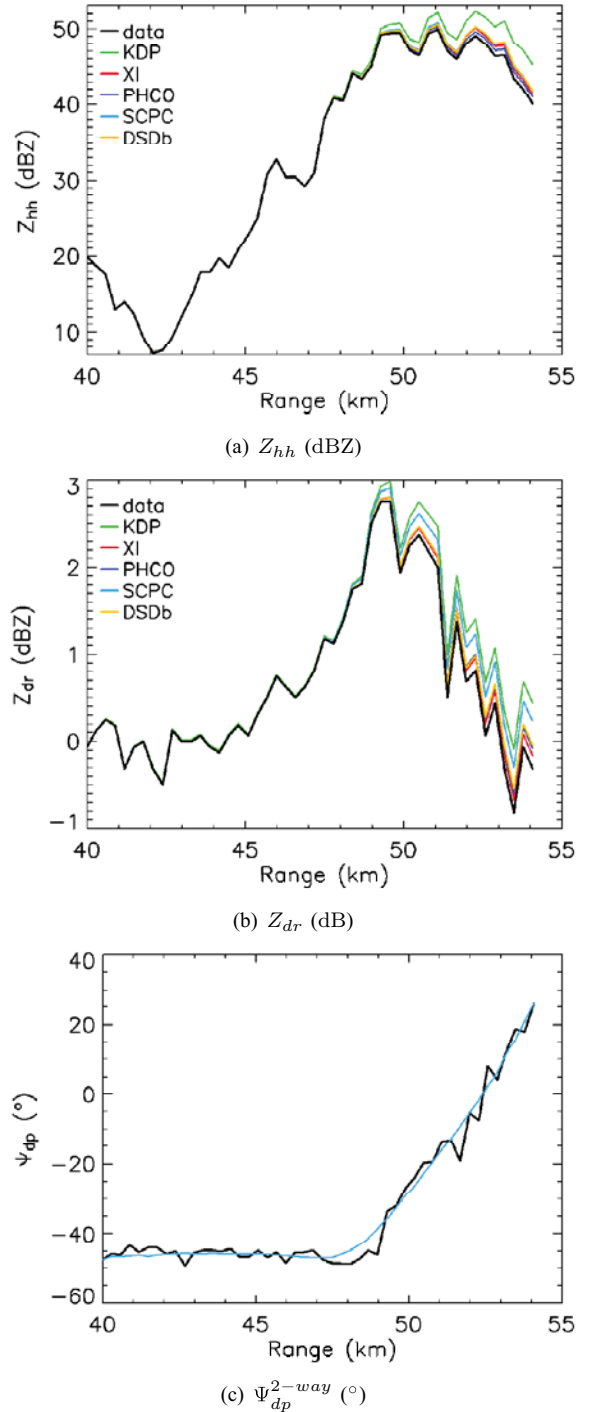


Fig. 2. Attenuation correction illustrated for a radar ray with an elevation of  $1^{\circ}$ , and an azimuth of  $210^{\circ}$ , measured by the POLDIRAD the 26<sup>th</sup> of August 1997 at 16:00 UTC. The measured radar observables are shown in black, (a)  $Z_{hh,att}$ , (b)  $Z_{dr,att}$ , and (c)  $\Psi_{dp}^{2-way}$ . The light blue curve in (c) shows the smoothed differential phase profile. The value of the differential phase in a range of 40 km is due to a differential system phase offset. The coloured curves in (a) and (b) show the results of the attenuation correction methods introduced in Section III.

and the forward scattering amplitudes of raindrops assuming a spheroidal shape have been computed for a frequency of

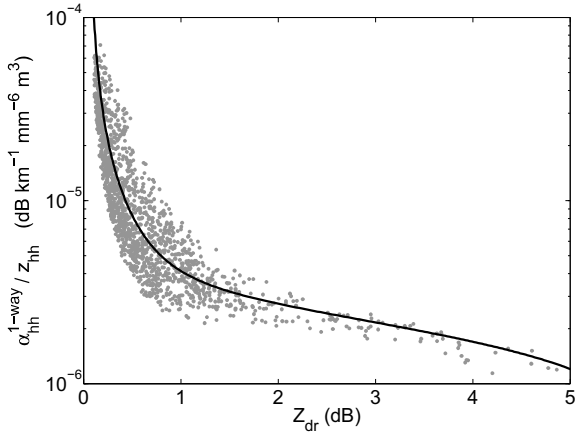


Fig. 3. Scattering computations of a set of 1500 raindrop-size distributions, demonstrating the microphysical variability of the  $\xi_{hh}$  versus the differential reflectivity  $Z_{dr}$  (grey dots). The black curve is  $\xi_{hh}$  for the KAB raindrop shape, a temperature of 10 °C, and a RDS shape factor of  $\mu = 0$  that was chosen for the attenuation correction method XI.

5.5 GHz (POLDIRAD) by the Fredholm Integral Method, Holt et al. (1978). The complex permittivity of water was calculated after Ray (1972). Three raindrop shape models served as input to the scattering computations: Pruppacher and Beard (1970), Keenan et al. (2001), and a combination of Keenan et al. (2001), Andsager et al. (1999) and Beard and Chuang (1987), henceforth the KAB raindrop shape. To display the variability of weather radar observables, a set of 1500 RDS's was established. For each RDS, the temperature was randomly chosen between 1 °C and 25 °C, and one of the three raindrop shapes was randomly selected. The parameters of the RDS's were varied within  $2 \leq \log [N_w(\text{mm}^{-1}\text{m}^{-3})] \leq 5$ ,  $0.5 \text{ mm} \leq D_0 \leq 3.5 \text{ mm}$ , and  $-1 \leq \mu \leq 5$  such that the resulting distribution of rain rates satisfies with close agreement the disdrometer measurements of Hagen (2001).

The propagation of electromagnetic waves through rain leads to attenuation of the measured reflectivity and the differential reflectivity:

$$Z_{hh,att}(r_n) = Z_{hh}(r_n) - 2 \int_{r_1}^{r_{n-1}} \alpha_{hh}^{1-way}(r) dr \quad (6)$$

$$Z_{dr,att}(r_n) = Z_{dr}(r_n) - 2 \int_{r_1}^{r_{n-1}} \alpha_{h-v}^{1-way}(r) dr \quad (7)$$

where the ranges  $r$  are defined in Fig. 1. The specific attenuation  $\alpha_{hh}^{1-way}$  (dB/km) and the differential attenuation  $\alpha_{h-v}^{1-way}$  (dB/km) in the equations above are given by

$$\alpha_{hh}^{1-way} = 8.686\lambda \int_D \Im [f_{hh}(D)] N(D) dD \quad (8)$$

and

$$\alpha_{h-v}^{1-way} = 8.686\lambda \int_D \Im [f_{hh}(D) - f_{vv}(D)] N(D) dD. \quad (9)$$

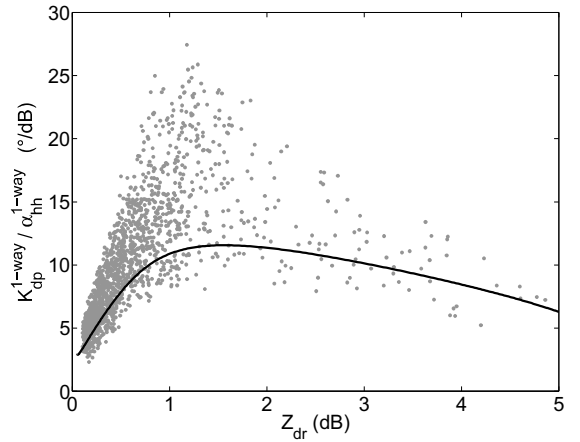


Fig. 4. Scattering computations of a set of 1500 raindrop-size distributions, demonstrating the microphysical variability of the  $\eta_{hh}$  versus the differential reflectivity  $Z_{dr}$  (grey dots). The black curve is  $\eta_{hh}$  for the KAB raindrop shape, a temperature of 10 °C, and a RDS shape factor of  $\mu = 0$  that was chosen for the attenuation correction method KDP.

A POLDIRAD measurement of rain is shown in Fig. 2 (black curves). Propagation effects are not immediately evident, looking at the reflectivity profile, Fig. 2 (a), or the differential reflectivity profile, Fig. 2 (b). Only the range-cumulative behaviour of the differential phase profile, Fig. 2 (c), reveals the presence of propagation effects. The coloured curves in Figs. 2 (a) and (b) are the reflectivities corrected for attenuation as outlined in the next section.

### III. ATTENUATION CORRECTION METHODS

In this section the attenuation correction methods that are then compared to each other are introduced.

#### A. Tan and Goddard (1997)

The attenuation correction method of Tan and Goddard (1997) is unconstrained, and based only on the reflectivity and the differential reflectivity. It relies on the application of the relation between the differential reflectivity and the ratio, Aydin et al. (1989),

$$\xi_{hh,vv} = \frac{\alpha_{hh,vv}^{1-way}}{z_{hh}} \quad (10)$$

where  $z_{hh}$  ( $\text{mm}^6\text{m}^{-3}$ ) is the co-polarised reflectivity at horizontal polarisation in linear units. Tan and Goddard (1997) pointed out, the direct application of Eqn. (10) to attenuated reflectivity measurements provides a good estimate of the specific attenuations due to the characteristics of  $\xi_{hh,vv}$ , Fig. 3. Thus, a possible error propagation due to a radar mis-calibration is avoided as in the case of the formulation of Hitschfeld and Bordan (1954). However, the estimated attenuations are only reliable for  $Z_{dr} > 0.3$  dB. Below that empirically derived  $Z_{dr}$  limit, the slope of  $\xi_{hh,vv}$  is too steep.

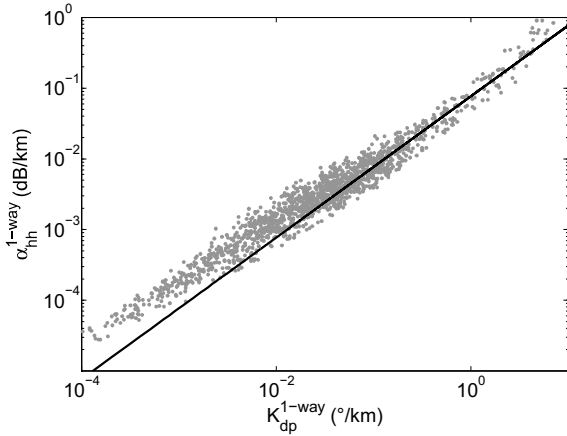


Fig. 5. Scattering computations of a set of 1500 raindrop-size distributions, demonstrating the microphysical variability of the relation between  $\alpha_{hh}^{1-way}$  versus the specific differential phase  $K_{dp}^{1-way}$  (grey dots). The black curve shows the linear relation of Eqn. (12).

#### B. Chandra et al. (1994)

The attenuation correction method of Chandra et al. (1994) makes use of the differential reflectivity and the ratio

$$\eta_{hh,vv} = \frac{\int_{r_a}^{r_b} \Psi_{dp}^{1-way}(r) dr}{\int_{r_a}^{r_b} \alpha_{hh,vv}^{1-way}(r) dr}. \quad (11)$$

The application of this ratio, Fig. 4, serves to adjust the relation between the differential phase and the attenuations. Note that  $\eta_{hh,vv}$  as well as  $\xi_{hh,vv}$  and  $Z_{dr}$  are independent of the RDS concentration parameter  $N_w$ .

In contrast to the method introduced by Chandra et al. (1994), we implement Eqn. (11) here on a single range-bin basis. Thus, the most significant source of uncertainty is expected in the estimation of the specific differential phase  $K_{dp}^{1-way}$  from the measured differential phase profile.

#### C. Chandra et al. (1990)

Using the measured  $Z_{hh,att}$ ,  $Z_{dr,att}$ ,  $\Psi_{dp}$ , one can estimate the three-parameter RDS, Eqn. (1). Subsequently, scattering computations can be carried out to determine the attenuations, Chandra et al. (1990). The first step is the estimation of the median volume diameter from the differential reflectivity that is measured within  $\pm 0.1$  dB by the POLDIRAD. Using the same approach as described in Otto et al. (2009), it was determined that this attenuation correction method can be applied at C-band for  $0.5 \text{ dB} \leq Z_{dr} \leq 3 \text{ dB}$  using the KAB raindrop shape, and limiting the RDS shape factor to values between  $-2 \leq \mu \leq 10$ . Since the RDS parameters are estimated from the attenuated reflectivities, they might be inaccurate. For this reason, the radar ray is partitioned into ray-segments that fulfill  $\Psi_{dp}(r_b) - \Psi_{dp}(r_a) \geq 5^\circ$ . The method is then applied ray-segment by ray-segment starting close to the radar at  $r_1$ , Fig. 1.

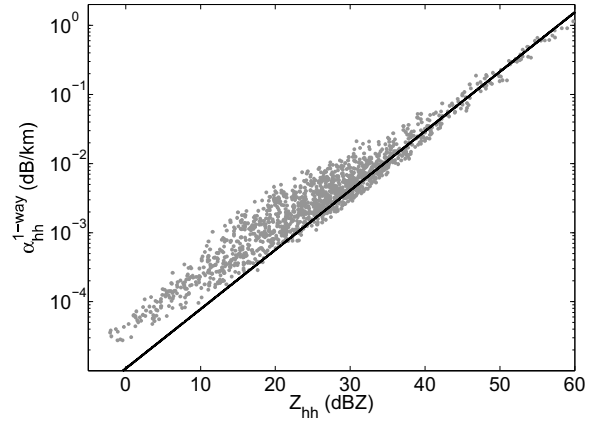


Fig. 6. Scattering computations of a set of 1500 raindrop-size distributions, demonstrating the microphysical variability of the relation between  $\alpha_{hh}^{1-way}$  versus the reflectivity  $Z_{hh}$  (grey dots). The black curve shows the relation of Eqn. (14).

#### D. Phase-constraint methods

Testud et al. (2000) combined the formulation of Hitschfeld and Bordan (1954) with a constraint on the  $PIA$  determined by the differential phase. The  $PIA$  is determined by applying the following relations

$$\alpha_{hh}(\text{dB/km}) = \gamma_{hh} K_{dp}(\text{°/km}) \quad (12)$$

and

$$\alpha_{h-v}(\text{dB/km}) = \gamma_{h-v} K_{dp}(\text{°/km}). \quad (13)$$

The coefficients of these equations  $\gamma_{hh} = 0.077$  and  $\gamma_{h-v} = 0.022$  have been determined by scattering computations for C-band (5.5 GHz), Fig. 5. Furthermore, the formulation is based on

$$\alpha_{hh}^{1-way} = a_{hh} z_{hh}^{b_{hh}} \quad (14)$$

and

$$\alpha_{vv}^{1-way} = a_{vv} z_{vv}^{b_{vv}} \quad (15)$$

with the coefficients  $a_{hh} = 1.08 \times 10^{-5}$ ,  $b_{hh} = 0.859$ , and  $a_{vv} = 7.25 \times 10^{-6}$ ,  $b_{vv} = 0.924$  again determined by scattering computations for C-band (5.5 GHz), Fig. 6. The reflectivities  $z_{hh,vv}$  ( $\text{mm}^6 \text{m}^{-3}$ ) are in linear units. The following equations of Testud et al. (2000) were employed

$$\alpha^{1-way}(r) = \frac{z^b(r) [10^{0.1bPIA(r_a:r_b)} - 1]}{I_{(r_a:r_b)} + [10^{0.1bPIA(r_a:r_b)} - 1] I_{(r:r_b)}} \quad (16)$$

with

$$PIA_{(r_a:r_b)} = \gamma [\Psi_{dp}^{2-way}(r_b) - \Psi_{dp}^{2-way}(r_a)] \quad (17)$$

and

$$I_{(r:r_b)} = 0.46 \cdot b \int_r^{r_b} z^b(s) ds \quad (18)$$

where  $r_a \leq r \leq r_b$  denote range-bins along the radar ray, Fig. 1.

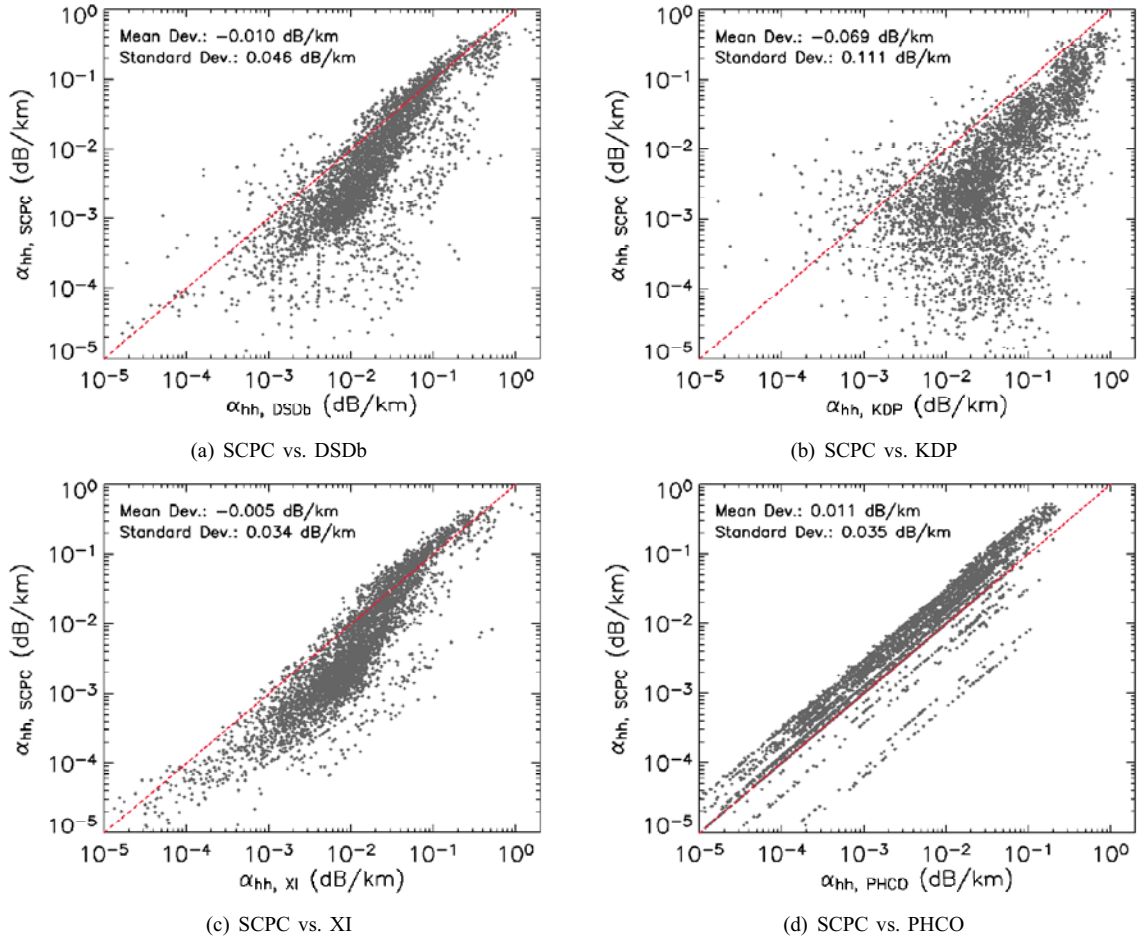


Fig. 7. Scatter plots of  $\alpha_{hh}^{1-way}$  estimated for a selection of POLDIRAD data by attenuation correction methods (Section III) compared to the SCPC attenuation correction method, see text for details. The mean and the standard deviations are indicated within the figures.

TABLE I  
COEFFICIENTS OF EQNS. (19) AND (20) AT C-BAND (5.5 GHz).

$c_1$	$c_2$	$c_3$	$c_4$
$9.051 \times 10^{-5}$	0.680	-0.514	0.323
$c_5$	$c_6$	$c_7$	$c_8$
$0.142 \times 10^{-3}$	0.452	0.495	0.607

As a reference for attenuation correction, the method of Gorgucci and Baldini (2007) was employed. This method applies in a first step the attenuation correction method of Testud et al. (2000), i.e. Eqn. (16). In a second step, the attenuations are adjusted by imposing self-consistency among all weather radar observables involved in the attenuation correction as

$$\alpha_{hh}^{1-way} = c_1 z_{hh}^{c_2} z_{dr}^{c_3} K_{dp}^{c_4} \quad (19)$$

and

$$\alpha_{h-v}^{1-way} = c_5 z_{hh}^{c_6} z_{dr}^{c_7} K_{dp}^{c_8} \quad (20)$$

where  $z_{hh}$  ( $\text{mm}^6\text{m}^{-3}$ ) and  $z_{dr}$  are in linear units, and  $K_{dp} = K_{dp}^{1-way}$ . The coefficients for the self-consistency

equations that were derived by scattering computations for C-band (5.5 GHz) are given in Table I.

#### IV. COMPARISON OF ATTENUATION CORRECTION METHODS

In order to compare the attenuation correction methods introduced in the preceding section, 68 radar rays with significant attenuation comprising a total of 8280 range-bins were selected out of eight C-band POLDIRAD datasets acquired in June and August 1997. The manual selection of the data by inspecting all polarimetric weather radar observables ensured that only data of rain were selected.

To identify the previously presented attenuation correction methods, they are denoted as:

- XI .. unconstrained attenuation correction method based on the reflectivities only, Section III-A,
- KDP .. estimation of the attenuation from the specific differential phase, Section III-B,
- DSDb .. combined estimation of the RDSD parameters with attenuation correction, Section III-C,

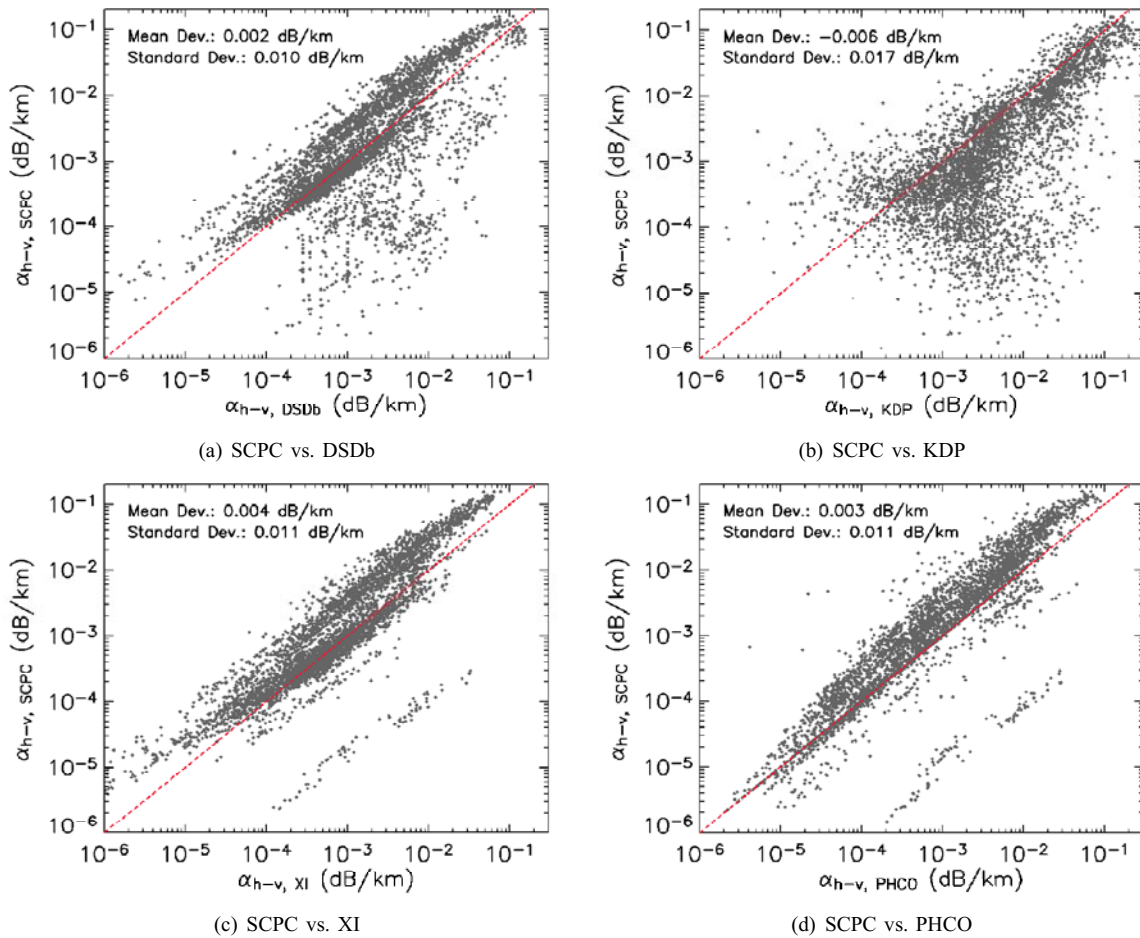


Fig. 8. Scatter plots of  $\alpha_{h-v}^{1-way}$  estimated for a selection of POLDIRAD data by attenuation correction methods (Section III) compared to the SCPC attenuation correction method, see text for details. The mean and the standard deviations are indicated within the figures.

PHCO .. phase-constraint method of Testud et al. (2000), Section III-D, and

SCPC .. phase-constraint method with imposed self-consistency of Gorgucci and Baldini (2007), Section III-D.

Figs. 7 and 8 show scatter plots of the specific attenuation at horizontal polarisation and the differential attenuation derived by the SCPC method versus the XI, KDP, DSDb and PHCO methods. The corresponding mean deviations and standard deviations have been calculated, and are displayed in the figures. The adjustment of the PHCO derived attenuations by imposing self-consistency is evident in Figs. 7 (d) and 8 (d). Generally, it seems that Eqns. (12) and (13) with the coefficients used, underestimated the *PIA*.

The largest variance compared to the SCPC method, is shown by the KDP method, Figs. 7 (b) and 8 (b). That is probably due to the uncertainty introduced by the determination of the specific differential phase from the measured  $\Psi_{dp}$  profile. Unexpectedly good results were achieved by the XI method although it is unconstrained. Also the DSDb method proved well compared to the SCPC method.

## V. CONCLUSION

The favoured choice for polarimetric weather radars measurements is the polarisation basis linear horizontal / vertical since depolarisation is low. Only the attenuation correction of the power-based observables, i.e. reflectivities, is required before a quantitative estimation of precipitation parameters. In this contribution, several attenuation correction methods have been reviewed. Using C-band polarimetric weather radar data they have been compared to each other. As reference, a phase-constraint attenuation correction method with imposed self-consistency among the weather radar observables was employed.

An accurate estimation of the specific differential phase is required when it is directly used to estimate the attenuations. In any case, the better choice is to use the measured profile of the differential propagation phase to estimate the *PIA*. This is achieved by the PHCO method. However, the application of the PHCO method should always be coupled to a self-consistency approach in order to account for the variability of the relation between the differential propagation phase and the attenuations.

If the parameters of the RDSB are of interest, the RDSB parameter retrieval can be combined at C-band with the attenuation correction as shown by the DSDb method. If only polarimetric power measurements are available, i.e. the reflectivity and the differential reflectivity, the XI method is the best choice for the attenuation correction at C-band.

However, since these conclusions are based on an intercomparison, they may not be regarded as absolute. For a more meaningful analysis of attenuation correction methods, it is suggested to compare data with independent measurements from another weather radar in the vicinity of the POLDIRAD, i.e. from the research radar of the German Meteorological Service (DWD) at Hohenpeißenberg.

#### REFERENCES

- K. Andsager, K. V. Beard, and N. F. Laird, "Laboratory Measurements of Axis Ratios for Large Raindrops," *J. Atmos. Sci.*, vol. 56, pp. 2673 – 2683, August 1999.
- K. Aydin, Y. Zhao, and T. A. Seliga, "Rain-Induced Attenuation Effects on C-Band Dual-Polarization Meteorological Radars," *IEEE Trans. Geosci. Remote Sens.*, vol. 27, pp. 57 – 66, January 1989.
- K. V. Beard and C. Chuang, "A New Model for the Equilibrium Shape of Raindrops," *J. Atmos. Sci.*, vol. 44, pp. 1509 – 1524, June 1987.
- V. N. Bringi and V. Chandrasekar, *Polarimetric Doppler Weather Radar*, 1st ed. Cambridge University Press, 2001, p. 410.
- V. N. Bringi, V. Chandrasekar, N. Balakrishnan, and D. S. Zrnić, "An Examination of Propagation Effects in Rainfall on Radar Measurements at Microwave Frequencies," *J. Atmos. Oceanic Technol.*, vol. 7, pp. 829 – 840, December 1990.
- V. N. Bringi, T. D. Keenan, and V. Chandrasekar, "Correcting C-Band Radar Reflectivity and Differential Reflectivity Data for Rain Attenuation: A Self-Consistent Method With Constraints," *IEEE Trans. Geosci. Remote Sens.*, vol. 39, pp. 1906 – 1915, September 2001.
- M. Chandra, A. Schroth, and E. Lüneburg, "The Influence of Raindrops Size Distribution on the Determination of Microwave Propagation Properties by Polarimetric Radars," in *Geoscience and Remote Sensing Symposium, IGARSS 90*, May 1990, pp. 1041 – 1045.
- M. Chandra, A. Schroth, and E. Lueneburg, "Retrieval of propagation induced attenuation from radar derived accumulated differential phase measurements," in *Geoscience and Remote Sensing Symposium, IGARSS 94, Surface and Atmospheric Remote Sensing: Technologies, Data Analysis and Interpretation*, vol. 1, August 1994, pp. 366 – 368.
- E. Gorgucci and L. Baldini, "Attenuation and Differential Attenuation Correction of C-Band Radar Observations Using a Fully Self-Consistent Methodology," *IEEE Geosci. Remote Sens. Lett.*, vol. 4, pp. 326 – 330, April 2007.
- E. Gorgucci, V. Chandrasekar, and L. Baldini, "Correction of X-Band Radar Observations for Propagation Effects Based on Self-Consistency Principle," *J. Atmos. Oceanic Technol.*, vol. 23, pp. 1668 – 1681, December 2006.
- M. Hagen, "On the variation of the parametrization of rainfall rate estimation by dual polarization techniques," in *30th Conference on Radar Meteorology, Munich, Germany, Preprints, 11B.3*, , American Meteorological Society, 2001.
- W. Hitschfeld and J. Bordan, "Errors inherent in the radar measurement of rainfall at attenuating wavelengths," *J. Meteorol.*, vol. 11, pp. 58 – 67, February 1954.
- R. J. Hogan, "A Variational Scheme for Retrieving Rainfall Rate and Hail Reflectivity Fraction from Polarization Radar," *J. Atmos. Oceanic Technol.*, vol. 46, pp. 1544 – 1564, October 2007.
- A. R. Holt, "Extraction of differential propagation phase from data from S-band circularly polarized radars," *Electron. Lett.*, vol. 24, pp. 1241 – 1244, September 1988.
- A. R. Holt, N. K. Uzunoglu, and B. G. Evans, "An Integral Equation Solution to the Scattering of Electromagnetic Radiation by Dielectric Spheroids and Ellipsoids," *IEEE Trans. Antennas Propag.*, vol. AP-26, pp. 706 – 712, September 1978.
- T. D. Keenan, L. D. Carey, D. S. Zrnić, and P. T. May, "Sensitivity of 5-cm Wavelength Polarimetric Radar Variables to Raindrop Axial Ratio and Drop Size Distribution," *J. Appl. Meteor.*, vol. 40, pp. 526 – 545, March 2001.
- A. Lim and V. Chandrasekar, "A Dual-Polarization Rain Profiling Algorithm," *IEEE Trans. Geosci. Remote Sens.*, vol. 44, pp. 1011 – 1021, April 2006.
- T. Otto, J. Figueras i Ventura, and H. W. J. Russchenberg, "Drop-size distribution retrieval of precipitation using a high-resolution polarimetric X-band weather radar," in *Proceedings of the 8th International Symposium of tropospheric profiling, Delft, The Netherlands, ISBN 978-90-6960-233-2*, A. Apituley, H. W. J. Russchenberg, and W. A. A. Monna, Eds., 2009.
- H. R. Pruppacher and K. V. Beard, "A wind tunnel investigation of the internal circulation and shape of water drops falling at terminal velocity in air," *Q. J. Roy. Meteor. Soc.*, vol. 96, pp. 247 – 256, 1970.
- P. S. Ray, "Broadband Complex Refractive Indices of Ice and Water," *Appl. Optics*, vol. 11, pp. 1836 – 1844, August 1972.
- T. J. Smyth and A. J. Illingworth, "Correction for attenuation of radar reflectivity using polarization data," *Q. J. Roy. Meteor. Soc.*, vol. 124, pp. 2393 – 2415, 1998.
- J. Tan and J. W. F. Goddard, "Attenuation correction for C-band radars," in *Preprints, 28th Conference on Radar Meteorology, Austin, TX, United States, American Meteorological Society*, 1997.
- J. Testud, E. Le Bouar, E. Obligis, and M. Ali-Mehenni, "The Rain Profiling Algorithm Applied to Polarimetric Weather Radar," *J. Atmos. Oceanic Technol.*, vol. 17, pp. 332 – 356, March 2000.

# Atmospheric Transmission Measurements for the PROCEMA Project

Susanne Hipp\*, Christian Chwala†, Uwe Siart\*, Thomas Eibert\*, Harald Kunstmann†

\*Institute for High-Frequency Engineering

Technische Universität München

Arcisstr. 21, 80333 München, Germany

Tel.: +49 89 289-23375, E-Mail: susanne.hipp@tum.de

†Institute for Meteorology and Climate Research IMK-IFU

Forschungszentrum Karlsruhe

Kreuzeckbahnstr. 19, 82467 Garmisch-Partenkirchen, Germany

## INTRODUCTION

In order to improve water resources quantification and sustainable management the accurate and high resolution estimation of spatial and temporal distributions of precipitation is still an important issue. The attenuation of microwave signals of cellular networks offers a completely new and highly innovative method to quantify ground-level precipitation. The joint virtual institute “Regional Precipitation Observation by Cellular Network Microwave Attenuation and Application to Water Resources Management” (PROCEMA) aims at the development, optimization and exploitation of this methodology in hydrological and meteorological sciences.

Within the PROCEMA project partners from Israel and Germany and from different scientific fields work together on this challenge. In their research program they focus on development of algorithms for relating the attenuation rate of cellular network back-haul link signals to rainfall intensity and on development of algorithms to convert line integrals into spatial rainfall fields. Furthermore experimental investigation on impact of atmospheric conditions on microwave propagation and validation and performance analysis of the methodology for applications in water balance analysis and integrated pilot test site inter-comparison will be carried through. PROCEMA particularly addresses the scientific challenge of rainfall estimations in mountainous environments, where both station- and radar based techniques often fail. Therefore the methods under development will also provide valuable supplementary data in addition to established monitoring devices like radar, rain gauges, and satellite measurements.

In this contribution the scope of the PROCEMA project and the measurement systems under development will be introduced.

## DESCRIPTION

Together with the Institute for Meteorology and Climate Research a polarimetric transmission measurement at frequencies 22 GHz and 35 GHz is currently being set up. We chose a monostatic configuration using a tetrahedral reflector to mirror the transmitted electromagnetic wave back to the receiver. Total path length is 1000 m and the measurement system is fully coherent and polarization agile. Discrimination between reflected and transmitted energy is achieved by timing control and range gating. Besides

attenuation in H- and V-polarization this system can also record amplitude and phase noise (scintillations) produced by the hydrometeors with a single-sideband bandwidth of up to 25 kHz. It is expected that the noise statistics provide significant information for both precipitation classification and rain rate estimation.

In addition to the coherent transmission measurement system data logging modules on selected commercial point-to-point back-haul links are being installed. They will record instantaneous values of transmit power and AGC level to allow for a monitoring of the overall link attenuation. The software behind was designed to record averaged values every minute and send the data via FTP to a dedicated server. With this data and algorithms already existing or developed by the simulation team precipitation maps of different kinds will be constructed.

The precipitation estimates obtained from data provided by the new transmission measurement system as well as from attenuation monitoring at back-haul links will be compared, calibrated, and verified with data from collateral meteorological measurements accomplished by the Institute for Meteorology and Climate Research in research areas nearby.

## ACKNOWLEDGMENT

This work is funded by the Helmholtz Association of German Research Centres under grant VH-VI-314 entitled “Regional Precipitation Observation by Cellular Network Microwave Attenuation and Application to Water Resources Management” (PROCEMA).

## REFERENCES

- [1] Bahrami, M., J. Rashed-Mohassel, and M. Mohammad-Taheri: *An Exact Solution of Coherent Wave Propagation in Rain Medium with Realistic Raindrop Shapes*. Progress In Electromagnetics Research, PIER 79:107–118, 2008.
- [2] Goldshtein, O., H. Messer, and A. Zinevich: *Rain Rate Estimation Using Measurements From Commercial Telecommunications Links*. IEEE Trans. Signal Process., SP-57(4):1616–1625, April 2009.
- [3] Hendratoro, G. and I. Zawadzki: *Derivation of Parameters of Y-Z Power-Law Relation From Raindrop Size Distribution Measurements and Its Application in the Calculation of Rain Attenuation From Radar Reflectivity Factor Measurements*. IEEE Trans. Antennas Propag., AP-51(1):12–22, January 2003.
- [4] Rahimi, A. R., A. R. Holt, G. J. G. Upton, and R. J. Cummings: *Use of dual-frequency microwave links for measuring path-averaged rainfall*. Journal of Geophysical Research, 108(D15):8–1–8–12, 2003.
- [5] Rahimi, A. R., G. J. G. Upton, and A. R. Holt: *Dual-frequency links—a complement to gauges and radar for the measurement of rain*. Journal of Hydrology, 288:3–12, 2004.

## **Sensors in Automotive Applications (Review Lecture)**

G. Wanielik

Professorship of Communications Engineering, Chemnitz University of Technology, Chemnitz

The field of applications based on electromagnetic wave propagation is growing, not only in the area of mobile communication but in the future also in the field of advanced driver assistance systems (ADAS). This paper deals with the use of different electromagnetic automotive sensors to observe the complete surrounding of a vehicle. The basis of this task are multispectral information gathered from sensors like 77 GHz and 24 GHz automotive radars, multilayer lidar, mono- and stereo- cameras, near- and far-infrared cameras as well as 3D-cameras. Multisensor-data-fusion techniques are used to process these observations and to extract meaningful information about the relevant “traffic involved objects”. It is necessary to investigate techniques for situational awareness in the sense of “understanding the vehicle’s surrounding”. Several sensor combinations and different applications of ADAS are addressed in order to give an overview and also inspirations for the relative new, important and fast growing field of ADAS.

# Improving radar based tracking of extended objects using clustering approaches

V. Leonhardt, G. Wanielik

**Abstract**—Radar is often used to detect and track large moving objects such as ships, airplanes or cars. Due to the increasing resolution of modern radar systems, the number of detections caused by such extended objects increases as well. Hence the simplified assumption of point objects can no longer be maintained. Depending on its kind, size and movement a varying number of detections per object is generated. In the case a scenery consisting of multiple moving objects has to be analyzed, the object is just relevant as a whole. Any additional detection is synonymous with further effort for tracking and for other processing steps and diminishes the whole system's performance. On the other hand, it provides the opportunity to discriminate faulty measurements from actual objects.

This paper points out how multiple-point target characteristics affect the process of object tracking on the basis of an automotive multi-beam radar sensor's detections. By comparison, two clustering algorithms demonstrate how related detections can be assigned, merged and preselected. Furthermore, the benefit gained is demonstrated on the example of an automotive object tracking system.

**Index Terms**—Automotive, clustering, extended object, radar, Region Growing, tracking

## I. INTRODUCTION

DEVELOPMENTS in the field of driver assistance systems were and are aiming to make driving safer, more comfortable and more energy-efficient. People should reach their destination fast, safe and relaxed. Thereby the car's task is not only to carry the drivers, but also to assist them. Recent driving assistance systems, such as the adaptive cruise control, the blind spot warning system or the lane change assistant, give hints, warn the drivers or call their attention. Other systems even take over subtasks, as emergency braking or parking. The driver needs an exact picture of the car's environment, and so does the assistance system. This includes problems like where the vehicle is located, where other road users are, where they are moving or where the lanes' margins are.

V. Leonhardt is with the Chemnitz University of Technology, Chemnitz, Germany (e-mail: [veit.leonhardt@etit.tu-chemnitz.de](mailto:veit.leonhardt@etit.tu-chemnitz.de)).

G. Wanielik is with the Chemnitz University of Technology, Chemnitz, Germany (e-mail: [gerd.wanielik@etit.tu-chemnitz.de](mailto:gerd.wanielik@etit.tu-chemnitz.de)).

In the car, the task of perception is performed by numerous sensors, such as cameras (color, grayscale or infrared), lidar, radar, or ultrasonic sensors. The characteristic feature of the radar sensor is its ability to detect the objects' velocity apart from their location. However, such sensors provide nothing but sets of measuring points. In order to get an object-oriented representation of the ego vehicle's environment, it is necessary to analyze and process these points. In the case of a frequency modulated continuous-wave radar (FMCW) multi-beam sensor, the data measured consist of a set of peaks in the Doppler spectrum. Each peak represents a reflection of one radar beam's radar wave and so it gives a clue of the presence of an object.

Thereby it may occur that one and the same object causes several reflections. In spite of that the object recognition has to describe each object as a whole. So the problem arises to have to realize which measurements belong together and to describe them as a unity. Moreover, along with the number of observations that have to be processed the computational effort to cope the amount of information increases as well. Otherwise groups of related observations offer the opportunity to draw conclusions regarding the objects' appearance. This can help to classify and reject observations in the run-up to the recognition process.

## II. SYSTEM DESCRIPTION

The central part of the process of object recognition is the object tracking. It bases on the observations made by the sensor and aims to detect and eliminate the measurement's errors and inaccuracies, respectively. For this purpose, the occurrence of observations is traced over time. Initially, the observations of one time step are utilized to make presumptions with respect to the presence of objects and their state. Subsequent measurements are related to the presumptions in order to confirm, to refine or to rebut (in the case of faulty measurements) them or in order to induce new ones.

The specific tracking algorithm used here bases on the widespread Kalman Filter whose initial version was presented by Rudolf Emil Kalman in 1960 [1]. It estimates a linear, time-discrete system's state and its uncertainty by utilizing control inputs known, the system's dynamics model, and associated measurements of any point in time. In doing so, it provides significantly better results than the estimation can do solely

basing on individual measurements. In the present case, the state of the system is modeled by location and movement of one object. By modeling the movement, constant turn rates and velocities (CTRV) [2] are assumed. However, this results in non-linear state transitions and not in linear behavior as required by the basic Kalman Filter. In order to work with a non-linear system, nevertheless, the Filter can be supplemented by a linearization. The Extended Kalman Filter [3] arises.

Any implementation of the filter forms a track that represents the estimation of the state of one object. The estimation depends on the observations associated with the object over time. Therefore, the observations measured have first to be assigned to existent tracks. This is accomplished by calculating each observation-track-pair's similarity. The similarity measure used is the normalized Mahalanobis-Distance [4], which describes the distance by considering the track's uncertainty. Afterwards, the assignment takes place according to the principle of Nearest-Neighbor. However, before tracks and observations can be related to each other, they have to be transferred into comparable forms. For that purpose, the Kalman Filter starts to predict the track's state at that point in time when the observations are measured. Apart from the prediction of the tracked object's movement, this includes the compensation of the movement performed by the vehicle that detects the objects. As a next step the filter makes use of the prediction and the measurement model assumed to deduce the observation that most probably will be induced by the object. So the required comparability of observations and tracks is achieved. The observations assigned to a track are subsequently utilized by the Kalman Filter to match the prediction with the actuality represented by the measurements. The tracking pass is completed by the step of track management, which controls the tracks' life cycle. In the process, not assigned observations are used to initiate new tracks whereas tracks that are not refreshed by observations for some time are eliminated.

The tracking is followed by a process of selection, whose task is to identify the most important target (MIT). The MIT is defined as the closest object which moves within the same lane as the ego vehicle does, because this is the most relevant and critical one. Two further modules are connected upstream to the tracking process. One of them is the ego motion filter. Its task is comparable to that of the object tracking. However, the motion of the ego vehicle, required by the ego motion compensation, is filtered and corrected. So the Kalman Filter is applied once more. A second module preselects incoming observations depending on their position and velocity.

The whole object tracking's structure is illustrated in Fig. 1. It is implemented as part of a project of a driver assistance system. Its focus is on the detection of vehicles driving ahead in extra-urban traffic scenarios using an automotive radar sensor. The resulting representation of the ego vehicle's surroundings forms the basis of the second, the actively intervening part of the assistance system.

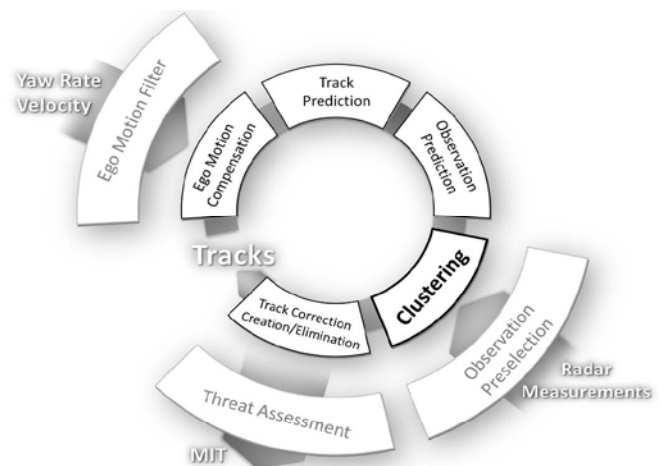


Fig. 1. Object tracking structure

The concept car Carai of Chemnitz University of Technology (see [www.carai.de](http://www.carai.de)) used in this project is equipped with an automotive single-layer FMCW radar sensor among other devices. It is a multi-beam sensor with 16 beams, with a range of up to 150 m, with an aperture angle of 15 degrees, and with a velocity range of  $\pm 55$  m/s. The accuracy of the measurement of range, angle, and velocity is  $\pm 1$  m,  $\pm 0.5$  degree, and  $\pm 0.75$  m/s respectively. Information about the vehicle's ego motion is delivered by its CAN-Bus.

### III. PROBLEM DESCRIPTION

As a consequence of using a sensor like that one described above intending to detect extended objects such as vehicles, the assumption of point objects cannot be maintained any longer. Depending on its distance, angle of view, and geometry, an object can induce more than just one observation.

On the one hand, the increase in the number of observations that are available for the object tracking constitutes a gain of information. On the other hand, the tracking algorithm must be able to handle them efficiently. Although the algorithm in its unchanged form is able to assign multiple observations to one and the same track, there is no plan how to induce those tracks usefully. Assuming that each observation represents an independent point object, all observations would originate their own tracks. Later on, all of them ought to pass through the steps of prediction, assignment, correction, and management. This would slow down the whole process of object tracking distinctly. Moreover, several tracks would compete for the observations of one and the same object. Hence, it could occur that none of the tracks becomes stable and the object is overlooked. If, on the contrary, observations would be assigned to several tracks, the high computational effort would be increased further. In any case, significantly more tracks would arise than objects actually exist. Besides, the opportunity would be wasted to classify and discard objects by means of their size or shape.

#### IV. CLUSTERING

One way to adapt the object tracking to the problem of extended objects is to conflate all information that can be associated with an object. If this happened subsequently to the tracking, i.e. at track level, the number of tracks per object could be decreased, but the problems of efficiency and reliability would still remain. On the contrary, the additional process step would further diminish the whole system's performance. Last but not least, the knowledge of the observations' relative position would remain unused.

Consequently, it seems to be worthwhile to group the radar's measurements as early as possible aiming to condense and pre-process the information for the tracking. Such a process of grouping entities, here: measurements, that belong together is also called clustering. According to the assumption that observations caused by one and the same object are similar to each other, the idea is to form groups (clusters) of similar observations. Then the clusters are substituted by single pseudo-observations. These are passed on to the tracking instead of all the observations measured. That way, it is possible to maintain the tracking algorithm and to avoid the problems described above. In order to counteract the information loss caused by the consolidation, the pseudo-observations can be supplemented by further attributes characterizing the corresponding clusters. For instance, to know the number, the variance or the minimum bounding box of a cluster's observations make information available to the object tracking about the cluster's internal structure and validity. Thus it is possible to evaluate and discriminate the observations gained.

Within the scope of this work, two different approaches were adopted to cluster the observations measured in the run-up of the object tracking. Thereby the main focus was on the speed-up and stabilization of the process of the object recognition concerning the detection of extended objects. Existing algorithm parts should be maintained if possible.

##### A. Clustering transversal rows of observations

The first of the two approaches presented bases on the realization that the rear of vehicles driving ahead cause several detections in a transversal row depending on the number of radar beams intersected. Thus, the objective of the approach is to find and to cluster observations that are in a transversal row.

For this purpose, the clustering starts with a sorting step. It utilizes the Quicksort algorithm developed by C. A. R. Hoare [5] in 1962. The necessary comparison of two observations' similarity is made by a cascaded comparison function. It compares the relative distances, the velocities and the lateral displacements of two observations (in that order). These Cartesian values are derived from the radar peaks' range, Doppler value, and angle. The comparison is unaffected by minor differences, which means that the pair's distance value, the most determining attribute, is compared first. If these values are not significantly different, the observations'

velocities are compared. This makes it possible to separate different objects by their velocity, despite their similar distance. If the velocity values are also similar, the observations are sorted by their lateral displacement. The process is controlled by thresholds for the minimum differences in the three dimensions.

Within the sequence of sorted observations, detections caused by the same object follow one another. A second step compares each pair of two consecutive observations and links those that are similar enough. Thus, lines of similar, directly or indirectly linked observations arise, which are the clusters. According to the assumption made, clusters that consist of more than one observation rate as caused by extended objects. They are reduced to their centers of gravity and passed on to the subsequent tracking process. Observations that are not arranged in a line are sorted out. So the object tracking obtains a single pseudo-observation for each relevant object in place of the many observations delivered by the sensor.

In order to evaluate the benefit of this clustering approach, it was applied as part of the object tracking described above. As a reference system, a second, unchanged instance of the object tracking system is used.

#### Results

Tests with various urban and extra urban road traffic scenarios could confirm that the approach is able to improve the tracking process. The additional computational effort to cluster the observations is opposed by the noticeable reduction of the observations that must be processed by the tracking step.

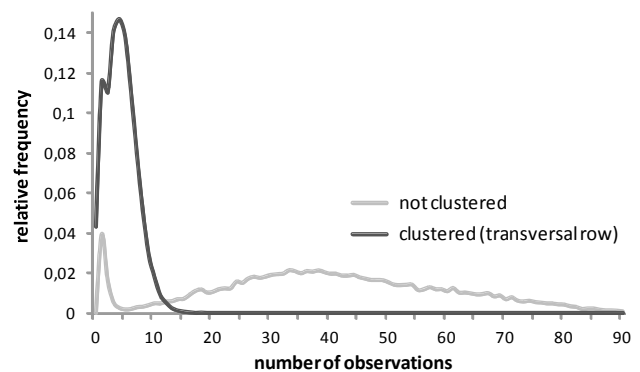


Fig. 2. Observations to be processed by tracking (transversal row approach)

As shown in Fig. 2, the 40.2 observations on average delivered by the radar sensor are substituted by just 4.3 pseudo-observations on average.

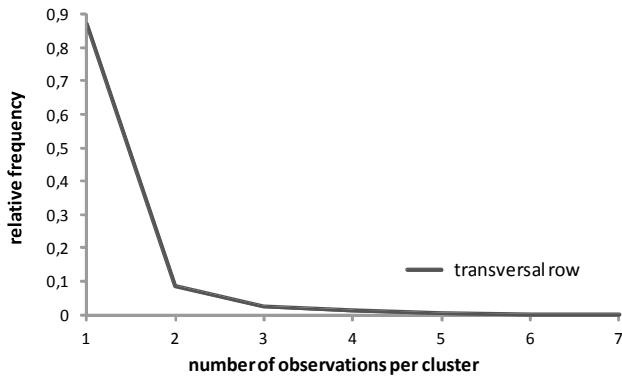


Fig. 3. Number of assigned observations per cluster (transversal row approach)

The replacing observations result from clusters that consist of more than one observation. Fig. 3 depicts the relative frequency of clusters of such a size. It indicates that fewer than one in six clusters induce a pseudo-observation. Hence, 18.7 percent of the reduction of the number of observations is achieved by pooling observations measured and 81.3 percent by sorting out isolated ones.

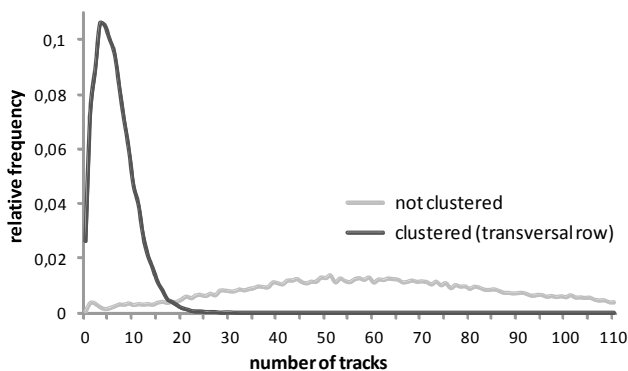


Fig. 4. Number of existing tracks (transversal row approach)

With the number of observations passed on to the tracking, the number of tracks that arise and that have to be handled diminishes as well. The mean number of existing tracks, illustrated in Fig. 4, decreases from 67.6, without any clustering, to 6.1, with the clustering delineated.

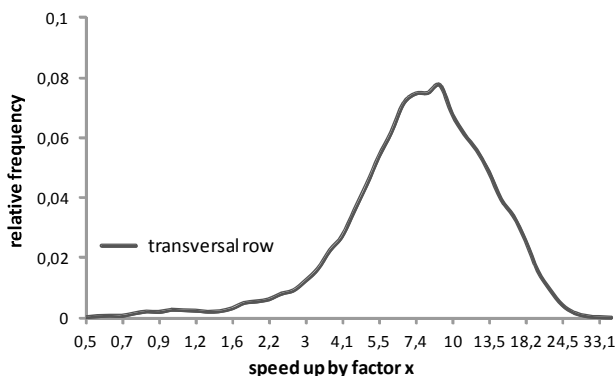


Fig. 5. Speed up of the tracking achieved by the clustering (transversal row approach)

As a consequence, the computational effort is reduced by more than 86 percent on average (see Fig. 5). Nevertheless, the whole system's ability to detect vehicles remains unaffected, provided that the assumption made is applicable and a vehicle's rear causes several detections in a transversal row. Additionally, it was found that far fewer tracks emerge that have to be ascribed to one and the same object or that result from detection faults.

The strength of the approach is in its simplicity. It avoids large numbers of (mostly high-dimensional) comparisons of two observations, which are a problem of many clustering approaches. However, in some cases the assumption made turns out to be too restrictive. This is apparent if an object's observations not only differ in their transversal but also in their longitudinal component so that none or not all observations are located in a single row. This can, in particular, be the case for very long vehicles such as trucks. The type of the sensor used and the angle of view affect the correctness of the assumption taken as a basis as well. In the event it is inapplicable, it can happen that not all related observations are pooled to a single cluster. Consequently, none or more than one cluster per extended object arises. Thus, the strength of the approach, i.e. the underlying assumption, is its weak point at the same time.

#### B. Clustering basing on Region Growing

An alternative, more general approach renounces specific assumptions relating to the relative positioning of the observations. Instead, it simply postulates the similarity of observations belonging together. In order to trace and form such groups of similar observations, the idea of Region Growing is adopted.

Region Growing is a standard region-based technique in digital image processing. Approaches of region-based clustering, or segmentation, try to group observations due to their vicinity. This can happen either in an agglomerative (or bottom-up) or a divisive (or top-down) way. Agglomerative algorithms start with each element being its own cluster. Afterwards they merge those clusters into successively larger clusters. Examples for this approach are Pyramid Linking [6] and variations of the aforementioned Region Growing [7]. In contrast, divisive algorithms start with the whole set of observations as a single large cluster. Afterwards the cluster is split into smaller clusters stepwise. Algorithms, such as e.g. Split and Merge [8], combine both strategies. Other types of region-based approaches attempt to find an optimal linkage by minimizing a cost function. For example, [9] employs the Fuzzy C-Means algorithm to cluster synthetic aperture radar images. However, [10] and [11] use the k-Means clustering in order to cluster groups of targets and observations of several radars, respectively.

The idea of Region Growing is to start with a given number of cluster seeds. Each seed represents one cluster's origin. Originating from these, the clusters expand to finally fill a coherent region. The growing of a region happens by adding

not yet assigned, similar, adjacent pixels iteratively. The decision on a pixel's assignment is made on the basis of a pixel-cluster-pair's similarity. For this purpose, a similarity measure is defined in such a way that it produces a high value if a pixel and a cluster are similar and produces a low one if they are dissimilar. Existent implementations primarily differ in the manner they choose the starting points, in the similarity measure used, and in the sequence the pixels are processed. Examples for the radar based applications of the Region Growing approach are [12] and [13]. However, they all apply the approach to grid-based problems.

Transferred to the given problem, the objective of the application of the Region Growing algorithm is to group all observations caused by the same object at a given time and to replace them by just one pseudo-observation before they are relayed to the tracking algorithm. For this purpose, a few adaptations have to be made to the basic clustering algorithm.

At first, not a digital video image or an image of a synthetic aperture radar is processed, but a multi-beam radar sensor's set of measurements. Thus, a set of scattered peaks in the radar's Doppler spectrum has to be clustered instead of a grid of evenly distributed pixels. Furthermore, each peak represents an observation whose information consists of the peak's Doppler value (a measure for the relative velocity of an object) and the location from which the measurement originates.

In order to tackle the initial problem of clustering approaches (the proper choice of the number and location of the cluster seeds) the tracking algorithm, delineated in this paper, utilizes tracks already formed by the object tracking. Thereby each existing track generates a seed for one cluster based on the track's estimated location and velocity.

Subsequently, the clustering algorithm starts to assign every single observation to the cluster (represented by its seed) with the greatest similarity. However, this would lead to a clustering that ignores the possibility of newly emerging objects and tracks, respectively. To avoid this, a minimum measure of similarity is defined. In case an observation's best similarity falls short of this value, the observation is marked as not assignable. In the following it can be used to initialize a new track.

This would, however, entail that every single not assignable observation would induce its own track. Ultimately, the clustering would have no effect on the number of tracks arising. To prevent this, it is permitted to observations to fuse into a cluster even without an assignment. In the event two observations are more similar to each other than to any cluster, they are pooled and induce a seedless auxiliary cluster. Such a cluster behaves like an observation. It can be assigned to a cluster caused by a track or it can be fused with other observations. Only those auxiliary clusters induce new tracks that are not assigned to any track until the clustering ends.

In addition, there is another problem. The restriction of an observation-cluster-pair's dissimilarity might result in the

distribution of the observations of a single object among various clusters. This can happen when the estimation of a track differs from the position of the real object. As a consequence, some observations of an object are similar enough to be assigned to a certain cluster whereas others are not assigned. In order to avoid this, the algorithm is changed in the way that already assigned observations gain influence on the location of the cluster. Thereby, a cluster's center corresponds to the center of gravity of the assigned observations and, if existing, the weighted cluster's seed. The thus calculated centers form pseudo-observations that are relayed to the tracking algorithm by substituting the observations measured.

### Results

As the first clustering approach delineated, the adapted Region Growing algorithm was implemented and evaluated. Thereby, both the data set of scenarios tested and the implementation of the object tracking utilized are the same as those used to evaluate the first algorithm. There is one exception: as the second approach already implies an assignment of tracks and observations, the original object tracking's step of assignment could be omitted.

The comparison of the results shows that the use of the Region Growing based clustering algorithm also distinctly reduces the number of observations, even though to a lesser extent than the other approach does. Compared to the reference object tracking (without any clustering) the mean number of observations that have to be processed by the tracking decreases from 40.2 to 7.5 on average (see Fig. 6).

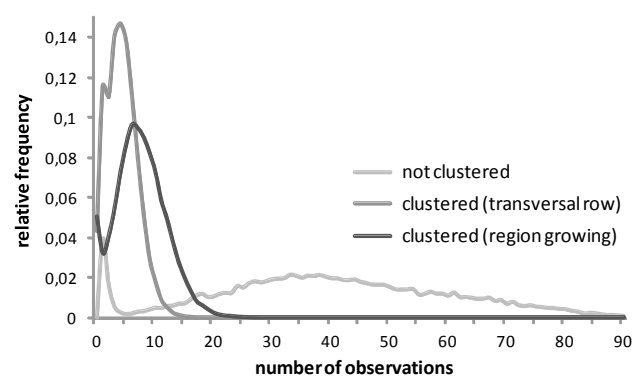


Fig. 6. Observations to be processed by tracking (comparison of the approaches)

Accordingly, the number of tracks that exist at a time is reduced as well. As the reference system handles 67.6 tracks with a standard deviation of 34.5 on average, the system under test only processes 10.0 tracks with a standard deviation of 5.5 on average (see Fig. 7). In comparison to this, the algorithm that searches for observations in a transversal row holds 6.1 tracks on average.

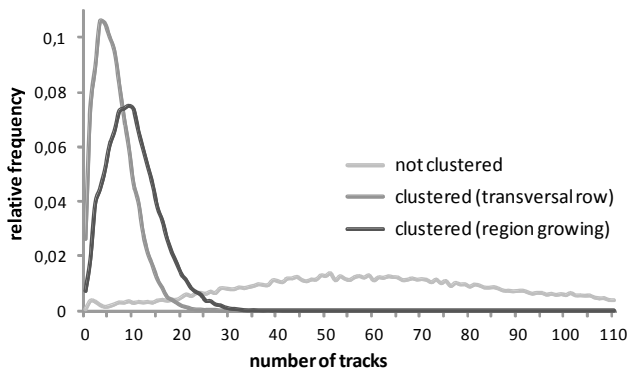


Fig. 7. Number of existing tracks (comparison of the approaches)

The noticeable reduction of the number of tracks arising results from merging observations and from rejecting undersized clusters. Hence, there is no difference in this compared to the approach presented first. However, considering the size of the clusters that are formed (illustrated in Fig. 8), it turns out that the second, more general approach (that simply assumes similarity) not only tends to generate more, but also larger clusters. Consequently, it detects more groups of observations belonging together, even such not being located in a transversal row.

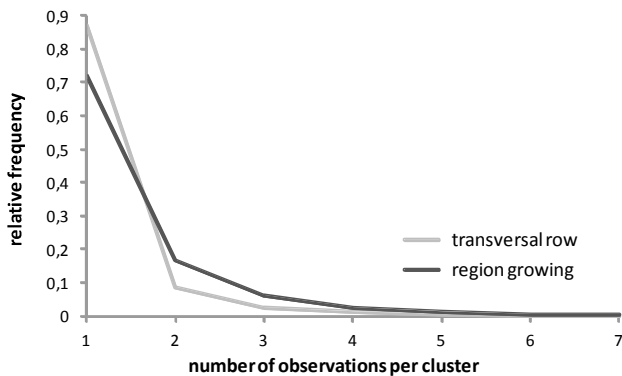


Fig. 8. Number of assigned observations per cluster (comparison of the approaches)

But the enhancement of the recognition performance is achieved by a more expensive algorithm. Whereas the simple approach requires relatively few, one-dimensional comparisons, the Region Growing based algorithm includes a lot of high-dimensional distance calculations caused by the iterated search for the most similar pair of clusters. However, the approach already implies an association of tracks and observations. This is to the benefit of the object tracking as its step of assignment can be omitted. Assigned and not assigned observations can immediately be used to correct tracks or to induce new ones, respectively. Hence, the second clustering algorithm nevertheless is able to speed up the whole process of object recognition by an average factor of 6.3 (see Fig. 9) compared to the reference system.

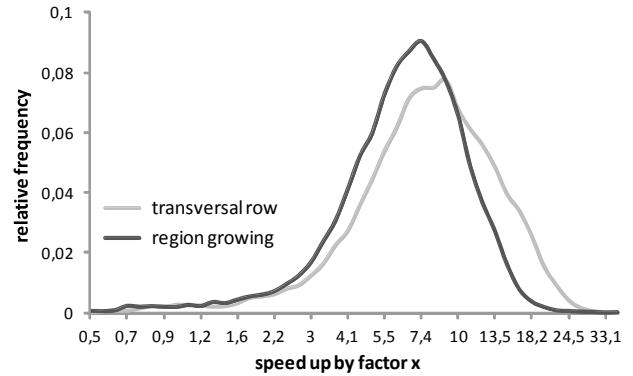


Fig. 9. Speed up of the tracking achieved by the clustering (comparison of the approaches)

In terms of efficiency the second approach is even superior to the first one. Considering the relative computational effort required per track, the Region Growing based approach is 36.5 percent faster than the search for transversal rows of observations. Should the system nevertheless exceed the computational effort that is allowed, the abort criterion of the clustering step offers the opportunity to make adjustments. In addition, it achieves qualitatively better results than the systems compared with do.

## V. CONCLUSION

Within the scope of the present work, the possibility was discussed to improve the tracking of extended objects by means of observation clustering. The given object tracking system used for evaluation is part of an automotive object tracking project and aims to detect and track vehicles driving ahead by utilizing the detections of an automotive FMCW multi-beam radar. Like many others, it relies on the assumption of point objects. Hence, it is affected by the targets' multi-point characteristics in such a way that the system is slowed down distinctly and that various tracks per object arise.

With the aim of avoiding those problems, two clustering approaches for radar-based object tracking have been presented in this paper. Thereby, the basic idea was to reduce the number of observations to a minimum passed on to the tracking algorithm by consolidating those caused by the same objects and by detecting detached observations.

The first approach takes advantage of the knowledge that the rear of vehicles driving ahead causes several detections in a transversal row and searches for them. The second approach described adapts and extends the idea of Region Growing aiming to conflate groups of similar detections. Thereby, it utilizes already existing tracks in order to initialize the clustering. Moreover, the clustering algorithm undertakes the task of associating observations and tracks as well.

Both approaches were implemented within the object tracking system mentioned above and were evaluated. That could prove that the clustering approaches presented here are

able to reduce the tracking's computational effort distinctly and, in addition, to yield better tracking results. The tracks remaining are more stable because they are rarely affected by faulty measurements and because observations belonging together are seldom distributed among various tracks. An additional step can be omitted that merges tracks caused by identical objects. However, the system without the clustering has to consider all observations first and to track them for a while in order to sort out invalid ones. It also happens more often that an object is represented by several tracks.

## VI. FUTURE WORK

Future work will aim to test alternative similarity measures for the approach based on Region Growing and will aim to optimize the algorithm's search for the most similar pair of combinable clusters in order to further improve and speed-up the whole tracking system. Another enhancement may be to replace the radar sensor used by one that also delivers a radar peak's power value. With that the clustering would be enabled to weight observations in accordance with their reliability.

## REFERENCES

- [1] R. E. Kalman, "A New Approach to Linear Filtering and Prediction Problems", *Transactions of the ASME, Journal of Basic Engineering*, Baltimore, United States of America, 1960, pp 35-45.
- [2] S. S. Blackman and R. Popoli, "Design and Analysis of Modern Tracking Systems", Norwood, MA: Artech House, 1999.
- [3] E. L. Haseltine and J. B. Rawlings, "Critical Evaluation of Extended Kalman Filtering and Moving-Horizon Estimation", *Ind. End. Chem. Res.* 2005, American Chemical Society, 2004, pp 2451-2460.
- [4] Y. Bar-Shalom and X.-R. Li, "Multitarget-Multisensor tracking: Principles and Techniques", Storrs, CT. YBS Publishing, 1995.
- [5] C. A. R. Hoare, "Quicksort", *The Computer Journal* 5(1), London, United Kingdom, 1962, pp 10-16.
- [6] B. Fardi, "Multisensorgestützte Bildverarbeitung zur Erkennung und Lokalisierung von Fußgängern im Fahrzeugumfeld", Shaker, Aachen, Germany, 2008, pp 63-65.
- [7] A. K. Jain, „Fundamentals of digital image processing“, Prentice-Hall, Englewood Cliffs, United States of America, 1989.
- [8] A. Tyagi and M. A. Bayoumi, "Image segmentation on a 2-D array by a directed Split and Merge procedure", *IEEE Transactions on signal processing*, Vol. 40, No. 11, 1992.
- [9] L. Gao, F. Pan and X. Li, "A New Fuzzy Unsupervised Classification Method for SAR Images", *International Conference on Computational Intelligence and Security*, Guangzhou, China, November 2006, Vol 2, pp 1706-1709.
- [10] D. Ma, A. Zhang, "CoreTracking: an efficient approach to clustering moving targets and tracking clusters", *Proceedings of the IEEE Radar Conference*, Philadelphia, United States of America, April 2004, pp 117-122.
- [11] Y. Zhang, H. Liu, W. Fu and H. Deng, "Multi-radar tracking based on weighted k-means clustering fusion", *IEEE International Conference on Granular Computing*, Hangzhou, China, August 2008, pp 813-816.
- [12] W. Xu and I. Cumming, "A Region-Growing Algorithm for InSAR Phase Unwrapping", *IEEE Transactions on Geoscience and Remote Sensing*, Edinburgh, United Kingdom, January 1999, Vol 37.
- [13] L. Chang, Z. S. Tang, S. H. Chang, Y.-L. Chang, "A region-based GLRT detection of oil spills in SAR images", *Pattern Recognition Letters* 29, Elsevier B.V., 2008, pp 1915-1923.

# Data Fusion of Thermal IR and Visible Light Video Sensors for a robust Scene Representation

Jan Thomanek, Holger Lietz, and Gerd Wanielik

Professorship of Communications Engineering, Chemnitz University of Technology  
Reichenhainer Str. 70, 09126 Chemnitz, Germany  
E-Mail: jtho@hrz.tu-chemnitz.de

**Abstract**—The proposed technique addresses a fusion of two imaging sensors, a thermal far-infrared camera and a visible light camera. The complementary nature of both sensors will result in a scene representation which is robust against illumination changes and weather conditions. Thus, the combination of the advantages of each camera will extend the capabilities for many computer vision applications, such as video surveillance and automatic object recognition. The presented pixel-based fusion technique is based on a multi-resolution decomposition. The two sensor images are first decomposed using the Dyadic Wavelet Transformation. The transformed data are combined in the wavelet domain controlled by a “goal-oriented” fusion rule. Finally, the fused wavelet representation image will be processed by the object detection system. Experimental results show that the proposed method improves an object detection performance under various environmental conditions.

**Index Terms**—image registration, pixel-based data fusion, dyadic wavelet transform, pedestrian recognition

## I. INTRODUCTION

The increasing variety of information acquisition techniques requires an increasing number of intelligent data fusion systems. *Data Fusion* is defined as the process of combining information from several sensors to provide a complete view of the environment in many applications. Similar to the human who uses all his senses simultaneously, data fusion systems use the process of combining substantial information from several sensors to provide a more accurate description of an observed scene than any of the individual sensor. Multi-sensor data fusion can be realized on different levels of representation [1]: Signal-level fusion refers to the direct combination of several signals. Pixel-level fusion generates a fused image in which each pixel is determined from a set of pixels in each source image. Feature-level fusion first employs feature extraction on the source data so that features from each source can be jointly employed for certain purposes. Symbol-level fusion allows

combining information from multiple sensors based on a decision rule.

Particularly for imaging sensors, e.g. visible light cameras or infrared cameras, is it advantageously to fuse on pixel-level or also called image-level. The goal of image fusion is to generate a single composite image by combining substantial information from the input sensor images using mathematical techniques. The fused image provides a better representation of the observed scene which is more useful for the human or following machine perception tasks, e.g. object recognition and classification. Therefore, pixel-based data fusion appears to be an essential pre-processing step for a various number of applications. A state-of-the-art overview of different Pixel-Level fusion techniques is given in [1] and [2].

The proposed image fusion scheme to combine far-infrared and visible light camera images is used to enhance a pedestrian detection system with respect to a robust detection in different conditions of illumination and background. The algorithm flow is depicted in Fig. 1.

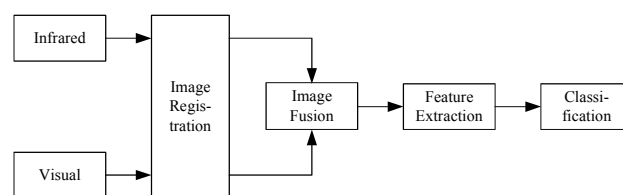


Fig. 1. Algorithm flow

This paper is organized as follows: Section 2 describes the essential image registration method applied on the sensor images so that both camera images will be in spatial alignment. In section 3 the used fusion techniques are presented. Section 4 describes the used features and classification algorithm for the pedestrian recognition system. Section 5 provides and compares results of the pedestrian detection using the fusion method.

## II. IMAGE REGISTRATION

An important pre-processing step for pixel-based fusion is the precise spatial alignment of the infrared and visual image, so that the corresponding pixels in both images represent the same location in real world. Usually this task is referred to as *Image Registration*.

Geometric transformations based on feature correspondences are often used to perform image registration which also allows compensation for distortion due to images taken from different viewpoints [3]. Though, these geometrical transformations are based on 2D point correspondences and map one image onto the other without taking into account the 3D viewing geometry of both cameras. Since objects in the observed scene may appear in different distances, one transformation for each distance plane is necessary for precise image registration. Therefore, we use *Image Rectification* to transform both camera geometries into a common stereo system with parallel optical axes (Fig. 2). Thereby, a perspective transformation projects the planes of the observed scene onto images which are tilt-free and of the desired scale.

The main objective in image rectification is to generate parallel *epipolar lines* (in our case vertical epipolar lines). Because of the geometry imposed by the camera viewpoints, the location of any point in one image constrains the location of the point in the other image to a line. This is called the *epipolar constraint*. After rectification, the epipolar lines run parallel with the y-axis and match up between both cameras. Hence, the disparities between the images disappear at least in one direction. To minimize the disparities in the other direction, we mounted both cameras as close as possible.

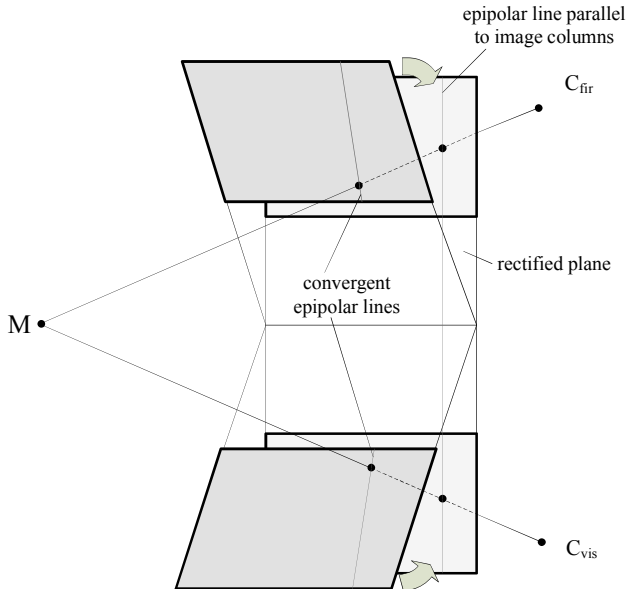


Fig. 2. Using two projective transformations to get images as if obtained by cameras with parallel optical axes

There are many ways to compute the rectification terms. We used Fusiello's algorithm [5] which can yield non-calibrated

stereo using *fundamental matrix* [4] only, in which rectification is achieved by a suitable rotation of both image planes. His approach can be regarded as seeking an approximation for the plane at infinity as the reference plane. The fundamental matrix of our rectified system (we mounted the FIR camera above the visual light camera) must have the specific form

$$F_{rec} = [\mathbf{u}_2]_{\times} = \begin{bmatrix} 0 & 0 & 1 \\ 0 & 0 & 0 \\ -1 & 0 & 0 \end{bmatrix} \quad (1)$$

It is the skew-symmetric matrix associated with the cross product of the vector  $\mathbf{u}_2 = [0 \ 1 \ 0]^T$ . With  $H_{fir}$  and  $H_{vis}$  as the unknown rectifying transformations and  $\{\mathbf{m}_{fir}^n, \mathbf{m}_{vis}^n\}$  as the point correspondences, we get according to the epipolar constraints

$$\left(H_{vis} \mathbf{m}_{vis}^n\right)^T [\mathbf{u}_2]_{\times} \left(H_{fir} \mathbf{m}_{fir}^n\right) = 0 \quad (2)$$

This equation must be valid for all observed corresponding points.  $N$  point correspondences lead to  $N$  non-linear equations in the unknown entries of  $H_{fir}$  and  $H_{vis}$ . However, the algebraic error on the left side in (2), which has to be minimized, is neither geometrically nor statistically meaningful. Therefore, according to Fusiello's approach, we used the *Sampson error* as the first-order approximation of the geometrical re-projection error:

$$\sum_n \frac{\left(\mathbf{m}_{vis}^n{}^T F \mathbf{m}_{fir}^n\right)^2}{\left(F \mathbf{m}_{fir}^n\right)_x^2 + \left(F \mathbf{m}_{fir}^n\right)_y^2 + \left(F^T \mathbf{m}_{vis}^n\right)_x^2 + \left(F^T \mathbf{m}_{vis}^n\right)_y^2} \quad (3)$$

where

$$F = H_{vis}^T [\mathbf{u}_2]_{\times} H_{fir} \quad (4)$$

denotes the fundamental matrix between the original images. The minimization of the geometric cost function in (3) is done by using an iterative technique based on a non-linear minimization algorithm. The parameterization of each rectifying transformation is based on

$$H = K_{rec} R K_{orig}^{-1} \quad (5)$$

The original intrinsic parameters of both cameras can be obtained by separate camera calibration or they can be estimated: principal point in the centre of the image, no skew and aspect ratio is equal to one. The focal length is unknown and will be part of the parameterization vector. The new intrinsic parameters of the rectified images can be set

arbitrarily, whereas horizontal focal length and the x component of the principal point are identical. For the 3-dimensional rotation matrices the angles about the axes used as unknown parameters except rotation about y-axes of the FIR camera. Finally, the rectifying transformations are parameterized by seven unknowns: two focal lengths and five angles (Fig. 3).

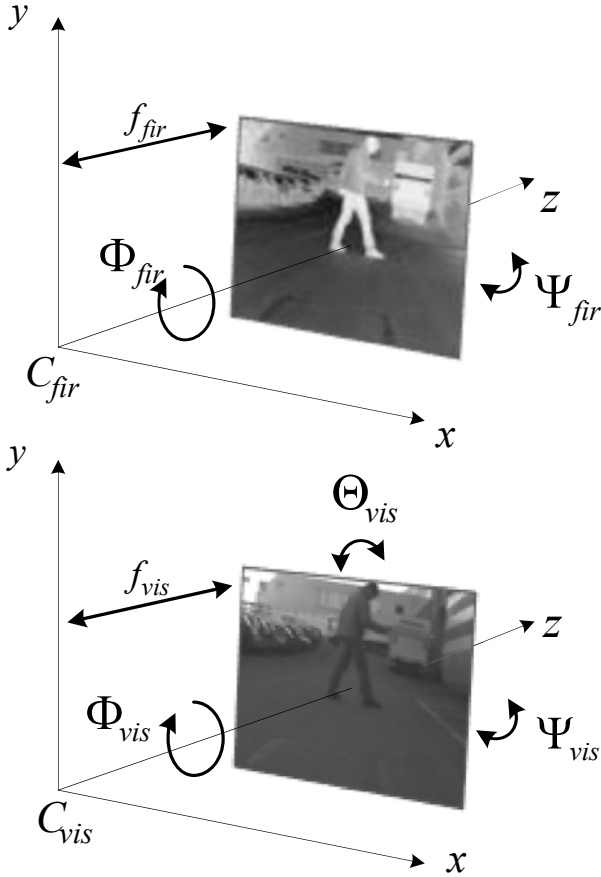


Fig. 3. Degrees of freedom in choosing the rectifying transformation

### III. PIXEL-LEVEL FUSION

#### A. Motivation

As already mentioned, the object of pixel-based fusion is to create a composite image that is more suitable for the purpose of computer vision tasks such as feature extraction and object recognition. In many scenarios, far-infrared cameras are more suited for detection of pedestrian than the visual light ones, especially if the background is colder than the human. But the FIR camera will fail the detection of pedestrians in case of hot and sunny weather. Therefore, the combination of far-infrared and visual images through pixel-based fusion should extend the capability of the detection system [6]. Ideally, the fused image shows the contour of a pedestrian in all different weather conditions, but it should suppress textures on the pedestrian clothes which are not relevant for classification.

There are many different pixel-based fusion algorithm and techniques. The use of a special fusion method depends on the application that will employ the fusion results. In this case, we want to improve the number of correct classifications of a pedestrian recognition system which based on the detection and classification of the distinctive shape of a human. That means the fused image should provide a complete contour of a pedestrian to enhance the classification results.

#### B. Multiresolution Image Fusion by Wavelet Transform

To preserve the contours of people, the sensor images are transformed into the frequency domain because edges are locations of high frequency in the image and more clearly depicted than in the spatial domain. We use for this transformation a wavelet-based approach from a multi-resolution (multiscale) point of view. The multiscale theory is concerned with the representation of images at more than one resolution. One advantage of this technique is the robustness against misinterpretations due to noisy data. Only edges, which can be detected in all scales, can be considered as real edges and will be taken into the fused image. Furthermore, the multiscale approach allows the characterization of edges, e.g. step-edges or Dirac-edges. Thus, for the fusion only step-edges are selected which can be caused by a rough outline of a human contour. However, spike-edges are often caused by noise or image texture and hence not relevant for the pedestrian detection and classification.

The rectified input images are decomposed into the frequency bands of different scales by a wavelet transform  $\Psi$ . The decomposed images in the frequency (wavelet) domain will have the same size as the input image. These wavelet representations are combined using some kind of fusion rule  $\Theta$ . An inverse transformation of the fused representation is not necessary, since the transformed domain will be used for the feature extraction (Fig. 4).

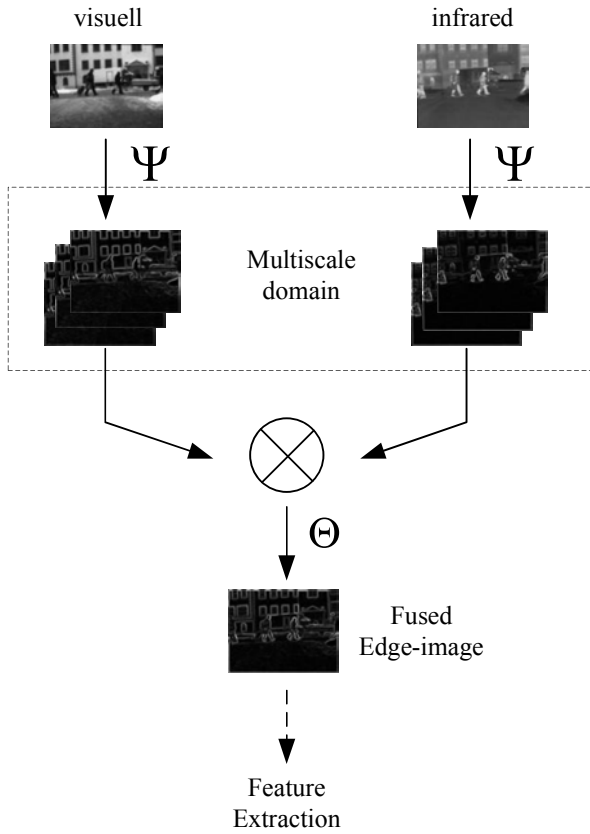


Fig. 4. Fusion scheme based on multiresolution decomposition

There are numerous types of wavelets transforms used for the multiresolution decomposition. The first is the *Continuous Wavelet Transform* (CWT). Despite its name, it can be calculated on discrete data, as well, in which all possible scaling factors are used. Consequently, the CWT is computationally expensive and for most application a dyadic approach is used instead. In the *Dyadic Wavelet Transform* (DWT): Since the image is smoothed by a filter during transformation, it only contains half of frequency information on the next scale. Hence, the image can be downsized at each level to suppress redundant information. But that downsampling process yields to a shift variant signal representation which is not suitable for edge detection applications. Therefore, we use the straight dyadic wavelet transform without this optimization.

To get the singularities of an image, the corresponding wavelet should be the first derivative of the signal measured on different resolution of the input image. In [7], Mallat notes that this is the case when the wavelet  $\psi$  is the derivative of a smoothing operator  $\theta$ . In case of an image as 2D-signal, the wavelets are the partial derivatives of the smoothing function:

$$\psi_x = -\frac{\partial\theta}{\partial x} \quad \text{and} \quad \psi_y = -\frac{\partial\theta}{\partial y} \quad (6)$$

In two directions, the dyadic wavelet transform of the image signal  $f(\mathbf{x})$  with  $\mathbf{x} = (x, y)$  at  $\mathbf{u} = (u_x, u_y)$  is

$$\begin{aligned} f^{\psi_x}(\mathbf{u}, 2^j) &= \langle f(\mathbf{x}), \psi_{x,2^j}(\mathbf{x} - \mathbf{u}) \rangle = f * \bar{\psi}_{x,2^j}(\mathbf{u}) \\ f^{\psi_y}(\mathbf{u}, 2^j) &= \langle f(\mathbf{x}), \psi_{y,2^j}(\mathbf{x} - \mathbf{u}) \rangle = f * \bar{\psi}_{y,2^j}(\mathbf{u}) \end{aligned} \quad (7)$$

where

$$\psi_{x,2^j}(\mathbf{x}) = 2^{-j} \psi_x(2^{-j} \mathbf{x}) \quad \text{and} \quad \bar{\psi}_{x,2^j}(\mathbf{x}) = \psi_{x,2^j}(-\mathbf{x}) \quad (8)$$

Derived from (6) and (7), the wavelet transforms  $f^{\psi_x}, f^{\psi_y}$  of an image signal  $f$  can be interpreted as the derivative of a smoothed version of  $f$  convolved with  $\theta$  on the scale  $j$  of the dyadic sequence  $\{2^j\}_{j \in \mathbb{Z}}$ :

$$\begin{aligned} f^{\psi_x}(\mathbf{u}, 2^j) &= 2^j \frac{\partial}{\partial u_x} (f * \bar{\theta}_{2^j})(\mathbf{u}) \\ f^{\psi_y}(\mathbf{u}, 2^j) &= 2^j \frac{\partial}{\partial u_y} (f * \bar{\theta}_{2^j})(\mathbf{u}) \end{aligned} \quad (9)$$

where

$$\theta_{2^j}(\mathbf{x}) = 2^{-j} \theta(2^{-j} \mathbf{x}) \quad \text{and} \quad \bar{\theta}_{2^j}(\mathbf{x}) = \theta_{2^j}(-\mathbf{x}) \quad (10)$$

That means, at the first scale  $j=1$ , the image is smoothed by convolving with the smoothing function  $\theta$ . At the next scale, the smoothing function is stretched by inserting zeros into the convolution kernel, and the image is convolved with it again. The process is repeated for a defined number of scales. At each scale, the wavelet coefficients are obtained by convolution with the wavelet filter kernel. Both, the wavelet and smoothing filtering is done using separate 1D-filter vertically and horizontally. Currently, we use the *Haar-Wavelet*, which is the derivative of a triangular hat function. Hence, the non-normalized convolution kernels of  $\theta$  and  $\psi$  on the first scale are  $[1 \ 2 \ 1]$  and  $[1 \ -1]$  resp.

The described transform can be referred to as one option of a *Multiscale Edge Detection*. The decomposition process is illustrated in Fig. 5.

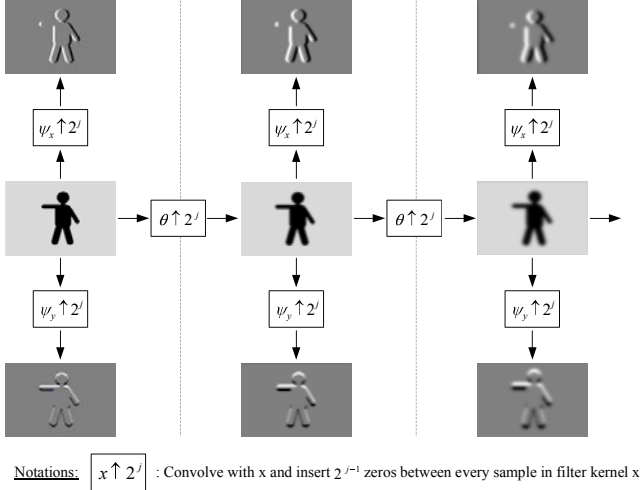


Fig. 5. Multiscale decomposition by dyadic wavelet transform

### C. Fusion Rules

After the decomposition of both far-infrared and visual images, the wavelet coefficients will be combined to obtain a single wavelet representation. The main component that controls the fusion is the *Activity Level Map*. There are separated maps for every sensor and each direction. The activity level  $a$  is used as a degree to which each coefficient is important for application. Thus, the wavelet coefficients of that input image on a defined position are taken for the fused representation, which has the higher activity level on that position. Since the fused wavelet representation is just a one-scale representation, the wavelet coefficients on the different scales of the input images are combined by a weighted summation:

$$f_{fus}^{\psi}(\mathbf{x}) = \begin{cases} \sum_j f_{fir}^{\psi}(\mathbf{x}, j) \cdot \alpha_j, & \text{if } a_{fir}(\mathbf{x}) \geq a_{vis}(\mathbf{x}) \\ \sum_j f_{vis}^{\psi}(\mathbf{x}, j) \cdot \alpha_j, & \text{if } a_{fir}(\mathbf{x}) < a_{vis}(\mathbf{x}) \end{cases} \quad (11)$$

The calculation of the activity level maps is the pivotal role of the fusion process and depends on three factors:

- Noise elimination of the wavelet representations
- Find local maximum modulus of wavelet coefficients
- Characterization of edges

For example, the activity level on a defined position has a high value if there is a maximum modulus of wavelet coefficient, the signal-to-noise ratio is high enough and the corresponding wavelet coefficient does not represent just a funnel or spike.

Noise elimination is one of the important applications of the wavelet transform. It can be accomplished by a simple thresholding which means, setting to zero the activity level whose corresponding absolute value of the wavelet coefficient is lower than the threshold. The statistician D. L. Donoho [8] recommend a threshold that depends on the number of

coefficients:

$$\tau = K \cdot \sqrt{2 \cdot \ln(N)} \cdot \sigma \quad (12)$$

where  $K$  is a constant of magnitude 1,  $N$  the number of wavelet coefficient which corresponds with number of pixels in the image, and  $\sigma$  denotes the standard deviation of the noise. Donoho notes that the most of the wavelet coefficients on the finest scale with diagonal orientation are caused by noise. Therefore, we calculate the standard deviation from the median of the finest-scale wavelet coefficients which have both vertical and horizontal components.

As observed above, local maximum modulus wavelet coefficients correspond with strong edges in the image. Usually, the second derivative is used to find them. However, in our implementation, a coefficient is a modulus maximum if it is larger than its neighbors within a defined window. All activity levels on the corresponding positions are set to zero if there is no local modulus maximum.

The multiscale approach allows extracting a lot of information about the edges. The singularities can be categorized into three basic geometric structures [9]: step-structure, roof-structure and Dirac-structure. To characterize these structures, it is necessary to quantify the local regularity of a signal. The *Lipschitz exponent*  $\alpha$  provides uniform regularity measurement over an interval. A function  $f$  is said to be uniformly Lipschitz  $\alpha$  over an interval if there is some constant  $K$  so that:

$$|f(x_1) - f(x_2)| \leq K |x_1 - x_2|^\alpha \quad (13)$$

Mallat showed in [9] that the Lipschitz regularity is related to the wavelet transform and that if the wavelet transform is Lipschitz  $\alpha$ :

$$|f^{\psi}(\mathbf{u}, 2^j)| \leq K(2^j)^{\alpha+1} \quad (14)$$

The Lipschitz regularity of the edge is estimated with (14) by measuring the slope of  $\log_2 |f^{\psi}(\mathbf{u}, 2^j)|$  as a function of  $j$ .

That means every kind of edge has its typical progression across the scales. However, it is difficult to apply the inequality (14) to detect edges directly in practice. Therefore, it is more convenient to analyze the properties of the wavelet transform of the basic edge structures. The wavelet transform of a step-edge at position  $x_0$  is a nonzero constant which is independent on the scale and has the equal sign on both sides of the neighborhood of  $x_0$ . On the other hand, the wavelet transform of a spike-edge at position  $x_0$  has two local maxima on both sides of the neighborhood of  $x_0$  with opposite signs (see Fig. 6). The mathematical proof is given in [10]. Hence, our implementation checks the wavelet coefficient distribution within a window around the detected local maximum modulus of the wavelet transform and compares it with the properties of the basic edge structures. Then, the activity level is set to zero if the distribution correlates to the properties of a spike-edge.

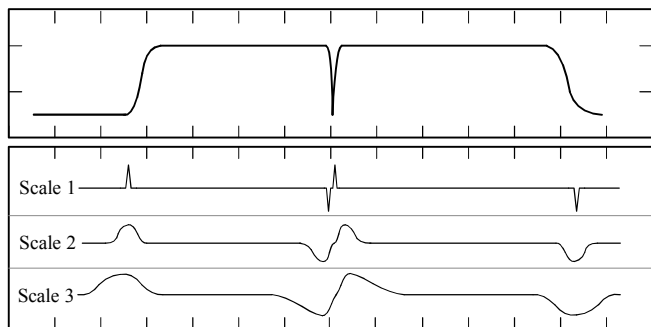


Fig. 6. Artificial 1-D signal and its wavelet transform

Finally, after the generation of separate fused wavelet representations for the horizontal and vertical direction, the modulus of wavelet transform of the fused image can be calculated by

$$M(\mathbf{x}) = \sqrt{\left|f_{fus}^{W_x}(\mathbf{x})\right|^2 + \left|f_{fus}^{W_y}(\mathbf{x})\right|^2} \quad (15)$$

The angle of the wavelet transforms is calculated using the formula:

$$A(\mathbf{x}) = \arctan\left(\frac{f_{fus}^{W_y}(\mathbf{x})}{f_{fus}^{W_x}(\mathbf{x})}\right) \quad (16)$$

The angle of the wavelet transform is discretized into nine sectors, by which we obtain a discrete image with nine gradient directions. Both, the modulus wavelet image and the orientation image are starting points for the feature extraction and classification which is briefly described in the next chapter. The complete fusion rule scheme is shown in Fig.7.

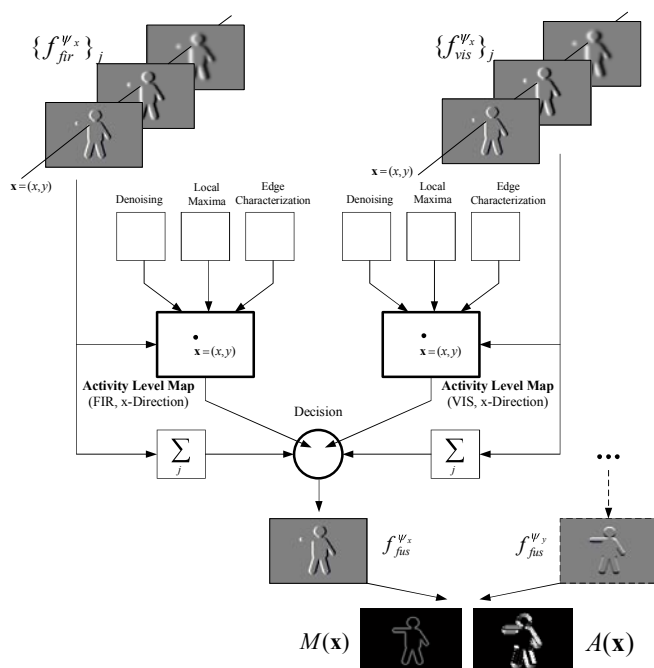


Fig. 7. The fusion rule scheme

#### IV. FEATURE EXTRACTION AND CLASSIFICATION

##### A. Feature Extraction

Our pedestrian detection system uses normalized *Histograms of Oriented Gradients* (HoGs) which were introduced by Dalal and Triggs [11]. The main conception of the HoGs is that objects within an image can be described by the distribution of intensity gradients and edge directions. The big advantage of the HoG features is its translation and illumination invariance. According to the wavelet orientation image, nine discrete directions were chosen for each histogram. Dalal combined four histograms to one block which induced 36 features per block. With 56 different block positions and sizes, we obtain a feature vector of 2016 elements. Such a feature vector is calculated for each *Region of Interest* (ROI) extracted from the image. There are different ROI sizes and position. Currently, more than 5000 ROIs per image frame are extracted. The feature extraction process is shown in Fig. 8.

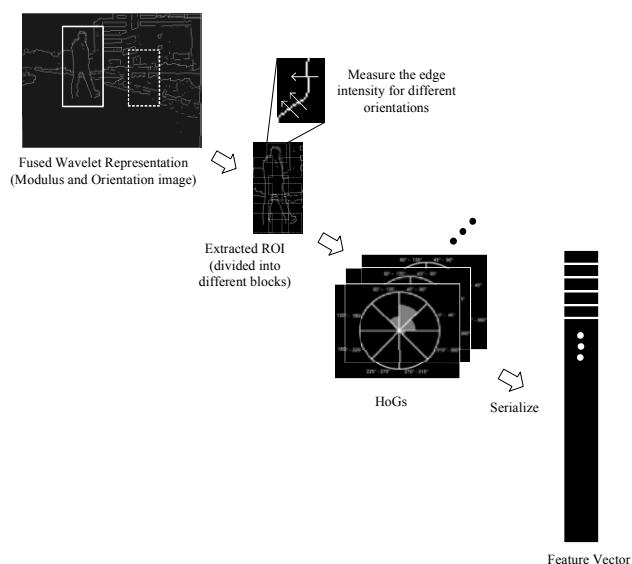


Fig. 8. The Feature Extraction Process

##### B. Classification

The extracted feature vector is classified using a trained classifier cascade which has been introduced by Viola and Jones [12]. It consists of a series of *AdaBoost* classifiers [13] which contains several decision trees as weak learner. The cascade output is positive if the ROI matches a pedestrian shape and the output will be negative if not. The cascade algorithm reports a region as pedestrian only if it has passed all its stages, but it can reject a ROI at any stage (Fig. 9). This leads to a dramatic performance boost, since the majority of the ROIs are usually non-pedestrians, where most of them are rejected in early cascade stages.

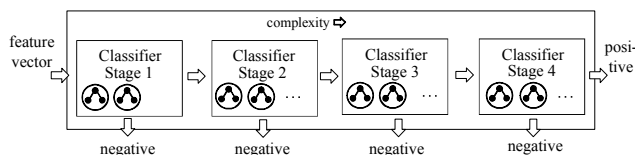


Fig. 9. Overall structure of the cascade classifier

## V. EXPERIMENTS AND RESULTS

The approached pixel-based fusion algorithm to combine far-infrared and visual light sensors was examined on several image sequences captured under different weather and illumination conditions. These sequences contain typical city centre scenes with pedestrians, vehicles, buildings etc. recorded in winter and summer, as well.

First, the far-infrared and the visual light image frames were transformed into the rectified plane. The corresponding rectification terms were calculated by an offline calibration step according to the procedure described in section 2. Then, the images were combined by the presented pixel-based fusion scheme. Finally, the fused stream was applied on the pedestrian detection system. Before, the classifier was trained using a learning set which based on pedestrian examples generated by the proposed fusion scheme.

To evaluate the results obtained from the fused sensor stream, common performance measures for classification are used: *Detection Rate* and *False Alarm Rate*. The detection rate specifies the ratio between the number of detected pedestrians and the number of maximum recognizable pedestrians. The false alarm rate gives the ratio between the number of incorrect pedestrian forecasts and the total number of extracted ROIs which do not contain any pedestrian. We calculated the detection rate and the false alarm rate for the sequences based on a single sensor and for the fused sequences, as well.

Actually, the fused image streams yield the best detection rate in all seasons and different weather condition. It is obvious, regarding to the proposed fusion method, the algorithm always picks up the best information for every frame, i.e. the stronger edges are taken into the fused image. Those results in clear and complete human shapes which can be more precise distinguished from non-pedestrian objects and can be easier to classify, consequently. In other words, the fused image exploits the advantages of both sensor images. For example, at night or on winter days when the background is colder than the humans, the fused image will surely contain the most information from the far-infrared sensor. But in contrast to that, on sunny days, the pedestrians are often not visible in the far-infrared image and the fused image is nearly exclusively obtained from the visual light camera data. Furthermore, in many cases, both sensors fail the pedestrian detection because the human outline is not complete enough using a single sensor. For example, there is a good contrast between human head and background and a bad contrast of human body caused by warm winter clothes in the FIR image. On the other side, there is a good contrast of the body in the visual light image but the head is not visible there. Hence, only

the pixel-based data fusion will provide a complete human contour that can be classified as pedestrian. Fig. 10 illustrates representative examples which demonstrate the described issue.

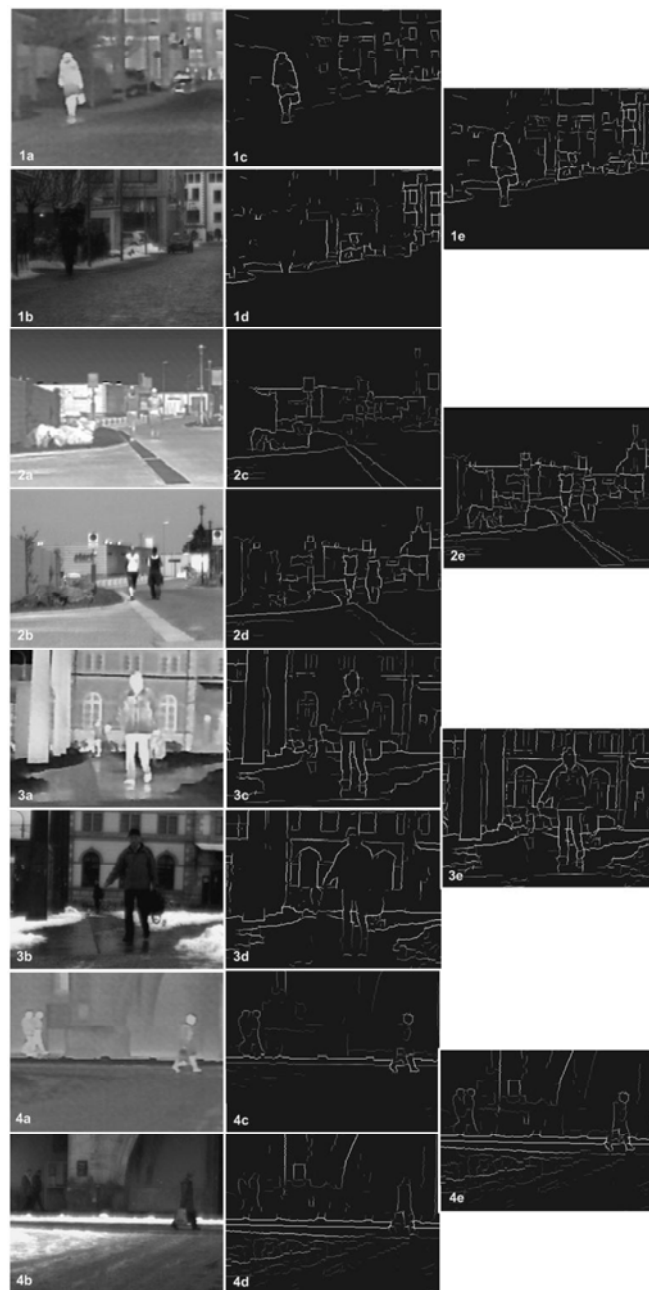


Fig. 10. Examples:

a: FIR image, b: Visual light image, c: FIR modulus wavelets transform representation, d: Visual light modulus wavelet transform representation, e: Fused modulus wavelet transform representation

- (1) Bad illumination conditions: pedestrian not visible in the visual light image – fused image contains information from the far-infrared image
- (2) Hot and sunny day – far-infrared sensor fails pedestrian detection – Fused images contains information from the visual light image
- (3) Single sensors fail detection because human shape not complete – Fused image contains information from both sensors
- (4) Single sensors fail detection because human shape not complete – Fused image contains information from both sensors

## REFERENCES

- [1] Blum, R. S., Xue, Z., Zhang, Z.: Multi-Sensor Image Fusion and Its Applications, Taylor & Francis Group, 2006
- [2] Stathaki, T., Image Fusion: Algorithms and Applications, Academic Press, London, Amsterdam, Burlington, San Diego, 2008
- [3] Goshtasby, A., 2-D and 3-D image registration for medical, remote sensing and industrial applications. John Wiley & Sons, Inc., Hoboken, New Jersey, 2005.
- [4] Hartley, R., Zisserman, A., Multiple View Geometry in computer vision. Second Edition. Cambridge University Press, 2003.
- [5] Fusiello A., Irsara L. Quasi-euclidean uncalibrated epipolar rectification. Research Report RR 43/2006, Dipartimento di Informatica - Università di Verona, 2006.
- [6] Bertozzi, M., Broggi A., Felisa, M., Ghidoni, S., Grisleri P., Vezzoni, G., Gómez, C. H., Del Rose, M.: Multi Stereo- Based Pedestrian Detection by Daylight and Far-Infrared Cameras. In: Augmented Vision Perception in Infrared: Advances in Pattern Recognition, p. 371-401, Springer, London, 2009
- [7] Mallat, S., A Wavelet Tour of Signal Processing. The Sparse Way. Third Edition. Academic Press, London, Amsterdam, Burlington, San Diego, 2009
- [8] Donoho, D. L., Nonlinear wavelet methods for recovery of signals, densities and spectra from indirect and noisy data, Proc. Symposia in Applied Mathematics, American Mathematical Society, 1993
- [9] Mallat, S., Zhong, S., Characterization of signals from multiscale edges. IEEE Transactions on Pattern Analysis and Machine Intelligence, 14(7):710-732
- [10] Tang, Y. Y., Wavelet Theory Approach to Pattern Recognition. Second Edition. Series in Machine Perception and Artificial Intelligence – Vol. 74, World Scientific Publishing Co. Pte. Ltd., 2009
- [11] Dalal, N., Triggs, B.: Histograms of Oriented Gradients for Human Detection. In: Proceedings of the IEEE Conference on Computer Vision and Pattern Recognition, Vol. II, pp. 886-893, 2005
- [12] Viola, P., Jones, M.: Rapid Object Detection using a Boosted Cascade of Simple Features. Proceedings of the IEEE Computer Society Conference on Computer Vision and Pattern Recognition - Volume 1, p.511, 2001
- [13] Freund, Y., Schapire, R.E.: A Decision-Theoretic Generalization of Online Learning and an Application to Boosting. In: Proceedings of the European Conference on Computational Learning Theory, pp. 23-37, 1995

# Propagation Effects in Satellite Mounted Radar Remote Sensing

(Invited Paper)

Andreas Danklmayer

DLR e.V. (German Aerospace Center)  
Microwaves and Radar Institute  
82234 Wessling, Oberpfaffenhofen  
Germany  
Email: Andreas.Danklmayer@dlr.de

**Abstract**—Space-borne Synthetic Aperture Radar (SAR) imaging is often considered to possess both day/night and all weather operational capabilities. However, as the operating frequencies of SAR-systems are increasing, visible image distortions due to heavy precipitation in SAR-images may become present. This holds especially for the case of convective rain events imaged at X-band frequencies and beyond. These rain-cell signatures are thoroughly investigated, and the physical background of the related propagation effects is provided. A review of rain cell signatures from former missions like SIR-C/X-SAR and the Shuttle Radar Topography Mission is given. Furthermore, the German spaceborne satellite TerraSAR-X delivered several measurements, which facilitate to study precipitation effects in SAR images. Based on these SAR images and simultaneously acquired weather radar measurements, a quantitative estimation of precipitation effects in SAR images is presented. In a further step, an attempt is made to extrapolate the effects observed in X-band SAR images to images acquired at higher nominal frequency bands such as Ka-band.

## I. INTRODUCTION

The philosophy and intention of this article is to give first an introduction to the basic image formation concept of Synthetic Aperture Radar (SAR) and its diverse applications. Then we will focus on the specific aspects related to microwave propagation in the atmosphere. This will hopefully make the presented material beneficial for young scientists entering to the field. Experts from other domains not familiar with the basic concepts will hopefully also gain from the introduction, which is necessary in order to understand the context for the more recent findings treated afterwards. In the following we itemize the aspects which are covered in this tutorial article:

- Synthetic Aperture Radar basic image formation concept and applications
- Review of relevant propagation effects
- Probability of rain induced effects in X-band
- Physical interpretation of rain cell signatures in SAR images
- Modelling of rain cell signatures in SAR images
- Short summary and conclusions

## II. ESSENTIAL BASICS OF SYNTHETIC APERTURE RADAR

Synthetic Aperture Radar represents a two-dimensional radar imaging technique based on active remote sensing of

the Earth or other planets. In contrast to optical sensors, SAR is independent of day- and nighttime and can penetrate through clouds. However, as will be shown, SAR can be affected by propagation effects through heavy rain under adverse weather conditions. Nowadays, SAR is widely used for remote sensing of the Earth using air- and spaceborne platforms. Storage of the phase history allows for synthesis of a large synthetic aperture which improves the resolution in the azimuth direction tremendously. This can be illustrated by a simple example. A space-borne system operating in X-band with an antenna length of 12 m, and altitude of 800 km would deliver only a poor resolution of 2000 m without using the synthetic aperture radar principle. However, with SAR the best achievable resolution that can be obtained is  $D/2$ , where  $D$  is the antenna length. This result may seem astonishing since the resolution is independent of range.

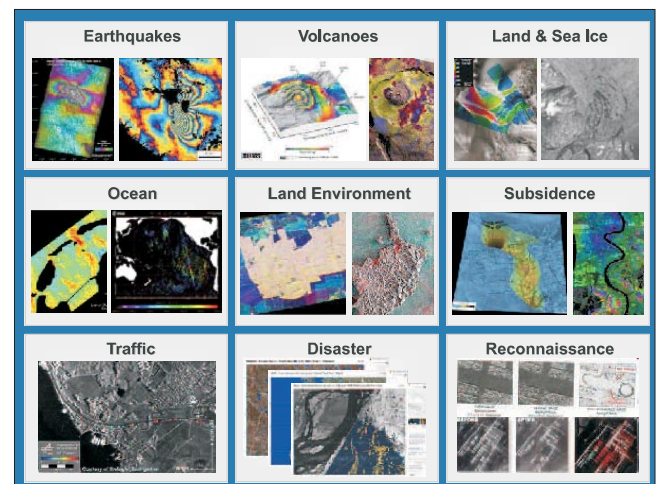


**Fig. 1:** A selection of applications for SAR (courtesy of G. Krieger).

The received radar signals contain information about roughness and geometrical structure as well as electrical properties of the imaged scene. Furthermore the signal may deliver information of the atmosphere and surface. Dependent on the wavelength also information of the subsurface can be gained.

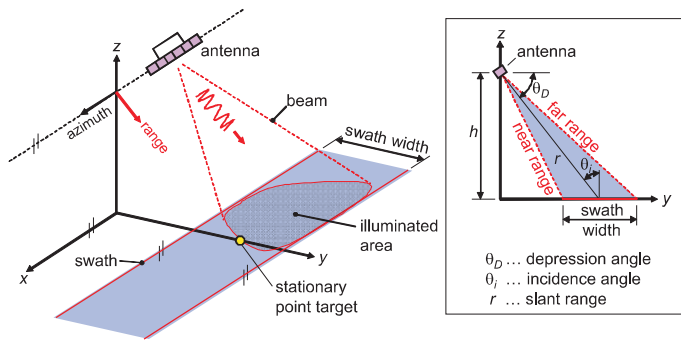


Fig. 2: A depiction of a SAR sidelooking imaging geometry.

Radar imaging has been proven to be very successful for a wide range of remote sensing applications and some of them are exemplarily given in Fig. 1.

A typical SAR imaging geometry is given in Fig. 2, which shows a side-looking antenna mounted on a moving platform. Due to their higher altitude, satellite incidence angles vary less than airborne incidence angles. This leads to more uniform illumination on satellite images than for airborne radar images. We emphasize, that the velocity  $v$  of the platform carrying the antenna is small in comparison to the transmitted signals, which are propagating at a constant velocity equal to the speed of light ( $c \approx 3 \times 10^8$  m/s). The antenna beam is pointing towards the earth and is illuminating the surface within the antenna footprint (intersection of beam with surface). The shaded area at the ground depicted in Fig. 2 is sometimes called the antenna footprint.

Note that the beam width is inversely proportional to the dimension of the antenna and the frequency, i.e. the larger the antenna and the higher the frequency, the smaller the beam width. The width of the so-called swath (ranging from near- to far range) limits the area of the surface which can be resolved in a processed SAR image in the across track dimension. The intersection of the vertical from the platform with the ground is called the *nadir*. In Fig. 2 the meaning of the depression- and incidence angle is shown.

The axis along the line of flight is called along-track or azimuth and the perpendicular direction is called in general range or across-track, where slant range and ground range have to be distinguished. The slant range denotes the distance from the aircraft to the scatterers, and the ground range the distance from the nadir to the observed scatterer. The term *squint* angle denotes the deviation angle between the main axis of the antenna beam and the plane perpendicular to the line of flight, where positive squint angles are by convention assigned to positive Doppler frequency shifts, and vice versa. We note that along-track and range directions are orthogonal to each other.

#### A. Image Formation Process

As the platform moves along the azimuth direction the pulses are transmitted by the antenna with a certain pulse repetition frequency (PRF). Instead of a short sharp pulse, a

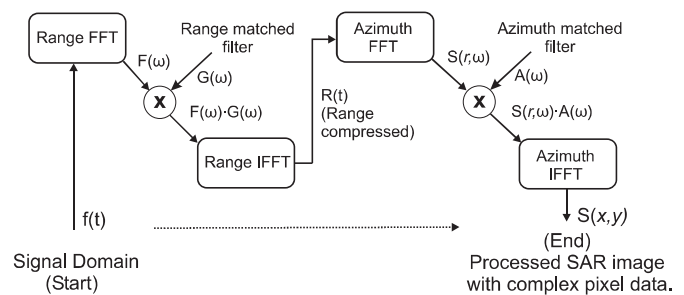


Fig. 3: A flow chart of range Doppler imaging.

pulse having a large time-bandwidth product is transmitted. For obtaining a small range resolution and the highest possible signal-to-noise ratio pulse compression is carried out using a matched filter. The output or focused signal, respectively, is given by the convolution of the received signal with the reference signal/function. Following the optimal filter theory, the reference or matched filter function, respectively, is the complex conjugated and time-reverted function of the SAR system response.

The data collected by SAR systems are represented by a two-dimensional complex matrix in order to be processed to obtain a two-dimensional representation of the illuminated area.

An appropriate algorithm in order to understand the processing procedure is called either Range-Doppler or rectangular imaging [1] described in the following. The flow chart depicted in Fig. 3 shows the main required steps to transform from the raw time signal domain into the complex image domain.

The basic procedure of compressing the raw data in order to obtain an image is a two-dimensional correlation with a reference function, which is a matched filter operation.

The starting point for image processing after acquisition and sampling of the received analog data is the two-dimensional raw data matrix containing complex entries. The fundamental algorithm called 'rectangular' algorithm is briefly discussed. The algorithm is based on the rectangular assumption, assuming that the order of processing in range and azimuth is irrelevant and can be executed separately. The principle of compressing the raw data in range and azimuth via matched filter operations represents a well established and fundamental processing algorithm. We limit the treatment of processing algorithms herein. A variety of references are available cf. [1]–[6] that detail the subject more broadly.

Being a well established and matured remote sensing technique, a large body of literature exists for various topics of SAR imaging; reference is given to [7]–[11].

### III. ASSESSMENT OF PROPAGATION EFFECTS IN SAR IMAGES

Amongst the many effects that may affect SAR images are delays, attenuation, noise, scintillation which are caused by atmospheric gases, rain (precipitation), clouds, fog or free electrons in the ionosphere.

Whether these effects are relevant depends on the signal parameters, the path geometry and the conditions prevailing in the ionosphere and the troposphere. The use of higher frequencies (X-band and beyond) minimises ionospheric effects on propagation, but tropospheric effects often increase or dominate as will be investigated in more detail.

The question to what extent atmospheric effects are critical depends also on the specific SAR application. For instance, for Synthetic aperture radar (SAR) interferometry, a powerful remote sensing technique for measuring the distance to the Earth's surface, the phase measurements is exploited. It requires that the surface is imaged by the radar at least twice from almost the same position in space. The differences in phase between the two images produce interferometric fringes that allows to deduce the topography of the surface. Any effect on the phase of the SAR signal will affect the accuracy of the height information. The focus in this contribution is mainly to the propagation effects that cause attenuation and backscattering in the image. For atmospheric effects on interferometric SAR techniques we refer to [12]–[14].

In the following some examples are shown how precipitation may affect SAR intensity images. The first example (Fig. 4) is taken from the SIR-C/X-SAR mission flown in 1994, where three images acquired in three different frequency bands are combined. The RGB-composite coding is (R) for X-band (G) for C-band, and (B) for L-band. As expected the "blocking" is most pronounced for X-band frequencies.

Three further examples of rain affected signatures in SAR images are given in Fig. 5 all of them taken from areas over tropical rain-forest, where heavy precipitation possesses highest probability on a world-wide scale.

For a recent measurement taken with TerraSAR-X, the German SAR satellite, launched in June 2007 and operating extremely successful since then [15], Fig. 6 is provided.

The physical processes are better elucidated with the help of Fig. 7 where a SAR amplitude cutout of cross-track profile through a rain cell is depicted. As diagrammatically shown, the backscattering is accompanied with higher amplitude values and the weak signals behind the first maxima belongs to the black shadows easily recognised in Fig. 7, where up to 20 dB difference in the dB level may be observed.

#### IV. TROPOSPHERIC EFFECTS

The troposphere, as the lowest part of the Earth's atmosphere, reaches from the surface to approximately 12 km above ground and causes, amongst other effects, attenuation of traversing signals due to hydrometeors (rain, snow, hail), atmospheric gases, fog and clouds [16]. Except at low elevation angles, the attenuation of frequencies below 1 GHz is negligible. Insignificant contributions to the attenuation will be obtained for frequencies up to 10 GHz due to fog and non-precipitating clouds. However the transmission spectrum exhibits peaks for frequencies around 22 GHz and 60 GHz due to molecular resonances from gases, i.e. water vapour and oxygen. Whereas absorption effects due to atmospheric gases are present constantly and everywhere, attenuation due to

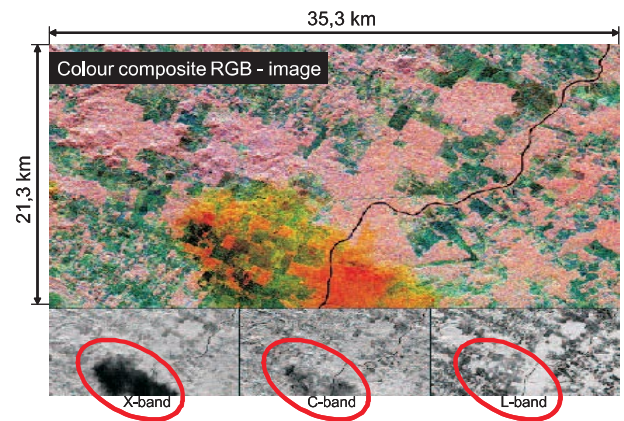


**Fig. 4:** Example of influence of rain on SAR intensity images, using the RGB composite corresponding to X-band (R), C-band (G), and L-band (B) measurements, respectively. The rain-induced 'blocking', as expected, is most pronounced in the X-band case. The images have been recorded during the X-SAR/SIR-C Mission conducted by DLR/NASA in 1994. The image is centered at  $11.2^\circ$  south latitude and  $61.7^\circ$  west longitude, respectively. North is toward the upper left.

condensed water in the form of precipitation, clouds and fog is infrequent and is limited to certain areas. Attenuation consists of two physical processes: the reduction of the wave's energy due to the heating of the water particles and, the scattering of energy away from the main direction of propagation.

##### A. Global Characteristics of Rain

On average, 50% of the Earth's surface is covered by clouds. However the rain to cloud ratio is seldom larger than 10%. This means that the upper bound of 5% on Earth's surface is receiving rain at a given time. Rain events are dominated by light rain events, however higher rain rates account for most of the total liquid water reaching the surface. Even for the areas with the highest rain rate, the percentage time in a year that exceeds 50 mm/hr is 0.1% (annual probability) = 526 min. And 150 mm/hr is exceeded less than 0.01% = 53 min.

##### B. Modelling of Attenuation and Backscattering in SAR Images

For the modelling of the attenuation and backscattering effects in SAR images, Fig. 8 is clarifying the underlying geometry [17]. The diagram provided at the bottom of Fig. 8 shows the qualitative variation of the normalised radar cross section (NRCS) due to the idealised rain cell. The detailed modelling and calculation is provided in the following two sections.

One of the major problems affecting microwave and millimetre wave bands for terrestrial and space-borne radars is the attenuation through rain [16]. A convenient way to describe the rain intensity is the so called rainfall-rate or rain-rate given in millimetres per hour. This quantity refers to a certain flux of rain towards the surface of the Earth and may be measured

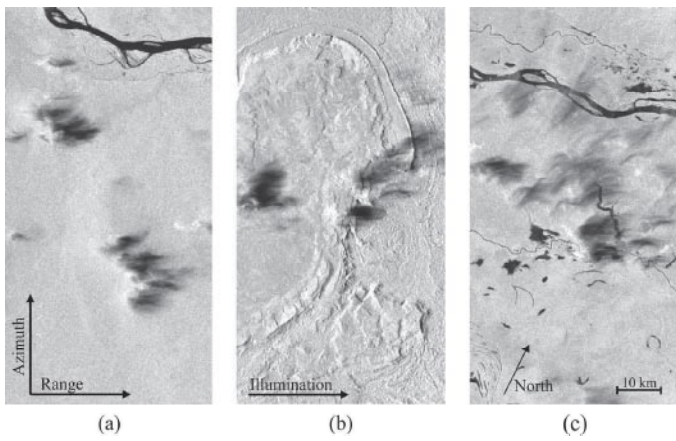


**Fig. 5:** Three examples of weather-corrupted SAR images from the SRTM mission (X-band: 9 GHz) from the Brazilian rain forest. The horizontal corresponds to range, and the vertical to the azimuth direction. The direction of illumination for all three images is given from the left- to the right-hand side. (a) DT: 087.070 Scene: 740. (b) DT: 150.050 Scene: 820. (c) DT: 039.070 Scene: 740.



**Fig. 6:** An example of a SAR image with rain-cell signatures recorded with TerraSAR-X in the US close to Baton Rouge. The white shading to the left of the dark spot is due to direct reflections from the rain region. The darkly shaded areas are due to rain attenuated (blocked) signals from the ground.

e.g. by gauges or weather radars. A widely accepted empirical relation of the form

$$\gamma(x, t) = a \cdot R^b \quad (1)$$

between specific attenuation  $\gamma(x, t)$  and rain rate  $R$  is used to calculate the specific attenuation for a given rain rate [16], [18]. The parameters  $a$  and  $b$  are dependent on the radio frequency, the raindrop size distribution, the polarization and other factors [18].

The total attenuation for a given instant of time can be obtained by adding up the specific attenuation along the path of propagation using the following expression [16]

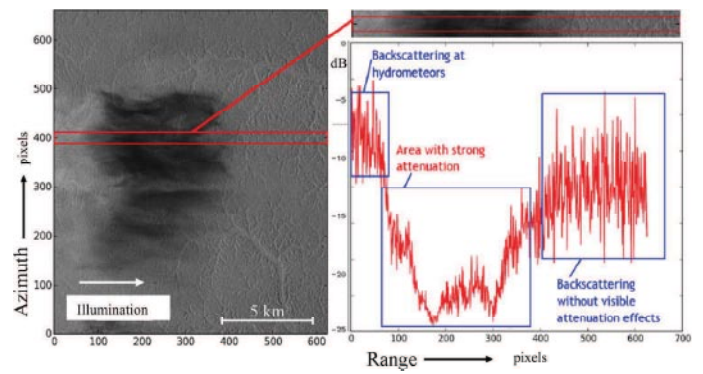


**Fig. 7:** Depiction of a slant-range reflectivity profile (“A-scope”) for the rain-cell cut from a very recent TerraSAR-X measurement over a tropical rain forest in Brazil. Such data sets may, at some stage, enable estimation of rain rate over such isolated areas. This figure was inspired by the study of Runge et al. [19] who analyzed reflectivity profiles of SRTM data taken over a tropical rain forest.

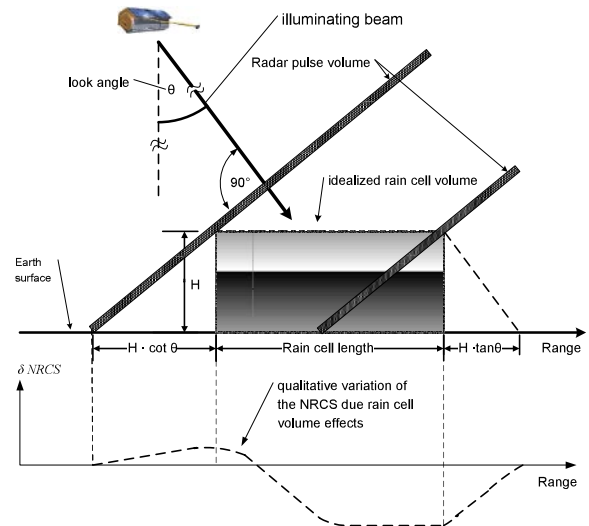


**Fig. 8:** A depiction of a SAR imaging scenario of an idealised rain cell. In the diagram the qualitative variation of the NRCS due to the rain cell volume effects is given. A combination of backscattering and attenuation can occur, where qualitatively the backscattering due to rain is the minor effect and attenuation the major [17].

$$A(t) = 2 \int_0^h \gamma(x, t) dx \quad [dB] \quad (2)$$

where

- $A(t)$  ... total attenuation for given time instant  $t$
- $t$  ... time
- $h$  ... path length
- $\gamma(x, t)$  ... specific attenuation
- $x$  ... position along the path of propagation

The specific attenuation along the slant path of propagation

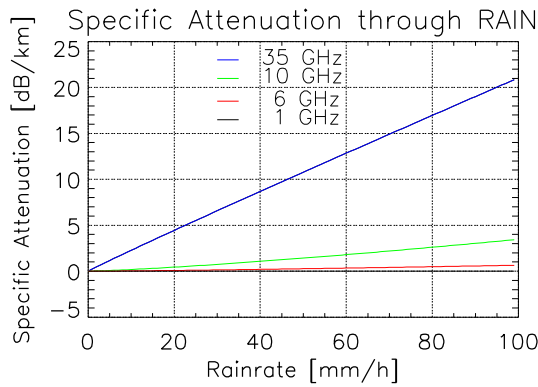


**Fig. 9:** A plot of the specific attenuation given in units of dB/km versus the rain rate in units of mm/h for four different frequencies (1, 6, 10 and 35 GHz) after [21].

has to be known. However, detailed knowledge of the medium through which the signal propagates is rather limited and the temporal and spatial variation of the medium require assumptions and some modelling. In the case of precipitation we may have some idea about the thermodynamic phase (ice, water, melting band) but no precise information. Using the calculated values for the specific attenuation in X-band provided in diagram Fig.9 for a 5 km long path through a heavy tropical convective rain (70 mm/h and more) suggests a 20 – 30 dB two-way attenuation, which was confirmed by comparing the backscattering coefficient of affected and non-affected region from data takes acquired by TerraSAR-X over Brazilien rain forest [20].

### C. Modelling of the Attenuation under Rain Conditions for Ka-band

For the calculations of the rain rate to cause visible attenuation in Ka-band SAR images, a simple model shown in Fig. 10 [17], is used. A reasonable height of 4 km is assumed, as well as a homogenous rain rate for the modelled cell. The incidence angle of the propagating signals was chosen 30°. With the help of (1) and by using the regression coefficients in Table I, the specific attenuation was calculated. These values are given in Table II. Finally, the values for the two-way path attenuation for different rain rates (5, 50 and 100 mm/h) can be found in Table III.

As a total two-way attenuation of 25 dB becomes visible in SAR images in X-band it is of interest which rain rate is necessary to cause such an attenuation for Ka-band (35 GHz) frequencies. To this end, the following equation is applied

$$\gamma(t) = \frac{A(t)}{2 \cdot \frac{H}{\cos(\theta)}} \quad [\text{dB/km}], \quad (3)$$

where the rain rate is found using (1) with the according parameters  $a$  and  $b$  for Ka-band

$$R = \sqrt[b]{\frac{\gamma(t)}{a}}. \quad (4)$$

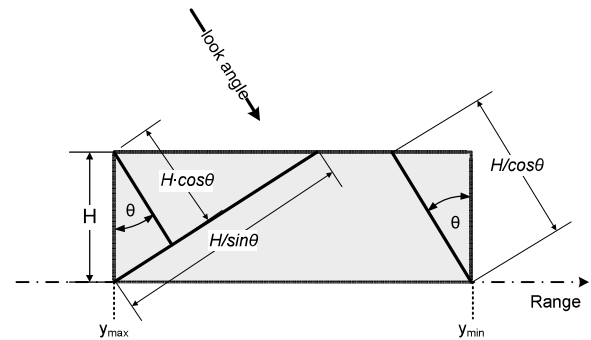


**Fig. 10:** The structure of an idealised rain cell used for the calculation in Section IV-C.

**TABLE I:** Regression coefficients used for the calculation of the specific attenuation cf. (1)

Frequency	DSD			
	Mar. Palmer		Joss Thunderst.	
	$a$	$b$	$a$	$b$
X-Band (10 GHz)	0.0136	1.15	0.0169	1.076
Ka-Band (35 GHz)	0.268	1.007	0.372	0.783

First calculations using the parameters of the idealised rain cell of 4 km and using 25 dB of total two-way attenuation, assuming the Marshall Palmer Parameters for Ka-band attenuation deliver a rain rate close to 10 mm/h. This simple example demonstrates that such rain rates are fully capable to distort Ka-band SAR measurements to a visible extent. In Fig. 11 the range of values for attenuation and rain rate are extended and the diagram shows the two-way attenuation versus the rain rate for different incidence angles at Ka-band. Similar information is provided for X-band frequencies in Fig. 12 for comparison. The aforementioned simple assumptions of a homogenous rain

**TABLE II:** Specific Attenuation [dB/km]

Rainrate [mm/h]	Specific Attenuation	
	10 GHz	35 GHz
5	0.08	1.31
50	1.22	7.95
100	2.4	13.69

**TABLE III:** Maximum attenuation for modelled rain cell [dB].

Rainrate [mm/h]	Specific Attenuation	
	10 GHz	35 GHz
5	0.739	12.1
50	11.26	73.43
100	22.17	126.46

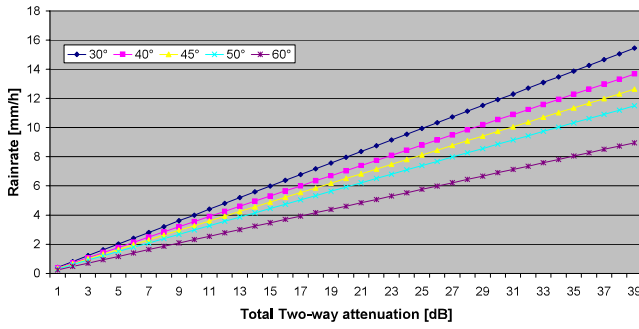


**Fig. 11:** A diagram of the two-way path attenuation and the corresponding rain rate for the modelled rain cell of 4 km height (Fig. 10) at Ka-band (35 GHz), for different look angles.

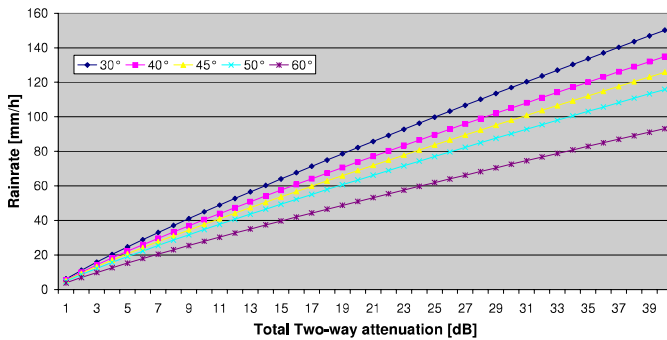


**Fig. 12:** A diagram of the two-way path attenuation and the corresponding rain rate for the modelled rain cell (Fig. 10) at X-band (10 GHz), for different look angles.

cell with constant precipitation may be somehow optimistic, since a melting layer precipitation may severely increase the total path attenuation.

#### D. Consideration of Backscattering Effects in SAR Imaging

The radar response (backscattering) from hydrometeors is determined by the raindrop size, shape, density, orientation, and temperature. Furthermore, the backscattering depends on the polarization of the wave interacting with the precipitation media. The theoretical concept that describes the scattering from a dielectric sphere was established by Mie in 1908. The relation to estimate the backscatter cross section of a volume of small particles by assuming the well-known Rayleigh approximation (the diameters  $D$  of the raindrops are much smaller than the wavelength  $\lambda$ ) is given as [23]

$$\sigma_b = \frac{\pi^5}{\lambda^4} |K|^2 \sum_{i=1}^N D_i^6 \quad (5)$$

where

$$K = \frac{m^2 - 1}{m^2 + 2} \quad (6)$$

and  $m$  is the complex index of refraction of the scattering

particle. The summation term for a distribution of particles can be given as

$$\hat{Z} = \int N(D_e) D_e^6 dD_e \quad [mm^6/m^3], \quad (7)$$

where  $\hat{Z}$  is termed the reflectivity factor,  $D_e$  is the diameter of each droplet and  $N(D_e)$  is the number of droplets per unit volume.

$$N(D_e) = N_0 e^{-\lambda_d D_e}, \quad \lambda_d = 4.1 \cdot R^{-0.21} \quad (8)$$

where  $N_0$  and  $\lambda_d$  are the parameters defining the drop size distribution (DSD). For the special case of the Marshall-Palmer distribution the parameter  $N_0$  is given as  $8000 \text{ m}^{-3} \text{ mm}^{-1}$  and  $\lambda_d [\text{mm}^{-1}]$  is related to the rainfall intensity  $R [\text{mm/h}]$  as shown in Eq. (8).

Note that  $\hat{Z}$  is commonly given in logarithmic units according to

$$Z = 10 \cdot \log_{10} \hat{Z} \quad [dBZ]. \quad (9)$$

As a practical basis for estimating the precipitation intensity directly from the measured reflectivity factor in still air, the following relation is used

$$\hat{Z} = a_1 \cdot R^{b_1}. \quad (10)$$

The parameters  $a_1$  and  $b_1$  are dependent on the frequency of the interacting EM waves and on the rain intensity  $R$  as well as the DSD. Furthermore, regional-dependent variations due to the rain type do exist. A number of  $Z - R$  relations were established by many research efforts and are provided, for instance, in [18]. A careful selection of the coefficients has to be performed by considering the appropriate conditions and respective parameters.

The power law in (10) provides an analogy to the calculations of the specific attenuation using (1) given in Section IV-C.

For a further in-depth analysis of the theoretical aspects of backscattering due to hydrometeors, we refer to [24]. For the case of SAR, it can be concluded that the backscattering due to hydrometeors is the minor effect and attenuation due to the precipitation volume is dominating, which is supported by the recent measurements of TerraSAR-X.

It has been observed that backscattering due to precipitation can easily enhance the backscattering about 5 dB compared to unaffected regions of the image.

#### E. Test Case and Comparison of SAR Data with Simultaneously Measured Ground-based Weather Radar Data

Fig. 13 shows a comparison of two different types of images measured almost at the same time, where the image on the left-hand side was acquired with TerraSAR-X [15] strip-map mode in ascending orbit over New York. The image on the right-hand side displays the corresponding weather radar image measured by a ground-based weather radar (WSR-88D) located in New York (Nexrad code: KOKX). The data were obtained using

the freely available Java NEXRAD viewer provided by the National Oceanic and Atmospheric Administration, U.S. A good agreement between visible artifacts shown in the SAR image (some of them encircled in red color) and the reflectivity plot on the right-hand side was observed. Such reflectivity maps display the echo intensity of the transmitted radar signals and are shown in dBZ. These maps are used to detect precipitation and evaluate storm structures. It is the best available means to compare precipitation volumes and precipitation-induced signatures in SAR images. The reason lies in the high achievable spatial resolution and the possibility to measure at almost the same instant of time. The red regions in the weather radar image correspond to reflectivities up to 50, in some cases 55 dBZ, which corresponds to high precipitation intensities typically occurring during thunderstorms. The comparison of ground-based weather radar and SAR data will be certainly useful in the process to derive rain intensity information from SAR-based measurements.

#### V. IDENTIFICATION OF MEASURES AND RECOMMENDATION TO COUNTERACT AND/OR ENHANCE PRECIPITATION EFFECTS ON SAR

In this section we briefly highlight some of the possibilities to overcome the limitations of the SAR system under investigation due to adverse meteorological conditions. The ideal strategy to identify rain induced signatures would be a multi-frequency SAR system, because attenuation through rain is wavelength dependent. Since current SAR systems are not equipped with such a multi frequency sensor set, other ways have to be taken into consideration. Wherever available, ground based weather radar would assist in the process to identify precipitation induced distortions in SAR images. However, world-wide coverage of ground based weather radars is limited to industrialized regions such as the USA or Europe. Especially over the oceanic regions no ground based weather radar data are available and so it is for the polar regions of the Earth. One simple measure to avoid or mitigate precipitation effects are multi-temporal acquisitions over the same scene, since the statistical probability for rain is rather low, as already shown before. As the look angle determines the path length of the propagation path through the precipitation media, steep look angles would reduce the attenuation due to rain, and conversely shallow look angles cause increased values of attenuation. The question to what extent scan-on-receive techniques are capable to improve, respectively enhance precipitation effects was addressed by [22], and deserves further consideration. A mitigation of the backscattering can be obtained. However, the attenuation will still be present for transmit and receive patterns as is diagrammatically shown in Fig. 14.

#### VI. CONCLUSIONS

A brief introduction to the SAR imaging concept was given followed by a discussion of propagation distortions and their influence on the image quality. Propagation effects can be very important and need to be considered in interpreting radar images. It has been shown that attenuation due to rain

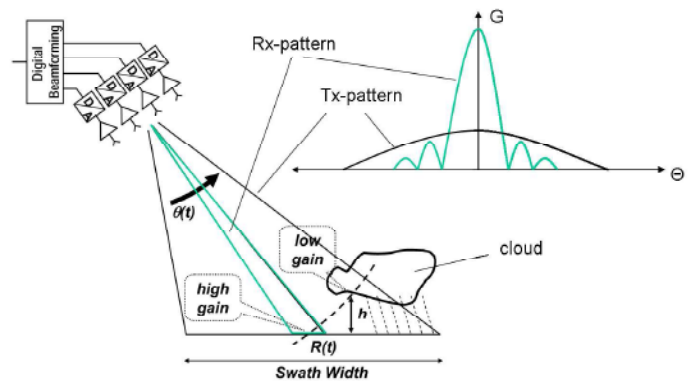


**Fig. 14:** A depiction of an imaging scenario with scan-on-receive technique. The different gain in receive Rx (pencil beam) and Tx allows for an improvement of the SNR in the presence of rain for backscattering. However, the attenuation can not be avoided.

is the dominating effect, together with backscattering from precipitation at higher frequency bands such as X- and Ka-band. Since the effects of backscattering and attenuation are interconnected to each other it is sufficient to consider at least the major disturbance (=attenuation through rain) in order to flag an affected SAR image. A model to quantify propagation effects in SAR images has been presented, which allows for a quantitative assessment of the pertinent effects. Depending on the climatic region on Earth, the availability of a Ka-band system will vary. Assuming a 5 dB acceptance of the attenuation due to rain, which corresponds to 2 mm/h at 30° incidence angle for the modelled rain cell used in this paper, the availability will be better than 98 % for the European regions and better than 95 % for rain-forest in Brazil. Clouds with little water liquid content, low rain rates and homogenous distribution will cause no or only little disturbance (visible artefacts). The disadvantage of rain cell signatures might offer the potential advantage to derive meteorological information.

#### VII. ACKNOWLEDGEMENTS

I would like to sincerely thank Prof. Madhukar Chandra from Chemnitz University of Technology, Chemnitz, Germany for the invitation to present this article at the 2<sup>nd</sup> WFMN (Wave Propagation and Scattering in Communications, Microwave Remote Sensing and Navigation) conference. Furthermore, I would like to sincerely acknowledge the proofreading and constructive comments by Dr. G. Krieger as well as the provision of Fig. 2 by Dipl.-Ing. S.V. Baumgartner.

#### REFERENCES

- [1] W. G. Carrara, R. S. Goodman, and R. M. Majewski. *Spotlight Synthetic Aperture Radar: Signal Processing algorithms*. Artech House, 1995.
- [2] I. Cumming and F. Wong. *Digital Processing of SAR Data*. Artech House, Norwood, MA, 2005.
- [3] J. C. Curlander and R. N. McDonough. *Synthetic Aperture Radar: Systems and Signal Processing*. J. Wiley and Sons, New York, 1991.
- [4] M. Soumekh. *Synthetic Aperture Radar Signal Processing with MATLAB Algorithms*. Wiley, 1999.
- [5] J. P. Fitch. *Synthetic Aperture Radar*. Springer Verlag, 1988.

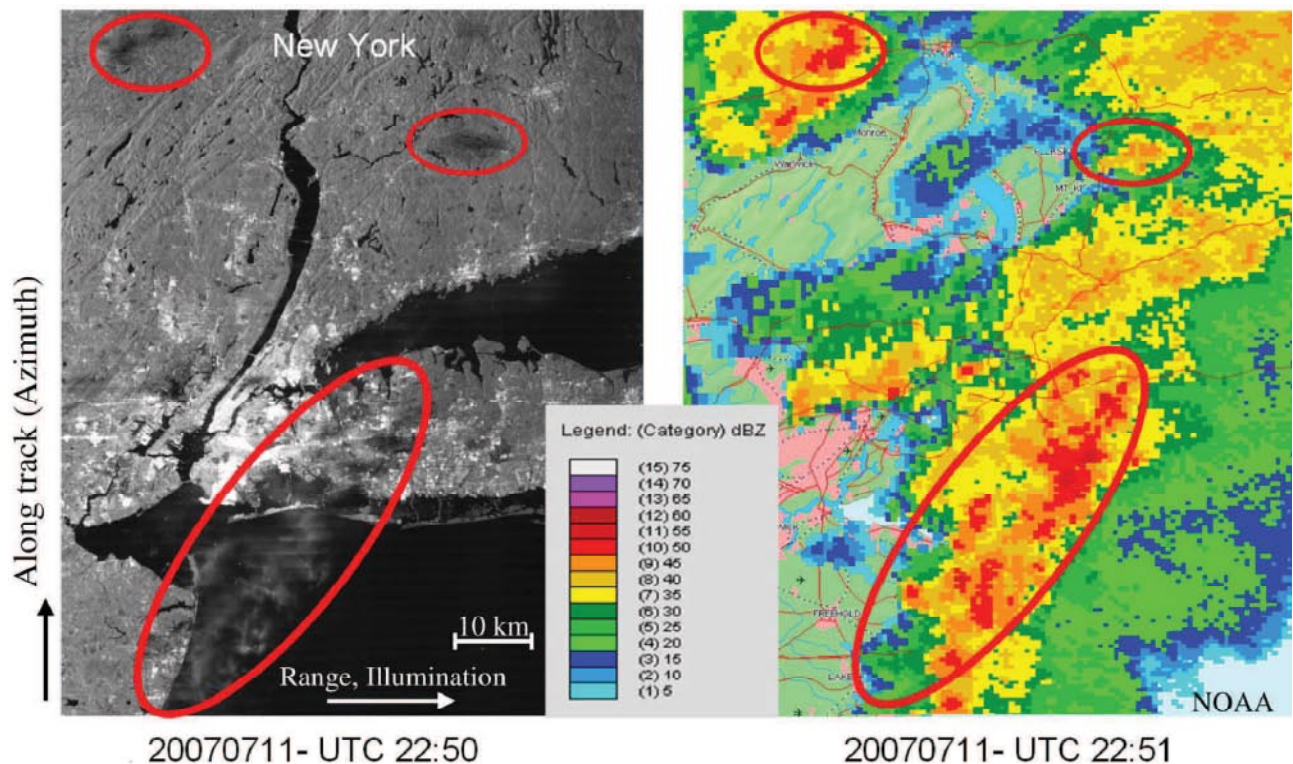


**Fig. 13:** Test case showing a comparison of TerraSAR-X and weather radar data acquired nearly simultaneously (within the same minute) over New York, U.S. A good agreement between the rain-cell signatures in (left) the SAR image and (right) the weather radar image can be observed. The effects are most pronounced for reflectivities of up to 50 dBZ. The SAR image was acquired in ascending orbit direction, and the range direction corresponds with the horizontal. The look direction was from left to right. The vertical corresponds to the along-track direction. Image dimensions are approximately 130 km in azimuth and 100 km in range direction.

- [6] H. Klausing and W. Holpp, editors. *Radar mit realer und synthetischer Apertur*. Oldenburg, München, Wien, 2000.
- [7] C. Oliver and S. Quegan. *Understanding Synthetic Aperture Radar Images*. Sci Tech, Raleigh, NC, 2004.
- [8] F. M. Henderson and A. J. Lewis, editors. *Manual of Remote Sensing, Principles and Applications of Imaging Radar*. Wiley, 1998.
- [9] C. Elachi and J. J. van Zyl. *Introduction to the Physics and Techniques of Remote Sensing*. Wiley, 05 2006.
- [10] H. Mott. *Remote Sensing with Polarimetric Radar*. Wiley, 2007.
- [11] J. S. Lee and E. Pottier. *Polarimetric Radar Remote Sensing*. CRC Press, 2009.
- [12] R. F. Hanssen. *Radar Interferometry: Data Interpretation and Error Analysis*. Kluwer Academics, 2001.
- [13] H. A. Zebker, P. A. Rosen, and S. Hensley. "Atmospheric Effects in Interferometric Synthetic Aperture Radar Surface Deformation and Topographic Maps." *Journal of Geophysical Research*, 102:7547–7452, 1997.
- [14] A. Danklmayer, E. Archibald, T. Boerner, D. Hounam, and M. Chandra. "Atmospheric Effects and Product Quality in the Application of SAR Interferometry." In: *Proceedings of EUSAR 2004*, Ulm, Germany. ISBN 3-8007-2828-1.
- [15] R. Werninghaus, St. Buckreuss, "The TerraSAR-X Mission and System Design" *IEEE Transaction on Geoscience and Remote Sensing*, accepted for publication in a Special issue on TerraSAR-X; available online [http://ieeexplore.ieee.org]; in hard copy to appear in 2010.
- [16] R. K. Crane. *Electromagnetic Wave Propagation through Rain*. John Wiley and Sons, 1996.
- [17] C. Melsheimer. *Signaturen von Regen in Radaraufnahmen des Meeres*. Aachen: Shaker Verlag, 1998.
- [18] R. L. Olsen, D. V. Rogers, and D. B. Hodge. "The  $a \cdot R^b$  Relation in Calculation of Rain Attenuation," *IEEE Transactions on Antennas and Propagation*, vol. 26, no. 2, pp. 318–329, 1978.
- [19] H. Runge, S. Cloude, M. Eineder, A. Fusco, E. Gill, I. Hajnsek, C. Heer, F. Jochim, M. Kirschner, G. Krieger, A. Moreira, T. Niederstadt, K. Papathanassiou, R. Romeiser, R. Scheiber, C. Sickinger, and S. Suchandt. *New Techniques for Simultaneous SAR Interferometry*. Eur. Space Agency, Noordwijk, The Netherlands, Final Rep. ESA Contract 16100/02/NL/EC, 2003.
- [20] A. Danklmayer, B. Döring, M. Schwerdt, and M. Chandra. "Assessment of Atmospheric Effects in SAR Images," *IEEE Transaction on Geoscience and Remote Sensing*, 2009, vol. 47, no. 10, pp. 3507-3518, October 2009.
- [21] Specific Attenuation Model for Rain for Use in Prediction Methods, 2005. *ITU-Recommendation P. 838-3*.
- [22] S. D'Addio, M. Ludwig, "Rain Impact on Sensitivity of Ka-band Scan-on-Receive Synthetic Aperture Radars," in *IEEE International Geoscience and Remote Sensing Symposium, (IGARSS) 2008*, vol 3, 7-11 July 2008 Page(s):III - 1174 - III - 1177, Boston, US
- [23] V. N. Bringi and V. Chandrasekar. *Polarimetric Doppler Weather Radar, Principles and Applications*, Cambridge University Press, New York, 2001.
- [24] T. Oguchi, "Electromagnetic Wave Propagation and Scattering in Rain and other Hydrometeors," *Proc. IEEE*, vol. 71, no. 9, pp. 1029-1078, Sep. 1983

# On Advantages of Free Space Optics Link Backup-ing by Radio Link

Ondrej Fiser

**Abstract** — Using the FSO link attenuation measurement at the Milesovka observatory a formula to estimate the fog attenuation was found. Through computed fog attenuation on FSO links on one hand and computed rain attenuation on reserve radio link on other hand the advantages of FSO link backup-ing by radio link are discussed. Such system is some times called „hybrid system“ and the „hybrid diversity“ improvement is presented in this contribution. It is shown that rain attenuation on radio links is negligible at instants of heavy fog (low visibility) when the FSO attenuation due to fog makes optical link unreliable.

**Index Terms**—Free space optics (FSO), hybrid systems, fog attenuation, rain attenuation

## I. INTRODUCTION

Free space optics (FSO) communication links, operating on wavelengths 850 nm or 1550 nm usually, are developing for their advantages in this time. For planning of technical parameters of FSO links it is necessary to consider propagation of the signal through the atmosphere. In the optical wavelength bands it is necessary to be familiar not only with the signal attenuation in fog and rain. Recent experiences have shown an impact of wind turbulences on signal power dispersion causing also the transmission attenuation.

But the FSO link is not affected by rain as much as the radio link (physical reasons). That's why in the case of heavy attenuation on FSO link due to fog or wind turbulences it is convenient to transmit the signal by a reserve radio link on preferred frequencies of 24.125, 58, 61.25, 122.5 and 245 GHz. Unfortunately the radio link suffers from random rain events causing attenuation.

The aim of this study is to compare FSO link attenuation due to fog and radio link attenuation in the presence of rain. A quantitative deduction of FSO link “backup-ing” by radio link in the case of heavy fog is a main part of this contribution.

## II. EXPERIMENTAL SITE

We measure FSO link atmospheric attenuation on

Ondrej Fiser works as scientist with the Institute of Atmospheric Physics of the Academy of Sciences of Czech Republic and as docent (associate professor) at the Faculty of Electrical Engineering and Informatics of the University of Pardubice (e-mail [ondrej@ufa.cas.cz](mailto:ondrej@ufa.cas.cz)). For more see <http://www.ufa.cas.cz/html/meteo/lide/fiser.html>

experimental FSO link on both wavelengths of 850 and 1550 nm for about two years. Experimental link of the 60m length is located at the meteorological observatory „Milesovka“ of the Institute of Atmospheric Physics (837 m.a.s.l) being about 75 km north-west to Prague and by a way, also 75 km south-east from Chemnitz. Observatory is on an isolated mountain Milesovka with frequent fog, low clouds and strong wind occurrence. In german it is called „Donnersberg“ and it was visited by many famous people, for instance also by Alexander von Humboldt. Continuous meteorological measurement is performed there for more than 100 years (for more see <http://www.ufa.cas.cz/> and click departments-meteorology-observatories).

Besides the FSO link there are two 3D anemometers, two visibility sensors, rain gauge and many other meteorological sensors. For the sensor arrangement look at Fig.1.

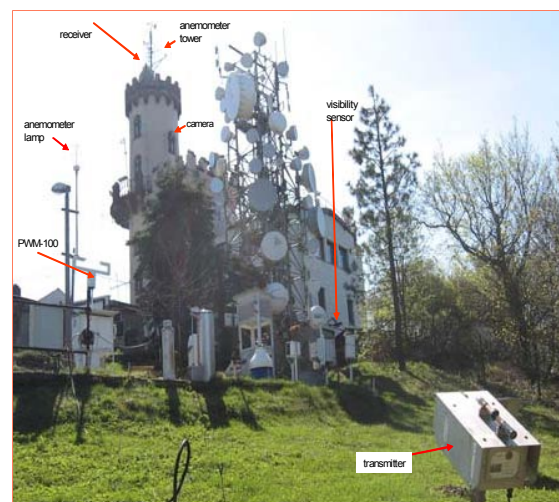


Fig. 1 Experimental site of the Institute of Atmospheric Physics at the “Milesovka” hill. The optical transmitter is on the right bottom.

## III. COMPUTATION OF FOG ATTENUATION ON OPTICAL LINK

Following all discussions in the literature we can accept fact that there is a negligible fog attenuation dependence on the FSO link wave length especially on short links. The following formula for specific FSO attenuation due to fog is usually used ([1],[2]):

$$\alpha = \frac{2600}{V} [\text{dB/km}] (B = 5\%); \text{ or} \quad (1)$$

$$\alpha = \frac{3400}{V} [\text{dB/km}] (B = 2\%) \quad (2)$$

where  $V$  is the meteorological visibility [m] and  $B$  is related to the used visibility definition. Visibility  $V$  is defined as a distance where the light radiance  $E$  becomes a value of the  $[B(\%)/100]$  multiple of  $E$  related to the free space situation (i.e. no fog, no rain). So we must be aware weather the available visibility data are related to 5% (0.05 multiple) or 2% (0.02 multiple) of the light radiance decrease.

After long term FSO link attenuation and visibility measurement ( $B=5\%$ ) analysis we have established an empirical formula to estimate the FSO specific attenuation  $\alpha$  [dB/km]

$$\alpha = \frac{2700}{V} \quad (3)$$

where  $V$  is the visibility in meters. This formula is similar to the equation (1).

#### IV. RADIO LINK ATTENUATION DUE TO RAIN

The specific rain attenuation  $A$  [dB/km] is proportional to the rain rate and usual approximation being used is the following one:

$$A = a R^b \quad (4)$$

where  $R$  is rain rate [mm/h], a quantity being available from meteorological measurement. Variables “ $a$ ” and “ $b$ ” are tabulated [3] depending on frequency of transmitting wave, polarisation and – if one wishes to be very accurate – on temperature.

To estimate the rain attenuation we selected the Assis-Einloft model (rain prediction method) [4] as it is physically based technique. This method enables the prediction of instantaneous rain attenuation on radio link in order to compare it with the FSO link attenuation at the same instant and thus to select the better transmission mean. Even if the natural “Assis-Einloft” model was intended to compute the statistical behaviour of rain attenuation (cumulative distribution-CD), its physical principle is suitable to estimate the instantaneous attenuation comparative with concurrent hypothetical attenuations on parallel FSO links.

The Assis-Einloft model converts the rain rate into the rain attenuation at given frequency and polarization. By other words the attenuation (in dB) is obtainable as a function of the independent variable “rain rate” on one hand and as a function of the link parameters (frequency, polarization, path length) on the other hand.

#### V. ATTENUATION COMPUTED FROM METEOROLOGICAL MEASUREMENT

First of all we computed fog attenuation on FSO link and

separately the rain attenuation on a hypothetical radio link. Attenuation on both radio relay link and optical link are computed from rain rates (radio links) and visibility (optical link). The measurement was performed at the Institute of Atmospheric Physics in Prague in 2008.

Table 1 shows attenuation values for given exceedance probabilities computed for a hypothetical FSO as well as radio links of 1 km length.

TABLE 1  
EXAMPLE OF COMPUTED CD OF ATTENUATION [dB] ON RADIO AND FSO LINK DERIVED FROM METEOROLOGICAL DATA FROM PRAGUE (2008)

Exc.prob	Radio	Radio	Radio	Radio	Radio	FSO
f [GHz]->	24.125	58	61.25	122.5	245	850nm
0.01	1.7	5	5.3	6.8	7.2	87.1
0.02	1	3.4	3.6	4.9	5.3	80.2
0.05	0.6	2.3	2.4	3.4	3.8	73.2
0.1	0.5	1.9	2	2.9	3.2	66.2
0.2	0.3	1.4	1.5	2.3	2.5	61.4
0.5	0.2	0.9	1	1.5	1.7	52.9
1	0.1	0.6	0.6	1	1.2	43.5
2	0.1	0.3	0.3	0.6	0.7	11.3
3	0	0	0	0	0	0

The cumulative distributions of rain attenuation and attenuation on optical link for frequencies listed in the frame of Tab. 1 per 2008 year are plotted in Fig. 2.

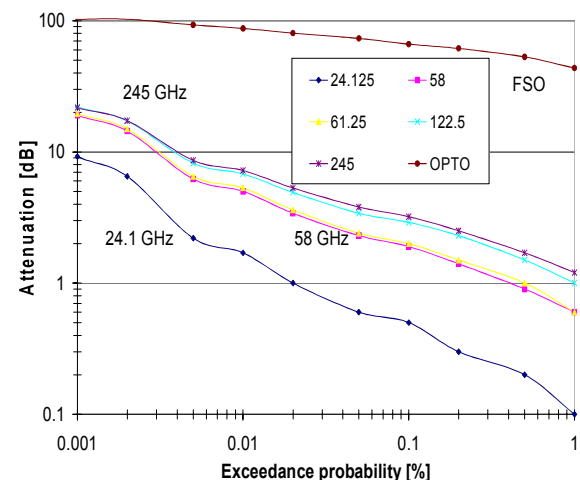


Fig. 2 Computed distribution of attenuation on hypothetical 1 km radio links operating on labeled frequencies and on 850 nm FSO link of the same length

One can see that FSO link attenuation achieves quite big values. Rain attenuation on radio link is strongly dependent on the frequency and does not exceed 22 dB for exceedance probabilities equal or less than 0.001

#### VI. SIMULATION OF HYBRID SYSTEM

To simulate a hybrid system we selected such fog events when the FSO link attenuation was exceeding “ $D$ ” dB. Usually the reliability is limited when “ $D$ ” exceeds 20 dB, but,

of course, also other “D” thresholds could be considered. They are applied in this contribution, too.

Only during these events the rain attenuation statistics on simulated radio links were computed. One year visibility and rain rate data from Prague were used. The results are obvious from Tab. 2. We can observe maximum, median, mean and standard deviation of such radiolink attenuation in cases FSO fog attenuation exceeded  $D=20$  dB. The parameter is the frequency of the reserve radio link. One can see that rain attenuation is very small in these cases. For instance, on the 58 GHz frequency the rain attenuation was never greater than 1 dB.

TABLE 2

BASIC STATISTICAL VALUES OF ATTENUATION ON RESERVE RADIO-RELAY LINK COMPUTED AT INSTANTS WHEN THE ATTENUATION ON OPTICAL LINK WAS EXCEEDING A VALUE OF 20 dB.

f [GHz]	24.125	58	61.25	122.5	245
max	0.2	1	1	1.6	1.9
mean	0.12	0.59	0.65	1.06	1.24
st.dev	0.06	0.23	0.25	0.36	0.43
median	0.1	0.6	0.7	1.1	1.3

Fig. 3 shows the situation on the cumulative distribution level. It is rain attenuation distribution derived from the time intervals when the optical link attenuation was exceeding value of 20 dB. As it is seen in Table 2, only small attenuations were met.

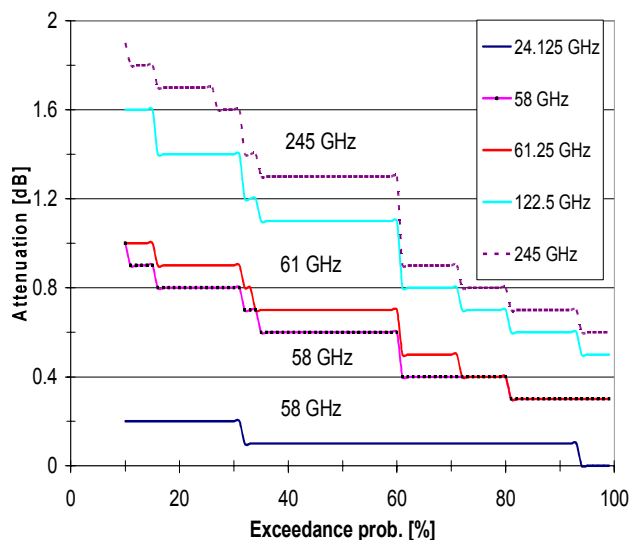


Fig. 3 Computed distribution of attenuation on hypothetical 1 km radio links operating on labeled frequencies derived from time intervals when FSO attenuation of the link of the same length was exceeding 20 dB. Input meteorological data were taken from Prague, 2008.

It was interesting to find out that rain attenuation in periods FSO link attenuation was exceeding only 18 dB, was much greater approaching 10 dB at the 0.01% exceedance level. Fig. 4 is documenting such situation in the form of cumulative distribution for all radio frequencies of interest.

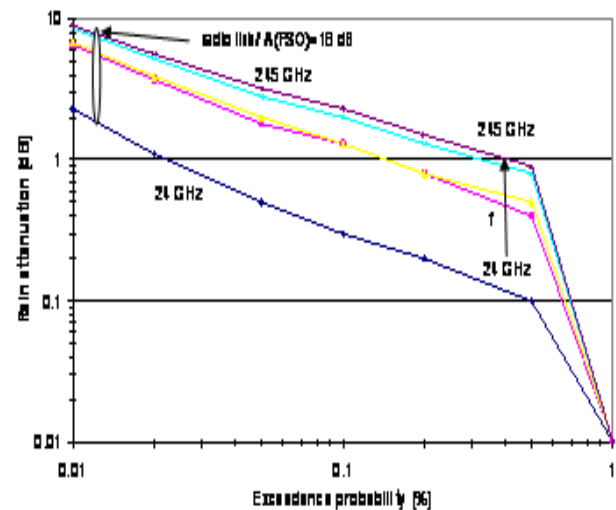


Fig. 4 Computed distribution of attenuation on hypothetical 1 km radio links operating on labeled frequencies derived from time intervals when FSO attenuation of the link of the same length was exceeding 18 dB. Input meteorological data were taken from Prague, 2008.

As it was mentioned in the chapter II, the Institute of Atmospheric Physics measures meteorological parameters on the mountain observatory Milesovka. Using these data and the same analysis like in the Prague data case, a cumulative distribution of rain attenuation at periods when FSO link attenuation was exceeding  $D=5, 10$  and  $15$  dB was computed and demonstrated in Fig. 5. One can see that radio link rain attenuation is decreasing with the increasing FSO link “D” threshold.

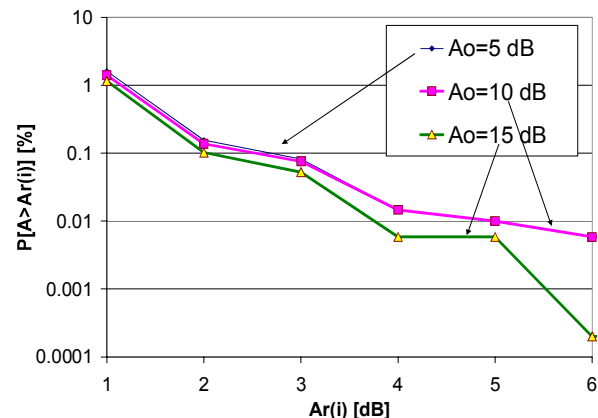


Fig. 5 Computed distribution of attenuation on hypothetical 1 km radio links operating on labeled frequencies derived from time intervals when FSO attenuation of the link of the same length was exceeding 5, 10 and 15 dB. Input meteorological data were taken from the Milesovka observatory, 2008.

## VII. DISCUSSION

After the oral presentation of this paper at the WFMN09 conference in Chemnitz there was a discussion concerning the negligibility of FSO link attenuation due to rain and radio link attenuation in the fog volume. We modeled consequently the propagation through both (fog and rain) volumes by the use of scattering theory to derive specific attenuation  $\alpha$  of a

volume filled in by dielectric scattering particles [5]. The resulting formula is

$$\alpha = 8.686 \cdot 10^3 \cdot \lambda \cdot \text{Im} \int f(D) \cdot N(D) dD \quad [\text{dB/km}] \quad (5)$$

where  $\lambda$  is the wave length,  $N$  is drop size distribution (DSD) representing the probability density of equivolumetric drop or droplet diameter  $D$  being in the unity volume. The product  $N(D) dD$  gives the number of drops of the diameter between  $D$  and  $D+dD$  in the unity volume. The scattering functions  $f$  were computed after Mie [7] in our analysis.

For radio link propagation through fog volume a fog DSD was needed. We generalized typical fog DSD taken from graphs in [6] by a simple formula:

$$N(D) = 500 D^{-3} \quad [\text{cm}^{-3} \mu\text{m}^{-1}] \quad (6)$$

where  $D$  is fog drop diameter in  $\mu\text{m}$ . The radio link attenuation in the frequency span 10-245 GHz was found to be under 1/1000 dB/km

The same technique (equation 5) was used for FSO signal propagation through the rain volume. DSD ( $N$  in equation 5) of rain drops was modeled after the well known Marshall-Palmer drop size distribution. The parameter of this DSD is the rain rate. The test having been performed for typical rain rate 10 mm/h and extreme rate 100 mm/h have proved that the specific attenuation for usual FSO links wavelengths are smaller than 1/100 dB.

## VIII. CONCLUSION

We can conclude that fog attenuation on FSO links can be large; this value can achieve about 90 dB/km (but on the low probability level). Generally speaking, rain attenuation can be also quite large depending on the radio link transmission frequency.

If we imagine a hypothetical hybrid link, i.e. the information transmission is switched from FSO to radio link in the case of big fog attenuation on primary FSO link, we can see optimistic situation: the radio link rain attenuation (being computed at moments when the attenuation on optical link is exceeding a value of 20 dB) is very low. Attenuation does not exceed 2 dB on 1 km path. This is a nearly a negligible attenuation.

This could be explained meteorologically. The correlation coefficient between optical- and radio-link attenuation is very weak; it varies between -4 and -7 percent depending on frequency of radio link. From meteorological point of view, it is expected because fog and rain are almost exclusive phenomena.

As it was demonstrated, the "back-uping" of the Free Space Optics link by parallel radio links makes the transmission much more reliable.

## ACKNOWLEDGEMENT

This contribution was thankfully supported by the GACR grant 102/08/0851 (FSO link fog attenuation from the meteorological visibility) and MSMT project OC09027 (radio link attenuation from rain rate).

## REFERENCES

- [1] Kim I. I., Mc Arthur B. and Korevaar E., "Comparison of laser beam propagation at 785 nm and 1550 nm in fog and haze for optical wireless communications," *Proc. of SPIE*, Vol. 4214, pp. 26-37, Boston, 2000
- [2] Nebuloni, "Empirical relationships between extinction coefficient and visibility in fog," *Applied Optics*, Vol. 44, pp. 3795-3804, June 2005
- [3] Rec. ITU-R P.383-3: Specific attenuation model for rain for use in prediction methods, 2005
- [4] Assis M. S., Einloft C. M.: A simple method for estimating rain attenuation distribution," Conference URSI, La Baule, p. 301, 1977
- [5] Van de Hulst, "Light Scattering by Small particles." J.Wiley pub., New York, 1957
- [6] H. Pruppacher, J.D. Klett "Microphysics of Clouds and Precipitation" Boston, D.Reidel Publishing Company, Boston, 1980
- [7] G. Mie, „Beiträge zur Optik trüber Medien, speziell kolloidaler Metallösungen.“ *Annalen der Physik, Vierte Folge*, 25(3), 377-445, 1908

## **THz Radiation and Applications (Review lecture)**

H.-W. Hübers, U. Böttger

Institut für Planetenforschung, DLR, 12489 Berlin, Rutherfordstr. 2, Germany

The TeraHertz spectral region - in the electromagnetic spectrum the region between millimeter waves and Infrared radiation - is on the cusp of pure academic investigation into the direction of practical applications. TeraHertz radiation is non-ionizing and can penetrate through materials like clothing, paper, plastics and ceramics. It is absorbed by the water vapor of the atmosphere. Thus it is predestinated for applications in a wide variety of industry and short distance communication.

In this presentation the specific properties of the THz region will be discussed in comparison to other spectral regions. Different THz radiation sources will be described. Applications of THz technology will be presented.

## Theoretical modeling of EM-Wave Absorption by a human body

S. Dreyßig<sup>1</sup>, R. Zichner<sup>2</sup>, M. Chandra<sup>3</sup>

<sup>1</sup> Kathrein Sachsen GmbH, Mühlau

<sup>2</sup> Fraunhofer ENAS, Chemnitz

<sup>3</sup> Professorship of Microwave Engineering and Information Technology, Chemnitz University of Technology, Chemnitz

Electromagnetic Waves incident on a human body are partly scattered and partly absorbed. The absorbed part of the incident EM-fields has become a subject of great interest because of its possible biochemical effects. The objective of this study is to provide a theoretical estimate of the amount of RF power absorbed by a human body when it is subjected to an incident EM-wave. In the study, the parts of human body, such as the limbs, torso and the head, have been modelled as simple flat rectangular or circular geometrical shapes that have a depth, thus imparting volume to the body parts. Such 'two-and-a-half dimensional' human body replicas were assumed to be filled with water. In the computational model, the human body 'phantom' constructed in this manner was illuminated with normally incident plane EM-waves. At the first 'air-to-body' interface waves are partially reflected and partially transmitted. The transmitted part is again partly reflected and transmitted at the ensuing second 'body-to-air' interface. This process leads to multiple reflections within the modelled human body. Using the complex dielectric properties of water at RF-frequencies, the energy dissipated by the EM-waves thus present within the body was estimated. The results of these investigations will be presented. The computed theoretical estimates of the RF-power absorbed by a human body should of interest to the RF-measurement community who have actually carried out laboratory measurements of the same. The results will emphasize the power absorption at 1 GHz.

# Fast Radio Wave Propagation Prediction by Heterogeneous Parallel Architectures with Incoherent Memory

Florian Schröder, Michael Reyer, Rudolf Mathar  
 Institute for Theoretical Information Technology  
 RWTH Aachen University  
 D-52074 Aachen, Germany  
 Email: {schroeder, reyer, mathar}@ti.rwth-aachen.de

**Abstract**—The present correspondence deals with radio wave propagation for urban scenarios on the cell broadband engine. Binary space partitioning trees are used to split the building data into manageable size for the parallel units of the cell. By choosing the size of the tree leafs both data transfer between units and runtime of the algorithm is significantly improved. The implementation of these techniques allowing for reflection demonstrates promising results for speeding up radio wave propagation.

## I. INTRODUCTION

Fast radio wave propagation plays an essential role in planning, analysis, and optimization of radio networks. A huge variety of prediction scenarios have to be evaluated. Consequently the predictions need to be fast. For the design of fast algorithms it has to be taken into account that the performance improvement of processors has shifted from higher clock speed to more cores. The paradigms of programming need to consider this hardware development resulting in many heterogeneous cores for general purpose calculations, e.g., multi core CPU, high performance graphics hardware (GPU), and so forth.

An overview of radio wave propagation models is given in [1] and [2]. Models proposed in the literature can basically be divided into (semi) empirical and ray optical models. Semi empirical models calculate the received power on the basis of frequency, distance, and an empirical part mainly describing the obstacle influence. The strength of such approaches is the speed of prediction. However, the prediction quality is low if the influence of deflection effects like diffraction, reflection, and transmission is high. This leads to ray optical approaches which identify ray paths through the scene to combat the lack of prediction quality at the cost of higher computation times.

In ray optical models the environment, e.g., buildings, is usually described by polyhedrons, formed of surface sections, called *facets* in the following. Several ray paths between the transmitter and receiver point are searched, regarding deflection effects as reflection on, transmission through, and diffraction at edges of the given facets. Ray optical models are classified as ray tracing and ray launching, depending on the way the ray paths are determined.

In ray tracing models all possible ray paths starting from a receiver point to the transmitter are searched. The set of possible ray paths is limited by a maximum number of deflection points, i.e., points where deflection effects occur. For each receiver point the possible ray paths have to be recalculated, as there might be complete different ray paths. This leads to multiple calculation of nearly identical ray path pieces, particularly, if receiver points are nearby located. Therefore, in [3] an extensive preprocessing is proposed which computes visibility of facets in advance. Hereby faster predictions are achieved.

Ray launching methods emit a finite set of rays from the transmitter in predetermined directions, cf. [4] and [5]. If rays hit a facet, possible deflection effects are performed. A receiver point is hit if the ray path crosses its proximity. As the rays disperse, important deflection points or even receiver points may not be hit. Alternatively, in [6] 3D cones are used instead of single rays. Beyond this work, mixed models have been investigated which follow partly rays and partly use empirical parameters, cf. [7]. Additional work on prediction algorithms, which is based on ray optical approaches, can be found for example in [8].

The high potential of parallel architectures is well known, especially for graphics cards it is discussed in [9], [10]. Using graphics cards for non graphical purposes is called GPGPU (General Purpose computations on Graphics Processing Unit), see [11]. There are numerous applications, e.g., physical simulation in [9] and sorting in [10]. With the introduction of the Playstation 3, for short PS3, in March 2007 the cell is available for research at low cost. The high potential of this architecture is described in [12].

Radio wave propagation has been applied on parallel architectures. Recent results for graphics cards may be found in [13], [14] and for the cell in [15].

The paper is organized as follows. We start with a description of radio wave propagation in Section II. After a brief introduction to parallel architectures in Section III, important principles of the implementation are presented in Section IV. This includes binary space partitioning of the data and a smart method of calculating intersections. In Section V results are

presented. Finally, we conclude this paper in Section VI.

## II. RADIO WAVE PROPAGATION

In this paper we use CORLA (Cube Oriented Ray Launching Algorithm) from [16] for radio wave propagation. The urban environment is described by a simple representation of three dimensional objects, particularly, buildings as polygons with one height, i.e., roof styles are neglected, see Figure 1. The model for the field strength prediction considers 1. line-

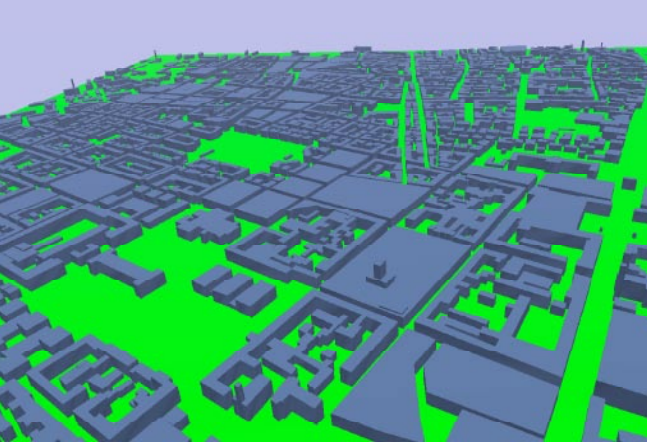


Fig. 1. Example of building representation in Munich, [1]

of-sight, 2. reflection, 3. horizontal diffraction, and 4. vertical diffraction as depicted in Figure 2. As building part of the

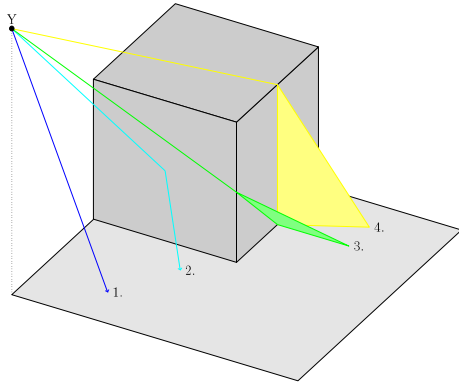


Fig. 2. Overview of ray optical effects

path attenuation we use a modification of the well known free space propagation formula. Using the overall distance  $d(p)$  of the path  $p$ , neglecting the antenna gains – this may be easily considered in a post processing –, adapting the path loss exponent  $\gamma$  according to the environment, and introducing an estimator  $z_A$  mitigating imprecise information about transmit powers leads to

$$L_0^{dB}(p) = 20 \lg(4\pi/\lambda) + z_A + 10\gamma \lg d(p),$$

where  $\lambda$  denotes the wavelength. The impact of the effects is modeled by polynomial terms of a low degree with the

change of angle of each effect as input. This results in the overall attenuation of a path  $p$

$$\begin{aligned} L^{dB}(p) &= L_0^{dB}(p) \\ &+ \sum_{i=1}^{n_R(p)} L_R^{dB}(\alpha_{R,i}(p)) \\ &+ \sum_{i=1}^{n_V(p)} L_V^{dB}(\alpha_{V,i}(p)) \\ &+ \sum_{i=1}^{n_H(p)} \sum_{j=0}^k z_{H,j} \alpha_{H,i}^j(p), \end{aligned} \quad (1)$$

$$(2)$$

$$(3)$$

where  $n_X(p)$  is the counter of the effect  $X \in \{R, V, H\}$  and  $\alpha_{X,i}(p)$  are the changes of angle of the  $i$ -th occurrence of the effect. Note, the functions  $L_X^{dB}$  given in (1) and (2) have the same structure as shown in (3). If multiple paths arrive at the same receiver point  $r$ , we do not add the paths but take the strongest path which is a reasonable approximation, see [8].

## III. PARALLEL ARCHITECTURES

Parallel architectures are widely spread nowadays. For a long time processing power was improved by increasing clock speed. But due to limitations in cooling and power consumption this is no longer applicable. Consequently, for further improvements processors move towards multi core layouts. Another trend is using specialized computational power for general purpose task. The most popular example is the GPU.

Generally speaking, systems with heterogeneous processor architectures and incoherent memory will be found more often and gain in importance.

### A. Heterogeneous Architectures

For heterogeneous architectures the task division is one of the challenging tasks. The CPU, a homogeneous architecture, is designed for all kinds of tasks, it is very flexible, and built for fast calculation and branching, while most other processing units are usually specialized for certain task. Regarding these tasks they are way faster than the CPU itself but on the price of being slow on other task or even incapable of executing them. On a homogeneous system your main concern is to supply each unit with the same work load, because the overall runtime is given by the slowest – in terms of runtime – unit. However, on heterogeneous systems it is also important to designate tasks with respect to the specialties of the hardware.

### B. Incoherent Memory

Many vendors make a great effort in offering systems with coherent memory. In such systems the hardware assures that all caches are at sync. Hence, if two units read a value from the memory, store it in their local caches, and one unit changes its value, without a coherency mechanism the second unit would work with an outdated value with undefined consequences. It is most likely that heterogeneous architectures have no coherent memory such that the software needs to take over the validity check of data from hardware. This has to be carefully considered when designing the software.

### C. Cell Broadband Engine Architecture

We use the the Cell Broadband Engine Architecture, for short cell or CBEA. It is designed amongst others to speed up memory processing and defying the memory wall, cf. [17], while keeping power consumption at low level as described in [18]. The cell processor is a chip with ten cores. These are a dual-core 64-bit IBM PowerPC for organizing tasks and running the operating system and eight additional cores called Synergistic Processing Elements, short SPE. It is a heterogeneous system on one chip with incoherent memory, the main memory accessible by all cores and the 256kB local memory of each SPE. This local memory is located between the main memory and the processor caches. It is very fast but of limited size compared to todays main memory. The SPEs use their own instruction set architecture for memory transfer and many optimized calculation operations. Its 128 registers are 128-bit wide supporting vector instructions – applying operations not on single data but on whole vectors in one step (SIMD - single instruction multiple data).

Our choice fell on this new type of processor, because it comprises the previous described attributes and has a high computational power on a low cost level. In order to exploit the processor potential the algorithms need to be parallelized and data structures must be designed to handle multiple access and keep their validity when handled by several processors. Particularly, the memory handling is very challenging due to the local SPE memories.

### IV. DATA STRUCTURES AND ALGORITHMS

The data structure of a program has a great impact on its performance. The importance of good data structure design gets more pronounced as the gain on speed for processors is much higher than for memory. This phenomenon, when a processor is burning cycles waiting for data to arrive, is called memory wall, see [17]. A careful designed data structure will reduce this effect. Good data structures should fulfill the following constraints: i) Partition the input data due to hardware constraints, like transfer block sizes etc. ii) Put the data in some order beneficial to the algorithms, e.g., data needed at consecutive steps should be grouped. iii) Enable fast access to subsets of data.

Applying those constraints on radio wave propagation for urban scenarios on a cell leads to binary space partitioning (BSP) trees with ropes. With BSP a set of data will be repeatedly divided into two subsets and saved into a tree structure. Each node of the tree represents a partitioning and each leaf denotes a subset of the final partition. In the following leaf is a synonym for subset. The leaves contain a set of facets and therefore the leaf size represents the number of facets within the leaf. Figure 3 shows a 2D representation of a tree, where each rectangle denotes a leaf and each line – excluding the outer frame lines – depicts the nodes. For example the vertical line roughly in the middle, splitting the image into two, is the root node followed by two horizontal lines splitting these halves again and so forth. Since the tree has no information about the neighborhood

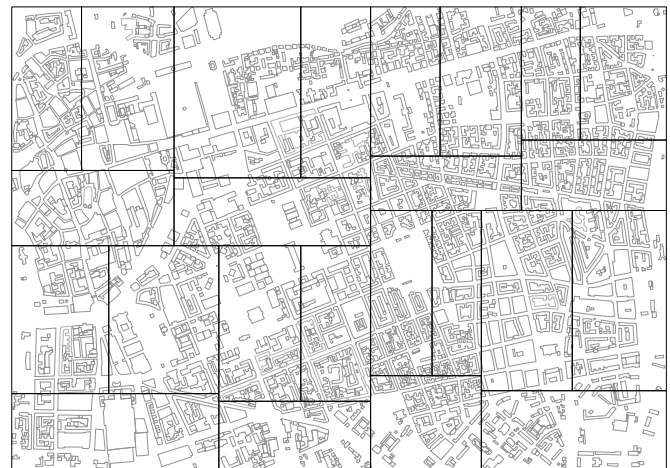


Fig. 3. Graphical representation of a BSP tree

of leaves, an additional structure is set on top of the tree, ropes. Ropes add to each leaf the information about their neighbors such that quick navigation among leaves is possible and constraint iii) is fulfilled. While constructing the BSP tree, it is ensured that the leaves need approximative the same size in memory. This size is set to a multiple of the optimal memory block transfer size for the hardware bus system of the PS3. It fits optimal into the limited local memory of the SPEs and it allows static memory allocation which is much more convenient then dynamic memory allocation on SPEs – not using dynamic allocation reduces memory management problems. Consequently constraint i) is fulfilled.

For explanation of constraint ii), the benefit to the algorithm, we need to explain the algorithm first. One of the most important parts of radio wave propagation is to determine which ray intersects with which facet. With a BSP tree it is very efficient to determine a subset (leaf) belonging to some coordinate or point; the complexity is at maximum the depth of the tree in binary decisions which is logarithmic for balanced trees. BSP trees are by design close to balance, i.e., there is very small variance of the leaf depth. For our purposes this needs to be generalized to the determination of all subsets lying on a path from transmitter to receiver. This can easily be performed by using the ropes providing the beneficial ordering of the data mentioned in constraint ii).

Hence, we have excluded a lot of subsets and all of its facets while determining the intersections. A detailed description of the algorithm to create such BSP trees can be found in [15].

For evaluation of the attenuation at receiver points paths to those points need to be calculated. Therefore, a sufficiently large amount of rays is launched from the transmitter into all directions. For each ray it is calculated, if the ray hits a i) receiver point, ii) a facet within the subset, or iii) the border of the subset. So either the attenuation is calculated or a ray optical effect has to be processed or the ray is followed in the neighboring subset.

As the calculation of the intersection between rays and

facets is an often repeated core component of this algorithm, its runtime should be minimized. Obviously the size of the leafs in the data structure may be chosen to optimize the number of candidates on which the intersection test is executed. A second measure is to carefully chose the number of rays while providing a certain level of accuracy for the resulting prediction. And thirdly, the number of calculations may be reduced by exploiting redundancy. In our case it is most likely that rays just differing in the vertical angle either all will hit a facet or pass over it. Meaning, in a full 3D calculation a bunch of rays will intersect the facet at same (similar) x and y coordinates but differing in the z coordinate, where z represents the height. By splitting up this 3D calculation into two 2D calculation, as suggested in [19], much of the redundancy is taken away. In Figure 4 the first phase is depicted where vertical overlaying rays are put together. The

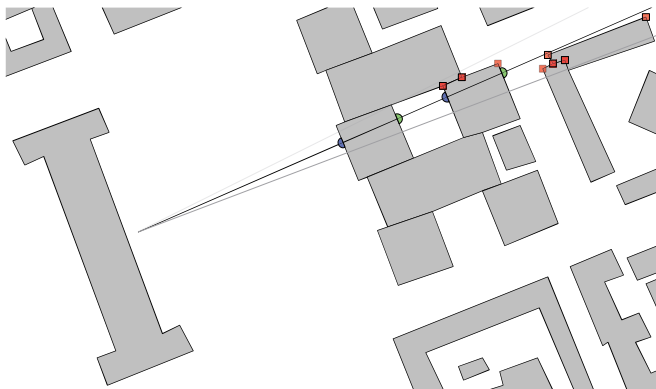


Fig. 4. First phase: determining intersections in xy-plane

green and blue half circles mark the position where a ray hits or drops out of a building. The red squares mark edges in a close cone around the ray, indicating candidates for horizontal diffraction. In the second phase the vertical overlaying rays are separated again to process the different effects. Figure 5 depicts the vertical diffraction in the second phase, where the numbers of vertical diffractions a path undergoes on its way to the receiving plane is given. So naturally a recursive

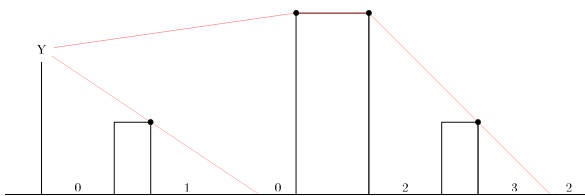


Fig. 5. Second phase: vertical diffraction

process is defined in which nodes can be discarded whenever all children are processed. The children are independent and therefore allow for easy parallelization.

V. RESULTS

As we have seen in the last section, the leaf size of a BSP tree has strong impact on the runtime and is therefore be

studied. Recall, the smaller the leaf size the fewer intersection calculations between rays and facets have to be performed per leaf, but at the cost of a higher complexity which is explained in the following. With a lower number of facets per leaf the number of leafs increases and therefore more ray transfers between leafs have to be executed. Additionally, the leafs cover a smaller area and consequently the probability that a facet crosses a leaf border grows. In such cases these facets have to be split up and stored in each leaf which increases the total amount of stored facets. In summary, the lower the leaf size the more memory is used, the more management in terms of transfers is needed and the more redundant calculations due to the doubling of cut facets have to be executed. Thus, it is to be expected that runtime will decrease with a decreasing leaf size, but that it will increase again for very low leaf sizes. Furthermore, it is to be expected that the number of leafs times the leaf size will not be constant – as it is in the optimal case – but increase with decreasing leaf size due to the doubling of facets.

The above observations can be clearly seen in Figure 6 comparing the solid red line representing the realized number of leafs and the dashed blue line displaying its lower bound. The solid red line is well above the blue one because on one hand the leaf size is a maximal and not an average value and on the other hand the number of leafs needs to be a natural number. The runtime is relative to the runtime with leaf size 2500 in which the number of leafs size is slightly greater than the number of SPEs; beyond this level side effects distort the measurement. Most interestingly, for big

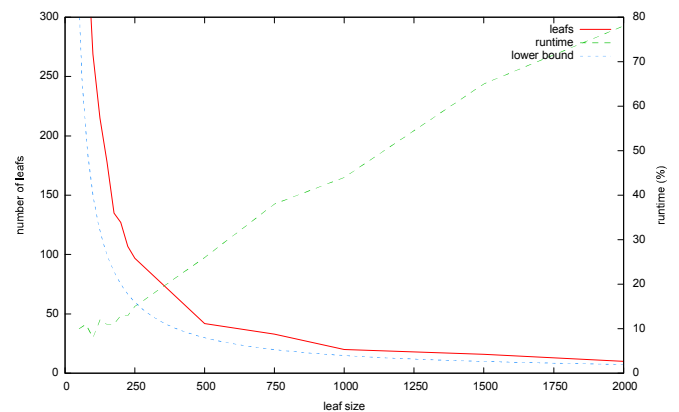


Fig. 6. Runtime and number of leafs over the leaf size

leaf sizes the relation to the runtime is approximative linear. For small leaf sizes the runtime is not monotonous. This effect is mainly motivated by the algorithm used for the BSP tree generation. To find the optimal partition is hard as the amount of facets within each subtree cannot be precisely determined with the information of the current set of facets because of the duplication of facets which cut a border line. Instead a greedy algorithm is used which in principle works as follows. Starting with all facets at the root the greedy algorithm divides the current set of facets generating two new children for the current node. This procedure is repeated until the desired leaf

size is reached. So a suboptimal solution with a relatively high degree of variation in the leaf size is attained. It is a topic for further research to optimize the generation of BSP trees which might be worthwhile taking into consideration that the BSP tree generation needs to be executed once for a given set of building data, whereas the radio wave propagation will be run quite often to get predictions for all base stations and their configurations within this area. Note, that those curves are strongly dependent on the evaluated scenario and therefore do not provide optimal values.

Ray generation has also an impact on runtime. While developing strategies for ray generation the trade off between prediction coverage and accuracy as well as speed needs to be considered. The prototype uses a uniform distribution of rays.

The receiver points are evaluated according to the path loss model of Section II. In Figure 7 an image representation of

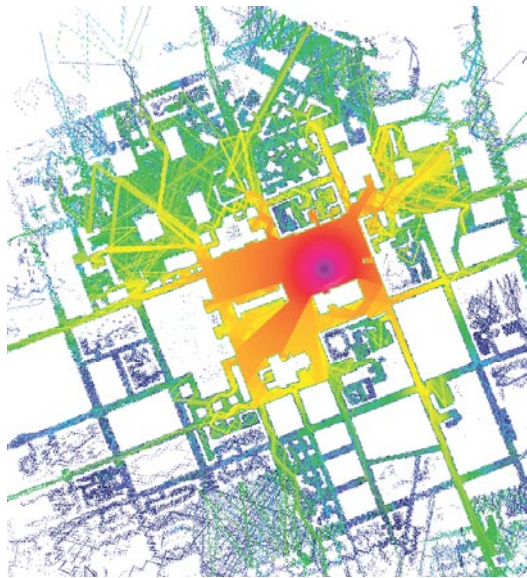


Fig. 7. Prediction with reflection in Munich, [1]

the result is shown. The receiver points are equally distributed on that area, i.e., each pixel represents a receiver point. Furthermore, only the reflection effect is activated.

The current implementation is comprised of a full 3D approach of ray evaluation and of a uniform distribution of rays. This results in a runtime of about 40 seconds for the Munich scenario which sounds slow at a first glance. However, the runtime per followed ray is comparable between cell and CPU implementations. Taking into account that more complex rays are followed on the cell, it is quite promising and should be significantly faster, when replacing the full 3D approach with the two times 2D version and introducing a smart ray generation and duplication. Note that both features are included in the CPU implementation already.

## VI. CONCLUSION

In this work a promising basis for speeding up radio wave propagation by parallel architectures is presented. The use of

binary space partitioning has shown two major advantages. Firstly, it enables for providing small independent data sets which can be processed in parallel. And secondly, the runtime of the algorithm can be sped up significantly as this partitioning also allows for a preselection of relevant data to be processed. First results show that the application on the cell broadband architecture will be significantly faster than a classical CPU implementation. This goal will be achieved after replacing the 3D ray launching approach by a two times 2D approach and a smart ray generation and duplication.

## ACKNOWLEDGMENTS

This research was partly supported by the UMIC excellence cluster of RWTH Aachen University

## REFERENCES

- [1] E. Damosso, Ed., *COST Action 231: Digital mobile radio towards future generation systems, Final Report*. Luxembourg: Office for Official Publications of the European Communities, 1999.
- [2] N. Geng and W. Wiesbeck, *Planungsmethoden für die Mobilkommunikation*. Springer, 1998.
- [3] G. Wölfle, R. Hoppe, and F. Landstorfer, "A fast and enhanced ray optical propagation model for indoor and urban scenarios, based on an intelligent preprocessing of the database," in *Proceedings PIMRC*, Osaka, Japan, 1999.
- [4] G. Durgin, N. Patwari, and T. S. Rappaport, "An advanced 3D ray launching method for wireless propagation prediction," in *Proceedings IEEE VTC Spring*, Phoenix, AZ, 1997, pp. 785 – 789.
- [5] M. Schmeink and R. Mathar, "Preprocessed indirect 3D-ray launching for urban microcell field strength prediction," in *Proceedings IEEE AP*, Davos, Switzerland, 2000.
- [6] T. Frach, "Adaptives hierarchisches Ray Tracing Verfahren zur parallelen Berechnung der Wellenausbreitung in Funknetzen," Ph.D. dissertation, RWTH Aachen University, 2003.
- [7] J. Beyer, "Ausbreitungsmodelle und rechenzeiteffiziente Methoden für die Feldstärkeprognose in städtischen Mikrozzellen," Ph.D. dissertation, Universität-Gesamthochschule Siegen, 1997.
- [8] R. Wahl, G. Wölfle, P. Wertz, P. Wildboz, and F. Landstorfer, "Dominant path prediction model for urban scenarios," *14th IST Mobile and Wireless Communications Summit, Dresden (Germany)*, 2005.
- [9] M. Harris, *GPU Gems*. Addison-Wesley, 2004.
- [10] P. Kipfer and R. Westermann, *GPU Gems 2*. Addison-Wesley, 2005.
- [11] "GPGPU." [Online]. Available: <http://www.gpgpu.org>
- [12] S. Williams, J. Shalf, L. Oliker, S. Kamil, P. Husbands, and K. Yelick, "The potential of the cell processor for scientific computing," in *CF '06: Proceedings of the 3rd conference on Computing frontiers*. New York, NY, USA: ACM, 2006, pp. 9–20.
- [13] M. Reyer, T. Rick, and R. Mathar, "Graphics hardware accelerated field strength prediction for rural and urban environments," in *Proceedings: European Conference on Antennas and Propagation (EuCAP)*, Edinburgh, Scotland, UK, November 2007, pp. 1–5.
- [14] A. Schmitz, T. Rick, T. Karolski, L. Kobbelt, and T. Kuhlen, "Simulation of radio wave propagation by beam tracing," in *Eurographics Symposium on Parallel Graphics and Visualization*, 2009.
- [15] F. Schröder, "Konzepte zur effizienten Umsetzung von Algorithmen für die IBM Cell-Architektur - Anwendung auf Verfahren der Feldstärkeprädiktion im Mobilfunk," Master's thesis, RWTH Aachen, 2008.
- [16] R. Mathar, M. Reyer, and M. Schmeink, "A cube oriented ray launching algorithm for 3D urban field strength prediction," in *Proc. IEEE International Conference on Communications ICC '07*, 2007, pp. 5034–5039.
- [17] W. A. Wulf and S. A. McKee, "Hitting the memory wall: Implications of the obvious," *SIGARCH Comput. Archit. News*, vol. 23, no. 1, pp. 20–24, 1995.
- [18] H. Hofstee, "Power efficient processor architecture and the cell processor," in *Proc. HPCA-11 High-Performance Computer Architecture 11th International Symposium on*, 2005, pp. 258–262.
- [19] J.-P. Rossi and Y. Gabillet, "A mixed ray launching/tracing method for full 3-D UHF propagation modeling and comparison with wide-band measurements," *Antennas and Propagation, IEEE Transactions on*, vol. 50, no. 4, pp. 517–523, Apr 2002.

## **Pre-Distortion for MF-MSK Systems in Nonlinear High Power Amplifiers**

L. F. Gergis

Misir Academy, Mansoura, Egypt

New communications services have created a demand for highly linear high power amplifiers (HPA's). HPA's are inherently nonlinear devices. The pre-distortion is one of the possible methods to compensate for HPA nonlinearities.

A proposed modulation scheme that produces a constant envelope continuous phase signal set with a power efficiency can be implemented by multiplexing of frequency / phase modulated signals and is referred to as multi-frequency minimum shift keying (MF-MSK) is described.

In this paper, the influence of the nonlinear distortions introduced by HPA of the transmitter is examined with the use of pre-distortion technique. The performance of the proposed scheme is checked through the analysis of MF-MSK signals. It is confirmed that the proposed pre-distorter with MF-MSK gives a good performance improvements in reduction of the bit error rate (BER) of the system.

# Towards a Realistic Propagation Prediction Model— A Self-tailored 3D-Digital Elevation Model with Clutter Information

Kin Lien Chee, Thomas Kürner<sup>1</sup>, <sup>1</sup>Senior Member, IEEE

**Abstract**—State-of-the-art propagation prediction models outperform the empirical and semi-deterministic models by taking into account terrain characteristics as well as clutter distribution. These models require all signature characteristics of the terrain and clutter are captured so that the wave propagation mechanisms can be further studied and analyzed using ray tracing [1] or ray launching algorithms [2] which are based on optical geometry. The effectiveness of such models prevails by the availability of accurate digital data of the environment. This paper presents an approach of constructing a 3D digital elevation model (DEM) of Hetzwege, Germany with extensive raw terrain and clutter data collected from on-site measurements using laser scanning. The accuracy of the self-tailored 3D DEM model will be verified by determining the LOS and NLOS signal level over a mobile WiMAX system (IEEE 802.16e) deployed in the region.

**Index Terms** — ray tracing, ray launching, DEM, mobile WiMAX

## I. INTRODUCTION

THIS investigation was defined under the framework of WiMAX pilot project Lower Saxony, Germany, with the aim to implement a 3.5 GHz WiMAX system (IEEE 802.16e) at Hetzwege and Abbendorf, within the county of Rotenburg (Wümme). The primary aim is to provide internet access to suburban or rural areas where optical fiber or cable can not be reached. It also serves as a good platform to provide a chance for collaboration between academic/research institutes and industries. Given a predefined base station site, our first task is to determine the possible coverage of the radio waves. With the transmitter overlooking the diversified landscape of Hetzwege with irregular terrain complements with areas largely covered by vegetation and man-made structures like houses, the coverage map will not be made accurate without considering the influence of terrain and clutter on wave propagation.

Having acknowledged the importance of terrain and clutter on outdoor wave propagation, the availability of such data especially in such a remote area is of great concern. Besides,

Manuscript received February 28, 2010. This work is supported by the Niedersächsischen Wirtschaftsministerium under the project “WiMAX in Niedersachsen”.

K. L. Chee is with the Institut für Nachrichtentechnik, Technische Universität Braunschweig, Schleinitzstrasse 22, 38106 Braunschweig, Germany (Tel: +49 531 391 2414; e-mail: [chee@ifn.ing.tu-bs.de](mailto:chee@ifn.ing.tu-bs.de)).

Prof. Dr. -Ing. Kürner, holds a full professorship at Institut für Nachrichtentechnik, Technische Universität Braunschweig, Schleinitzstrasse 22, 38106 Braunschweig, Germany (e-mail: [kuerner@ifn.ing.tu-bs.de](mailto:kuerner@ifn.ing.tu-bs.de)).

the integrity and precision of such information should not be overlooked especially in an environment surrounded by object sizes comparable to the corresponding wavelength of the propagating wave. Obstacles that may be deemed to be irrelevant to wave propagation in GSM or UMTS bands might be the reason for link failure in the case of 3.5 GHz WiMAX. Having considered all these effects, this paper details an approach of constructing a 3D digital terrain model from scratch and later furnishing the model with clutter data collected from on-site measurement using laser scanning, in order to deliver a 3D digital elevation model (DEM) of Hetzwege, Germany. To investigate whether the precision of the self-tailored 3D DEM model meets the need for wave propagation prediction at 3.5 GHz, the regions which fulfill the line-of-sight (LOS) and non-line-of-sight (NLOS) conditions are determined and later the simulation results are verified with the signal levels derived from the measurement campaign on-site.

This paper is organized as follows. An overview of the construction of 3D DEM is presented in section II. Section III details the approach of deriving and processing the clutter information. Section IV discusses the construction of digital terrain model and how the derived clutter information is integrated into the terrain data to deliver a final digital elevation model with clutter information. The verification of the model using simulation is discussed in section V and section VI details the measurement campaign on site. Section VII compares the simulation results with measurements and a final conclusion is presented in section VIII.

## II. HOW IS THE 3D DEM MODEL CONSTRUCTED

The construction of the 3D DEM starts from obtaining the raw terrain data derived from a relevant source. With the advancement of geospatial data acquisition technology, topographic data derived from various remote sensing technologies have been studied. These include air and space-borne imagery, light detection and ranging (LiDAR), sonar as well as terrestrial 3D laser scanning data [3] etc. Depending on the targeted applications, a technique that delivers data with higher accuracy than the other may demand higher degree of resources for example processing time.

Having in mind our primary aim here is to construct a DEM model not meant to compete with other remote sensing technology, rather, we aim to build a model with reasonable

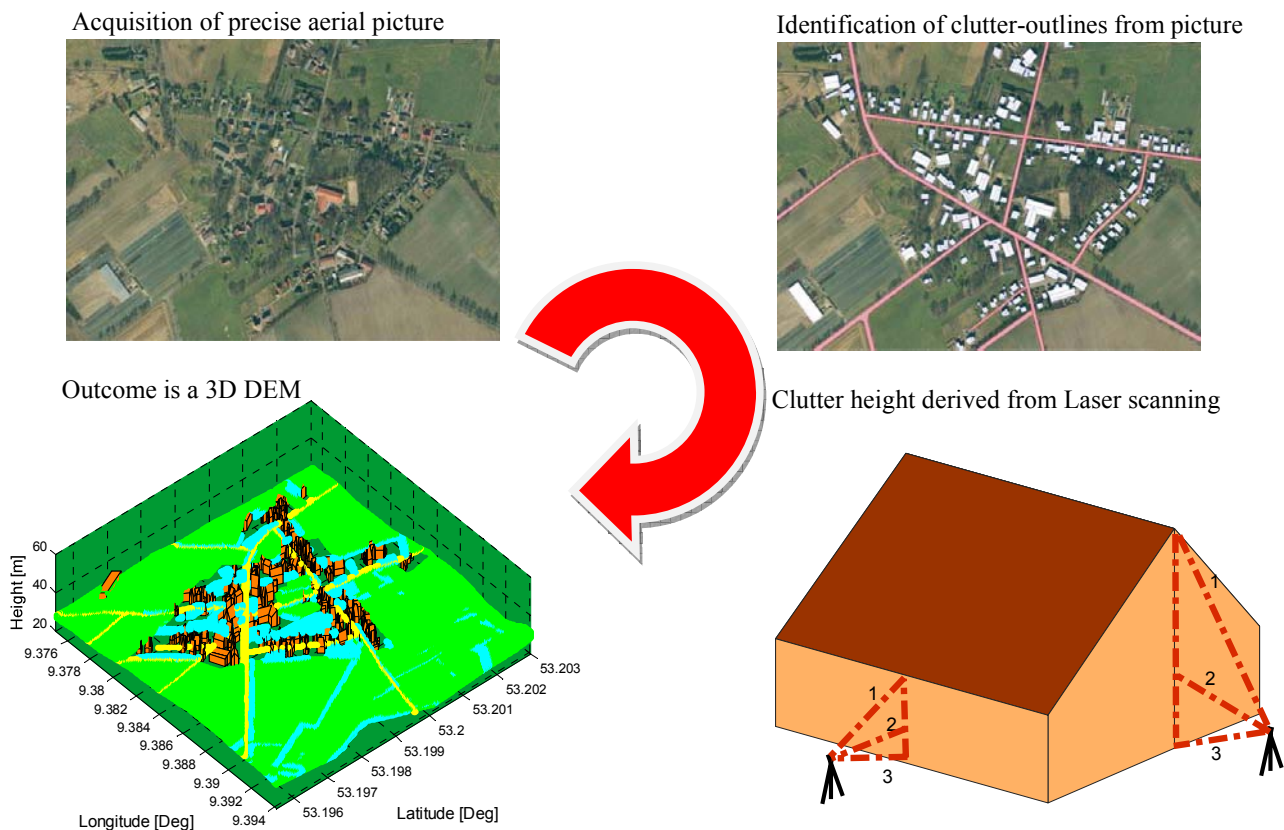


Fig. 1: Final Digital Elevation Model of Hetzwege

accuracy that suits the need as a background environment for the radio network planner. A reliable data source that is freely available has become an important concern for us when choosing the data source, therefore, in this paper, the raw data from Shuttle Radar Topography Mission (SRTM-3) [4] is used. SRTM is an international research effort spearheaded by the National Geospatial-Intelligence Agency (NGA) and the National Aeronautics and Space Administration (NASA) which flew onboard the Space Shuttle Endeavour during the 11-day mission in February 2000 in order to deliver the high resolution digital elevation data of the earth. The raw data are freely available for research purposes with a resolution as high as 30 m in the US region (SRTM-1) and 90 m (SRTM-3) for the rest of the world.

Figure 1 summarizes the steps concerning the construction of a 3D DEM. An aerial view with high precision of Hetzwege has been purchased from the land surveying authority of Lower Saxony (Landesvermessung und Geobasisinformation Niedersachsen, LGN). The clutter outlines can be identified from the geo-referenced aerial picture using Mapwindow GIS program and saved as 2D polygon shapefiles. To further extend the 2D shape data into 3D, the clutter heights are derived from on site measurement using laser scanning. For this purpose, a Laser distance meter from Leica DISTO D8 is used. The laser distance meter is equipped with an integrated camera which enables identifying the reflected laser point on the LCD screen. Optionally, the measured data can be saved on the

built-in memory and later the data can be imported into a AutoCAD software. After combining the 2D shape data and the clutter height information derived from on site measurement, the clutter information is organized and thereafter extracted from the aerial picture so that it can be combined with the terrain data to deliver a 3D digital elevation model.

### III. CLUTTER INFORMATION

The clutter information is obtained from the high precision aerial picture of Hetzwege which was purchased from LGN. The clutters that can be identified from the picture can be categorized as follows (i) streets, (ii) houses, (iii) trees, (iii) green fields. Streets include all roadways that can be identified from the map. Footpaths among the vegetation as well as bicycle alleys which are common in these areas are included as long as they can be identified on the high precision aerial picture. Houses includes all types of man-made structures including all residential buildings, schools, restaurants as well as storage units or garages that are separated from the main residential unit. Having known that the area is largely covered with vegetation, a single vegetation category may not accurately describe the environment. Therefore the vegetation is split into trees and green fields. The category trees mainly includes plants along roadsides or in the area which can be identified from the map. The category green fields is defined to include those agriculture plantations or wild areas covered with

grass which can be separated from trees. The outlines of all these different clutter types are first identified from the aero-photo using the software Mapwindow GIS as polygon shape data, thereafter the coordinates are extracted and organized as respective 2D shape data formats which consist of longitude and latitude attributes of the polygons. To further extend the 2D clutter information to 3D, clutter heights are obtained from on site measurement using laser scanning. The aero-photo indicates about 250 houses that can be identified in the region of Hetzwege. A Laser distance meter is used to measure the height of the vertices of each identified polygon on site. The clutter heights can be measured either with the aid of reflected laser point from the target or by 3-points measurement using the cosine law of Pythagoras which can be automatically given by the Leica DISTO D8.

To effectively work with the large amount of clutter information collected, data mining technique is used. Here, a number is assigned to each of the houses in the clutter. Each of the houses may consist of  $j$  parts, for example a garage or store room may be separated from the main living unit. Furthermore, each part should consist of  $k$  sides, where  $k=1$  is always the roof top etc. Each of the sides can be regarded as a polygon which is defined by its  $m$  vertex, where each of the vertices is described by 3 attributes, i.e. longitude, latitude and height. Figure 2 describes the classification of house clutter. Similarly, streets, trees and vegetations are grouped according to their location as polygons, each of the groups is assigned a number and they are described by the vertices of the polygons in terms of longitude, latitude and height as discussed in the house clutter.

### Classification of Houses

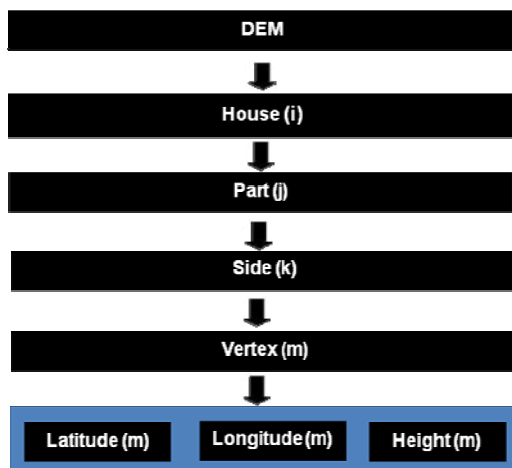


Fig. 2: Classification of House Clutter

#### IV. DIGITAL ELEVATION MODEL

As mentioned before, our 3D digital terrain model is built based on the SRTM-3 raw data. There is no doubt that these data which are available on the mission webpage are interesting for research purpose since the result achieved by these data can be easily reproduced due to free data source; however, two challenges have been identified and must be resolved in order

to keep the accuracy of the model manageable. (i) The SRTM-3 data has a rather poor resolution of 90 m, therefore the distance within 90 m must be interpolated. (ii) SRTM data are obtained using a specially modified radar system installed onboard the Space Shuttle which flew over the earth, the raw elevation data obtained should have included the height of the clutter information. Therefore, it may sound logic to directly adopt the SRTM elevation data as complete DEM with clutter information. Nevertheless, elevation data obtained from Space Shuttle are poorly resolved in the existence of vegetation due to the water content of plants. Several approaches have been proposed to revise the SRTM data [5,6,7], for example by correlating these with the ground-measured vegetation canopy height via linear regression [5]. Having considered the above mentioned problems concerning the poor resolution of the SRTM data, it is justifiable that the resolution of SRTM data is merely sufficient to describe the terrain surface. This implies that the clutter information must be separately integrated into the terrain data in order to construct a complete DEM with clutter distribution.

The construction of the terrain start by identifying the area of interest from the aerial picture. It should include the base station and all potential customers who may be interested to subscribe for internet access via the implemented WiMAX system on site. The area of interest is partitioned into equal sized-grids of 2m which gives a 300 x 900 pixel matrix. The terrain model of the area of interest is interpolated from the SRTM data. To remove the effect comes from the clutter distributions, the raw SRTM data must be preprocessed. Given the fact that the SRTM-3 is merely as accurate as 90 m, the clutter heights that randomly distributed within each 90 m grid can be regarded as positive noises added to the terrain surface data. To effectively remove these positive noises from the terrain surface, the distribution and height information of the identified clutters presented in the previous section must be used. Figure 3 shows the histogram of the clutter distribution, with the clutter height given in x-axis and y-axis showing the corresponding frequency of occurrence in pixels. The two Gaussian distributions with mean values located at 4 m and 11 m represents the corresponding mean value for houses and

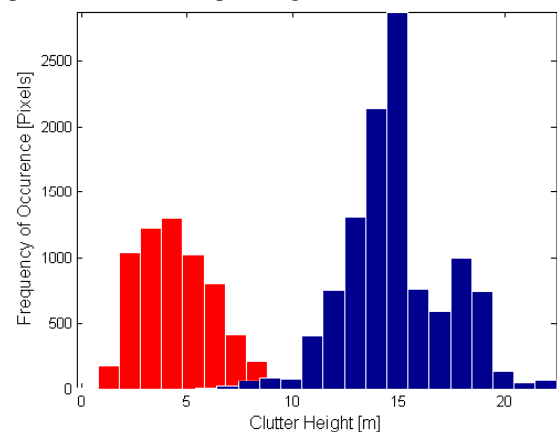


Fig. 3: Histogram of clutter distribution for Houses (red) and Trees (blue)

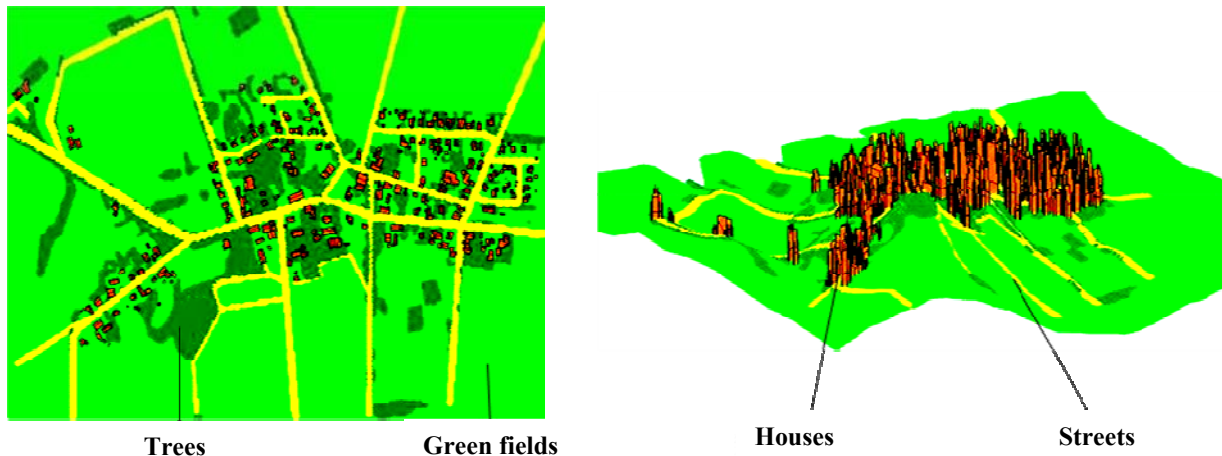


Fig. 4: Final digital elevation model of Hetzwege

trees. To remove the effect due to these two main clutter types, at each pixel where the clutter is identified, the height value from the original SRTM data is subtracted by the corresponding mean values, depending on whether the positive noise results from houses or trees. Upon removing the clutter information from the original SRTM data, the terrain model must be smoothed with a moving average filter to deliver a smooth terrain surface model which can better describe the real terrain surface on site. The clutter information described in Section III can then be integrated into the terrain model in order to deliver a complete DEM with detailed clutter information. To simplify the complexity working with different clutter layers and terrain surface data, all clutter information is integrated into the terrain data to deliver a final raster map. Due to the fact that houses are merely described by their vertices, those data points fall within a particular polygon (rooftop, side with  $k=1$ ) must be sampled in order to reflect the clutter height. The equation of a plane can be represented as follows

$$Ax + By + Cz + D = 0. \quad (1)$$

With the coefficients A, B, C and D can be derived from the vertices coordinates that are used to describe a polygon. The  $x_1$ ,  $y_1$  and  $z_1$  correspond to the longitude, latitude and height of the first vertex point of the polygon etc,

$$A = \begin{vmatrix} 1 & y_1 & z_1 \\ 1 & y_2 & z_2 \\ 1 & y_3 & z_3 \end{vmatrix}, B = \begin{vmatrix} x_1 & 1 & z_1 \\ x_2 & 1 & z_2 \\ x_3 & 1 & z_3 \end{vmatrix},$$

$$C = \begin{vmatrix} x_1 & y_1 & 1 \\ x_2 & y_2 & 1 \\ x_3 & y_3 & 1 \end{vmatrix}, D = \begin{vmatrix} x_1 & y_1 & z_1 \\ x_2 & y_2 & z_2 \\ x_3 & y_3 & z_3 \end{vmatrix} \quad (2)$$

Therefore the height  $z$  of each of the sampled points ( $x$  and  $y$ ) within a particular polygon can be interpolated with equation (1). Figure 4 presents our final 3D DEM with detailed clutter information.

## V. MODEL VERIFICATION

Having the self-tailored 3D DEM on hand, it would be interesting to know how accurate the model is or whether the model meets the requirements as a 3D map that can be used for our wave propagation study. In other words, some ways to assess the accuracy of the model must be developed before it is confirmed that the model fits its original purpose. Given a map that shows the actual environment of the radio network, it would be interesting to know whereabouts in this map a good coverage can be achieved given a predefined base station location. This prompts us to develop a mechanism to separate LOS and NLOS area from the map. Before any mechanism is developed, it is worth looking at definition of LOS. One of the possible definition will be to search for direct connection between the transmitter and the receiver. As long as the straight line joining the two antennas are not interrupted by terrain, LOS condition is given. This seems to be only able to confirm those points where NLOS condition is fulfilled. However, for points that are surrounded by obstacles but just with narrow slit so that the direct line connecting the two antennas is cleared, it would be unfair to deem these points as LOS, as the diffraction loss results from the surrounding obstacles can not be ignored. Owing to this, a more pronounced method to take into account

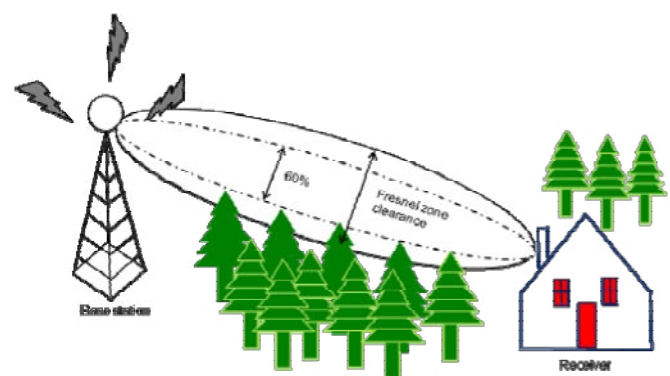


Fig. 5: Definition of LOS

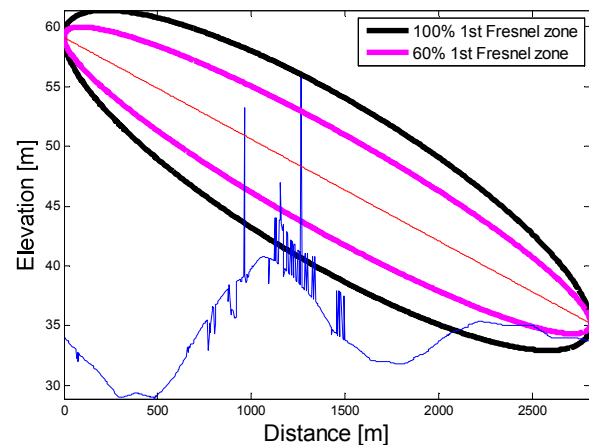
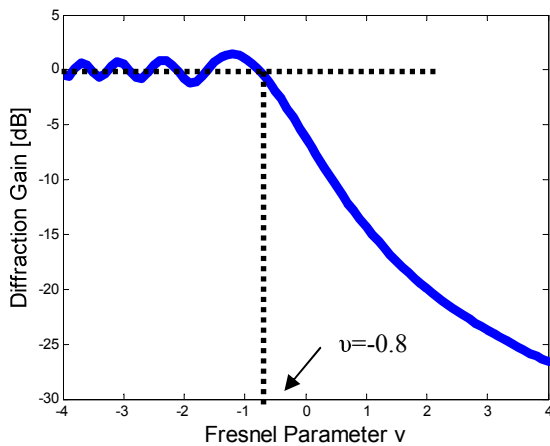


Fig. 6: (a) Single Knife Edge Diffraction, (b) Example of Terrain Profile Generated from Double Bresenham Algorithm

the direct environment close to the straight line connecting the two antennas must be used. Figure 5 shows the scenario about how a more pronounced LOS condition is defined in this paper. For each of the point on the map, a Fresnel zone is established between the transmitter and the receiver, which is defined as

$$F_n = \sqrt{\frac{n\lambda d_1 d_2}{d_1 + d_2}} \quad (3)$$

Where  $n=1$  represents the first Fresnel zone,  $\lambda$  is the wavelength of the operating signal,  $d_1$  and  $d_2$  are the distance from the transmitter to the main obstacle and from the receiver to the main obstacle, respectively. To obtain a LOS connection, no obstacle should stay within 60% of the first Fresnel zone. The 60% corresponds to Fresnel parameter  $v = -0.8$  used in the single knife edge diffraction equation, where diffraction loss for a Fresnel parameter smaller than  $-0.8$  can be ignored as shown in Figure 6(a), with

$$v = \frac{\sqrt{2} \cdot h}{F_1} \quad (4)$$

$$h = 0.5657 \cdot F_1 \quad (5)$$

In order to determine whether the LOS condition is fulfilled, the detailed terrain profiles between the transmitter and each point on the map serving as receiver are needed. Choosing a suitable computer graphic methodology to generate terrain profiles between two points from the raster map, is a matter of choice between accuracy and computation time. Methods which generate terrain profiles with high accuracy may involve complicated path search mechanism that leads to high computation time. In this paper, the Bresenham algorithm [8] is used. A single Bresenham algorithm performs path search either horizontally or vertically which runs parallel to the coordinate axes. A double Bresenham algorithm further improves the path search diagonally therefore allowing a subset of nodes of the single Bresenham algorithm to be identified.

Figure 6(b) shows an example of the terrain profile generated from the algorithm, where the pink ellipse corresponds to 60% of the first Fresnel zone and the black ellipse corresponds to 100% of the first Fresnel zone. Those LOS points where obstacles extend into 60% of the first Fresnel zone are deemed as obstructed LOS. Figure 7 shows the LOS and NLOS distribution at Hetzwege determined using the described algorithm, where yellow represents the area with LOS condition fulfilled and blue represents the area where either obstructed LOS or NLOS condition are determined. The observation point is set at 25m above ground (or 59 m in absolute height) as marked with red 'x'.

## VI. MEASUREMENT CAMPAIGN

To further verify if the simulation results presented in section V represent the actual fact, a measurement campaign was defined and conducted in July 2009 using the WiMAX system deployed at Hetzwege where the base station (BS) antenna is installed on a mast of 25m above ground. The BS antenna is located north-west of the area as shown in the 3D DEM. A 4-column array antenna from Andrew, APW435-12014-0N, is used with azimuth of  $115^\circ$  and downtilting of  $2^\circ$ . The sectorized antenna operates at 3.5 GHz with a maximal gain of 23 dB at the boresight, a horizontal beamwidth of  $25^\circ$  and a vertical beamwidth of  $50^\circ$ . The input power from the base station is 3.2 W. At the receiver side, the TSMW WiMAX scanner from Rohde & Schwarz is used, where the omni-directional antenna was mounted on the vehicle roof. External GPS is used to correlate the measured position to the measurement data and both data are output to a laptop operating with dedicated software ROMES v4.11 delivered together with the TSMW scanner. The scanned signal can be displayed on screen as well as recorded continuously for further processing. The TSMW scanner is installed on a vehicle can be displayed on screen as well as recorded continuously for further processing. The TSMW scanner is installed on a vehicle which is driven around all possible routes in the area at a speed of 40 km/h meanwhile the received signal strength is recorded. Figure 8 shows the base station and the receive antenna used during the measurement campaign.



Fig 7: LOS (yellow) and Obstructed LOS/NLOS (blue) distribution at Hetzwege

## VII. RESULTS

Figure 9 shows the path loss determined from the measurements by considering the angle of departure (AOD) so that the effect of antenna is excluded. Points that are measured from location where LOS condition is determined in the simulation before are displayed in red, while measurement points determined from the area that are classified either under obstructed LOS or NLOS from the simulation are given in blue. The result indicates that the signals received at locations where LOS is predicted in the simulation have lower path losses. The path losses at these positions can be better described by free space loss as given in cyan color. Path loss levels at positions where obstructed LOS or NLOS condition is predicted have obviously higher path losses which can be attributed to the



Fig 8: Base Station Antenna (left), Receiver Antenna (right)

presence of diffraction induced by the terrain or clutter. The two distinctive signal levels derived from on-site measurement using the deployed WiMAX system match well the predictions obtained from simulation which are based on the self-tailored 3D DEM. This implies the validity of the 3D DEM for wave propagation studies and hence allows further derivation of the propagation channel model based on this 3D DEM

## VIII. CONCLUSION

An approach of constructing a self-tailored 3D DEM for Hetzwege is presented in this paper. This approach aims to deliver a DEM for remote area where digital maps are neither

freely available nor readily available for purchase with reasonable accuracy suitable for wave propagation study. The proposed DEM captured all important clutter information which contributes significantly to the wave propagation at 3.5 GHz. The proposed DEM is constructed on the basis of the readily available SRTM data with clutter information derived using laser scanning. Typical clutter groups that are identified in this area include houses, streets, trees and green fields. To verify whether the accuracy of the model meets the requirements as a 3D map for network planning, a mechanism

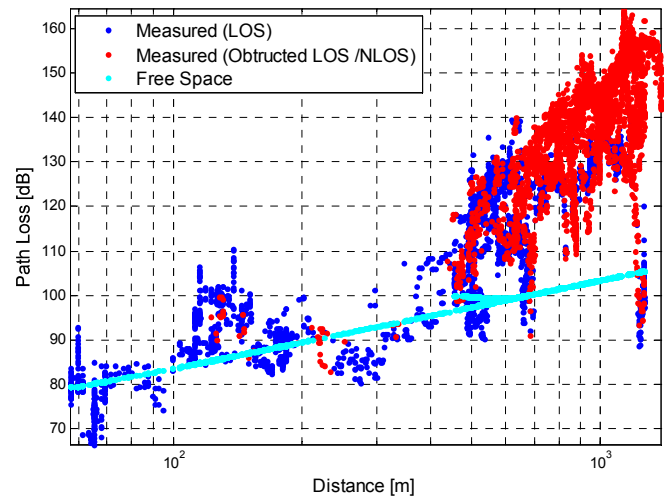


Fig 9: Path Loss [dB] Versus Distance [m] from Base Station at Hetzwege

is proposed to determine the area where LOS conditions are fulfilled. The simulation aims to separate the area with good coverage from the remaining area for a predefined base station location. It takes into account the Fresnel zone between the transmitter and the receiver positions to determine if the diffraction loss plays a significant role when LOS propagation is concerned. In order to further verify if the simulation results reflect the truth, measurement campaigns were conducted on site using the deployed WiMAX system at Hetzwege. The path loss derived from measurements shows two distinctive signal levels which correspond to the signal levels at LOS and NLOS (including obstructed LOS). The path loss at those positions where LOS is predicted can be well described by free space loss. The path loss at positions where obstructed LOS or NLOS conditions are predicted are higher, this can be attributed to the presence of diffraction induced by terrain or clutter distribution. The well matching between the simulation and measurement results validates the accuracy of the self-tailored DEM. Future work includes study of wave propagation in NLOS regions where diffraction and scattering are dominant. Furthermore, given the fact that the areas are largely covered by vegetation, wave propagation at vegetation will be investigated. In addition, multipath effect results at dense housing areas are yet to be studied. The wave propagation effects can first be studied empirically and then eventually serve as background map for ray tracing simulation.

## REFERENCES

- [1] Kürner, Thomas; Cichon, Dieter J.; Wiesbeck, Werner, Concepts and results for 3D digital terrain-based wave propagation models, *IEEE Journal on Selected Areas in Communications* 11 (7), pp. 1002-1012
- [2] Durgin, G.; Patwari, N.; Rappaport, T.S. Improved 3D ray launching method for wireless propagation prediction, *Electronics Letters* Volume 33, Issue 16, 31 July 1997 Page(s):1412-1413
- [3] Tarig A. Ali, "Building of robust multi-scale representations of LiDAR-based digital terrain model based on scale-space theory", *Optics and Lasers in Engineering* 48 (3), pp. 316-319.
- [4] Werner, M., 2001, Shuttle Radar Topography Mission (SRTM), Mission overview, *J. Telecom.(Frequenz)*, v. 55, p. 75-79.
- [5] J.M. Kellndorfer, W.S. Walker, and M.C. Dobson, J. Vona, M. Clutter, „Vegetation Height Derivation from Shuttle Radar Topography Mission Data in Southeast Georgia, USA“.
- [6] B. Smith and D. Sandwell, "Accuracy and resolution of Shuttle Radar Topography Mission data." *Geophysical Research Letters*, vol. 30, pp. 1467-1470, 2003.
- [7] C.G. Brown, "Tree height estimation using Shuttle Radar Topography Mission and ancillary data." Ph.D. Thesis. Dept. of Electr. Engineering and Computer Science, The University of Michigan, Ann Arbor, Michigan, 2003.
- [8] J.E. Bresenham, "Algorithm for computer control of a digital plotter", *IBM System Journal* Vol. 4, No. 1, 1965.

# Effect of Multipath on Code-Tracking Error Jitter of a Delay Locked Loop

Mariano Vergara , Felix Antreich , Achim Hornbostel  
German Aerospace Center (DLR), Germany

## ABSTRACT

The degradation caused by multipath to the tracking performance of a Delay Locked Loop (DLL) entails two factors: a bias in the pseudorange estimation arises, and the tracking jitter is altered. While the former aspect is well known, the latter has received scant attention in the navigation literature. In this contribution we want to show that a very straightforward mathematical modelling of these phenomena provides a helpful tool for the assesment of the performance of a GNSS (Global Navigation Satellite System) receiver.

## INTRODUCTION

The impact of multipath on code tracking accuracy is often represented by the maximum mean error resulting from the propagation along the Line-Of-Sight (LOS) and a secondary path, the latter being either in-phase or in opposition of phase with respect to the LOS, as a function of the relative delay of the secondary ray. Amongst the limits of this so called "multipath envelope", two in particular are to be noted: the multipath envelope is valid only for a two-paths scenario and furthermore the multipath envelope brings information only about the maximum mean value of the error. This is a very poor statistical characterization for assessing the performance of any other estimator. Indeed also the variance of the tracking error is important and this is also affected by multipath, albeit the latter phenomenon seems to have been overlooked in the recent works. In partoculat, adopting the same variance for both a LOS scenario and a multipath scenario is not always reasonable, because in general multipath propagation alters the way the input noise affects the tracking process.

The full description of the role played by channel noise in a synchronous control system as the Delay Locked Loop (DLL) poses a very complex mathematical problem, ow-

ing to the specific nonlinearity of the system. Nevertheless, if some assumptions are made, the problem can be still solved satisfactorily with linear theory, and with this approach it has been possible to determine the variance of the tracking error as a function of noise, signal and receiver parameters. This model, though, is valid in the case in which only the Line-Of-Sight (LOS) is present. In the first part of this work we extend the linear model of the tracking error variance to the case of a multipath scenario. Once that the tracking error variance and the tracking error bias experienced by a DLL in a mulipath scenario with an arbitrary number of paths are expressed in a closed form, the multipath tracking performance of a DLL is described in a more complete way. The main contribution of this work, indeed, is to propose a new "metric" in the characterization of the multipath error of a DLL. Instead of characterizing the multipath effect by means of the *multipath envelope*, which is valid only in a two-paths scenario and looks only at the mean value of the tracking error , we propose to describe the performance degradation due to multipath in terms of Root Mean Square Error (RMSE): for a given realization of a multipath channel with an arbitrary number of paths, the bias and the variance of the tracking error are calculated as function of the channel and receiver parameters; these two quantities are then merged into the RMSE. In this way, in only one parameter the joint effect of noise and multipath propagation is expressed. This new metric provides a simple tool to assess the multipath performance of any single-antenna GNSS receiver based on a DLL structure.

## SIGNAL MODEL

In order to characterize the influence of multipath, we model the GNSS signal impinging on the receiver, after

Doppler removal and base-band conversion, as:

$$r(t) = \sqrt{P} c(t - \tau) + \sqrt{P} \sum_{n=1}^N \alpha_n c(t - \tau - \tau_n) e^{j(2\pi D_n t + \vartheta_n)} + n(t), \quad (1)$$

in which:

$c(t)$  : Pseudo-noise (PN) code of unitary power.

$P$  : Signal carrier power.

$\tau$  : Code phase of the LOS component.

$f_0$  : Carrier frequency of the LOS component. It is the sum of the carrier frequency of the GNSS signal plus the LOS Doppler.

$N$  : Number of the multipath rays.

$\alpha_n$  : Multipath relative amplitude of the n-th ray.

$\tau_n$  : Multipath excess Delay of the n-th ray. From now on, simply Multipath delay.

$D_n$  : Relative Doppler shift or residual Doppler. Said  $f_n$  the carrier frequency on the n-th ray, then  $D_n = f_n - f_0$ .

$\vartheta_n$  : Carrier phase for the n-th path.

$n(t)$  : White Gaussian noise.

The PN code is a DS-CDMA signal spread with a BPSK signal:

$$c(t) = \sum_{k=-\infty}^{\infty} a_k p(t - kT_c) \quad (2)$$

with

$T_c$  : Chip interval.

$a_k$  : Binary pseudo-noise signature sequence. Its elements are random, independent, aperiodic equally likely.  $a_k \in \{0; 1\}$ .

$p(t)$  : Impulse response of the pulse shaping filter.

For long sequences the power spectrum of the PN code is asymptotically equal to the spectrum of the pulse. Holding this, the cross-correlation between the incoming PN code and the locally generated code can be expressed as a function of the pulse spectra:

$$R_{c\hat{c}}(\varepsilon) = \frac{1}{T_p} \int_{T_p} c(t - \tau) \hat{c}(t - \tau) dt = \int_{-B}^B C(f) \hat{C}^*(f) e^{j2\pi f \varepsilon} df, \quad (3)$$

where:

$C(f)$  : Pulse spectrum.

$\hat{c}(t)$  : Locally generated PN code.

$\hat{C}(f)$  : Spectrum of the pulse of the locally generated PN code.

$\hat{\tau}$  : Estimate of the code phase  $\tau$ .

$T_p$  : Integration time.

$B$  : Pulse bandwidth.

$\varepsilon = \tau - \hat{\tau}$  : Tracking error.

By defining the cross-correlation in the frequency domain as in (3), it is possible to carry out a general formulation which is independent of the pulse used. In this model the multipath is fully described by time invariant deterministic parameters, that can be arranged in the vectors  $\alpha$ ,  $\mathbf{D}$ ,  $\tau$ ,  $\vartheta$ , each of which containing N entries, one for every multipath ray. Modeling the multipath in this fashion for a DLL requires the channel, and hence the multipath parameters, to be static in a time span equal to the inverse of the loop bandwidth [1].

The objective of the DLL is to estimate the code phase (time-delay)  $\tau$  and to track this quantity as the users and the satellite move. The most important statistical characterization of an estimation error involves the determination of its bias and variance. In other words, the tracking error is to be characterized in terms of moments of the first and second order. In doing this we will make two assumptions:

**Steady-state tracking** : the DLL is already "tracking" or "in-lock" and the joint effect of multipath and noise does not cause a loss-of-lock.

**Small tracking jitter** : The tracking point oscillates around the lock point in a restricted set of values, for which the composite discriminator is approximately linear.

## TRACKING ERROR BIAS

When as input to the DLL there is the composite incoming signal (1), rather than only the desired Line-Of-Sight (LOS), the cross-correlation with the reference PN code becomes distorted. This happens because the multipath is a sort of disturbance that is highly correlated with the useful signal. As a consequence of that also the discriminator function is distorted, and with it also the overall tracking performance of the DLL is altered. We call the distorted discriminator "composite discriminator", and we denote it by  $S_c(\varepsilon)$ . If the multipath propagation is modeled as in (1), it is possible to express the composite discriminators as function of the multipath parameters, the pulse spectra of the transmitted PN code and of the locally generated PN code and of the correlator spacing. The expression depends of course on the kind of DLL structured used, and then on the particular discriminator function.

Before writing all the composite discriminator functions, we introduce the Doppler attenuation coefficient, which is the attenuation that every ray undergoes because of its relative Doppler shift. This attenuation depends jointly on the integration time  $T_p$  and its relative Doppler  $D_k$ , namely on the product of both  $D_k T_p$ :

$$G_k = \int_{-\frac{T_p}{2}}^{\frac{T_p}{2}} e^{j(2\pi D_k t + \theta_k)} dt = \text{sinc}(D_k T_p) e^{j\theta_k} \quad (4)$$

We define the overall attenuation coefficient, which takes into account both the one already described by the coefficient  $\alpha_k$  and the one due to Doppler, as:

$$\gamma_k = \alpha_k |G_k| = \alpha_k \text{sinc}(D_k T_p) \quad (5)$$

In Table 1 the several composite discriminators are reported. There we have used the notation  $S_{c, DLL \text{ type}}(\varepsilon)$ , where the field "DLL type" stands for the DLL structure:

**Coh** : Coherent DLL.

**Nc** : Non-Coherent DLL.

**Dp** : Dot-product DLL.

$\Delta\Delta$  : Double delta DLL (Coherent).

The term  $\vartheta_c(\varepsilon)$  appearing in Table 1 is the so called "composite phase". This is the steady-state error bias that due to the inability of the PLL to discern the carrier phase of the LOS from those of the other multipath components. The composite phase amounts to:

$$\vartheta_c(\varepsilon) = \arctan \left\{ \frac{\sum_{k=1}^M \alpha_k \text{sinc}(T_p D_k) R_{c\hat{c}}(\varepsilon + \tau_k) \sin(\theta_k)}{R_{c\hat{c}}(\varepsilon) + \sum_{k=1}^M \alpha_k \text{sinc}(T_p D_k) R_{c\hat{c}}(\varepsilon + \tau_k) \cos(\theta_k)} \right\} \quad (6)$$

The term "Double Delta DLL" is a general expression for a DLL which employs two correlator pairs with different correlator spacings. The circulating expressions "High Resolution Correlator" (HRC), "Strobe Correlator", "Pulse Aperture Correlator" (PAC) are all equivalent from the conceptual point of view. In this work we will consider only the *Coherent Double Delta*, but also a *Non-coherent Double Delta* or eventually a *Dotproduct Double Delta* are possible. In writing the discriminator of the Double Delta DLL, we will indicate by  $2\Delta_1$  the smaller correlator spacing and by  $2\Delta_2$  the larger one.

The multipath error bias experienced by a DLL is any stable lock point different from zero, to which a DLL converges, after the transient tracking error subsequent to the code acquisition has faded away. Denoting by  $S_c(\varepsilon)$  a generic composite discriminator function, and by  $S_c(\varepsilon)$  its counterpart in absence of multipath, a stable lock point is a value  $\varepsilon_{lock}$  of the tracking error for which two conditions are fulfilled:

$S_{c, Coh}(\varepsilon) =$	$2 \sum_{k=0}^N \gamma_k \text{sinc}(T_p D_k) \cos(\theta_c(\varepsilon) - \theta_k) \cdot \left\{ \int_{-B}^B C(f) \hat{C}^*(f) \sin(2\pi f(\varepsilon + \tau_k)) \sin(2\pi f \Delta) df \right\}$
$S_{c, Nc}(\varepsilon) =$	$\sum_{n=0}^N \sum_{m=0}^N \gamma_n \text{sinc}(T_p D_n) \gamma_m \text{sinc}(T_p D_m) \cos(\vartheta_n - \vartheta_m) \cdot \left\{ \int_{-B}^B C(f) \hat{C}^*(f) e^{j2\pi f(\varepsilon - \Delta + \tau_n)} df + \int_{-B}^B C(f) \hat{C}^*(f) e^{j2\pi f(\varepsilon - \Delta + \tau_m)} df + \int_{-B}^B C(f) \hat{C}^*(f) e^{j2\pi f(\varepsilon + \Delta + \tau_n)} df + \int_{-B}^B C(f) \hat{C}^*(f) e^{j2\pi f(\varepsilon + \Delta + \tau_m)} df \right\}$
$S_{c, Dp}(\varepsilon) =$	$\sum_{n=0}^N \sum_{m=0}^N \gamma_n \text{sinc}(T_p D_n) \gamma_m \text{sinc}(T_p D_m) \cos(\vartheta_n - \vartheta_m) \left\{ \int_{-B}^B  C(f) ^2 \cos(2\pi f(\varepsilon + \tau_n)) df + 2 \int_{-B}^B  C(f) ^2 \sin(2\pi f(\varepsilon + \tau_m)) \sin(2\pi f \Delta) df \right\}$
$S_{c, \Delta\Delta}(\varepsilon) =$	$2 \sum_{k=0}^N \gamma_k \text{sinc}(T_p D_k) \cos(\vartheta_c(\varepsilon) - \theta_k) \cdot \left\{ \int_{-B}^B C(f) \hat{C}^*(f) \sin(2\pi f(\varepsilon + \tau_k)) \cdot [\sin(2\pi f \Delta_1) - \frac{1}{2} \sin(2\pi f \Delta_2)] df \right\}$

**Table 1** Composite discriminators

- $S_c(\varepsilon_{lock}) = 0$
- $\text{sign} \{S'_c(\varepsilon_{lock})\} = \text{sign} \{S'(0)\}$

in which  $S'_c(\varepsilon) = \frac{\partial S_c}{\partial \varepsilon}(\varepsilon)$ .

The quantity  $S'(0)$  is called "discriminator gain" and it is positive if an early-late discriminator is used. If we take on this convention, then a stable lock point is any point at which the discriminator crosses zero with a positive slope. When only the LOS component impinges on the receiver,  $\varepsilon = 0$  is always a stable lock point. If the correlation function of the PN code has only one maximum, this lock point is unique. In a multipath scenario the S-curve is distorted in a way that the  $\varepsilon = 0$  might not be a lock point any more, and additional lock points might be introduced. Which of these zero crossing becomes the multipath error bias depends on the acquisition phase. Let  $\varepsilon_0$  be the value of the tracking error after the initialization. If  $\varepsilon_0$  is such that  $S(\varepsilon_0) > 0$ , the DLL will search the lock point among value smaller than  $\varepsilon_0$ . Vice-versa if  $\varepsilon_0$  is such that  $S(\varepsilon_0) < 0$ , the DLL will search the lock point among value larger than  $\varepsilon_0$ .

Let us define the set, whose elements are all the stable lock points; that is to say of all of the zero crossings by which the discriminator slope is positive:

$$Z_{S_c} \triangleq \left\{ \varepsilon_{lock} \mid S_c(\varepsilon_{lock}) = 0 \wedge \frac{\partial S_c(\varepsilon)}{\partial \varepsilon}(\varepsilon_{lock}) > 0 \right\} \quad (7)$$

Using this definition we can then express the tracking error bias due to multipath as :

$$b_\varepsilon = \underset{\varepsilon_{lock} \in Z_{S_c}}{\text{argmin}} \left\{ \left| \varepsilon_{lock} - \varepsilon_0 \right| \right\} \quad (8)$$

subject to

$$\begin{cases} \varepsilon_{lock} < \varepsilon_0, & \text{if } S(\varepsilon_0) > 0, \\ \varepsilon_{lock} \geq \varepsilon_0, & \text{if } S(\varepsilon_0) \leq 0, \end{cases}$$

Starting from the initial point  $\varepsilon_0$ , the bias is to be sought by inspecting values of the tracking error that are larger or smaller than  $\varepsilon_0$ , if  $S(\varepsilon_0)$  is respectively negative or positive. Equation (8) represents the value of the tracking error bias in a static scenario.

### TRACKING ERROR VARIANCE IN MULTIPATH

A full non linear description of the effect of noise on a Phase Lock Loop (PLL) can be found in [6]. Most of the principles apply also to a Delay Locked Loop. Nevertheless in this paragraph we will derive the expression of the tracking error variance in presence of multipath by linearizing the model. Indeed, as we will show, the the linear model can be modified and multipath can be included in it. The error signal of a DLL in presence of multipath propagation is:

$$e[k] = \begin{cases} \sqrt{P} S_c(\varepsilon; k) + n_T[k], & \text{Coh and } \Delta\Delta \\ P S_c(\varepsilon; k) + n_T[k], & \text{Nc and Dp} \end{cases} \quad (9)$$

where  $S_c(\varepsilon; k)$  is the composite S-curve at the k-th epoch, and  $n_T[k]$  is the noise term. Both the composite S-curve and the noise term of the error signal depend on the DLL structure. The multipath alters only the discriminator, but not the noise. So the statistical characterisation of the noise term  $n_T[k]$  is exactly the same as in the single path case.

A discriminator unaffected by multipath shows a linear behavior around the point  $\varepsilon = 0$ . This means that for values of the tracking error around 0, a linearization of the S-curve is reasonable. Multipath propagation distorts the S-curve by adding to the LOS S-curve other shifted and attenuated S-curves. The main result of this, is that the zero crossing of the composite S-curve does not take place any more at  $\varepsilon = 0$ , but at another point  $\varepsilon = b_\varepsilon$ . The shape of the S-curve is also distorted, but it is always possible to find a small region around the lock point  $\varepsilon = b_\varepsilon$ , for which the S-curve can be linearized. The extension of the linear region depends on the discriminator type, as well as on the multipath conditions. However, the linearization around  $\varepsilon = b_\varepsilon$  is always licit for "small" elongations from the lock point, that is to say for:

$$|\varepsilon - b_\varepsilon| \simeq 0 \quad (10)$$

This is the equivalent condition of the "small tracking" error used to calculate the variance in the case of single path: simply here the elongations around the stable point must be small and not their absolute values. In the single path case the two things were coinciding. If (10) holds,

then (9) can be linearized around the point  $\varepsilon = b_\varepsilon$ :

$$e[k] = \begin{cases} \sqrt{P} S'_c(b_\varepsilon; k)(\varepsilon - b_\varepsilon) + n_T[k], & \text{Coh and } \Delta\Delta \\ P S'_c(b_\varepsilon; k)(\varepsilon - b_\varepsilon) + n_T[k], & \text{Nc and Dp} \end{cases} \quad (11)$$

where  $S'_c(b_\varepsilon; k)$  is the derivative of the composite S-curve calculated at the point  $\varepsilon = b_\varepsilon$ , at the k-th epoch.

If we examine (11) without considering the noise term, it is evident that the error signal is zero when  $\varepsilon = b_\varepsilon$ . When this happens there is no feed-back, and the loop is stable. We are interested in the oscillations of the tracking error around this lock point, more specifically in the centered moment of the second order of the random variable  $\varepsilon$ :

$$E \left\{ \left( \varepsilon - E\{\varepsilon\} \right)^2 \right\} = \sigma_{\varepsilon, \text{mpath}}^2 \quad (12)$$

If the assumptions of steady state tracking are applicable, we can state that:

$$E\{\varepsilon\} = b_\varepsilon \quad (13)$$

Let us now define the tracking error around the stable point, or in other words biased tracking error as:

$$\varepsilon_b \triangleq \varepsilon - b_\varepsilon \quad (14)$$

in this way (11) can be rewritten as:

$$e[k] = \begin{cases} \sqrt{P} S'_c(b_\varepsilon; k)\varepsilon_b + n_T[k], & \text{Coh and } \Delta\Delta \\ P S'_c(b_\varepsilon; k)\varepsilon_b + n_T[k], & \text{Nc and Dp} \end{cases} \quad (15)$$

In steady state tracking, the mean value of  $\varepsilon_b$  is zero and its means-square value is equivalent to (12):

$$E\{\varepsilon_b\} = 0 \quad (16)$$

$$E\{\varepsilon_b^2\} = \sigma_{\varepsilon, \text{mpath}}^2 \quad (17)$$

The variance of the tracking error in the single path case has been found in [3] as a function of the noise power spectrum, by calculating the mean square value of the random variable  $\varepsilon$ : since  $\varepsilon$  is zero mean, the mean square value and the variance of  $\varepsilon$  are the same. If we now look at (15), the error signal is the same as in [3], with the only difference being:

- $S'_c(b_\varepsilon; k)$  in the place of  $S'(0; k)$
- $\varepsilon_b$  in the place of  $\varepsilon$

This means that the effect of multipath on the error signal is twofold: changing the slope of the S-curve around the stable point, and shifting the stable point away from zero. While the latter effect is important for the bias, it plays no role in the variance of the tracking error: the variance of a random variable is an indication of how much the values of the random variable are spread around the mean, whatever the mean value is. Having said that, we can calculate

the mean-square error of  $\varepsilon_b$ , that is equivalent to the variance of  $\varepsilon$  (16), by following the same passages done in [3] and using (15) as the expression of the error signal.

$$E\{\varepsilon_b^2\} = \sigma_{\varepsilon,mpath}^2 = \begin{cases} \frac{2B_L N_T(0)}{P[S'_c(b_\varepsilon)]^2}, & \text{Coh and } \Delta\Delta \\ \frac{2B_L N_T(0)}{P^2[S'_c(b_\varepsilon)]^2}, & \text{Nc and Dp} \end{cases} \quad (18)$$

in which  $N_T(f)$  is the power spectral density of the noise, that depends on the DLL type. The autocorrelation of the noise term  $n_T[k]$  is not altered, and so its power spectrum; the quantity  $N_T(0)$  is the same to be found in a multipath free analysis. For completeness, we report in Table 2 its value for all DLL types.  $R_{\hat{c}}$  indicates the autocorrelation of the local reference:

$$R_{\hat{c}}(\xi) = \int_{-B}^B |\hat{C}(f)|^2 e^{j2\pi f \xi} df, \quad (19)$$

By combining (18) with the quantities given in Table 1 and Table 2, it is possible to give an explicit formulation of the tracking error variances for all DLL types, where  $B_L$  is the loop bandwidth:

$$\sigma_{\varepsilon,mpath,Coh}^2 = \frac{2B_L}{P[S'_{c,Coh}(b_\varepsilon)]^2} N_0 [1 - R_{\hat{c}}(2\Delta)] \quad (20)$$

$$\sigma_{\varepsilon,mpath,Nc}^2 = 2 \frac{N_0 B_L}{P[S'_{c,Nc}(b_\varepsilon)]^2} \left\{ 4R_{\hat{c}}^2(\Delta) [1 - R(2\Delta)] + \frac{N_0}{PT_p} [1 - R_{\hat{c}}^2(2\Delta)] \right\} \quad (21)$$

$$\sigma_{\varepsilon,mpath,Dp}^2 = \frac{2B_L N_0}{P} \frac{[1 - R_{\hat{c}}(2\Delta)]}{[S'_{c,Dp}(b_\varepsilon)]^2} \left\{ 1 + \frac{N_0}{2T_p P} \right\} \quad (22)$$

$$\sigma_{\varepsilon,mpath,\Delta\Delta}^2 = \frac{2B_L}{P[S'_{c,\Delta\Delta}(b_\varepsilon)]^2} N_0 \left\{ [1 - R_{\hat{c}}(2\Delta_1)] + \frac{1}{4} [1 - R_{\hat{c}}(2\Delta_2)] - [R_{\hat{c}}(\Delta_2 - \Delta_1) - R_{\hat{c}}(\Delta_2 + \Delta_1)] \right\} \quad (23)$$

$N_T(0)_{Coh} =$	$N_0 [1 - R_{\hat{c}}(2\Delta)]$
$N_T(0)_{Nc} =$	$4N_0 P R_{\hat{c}}^2(\Delta) [1 - R(2\Delta)] + \frac{N_0^2}{T_p} [1 - R_{\hat{c}}^2]$
$N_T(0)_{Dp} =$	$P N_0 [1 - R_{\hat{c}}(2\Delta)] + \frac{N_0^2}{2T_p} [1 - R_{\hat{c}}(2\Delta)]$
$N_T(0)_{\Delta\Delta} =$	$N_0 \left\{ [1 - R_{\hat{c}}(2\Delta_1)] + \frac{1}{4} [1 - R_{\hat{c}}(2\Delta_2)] - [R_{\hat{c}}(\Delta_2 - \Delta_1) - R_{\hat{c}}(\Delta_2 + \Delta_1)] \right\}$

**Table 2** DC component of the noise term  $n_T[k]$  of the error signal.

In (20), (21), (22), (23) appears the derivative of the composite discriminator calculated at the point  $\varepsilon = b_\varepsilon$ . This quantity can be easily found by deriving the respective expression in Table 1.

## TWO-PATH SCENARIO FOR TRACKING ERROR VARIANCE

Exemplarily we particularize these results for the well known two-paths propagation scenario. In the present figures the standard deviation is depicted, for the two cases in which the second path is either in phase ( $\vartheta_1 = 0$ ) or in opposition of phase ( $\vartheta_1 = \pi$ ). In every figure the multipath standard deviation for a particular DLL structure is shown. The parameters used to obtain these figures are represented in Table 3. In all the four figures the multipath standard deviation is compared with the standard deviation of the tracking error in absence of multipath.

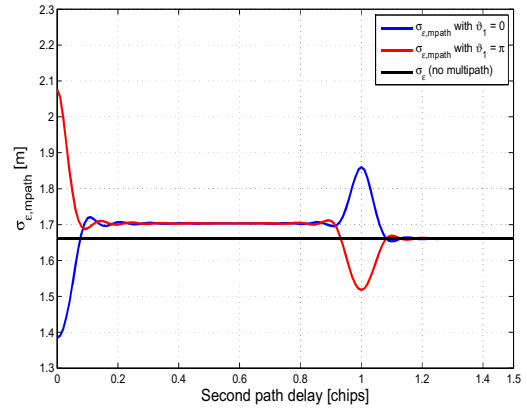


**Fig. 1** Two-paths standard deviation of the tracking error for a **Coherent DLL**. The second path has a normalized amplitude  $\alpha_1 = 0.2$ . The other parameters are specified in Table 3.

Parameter	Value
Correlator spacing( $2\Delta$ )	$0.1T_c$
Loop filter bandwidth	1 Hz
Integration time ( $T_p$ )	1 ms
$C/N_0$	30 dB
Pulse type	rectangular pulse
Pulse bandwidth	10.23 MHz
multipath relative amplitude( $\alpha_1$ )	0.2

**Table 3** Parameters used for the calculation of the multipath standard deviation of the tracking error represented in the figures.

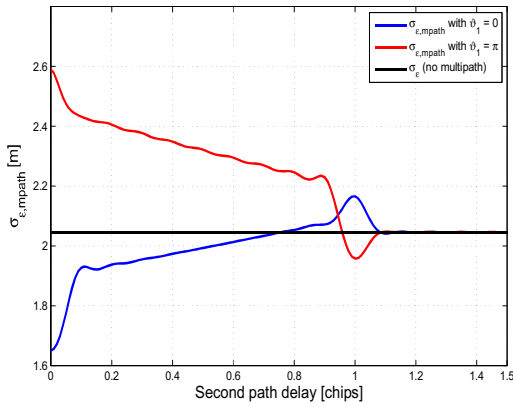


**Fig. 2** Two-paths standard deviation of the tracking error for a **Non-coherent DLL**. The second path has a normalized amplitude  $\alpha_1 = 0.2$ . The other parameters are specified in Table 3.

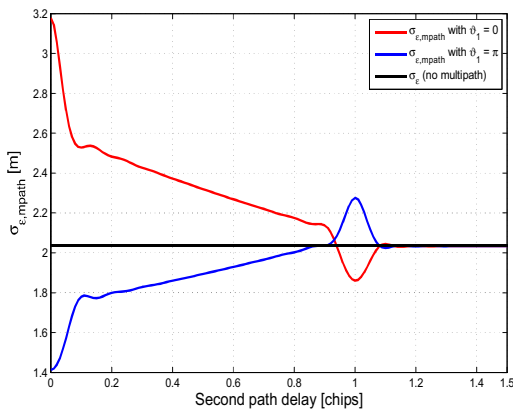


**Fig. 3** Two-paths standard deviation of the tracking error for a **Dot-product DLL**. The second path has a normalized amplitude  $\alpha_1 = 0.2$ . The other parameters are specified in Table 3.

It is not difficult to notice that, for small multipath delays, the values of the tracking error variance differs highly from the value calculated for only the LOS. In particular in the case in which the phase of the second path is  $\pi$ , the multipath variance is higher than the LOS variance, and the case having the second path in-phase presents a multipath variance which is lower.

Although these figures depict a restrictive propagation case, some general considerations can be drawn out of that. First of all, short multipath delays are the ones for which the influence of multipath over the tracking jitter is most heavily felt. Even though in a realistic scenarios the multipath phases are usually to be averaged, one has to keep in mind that there can be unlucky cases in which the tracking jitter can be particularly high. Eventually these "unlucky" cases can cause a *loss of lock*. As a last point, it

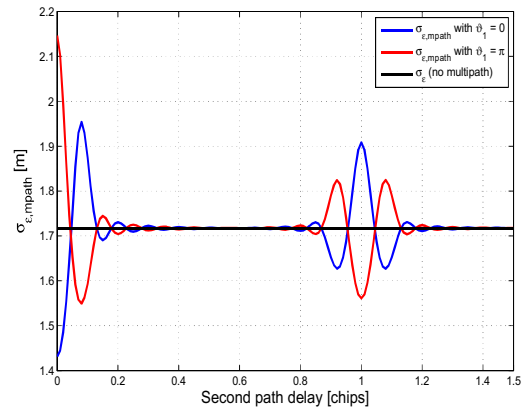


**Fig. 4** Two-paths standard deviation of the tracking error for a **Double Delta DLL**. The second path has a normalized amplitude  $\alpha_1 = 0.2$ . The other parameters are specified in Table 3.

is interesting to see, that the Double Delta DLL has better performance also from the point of view of the tracking jitter, especially for short multipath delays.

## MEAN SQUARE ERROR

Having determined the variance as a function of the multipath parameters, now the statistical characterization of the tracking error in presence of multipath is more complete: the bias and the variance of the tracking error depend on the multipath parameters through (8) and (18), and the MSE can be obtained

$$MSE_{\epsilon}(\alpha, \mathbf{D}, \tau, \vartheta) = b_{\epsilon}^2 + \sigma_{\epsilon,mpath}^2 \quad (24)$$

While the MSE is of value in many applications, the knowledge of the bias and the variance of the estimator provide a more complete picture of the performance than the MSE alone. Indeed it is possible to see what is the contribution of the bias to the MSE, and what the one given by the variance. Moreover, from the bias and the variance of the estimator other measures can be derived as the bias/variance ratio and the generalized  $MSE = \alpha g_1(b_{\epsilon}) + (1 - \alpha)g_2(\sigma_{\epsilon})$ , where  $\alpha \in [0, 1]$  and  $g_1, g_2$  are nonnegative functions [7].

## CONCLUSION

In this work we have shed some light on the possibility of assessing the influence of multipath on the tracking jitter of a DLL by means of mathematical description. When the channel is known and static, or at most slowly varying, it is possible to calculate the bias and the variance of the tracking error. Knowing the two means that one knows also the MSE, a very well known error metric. This analytical approach allows to evaluate the tracking performance

of a DLL by means of mathematical formulas, avoiding time-consuming simulations.

Future works on this line include a validation of the presented results by means of hardware signal simulations and also a further mathematical analysis on the relationship between multipath and the probability of losing lock.

## REFERENCES

- [1] Elliot D. Kaplan, "Understanding GPS: principles and applications", Artech House, Inc, 1996.
- [2] G.A. McGraw, M.S. Braasch, "GNSS Multipath mitigation using gated and High Resolution Correlator concepts", Proceedings of the National Technical Meeting of the Satellite Division of the Institute of Navigation, ION NTM, 1999.
- [3] Jack J. Holmes, "Spread spectrum systems for GNSS and wireless communications", Artech House, Inc, 2007, pag 478-481.
- [4] Markus Irsigler, Jose Angel Avila-Rodriguez, Gnther W. Hein, "Criteria for GNSS Multipath Performance Assessment", Proceedings of the 18th Annual International Technical Meeting of the Satellite Division of the Institute of Navigation (ION), Long Beach, CA, USA, September 2005.
- [5] Mariano Vergara , Felix Antreich , Geraldine Artaud, Michael Meurer, and Jean-Luc Issler, "On Performance Assessment of GNSS Receivers", ION GNSS 2009, Savannah, September 2009.
- [6] William C. Lindsey "Synchronization Systems in Communication and Control", Prentice Hall, 1972.
- [7] Alfred O. Hero, Jeffrey A. Fessler, Mohammad Usman, "Exploring Estimator Bias-Variance Tradeoffs Using the Uniform CR Bound", *IEEE Trans. Signal Processing*, 44(8) : 2026-2041, Aug. 1996.

## **Mobile broadband data reception in vehicles (Review lecture)**

G. Hirtz

Professur Digital- und Schaltungstechnik, TU Chemnitz, Chemnitz

Within introduction of DVB-T (Digital Video Broadcast Terrestrial and DAB (Digital Audio Broadcast) a new opportunity for broadband data reception in vehicles is given. Those digital transmission standards, developed for reception of entertainment content like TV and radio, just carry broadcast data, which can have any content.

Using this TV-broadcast infrastructure it's possible to transmit entertainment like TV-signals but also other data like traffic information, updated navigation maps, traffic signs etc. These data require a high data volume which cannot be handled by today's technology like RDS (Radio Data System) but the digital TV transmission schemes. The advantages and disadvantages of the different standards worldwide introduced are discussed.